International School for Advanced Studies

Modeling CO adsorption on Pt and Au monatomic chains and nanocontacts

Thesis submitted for the degree of

Doctor Philosophiæ

Candidate:
Gabriele Sclauzero

Supervisor:
Prof. Andrea Dal Corso

Trieste, April 2010

Contents

Introduction

Nanotechnology has become a word of common use and is attracting a lot of interest since it promises revolutionary applications and technological breakthroughs in many areas, from electronics to medicine, from information and communication technology to environmental and energy solutions, and several others. The term itself has acquired a broad meaning and encompasses a wide range of fields in many disciplines, but a common denominator of whatever falling within the scope of nanotechnology exists: it concerns the design, characterization and production of structures, devices and systems by controlling their shape and size at the nanometer scale. Many nanotechnology applications have already been realized or are on their way. Some examples are nanomaterials, materials which acquire novel properties and desired functionalities thanks to an atomic scale processing (obtained for instance by "functionalization" of coatings or paintings with nanoparticles); nanolithography in electronics; nanomedicine (nanosensors, drug delivery procedures); bottom-up approaches such as molecular self-assembly for DNA technology, and so on.

Besides the ability to engineer materials at the nanometer scale, or even to manipulate individual atoms and molecules, a necessary condition to go further in the realizations of nanotechnology is a full theoretical and experimental understanding of the physical phenomena and processes happening at this length scale in *low dimensionality* systems. A very important progress in this respect was achieved in 1981 with the invention of the Scanning Tunneling Microscope (STM) at IBM by Gerd Binning and Heinrich Rohrer (who later won the 1986 Nobel Prize in Physics for this accomplishment). That event is recognized by some as the birth of nanotechnology, since it actually launched the implementation of nano-manipulations of matter. The new experimental technique has enabled one to visualize atomic-sized features at the surface of solids, and later also to move around individual atoms in order to assemble artificial "nanoscopic" structures. Although the STM was conceived to operate in the tunnelling current regime (without making a tip-substrate contact), it became soon evident that it could also be used to gently touch or indent the sample with its very sharp metallic tip, in order to intentionally form tip-substrate contacts with dimensions of the order of a few nanometers.

When a contact shrinks down to dimensions of the same order or smaller than the electron mean free path, the conductance becomes *independent* on the contact length. This behaviour is well accounted for by the theory of *ballistic transport*, where the current is carried by electrons which can travel through quantum channels across the contact without losing phase coherence or suffering inelastic scattering events [1]. By tuning the tip-sample distance, contacts of several sizes can be studied, down to nanocontacts with a single atom in their narrowest part (the "constriction"). As such contacts become increasingly narrow while withdrawing the tip slowly, consecutive current measurements show that the conductance decreases in a stepwise fashion: plateaus alternate with abrupt jumps of the order of one quantum unit of conductance, $G_0 = 2e^2/h$ (where e is the electron charge and h is Plank's constant). In the theoretical framework of ballistic transport this stepwise behaviour can be explained by assuming that a conductor encompasses a number of channels N roughly proportional to the cross section of its narrowest part and a conductance of order $N \cdot G_0$ [2, 3]. Each time one or more of these channels is lost because of the narrowing process, the conductance is reduced by a discrete amount (approximately the number of excluded channels times G_0). Since the detailed atomic geometry of the nanocontact is not easily controllable, a discrepancy in the conductance can be observed for different contact realizations of equal cross-section. In order to extract information related exclusively to the specific material employed, and not on the particular realization of the nanocontact, data collected from many conductance traces are often cast in *conductance histograms*. These histograms generally show peaks at several values of conductance, corresponding to those atomic configurations of the contact which are realized more frequently.

If the constriction consists in a few rows of atoms, so that only a small number of electronic channels are available, the chemical nature of the atoms involved plays a fundamental role in determining the electron transport properties of the nanocontact. Consequently, the theoretical description of this kind of phenomenology requires a full quantum mechanical treatment of the system through suitable *ab initio* methods. A significant example of how crucial the chemical nature of atoms can be, is represented by atomic point contacts and monatomic chains, which are made up, respectively, of a single atom or of a free-standing row of atoms suspended between tips [3]. Such ultimately-thin structures can form sometimes in nanocontacts as the last stage before contact breaking and are responsible for the last conductance plateau in a conductance trace (before going to the tunneling current regime) or, equivalently, for the lowest conductance peak in the correspondent conductance histogram. In these one-atom-thick conductors the number of valence electrons of the material sets the upper limit of the conductance. As a consequence, the ballistic conductance is invariably very close to $1\,G_0$ in monovalent metals (Na) and noble metals with a filled d shell (Au,

Ag, Cu), where only one spin-degenerate, well-transmitted s conduction channel is present, while it can in principle be larger in transition metals with an open d shell, where additional conduction channels are provided by d electrons.

The formation process of metallic *monatomic chains* and their mechanical and conduction properties have been widely investigated in the last decade, both from the experimental [3–8] and the theoretical point of view [9–12]. Monatomic chains have been observed for the first time in gold nanocontacts: the row-by-row thinning, down to a single strand of atoms, of a gold nanocontact formed in a STM has been imaged by Ohnishi et al. [4] using a high-resolution transmission electron microscope. They have measured a conductance value very close to $1\,G_0$ for the linear single strand of gold atoms. At the same time, Yanson and coworkers [5] demonstrated that monatomic gold chains can be produced in mechanically controllable break-junctions too, showing that the exceptionally long last conductance plateaus observed in the conductance traces were actually caused by the formation of monatomic chains of length given by the plateau length. It was later discovered that long monatomic chains can be pulled also for some other heavy elements (besides Au, also Ir and Pt), while nanocontacts of lighter elements (such as $3d$ and $4d$ transition metals) break at the stage of a single-atom contact and have low probability of forming chains [6, 10, 12].

The reduced dimensionality of atomic-sized contacts (down to 1D in the limit of monatomic chains) favors the adsorption of *impurities* at the atoms in the constriction, owing to their lower coordination with respect to those in the bulk or at the surface [13–16]. It is nowadays well understood that accidental or controlled contaminations with small impurities may change substantially the nanocontact conductance. A possible range of applications has been already envisaged, from nanosensors [15], to electronic nose systems [17], or even electric current nano-switches [18]. From the experimental side a large number of case studies have been already examined, such as H_2 on Pt [19–21], Au [22, 23], and Pd [24] nanocontacts, but also on Fe, Co, and Ni nanocontacts [25]; CO on Pt [25, 26], Au, Cu, and Ni [26] nanocontacts; O_2 on Au and Ag nanocontacts [27]; and many others. The effect of contamination is usually visible in the conductance histogram: quite often the distribution of peaks is significantly altered after the admission of impurities in proximity of the nanocontact [19, 21, 22, 25–27]. Depending on the hosting metal, on the adsorbate atom or molecule, and on the adsorption geometry, very different outcomes on the low-bias conductance can be found: from a renormalization or broadening of the *histogram peaks*, to a removal of some peaks or to the appearance of new ones. For instance, in Pt nanocontacts the presence of H_2 causes the suppression of the peak at $1.5\,G_0$ and the formation of new peaks at $1\,G_0$ and $0.1\,G_0$ [19, 21]. Instead, in Au nanocontacts the intentional contamination with molecular hydrogen does not suppress the

main peak at 1 G_0, although its intensity slightly decreases; also in this case new features appear in the low-conductance region, such as a smaller peak near $0.5\,G_0$ and a low-conductance tail [22, 23]. In some cases the adsorption changes the formation process and the structural properties of the chain [27]: a remarkable example is the enhancement of monatomic chains formation for gold nanocontacts in O_2-enriched atmosphere, which has been attributed to atomic oxygen embedded in the chains [27, 28].

Unfortunately, up to now no direct imaging of impurities adsorbed on nanocontacts has been done, hence the adsorption geometries are not known directly from experiments. Sometimes the orientation of the molecule is deduced indirectly, for instance by studying its vibrational modes with point-contact spectroscopy [20]. In other cases the adsorption configuration is inferred in nanocontact simulations by comparing the theoretical conductance of some plausible geometries with the new peaks in the conductance histograms [18, 29, 30]. STM images of CO adsorbed on monatomic chains are instead available for chains deposited on a substrate template, such as Au chains grown on a NiAl substrate [31] or self-assembled dimer Pt chains on the reconstructed (001) surface of Ge exposed to Pt [32–34] (although in the latter case there is a debate on the real nature of these chains [35, 36]). However, a simultaneous measurement of conductance *through* the chain is not possible in these cases.

Although several theoretical studies have been carried out so far in this field [13, 18, 23, 28, 37–41], the comprehension of the physical properties for such systems is far from being complete. While the adsorption processes of small molecules on surfaces have been characterized in detail and thoroughly in the scientific literature for the majority of substrate/adsorbate complexes, an analogous understanding for the chemistry of adsorption on nanocontacts and nanowires is still lacking. For instance, the energetics of different adsorption geometries have not been investigated systematically and the influence of the geometrical strain of the chain on the adsorption process is poorly known. Another point which needs to be studied in more detail is the importance of the finite chain length in the adsorption process and the degree of applicability of the conclusions obtained in a 1-D system (such as the free-standing monatomic chain) to the suspended chains actually produced in nanocontacts. Finally, it is not completely clear in which cases standard density-functional theory (DFT) simulations can give a correct quantitative (or even qualitative) description of the system, especially for what concerns its conductance properties. The conventional methods based on the Landauer-Büttiker theory are quite successful in many cases [3], but can fail completely in others, for instance in weakly coupled molecular junctions (see, e.g., Refs. 42–45, and references therein) or systems characterized by Kondo physics [46].

In order to take some steps forward in the understanding of these issues, in this thesis we studied CO adsorption on Pt and Au chains from first principles within

DFT, using the QUANTUM ESPRESSO suite of electronic structure codes [47]. We have chosen this particular molecule (carbon monoxide) because Kiguchi et al. [26] have recently investigated CO adsorption on metallic nanocontacts comparing four different metals, namely Au, Cu, Pt and Ni. Their experimental study shows that CO adsorption takes place in all these metals, but the conductance histograms modifications are metal-dependent. Histograms of transition metals (Pt and Ni) are subject to big changes, such as major peak shifts and appearance of new peaks, while histograms of more noble metals (Au and Cu) conserve their original features to a large extent. Among these four metals, we have chosen Pt and Au as representatives, respectively, of a noble metal and of a transition metal. Both of them are known to develop monatomic chains in nanocontact experiments [3, 6, 10]. The experimental evidence that the nanocontact conductance after CO adsorption depends strongly on the metal suggests that an accurate chemical description of the molecule/chain interaction is fundamental to address the problem.

A few theoretical studies of CO adsorption on Pt and Au monatomic chains have appeared to date. CO on Pt nanocontacts has been studied from first principles by Strange et al. [29], who have identified a stable "tilted bridge" configuration for the Pt-CO-Pt contact which could be responsible for the fractional peak appearing in the conductance histogram of Pt after exposition to CO gas [25]. A more recent study calculated the chemisorption energies and ballistic conductances for a few adsorption configurations, trying to identify the configurations responsible for the individual peaks in the conductance histograms of Pt contaminated with CO [30]. CO adsorption on Au nanocontacts has been investigated prevalently to explain possible modifications in the structure and stability of Au chains [13, 48]. The effect of CO adsorption on the electronic structure and ballistic conductance of a monatomic gold chain has been studied only for a few particular configurations: for instance, CO in an ontop position on a stretched chain [49], chosen in order to match the experimental geometry of CO on short supported Au chains [31]. Both the experiment and the theory agree that CO should act as a "chemical scissor" of the electronic delocalization of some metallic states in the chain, and ballistic conductance calculations show that CO ontop suppresses the coherent electron transport across the chain [49, 50]. These results are not adequate to explain the experimental findings of Kiguchi et al., since the conductance histogram of Au in presence of CO does not display any low conductance tail, which should instead be present as long as the electron transport in Au chains could always be blocked by CO. Indeed, a more recent theoretical study by Xu et al. [51] reported that the bridge site should be favored in short suspended Au chains and that the conductance of the chain is not reduced sensibly by CO adsorption.

The aim of our theoretical study is to characterize in detail the chemical bond

between CO and chains of Pt or Au and to establish a tight connection between ballistic transmission modifications and adsorption-induced features of the electronic structure. For this purpose we started from the simplest model: a single CO molecule attached to an infinitely-long, straight monatomic chain at equilibrium spacing. By comparing a selected set of plausible adsorption sites, such as an upright CO atop of one metal atom, CO bridging two metal atoms (which we find to be favoured), and a substitutional CO in a longitudinal configuration, we highlight differences and similarities related to the adsorption geometry. We find that the adsorption mechanism of CO on Pt and Au chains can be described by a donation-backdonation process, in a much similar way as in the well-known Blyholder model [52] for CO adsorption on transition-metal surfaces (and its successive refinements [53, 54]). In the simplest version of this model, the mechanism and strength of adsorption are governed by a balance between *donation* of σ electrons from the molecule to the metal and *backdonation* of electrons from the metal to the $2\pi^\star$ empty orbitals of the molecule. We also find that transmission channels corresponding to those electronic states of the chain which are more involved in the chemical bond suffer stronger reflections and, in some cases, are almost completely blocked by the barrier represented by the impurity. Additionally, we pinpoint an interesting correspondence between particular peaks in the density of states and transmission dips or depressions centered at the same energies, especially for those peaks which originate from a direct hybridization of the metal s band with the orbitals of CO. Each peak is characterized by an energy position and a broadening width which are determined not only by the specific metal of which the chain is made up, but also by the adsorption site of CO. Although this aspect might be of secondary importance in Pt chains, where also d electrons contribute to the conductance, it turns out to be more crucial in Au chains, where the conductance can be entirely attributed to s electrons.

During the pulling process of a nanocontact, monatomic chains can pass through different states of *strain*, which could possibly result in a different catalytic activity of the Au chains [16] or in a change of the details of the molecule/chain interaction. We therefore investigated what is the effect of strain both on the chemical bond between CO and Au chains and on the adsorption-induced features of the electron transmission. We demonstrate that the position of these metal- and site-dependent transmission dips, which set in because of the interaction with CO, are also sensitive to strain and strongly influence the conductance of stretched Au chains with CO ontop. The conductance of this system decreases with increasing strains and is almost suppressed in highly stretched configurations because of a transmission dip moving close to the Fermi level (in agreement with previous calculations [49, 50]). At opposite, we find that the conductance of Au chains with CO at the bridge site is much less reduced with respect to the pristine chain than in the ontop geometry and it slightly

increases with strain. The same mechanism does not apply to Pt chains, since the transmission dips in the s channel are much higher in energy and also d channels contribute to the conductance, and hence the bridge and ontop geometries have similar conductance properties in Pt.

In monatomic chains of Pt and Au (or any other transition metal), the reduced coordination typical of one-dimensional systems gives rise to a narrowing of their $5d$ bands, leading to a much larger dependence of the results on the so-called self-interaction error (SIE), which stems from the inexact cancellation between Hartree and exchange energy terms [55]. In Au chains at lower strains, the SIE of $5d$ levels pushes the edges of the two $|m| = 1$ bands very close to the Fermi energy, giving rise to two additional conduction channels and a Stoner-like magnetic instability which results in a wrong, slightly magnetic ground state [56]. Therefore, DFT predictions of the conductance in infinite Au chains at spacings around the equilibrium value are not much reliable and consequently this system is usually studied at a much larger Au-Au spacing to remove the spurious d channels from the conductance. As reported by Wierzbowska et al. [57] for transition metal monatomic wires, a DFT+U approach can cure the SIE of localized d electrons, shifting down in energy filled or almost filled electronic bands. We will show that by employing a standard DFT+U scheme [58, 59] a non-magnetic ground state can be recovered in the Au chain at equilibrium, since the position of the ($5d$) $|m| = 1$ bands is rapidly pushed down already at small values of U. The same result can be obtained by building the local atomic occupations entering in the DFT+U formalism from the overlap with pseudopotential (PP) projector functions (which are localized within the atomic spheres), instead of using the full, non-localized atomic wavefunctions [60]. This simplification allows to include straightforwardly the Hubbard term of the potential in the scattering equation for the transmission by simply changing the PP coefficients. In this way we could enable the calculation of complex band structures and transmission properties within the DFT+U framework in `PWcond`, the plane wave PP code for ballistic transport used in this work [61]. This method applied to Au chains at equilibrium spacing allows to restore the correct number of conduction channels and get rid of spurious $5d$ contributions to the conductance (which is an artifact of the SIE). Because of the above-mentioned transmission dip, which is much closer to E_{F} in the ontop geometry, a noticeable difference between the conductances of the non-strained bridge and ontop geometries is unveiled by the DFT+U result, while in the plain DFT calculation it was hidden by the spurious contribution of d channels.

Since Pt and Au are heavy elements, *spin-orbit coupling* (SOC) also play an important role in the band structures and transmission properties of Pt and Au monatomic chains [56], but nevertheless these effects are often disregarded. SOC can be introduced in the Kohn-Sham equations and in the scattering equation for ballistic trans-

port [62] through *fully-relativistic* (FR) PPs [63, 64]. We recomputed geometries, chemisorption energies and transmission functions for the case of CO on monatomic Pt chains using FR PPs: our calculations showed that, in this specific case, SOC produces small effects on the geometry and on the ballistic conductance, but transmission properties at energies below the Fermi energy are heavily modified. In the case of CO ontop of a stretched Au chain, the FR conductance predicts a higher value with respect to the *scalar-relativistic* (SR) value (which is close to zero), but this result is again affected by the wrong position of $5d$ states caused by the SIE, which at the moment we are not able to correct in the FR case.

Finally, by simulating short suspended chains between (001) surfaces of gold, which allow to describe a geometry more similar to the experimental one, we studied how the conclusions for CO adsorption on an ideal quasi-1D conductor (such as the infinite monatomic chain model studied so far) are modified by a finite length of the chain or by the presence of surfaces and tips. Although there are quantitative differences with the simpler free-standing chain model, key properties such as the adsorption site preference or the clear-cut distinction between ontop and bridge conductances are verified for long enough chains (at least 4 Au atoms). Chemisorption energies and ballistic conductances are comparable with those obtained with the unsupported infinite chain model and confirm that CO is able to suppress the conductance of stretched gold chains only when adsorbed ontop, but not when at the bridge. The value of the conductance of the bridge geometry nicely agrees with the lowest conductance peak found by Kiguchi and coworkers for Au nanocontacts in presence of CO, while the difference in adsorption energy between ontop and bridge geometries (which favors the latter by more than 1 eV) could explain why a low conductance tail due to ontop adsorption is not observed in MCBJ experiments.

The material of this thesis is organized as follows. In the first chapter we give a brief overview on the fabrication techniques of metallic nanocontacts and nanowires, we introduce some concepts about ballistic transport and make a survey of experimental results. The second chapter is devoted to a description of the theoretical methodology and technical details behind the *ab initio* electronic structure and ballistic transport calculations. Here we will also describe a way to easily include in ballistic transport calculation a DFT+U scheme, by employing local projections truncated at the atomic sphere radius. In the third and fourth chapter we present our results about the interaction between CO and (infinite) monatomic chains made of Pt or Au, respectively, and how this interaction changes the electronic transmission in tipless chains. In the successive chapter we describe the energetics and ballistic conductance of short Au chains suspended between surfaces (or between smoother tips in a few test cases) with and without one CO molecule adsorbed at the central site of the chain, and we make a comparison with the results from tipless geometries. In the Appendix, a section is

dedicated to a comparison of spin-orbit splittings computed either with FR-USPPs or within first-order perturbation theory, motivating the usage of this kind of PP to describe SOC effects, while another section contains some reference data on the isolated CO and on the isolated chains of Pt and Au.

CHAPTER 1

Ballistic conductance: experiments and theory

Metallic contacts with cross sections of the order of a nanometer in their narrowest part can be realized routinely with modern experimental techniques. For some metals, the cross section of such *nanocontacts* may even be as small as a single atom. In most experiments, a nanocontact is usually detected and characterized by measuring its conductance. Precise conductance measurements for a variety of nanocontacts have brought to light phenomena which cannot not be explained by the familiar Ohm's law. A breakdown of the classical picture of charge transport in metals occurs once the nanocontact shrinks down to dimensions close to, or smaller than, the electron mean free path (which ranges from a few nanometers in metals, to several tens of microns in high-mobility semiconductors). It is then necessary to adopt a ballistic theory of the electron transport in order to explain these conductance measurements. Moreover, because the cross section can often have a diameter of the order of the Fermi wavelength λ_F (which is a few angstroms in metals, thus comparable to an atomic radius), the wave nature of matter must be taken into account and a full quantum mechanical treatment of the problem is required. The ballistic conductance in such low-dimensional systems is also tightly connected to the chemical nature of the atoms making up the nanocontact. In experiments different kinds of metals can

be distinguished by their typical conductance values; the chemical modifications in the narrowest part of the nanocontact, induced, for instance, by local adsorption of small impurities, can modify these values in a variety of ways.

In this chapter, after having introduced the main techniques for nanocontacts fabrication, we will explain the Landauer-Büttiker approach for the ballistic conductance and report some evidences of ballistic transport phenomena in experiments with metallic nanocontacts and of the existence of monatomic Pt and Au chains. We will then focus on the effect of CO on the ballistic transport properties of Pt and Au atomic-sized contacts and chains, reporting on some experimental and theoretical studies which have appeared in the literature.

1.1 Nanocontact fabrication techniques

A nanocontact can be defined as a nanometer-size metallic constriction connected to two macroscopic electrodes in such a way that the current flows through the narrowest part of the contact. There are mainly three widely used experimental techniques for building metallic contacts of nanometer cross section: the Scanning Tunneling Microscope (STM), the mechanically controllable break-junction (MCBJ) and the high-resolution transmission electron microscope (HRTEM). A large part of the nanocontact experiments nowadays employ one of these techniques or combine two of them.

1.1.1 Scanning Tunneling Microscope

The STM, introduced in 1981 by Gerd Binning and Heinrich Rohrer, has rapidly become an instrument of widespread usage to study properties of materials at the nanometer length scale [65]. This technique enabled to scan the surface topology of conducting materials with a previously unachieved spatial resolution: it is now even possible to visualize single atoms deposited at surfaces. A STM setup consists of a very sharp metallic head (called "the tip") which can be positioned very close to the surface to be imaged and connected to an electrical circuit that simultaneously measures the tunneling current between the surface and the tip.[1] The surface-tip distance can be controlled with high precision thanks to the exponential decay of the tunneling current with length: atoms at the surface feel the interaction with the atoms at the tip apex only, if the latter is sufficiently sharp. The tip-surface distance is kept constant through a feedback circuit that controls the tip elevation in such a way that a steady tunneling current is maintained.

[1] This procedure can be utilized directly only with metallic surfaces, while surfaces with an insulating behaviour need to be treated with a preceding metalization phase.

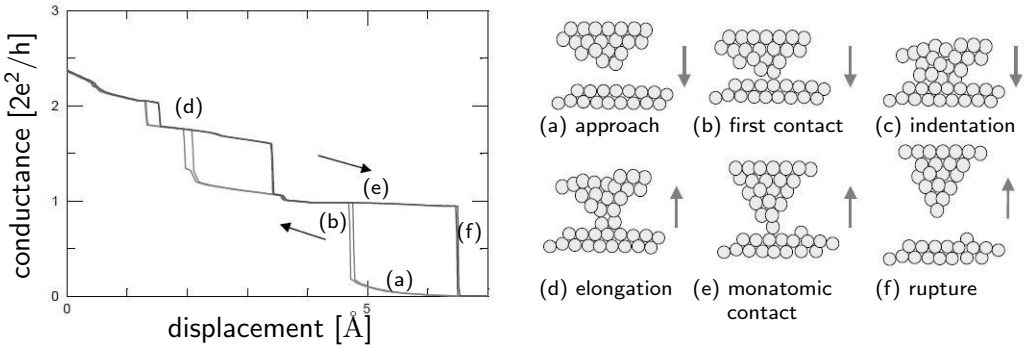

Figure 1.1: *Conductance trace for a gold nanocontact obtained in a STM experiment at low temperatures (left side). Schematic illustration of the fabrication steps of a clean nanocontact through indentation (right side). Reprinted from Ref. 3.*

In the standard mode of usage, a full contact between the surface and the tip is carefully avoided in order not to damage the tip, but several experiments showed that single adatoms can be dragged around the surface by STM tip, altering artificially the atomic structure of the sample. This second usage mode is also a very effective way to produce and study metallic nanocontacts: when the surface is touched by the tip, the transition from the tunneling regime to the contact regime can be identified by the sudden rise of the conductance [3]. This jump in the conductance is clearly visible in Fig. 1.1, which shows a conductance measurement as a function of the tip-substrate displacement in a STM experiment. The thinnest line in the plot corresponds to the tip approaching the surface and shows the exponential growth with length of the tunnel regime (a), followed by an abrupt increase (b).

It is not always easy to make a clean metallic junction because of contaminants or oxides which can be present in the atmosphere or on the surface and may prevent a direct contact between the atoms of the tip and those at the surface, especially in experiments performed at room temperature and not in ultra-high vacuum (UHV) conditions. A widely-adopted practice to solve this problem is the so-called "indentation": the tip is repeatedly crashed against the surface, so that it can penetrate slightly into the sample. In this way contaminants accidentally adsorbed nearby are pushed aside from the indentation area, leaving an uncontaminated region where a clean metallic contact can be established straight after [3]. This sequence of operations is sketched schematically in the six panels, (a) through (f), in Fig. 1.1 on the right side.

Once the indentation procedure has been completed, conductance traces (such as those on the left side in the same figure) can be recorded by repeating steps (a),(b),(d),(e) and (f), skipping the indentation step (c). Each time the two ends

come back together and form a contact, a conductance jump from the regime of tunneling current (a), to that of metallic conduction (b) can be observed. When the tip is pushed further against the surface (i.e., going to smaller values of the displacement in Fig. 1.1), the conductance trace displays *plateaus* of variable length alternating with sudden *jumps*. Experiments combining STM and atomic force microscope (AFM) techniques, where the conductance trace is complemented with a measurement of the force exerted on the sample by the tip, have demonstrated that plateaus can be associated to the elastic deformation of stable configurations of the atoms in the nanocontact, while jumps can be matched with very fast rearrangements of its atomic structure. Throughout the elongation process, when the tip is slowly withdrawn from the surface, a sequence of alternating jumps and plateaus can be observed too. It has been widely accepted that also in this case stable atomic configurations, subject to an elastic stretching, are followed by inelastic deformations, consisting in a restructuring of the atomic configuration, triggered by an increase of the tension over the sustainability threshold. In conductance traces, like that shown in Fig. 1.1, the *last plateau* before going to the tunneling regime is usually associated to an atomic configuration with a contact made of a *single atom* (often called "monatomic" contact), as exemplified in step (e).

1.1.2 Mechanically controllable break-junction

The exact arrangement of atoms in the nanocontact cannot be controlled during the formation and breaking cycles and can be very different from one cycle to the next. This shortcoming leads to a lack of reproducibility of the individual conductance measurements, therefore several repetitions of the contact formation/breaking cycle are performed so that the conductance can be averaged over the atomic configurations of the nanocontact. The averaged conductance is more representative of the material under exam, rather than of a particular realization of the nanocontact. In order to accumulate statistics more rapidly and efficiently, it has proven convenient to use the MCBJ technique, since it allows for much faster formation/breaking cycles than those attainable with a STM.

The MCBJ was introduced by Moreland and Ekin in 1985 and later developed and modified by Müller [3]. The technique is based upon the mechanism illustrated on the left side in Fig. 1.2: a very thin wire of the material under exam (1) is disposed on a substrate (3), which must be elastic and insulating. The wire is notched in the middle in order to reduce its cross section in the central region and it is then glued on the substrate. The bending beam can be curved by pushing upwards the extensible central support (5), causing an expansion of the upper surface of the beam and a thinning of the contact in proximity of the notch (region indicated by "u"

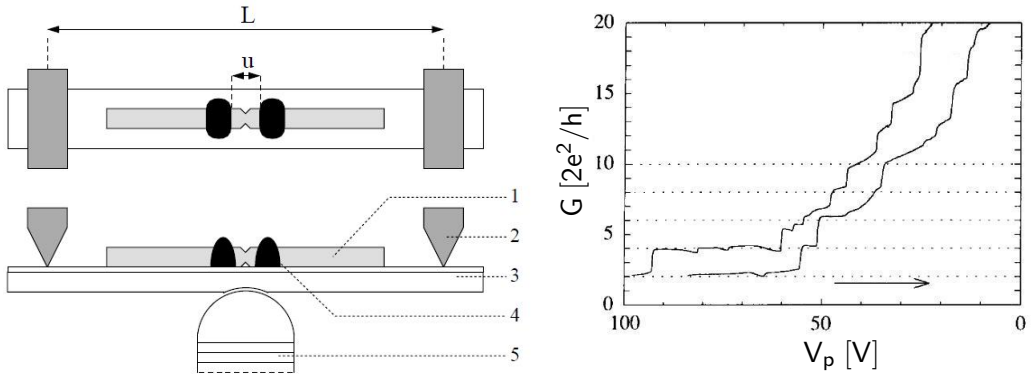

Figure 1.2: *Left: Schematic view of a MCBJ setup, with the notched metallic sample (1), two counter supports (2), the bending beam (3), epoxy drops (4), and the extensible support made of stacked piezoelectric elements (5). Right: Two examples of conductance traces for Pt nanocontacts obtained in MCBJ experiments. The electrodes are pushed together by lowering the voltage V_p on the piezo-element; an estimate of the displacement is* 10 V $\sim$ 1 Å. *Pictures reprinted from Ref. 3.*

in the picture), where the strain is concentrated. After the rupture of the contact, the two cleanly exposed surfaces thus created can be brought together to form a new contact by retracting the extensible support. The two surfaces generated after contact breaking can be quite irregular, therefore the junction formed after coming back to contact is expected to be composed of a single atom. Sample conductance traces obtained from a MCBJ experiment are shown in Fig. 1.2 on the right side: this typical measurement is characterized by plateaus interleaved with abrupt jumps, analogous to those shown previously in Fig. 1.1 (from a STM experiment).

1.1.3 High-resolution transmission electron microscope

Nanocontacts fabricated through the HRTEM can be directly imaged at an atomic resolution right after their production. The fabrication procedure, due to Kondo and Takayanagi [66], starts with the perforation of an ultra-thin metallic film by focusing an high-intensity electron beam in order to make two adjacent holes. If the holes are sufficiently close to each other, a few nanometers wide metallic bridge forms at the touching point. When such atomic bridge shrinks down to the size of one or two nanometers and is next to rupture, the electron beam intensity is reduced to the operational level for the imaging process and a real time picturing of the nanocontact can be realized.[2] Owing to thermal vibrations and mechanical instabilities, the cross-

[2]At the stage when the bridge is being produced, instead, the metallic film is vibrating because of the electron flow and imaging is not possible. See Ref. [8] for a more detailed description of the whole procedure.

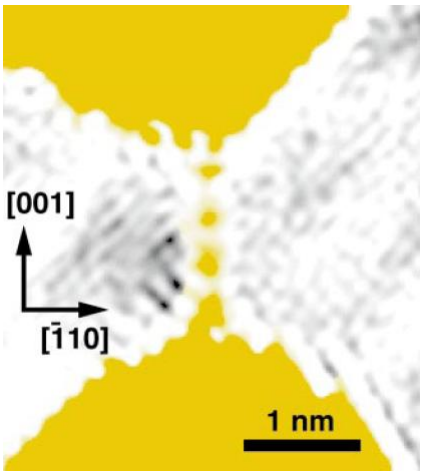

Figure 1.3: *HRTEM image of a single strand of gold atoms (four of them, colored yellow) which bridges two banks in a gold film (colored areas). The atomic row is oriented along the [001] direction of the (110) gold film and the spacing between gold atoms in the wire is about* $3.5 \div 4.0$ Å. *Reprinted from Ref. 4.*

section of such contacts reduces progressively, until nanowires made of a few parallel rows of atoms are formed. Nanowires produced in this way are relatively stable since they are embedded in the monolithic crystal structure of the metallic film, nevertheless they tend to thin down until they break at some point. The thinnest structure that can be formed is a single linear strand of atoms between the edges of the film, such as the four-atom-long gold nanowire shown in Fig. 1.3; gold nanowires produced in this way can be kept stable for a few minutes before breaking [4].

1.2 Theoretical notes on ballistic transport

Electronic transport in macroscopic conductors is described by Ohm's law, which allows to compute the conductance G of a metallic bar (given its geometry and the conductivity, σ, of the material):

$$G = \sigma \frac{A}{L} , \tag{1.1}$$

where A is the cross section and L the length of the bar. The relation in Eq. (1.1) can be applied only if the transport regime is *diffusive*. This is the case for metallic samples with dimensions much larger than the electron mean free path l_{m}, that can be roughly considered as the average distance between two consecutive collision events suffered by a conduction electron. In the semi-classical picture of charge transport, the motion of the electrons in the diffusive regime ($L \gg l_{\mathrm{m}}$) is described by a random walk. The electronic transport turns into the *ballistic* regime when the dimension of the contact become comparable or smaller than the electron mean free path ($L < l_{\mathrm{m}}$). If we look at even smaller conductors, when the contact cross-sections approaches the size of an atom we enter in the quantum transport regime. The length scale which

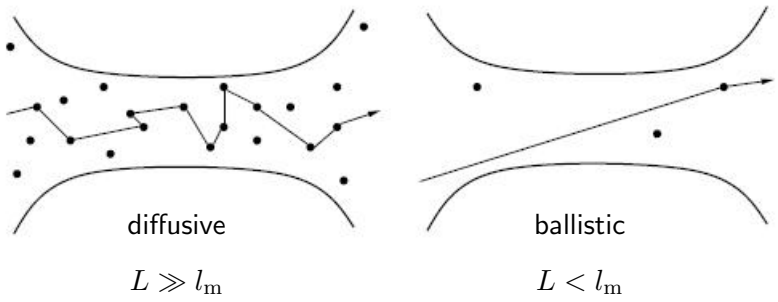

Figure 1.4: *Schematic illustration of ballistic and diffusive transport regimes in metallic nanocontacts (adapted from Ref. 3).*

distinguishes this transport regime from the semi-classical one is the Fermi wavelength, $\lambda_F = 2\pi/k_F$ (where k_F is the Fermi wavevector modulus), usually of the order of a few angstroms in metals. When considering metallic contacts of nanometer (or sub-nanometer) dimensions it is mandatory to take fully into account the quantum mechanical nature of the electron in order to get reliable predictions about the conductance.

The low-bias conductance of nanocontacts in the ballistic quantum transport regime is usually calculated within the Landauer-Büttiker approach,[3] which links the conductance to the transmission probabilities of the electronic wavefunctions at the Fermi energy. Within this approach, a nanocontact is generally modeled as a scattering region connecting two electron reservoirs through a couple of metallic leads, as depicted schematically in Fig. 1.5. Inside the leads, electrons behave as propagating Bloch waves along the longitudinal direction, while in the perpendicular directions their momentum is quantized because of the lateral confinement. If a small bias voltage is applied between the reservoirs, the current is carried by a finite number of left- and right-moving "modes", in close analogy with the transmission process of the electromagnetic field in metallic waveguides. The number of modes allowed by the lateral confinement of the metallic constriction obviously depends on the size in the transverse directions: in the limit of an infinitesimal cross section, one can assume that only one transverse mode is admitted, hence there will be only one channel available for charge transport.

In order to derive a formula for the conductance within Landauer and Büttiker's method some assumptions about the reservoirs and their coupling with the leads are needed. The two reservoirs are considered as ideal sources and sinks of charge and the electron distribution in the inner region of the reservoirs is unaffected by the processes taking place in the surroundings of the resistive region. The small voltage

[3]For a more detailed discussion of the topic the reader can refer to the book by Datta [1].

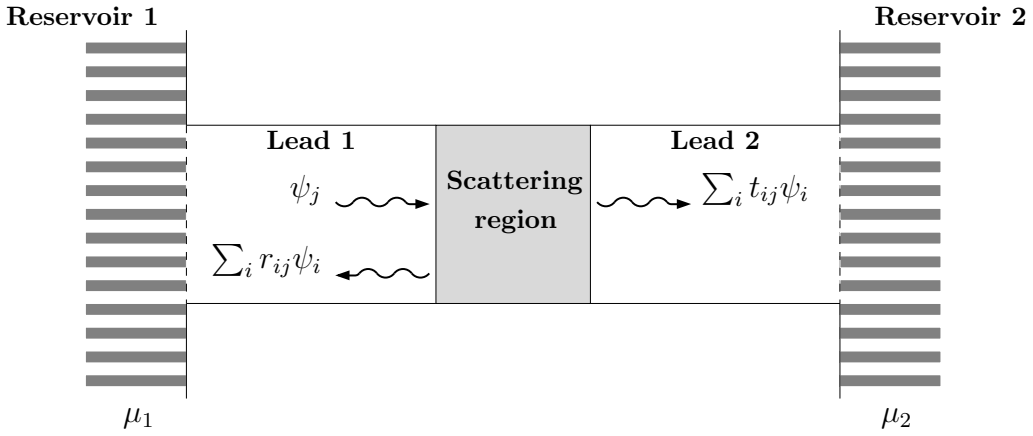

Figure 1.5: *Model of multi-mode conductor for ballistic transport calculations within the Landauer-Büttiker approach. An incoming mode ψ_j is transmitted into mode ψ_i of Lead 2 with probability t_{ji} and reflected into mode ψ_i of Lead 1 with probability r_{ij}.*

drop V between the reservoirs drives a tiny imbalance of the electronic populations inside the two electrodes (we indicate the left one with f_1 and the right one with f_2). Since the reservoirs are in a quasi-equilibrium condition, the electronic populations f_1 and f_2 can be approximated by two Fermi distributions: the former is described by a chemical potential, μ_1, while the latter by a slightly different one, μ_2, both very close to the Fermi energy for the system at the equilibrium, such that $(\mu_1 - \mu_2) = eV$ (where e is the electron charge). An ideal coupling between the reservoir and the lead on each side is assumed, so that the interfaces do not introduce for the outgoing waves any additional back-scattering or reflection to those originating in the resistive region. Since a right-moving electron inside Lead 2 is perfectly transmitted to Reservoir 2 (and, similarly, a left-moving electron inside Lead 1 is perfectly transmitted to Reservoir 1), the distribution of electrons with wavevector $+k$ inside Lead 1 and the distribution of electrons with wavevector $-k$ inside Lead 2 are fixed by the electron distribution in the corresponding Reservoir (f_1 and f_2, respectively). The electric current from Reservoir 1 to Reservoir 2 originates from the imbalance of the electronic populations and only states belonging to the energy range between μ_1 and μ_2 give a net contribution, while below μ_1 the current carried by electrons with wavevector $+k$ is exactly counterbalanced by the electrons with wavevector $-k$.

These hypotheses let us calculate the conductance for a one-dimensional conductor which has a single active mode. The current is directly proportional to the group velocity of the electron,

$$v_k = \frac{1}{\hbar}\frac{\partial E_k}{\partial k} \ , \tag{1.2}$$

and to the difference between the electronic populations at $+k$ and at $-k$, hence it

can be written as:

$$I = \frac{e}{L_z} \sum_{k\sigma} v_k \big(f_1(E_k) - f_2(E_k) \big) \,, \tag{1.3}$$

where L_z is the longitudinal size of the conductor and the summation is performed over the allowed k only. For long enough conductors we can replace the summation over k with the appropriate integral and, thanks to the relation between the group velocity v_k and the density of states $\rho(E) = 1/v_k\hbar$, we can rewrite the integral as follows:

$$I = \frac{e}{\pi} \int v_k \big(f_1(E_k) - f_2(E_k) \big) \, \mathrm{d}k = \frac{2e}{h} \int \big(f_1(E) - f_2(E) \big) \, \mathrm{d}E \,, \tag{1.4}$$

where in the first passage we have summed over the spin σ assuming spin degeneracy. When the reservoirs are at the same chemical potential, $\mu_1 = \mu_2 = E_F$, the current vanishes since the electronic distribution in both reservoirs becomes equal to the Fermi distribution for the system at equilibrium:

$$f_0(E) = \left[\mathrm{e}^{(E-E_F)/k_B T} + 1 \right]^{-1} \,, \tag{1.5}$$

but if a small bias voltage, $\delta V = (\mu_1 - \mu_2)/e$, is applied between the reservoirs a current δI will flow across the junction.

In the *linear regime*, the current δI is proportional to the bias voltage and the ballistic conductance becomes:

$$G = \frac{\delta I}{(\mu_1 - \mu_2)/e} = \frac{2e^2}{h} \int \left(-\frac{\partial f_0}{\partial E} \right) \mathrm{d}E \,. \tag{1.6}$$

At low temperatures the Fermi distribution and its derivative can be approximated with

$$f_0(E) \simeq \theta(E_F - E) \,, \qquad \frac{\partial f_0}{\partial E} \simeq \delta(E_F - E) \,, \tag{1.7}$$

where θ is the step function and δ is the delta Dirac distribution, therefore Eq. (1.6) gives $G = 2\,e^2/h \equiv G_0$, the quantum unit of conductance. According to this expression for the conductance, even a perfect conductor between two electrodes has a finite resistance, which in a single-mode conductor is equal to $G_0^{-1} \simeq 13.8\ \mathrm{k}\Omega$.

Because of the scattering phenomena taking place inside the resistive region, the single current-carrying mode has a probability $T(E)$ of being transmitted into the lead at the opposite side and a probability $R(E) = 1 - T(E)$ of being reflected back, hence the formula for the current in Eq. (1.4) can be generalized as [1, Sec. 2.5]:

$$I = \frac{2e}{h} \int T(E) \big(f_1(E) - f_2(E) \big) \, \mathrm{d}E \,, \tag{1.8}$$

and, repeating the passages above with this new expression for I, the conductance becomes:

$$G = \frac{2e^2}{h} T(E_F) \; . \tag{1.9}$$

This relationship states that, within the linear regime, the conductance can be obtained by simply evaluating the transmission coefficient at the Fermi energy. The single-mode ideal conductor corresponds to the limiting case of a perfectly-transmitted mode, $T(E_F) = 1$, which gives a conductance of G_0.

We will now introduce a more general formalism, which can be applied to conductors with more than one mode available for electron transport. Each mode can be partially reflected and partially transmitted into itself or into the other modes. If we suppose that, at a fixed scattering energy, N_1 modes are active in the left lead (Lead 1) and N_2 modes are active in the right lead (Lead 2), the amplitudes of the incoming modes and those of the outgoing modes are connected by the so-called "scattering matrix" $\mathbf{S}$, which is block-partitioned as follows:

$$\mathbf{S} = \begin{pmatrix} \mathbf{s}_{11} & \mathbf{s}_{12} \\ \mathbf{s}_{21} & \mathbf{s}_{22} \end{pmatrix} = \begin{pmatrix} \mathbf{r} & \mathbf{t}' \\ \mathbf{t} & \mathbf{r}' \end{pmatrix} \; , \tag{1.10}$$

where $\mathbf{s}_{\alpha\beta}$ is a $N_\alpha \times N_\beta$ matrix with elements $(\mathbf{s}_{\alpha\beta})_{ij}$ equal to the ratio between the amplitude of an outgoing mode ψ_i of Lead α and the amplitude of an incoming mode ψ_j of Lead β (see also Fig. 1.5).

One can prove that the expression in Eq. (1.9) can be used straightforwardly to calculate the linear regime conductance also in multi-mode conductors by substituting the transmission coefficient evaluated at the Fermi energy with the following expression [67]:

$$T(E_F) = \mathrm{tr}\left[\mathbf{t}^\dagger \mathbf{t}\right] = \sum_{ij} |t_{ij}|^2 \; . \tag{1.11}$$

It must be noted here that the conductance can be computed with $T(E_F)$ as in Eq. (1.11) only if the scattering matrix elements $(\mathbf{s}_{\alpha\beta})_{ij}$ have been defined as the ratio between normalized amplitudes (i.e., of modes carrying unitary current). In that case, the conservation of charge ensures that the $\mathbf{S}$ matrix is unitary [67], hence the following relationship between matrix blocks $\mathbf{r}$ and $\mathbf{t}$ holds:

$$\mathbf{r}^\dagger \mathbf{r} + \mathbf{t}^\dagger \mathbf{t} = \mathbb{1} \; , \tag{1.12}$$

as well as an analogous expression for blocks $\mathbf{r}'$ e $\mathbf{t}'$.

If we know only the matrix $\widetilde{\mathbf{S}}$, with elements $(\tilde{\mathbf{s}}_{\alpha\beta})_{ij}$ defined in terms of the non-normalized amplitudes of modes ψ_i and ψ_j (not carrying unitary current), we cannot compute the transmission coefficient directly through the formula in Eq. (1.11), since

$\widetilde{\mathbf{S}}$ is in general a non-unitary matrix. However, we can bring $\widetilde{\mathbf{S}}$ into a unitary form which can be used in Eq. (1.11) by properly normalizing its elements in the following way [1, Sec. 3.1]:

$$(\mathbf{s}_{\alpha\beta})_{ij} = \sqrt{v_i/v_j}\,(\tilde{\mathbf{s}}_{\alpha\beta})_{ij}\ , \tag{1.13}$$

where v_i is the electron group velocity for state ψ_i, given by Eq. (1.2) for states normalized within the volume. A method for computing the scattering matrix and the normalization coefficients for realistic systems treated from first-principles will be described in Sec. 2.6

Since the matrix $\mathbf{t}^\dagger\mathbf{t}$ is Hermitian, there always exists a unitary transformation $\mathbf{U}$ such that $\mathbf{U}^{-1}\mathbf{t}^\dagger\mathbf{t}\,\mathbf{U}$ is diagonal with the N_1 real eigenvalues $\tau_1, \tau_2, \ldots \tau_{N_1}$ on the main diagonal. Owing to the unitary condition of the scattering matrix, from Eq. (1.12) it follows that $\mathbf{r}^\dagger\mathbf{r}$ e $\mathbf{t}^\dagger\mathbf{t}$ can be diagonalized through the same transformation U and that the eigenvalues of $\mathbf{t}^\dagger\mathbf{t}$ satisfy to $0 \leqslant \tau_i \leqslant 1$, $\forall\, i$, since both matrices are positive definite. The eigenvectors of $\mathbf{r}^\dagger\mathbf{r}$ and $\mathbf{t}^\dagger\mathbf{t}$ are called *transmission eigenchannels* and correspond to particular linear combinations of incoming modes which propagate independently from each other. Within the eigenchannels basis the transport problem becomes a simple superposition of N_1 independent channels, each characterized by its transmission probability τ_i, and the conductance can be conveniently rewritten as:

$$G = \frac{2e^2}{h}\sum_{i=1}^{N_1}\tau_i\ . \tag{1.14}$$

In the limit of perfectly transmitted eigenchannels (i.e. $\tau_i = 1,\ \forall i$), the relation in Eq. (1.14) gives the conductance of a perfect multi-mode conductor with N_1 spin-degenerate modes, $G = N_1 \cdot G_0$.

It is worth mentioning here that the formulas in Eq. (1.9) and Eq. (1.11) or, equivalently, that in Eq. (1.14) allow us to compute the linear regime conductance measured across the two reservoirs (see Fig. 1.5), because μ_1 and μ_2 are the chemical potentials for the electrons at equilibrium well inside the reservoirs. However, this does not require us to solve the scattering problem between the reservoirs, which involves a huge number of modes. Thanks to the absence of back-scattering at the lead/reservoir interfaces that has been previously assumed, it is sufficient to evaluate the scattering matrix $\mathbf{S}$ taking into account only the modes (generally a small number) propagating within the leads [1, Sec. 3.1]. By evaluating the transmission coefficient *across the leads* we can thus compute the contact conductance *across the reservoirs* using the relation $G = (2e^2/h)\,T(E_F)$.

1.3 Ballistic conductance measurements in nanocontacts

As seen in Sec. 1.1, during contact formation and breaking cycles the transition point from the tunneling regime to the metallic conduction is easily detectable in conductance traces. The evolution of a conductance trace in the regime of metallic contact is closely related to the structural modifications of the nanocontact and to the material of which it is composed. Notwithstanding this, all conductance traces show some remarkable similarities, which can be spotted out by comparing the traces for gold in Fig. 1.1 and Fig. 1.8 with those for platinum in Fig. 1.2. All plots display a clear sequence of plateaus: these are quite flat at low conductance values, but they have a negative slope at higher conductances. Each plateau is followed by an abrupt jump, which usually corresponds to a change in the conductance of the order of $1G_0$. These abrupt changes in the conductance during the pulling or pushing of the contact have been addressed by experiments combining the usual conductance recording with simultaneous atomic force measurements on the nanocontact. This kind of conductance variations have been explained with almost instantaneous rearrangements of the atomic structure of the nanocontact, rather than to conductance quantization effects in a junction with a smoothly varying cross section. According to this picture, plateaus correspond to meta-stable atomic configurations which are destabilized when the stress applied externally to the contact grows above a certain threshold. The observation of hysteresis phenomena and spontaneous fluctuations between two conductance levels seems to confirm this view.

The scarce reproducibility of plateau lengths and of their conductance values from one trace to the next (and also from one experiment to another) suggests that the conduction of a nanocontact during formation/rupture cycles is tightly connected to the detailed atomic structure in proximity of the nano-junction. However, with the exception of a few cases, experimental measurements do not determine simultaneously the conductance and the precise atomic geometry of a nanocontact step by step. Therefore the conductance properties of nanocontacts are often described by collecting in form of an histogram a great number (usually thousands) of conductance traces similar to those reported in Fig. 1.1 and Fig. 1.8. This procedure allows one to average the conductance over a large set of atomic configurations of the nanocontact, retaining only those features which are characteristic of the material under examination and of its electronic structure properties.

An example of conductance histogram is shown in Fig. 1.6 for gold. The conductance values are reported on the abscissa, which is subdivided into bins of fixed width; each conductance measurement during a contact formation/breaking cycle corresponds to an event which is added to the count of the corresponding bin, according

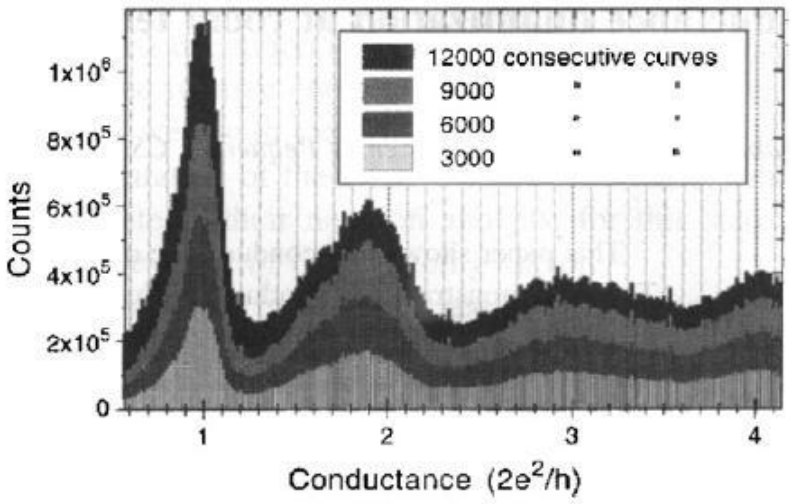

Figure 1.6: *Conductance histogram for gold nanocontacts recorded at room temperature (data from [68]). Curves drawn with progressively darker color show the histogram evolution as the number of conductance traces used to build it is increased.*

to the conductance value. One or more peaks are usually visible in such kind of histograms: the peak centered at the lowest conductance value is generally attributed to an atomic configuration of the contact with a single atom, or a strand of atoms, in the narrowest part of the junction [3]. The distribution of peaks in the conductance histogram is quite well reproducible for some metals, even under very different experimental conditions. *Gold* is the archetypal of this class of metals: conductance histograms for this material are the less sensitive to differences in the environmental conditions where the junction is formed, which can vary a lot from one experiment to the other. Peaks at $1\,G_0$, $2\,G_0$, and $3\,G_0$ are quite common in conductance histograms of gold nanocontacts and the peak at $1G_0$ survives in all circumstances [3–6, 26]: it can be matched with the last plateau before rupture, which is always present in the conductance traces of gold.

Other metals do not display such a striking regularity; however a peak centered at $1\,G_0$ (or at a slightly lower conductance) is commonly seen in other noble metals (such as Cu and Ag, besides Au) and in alkaline metals (Li, Na, K) [3]. This peak is assigned to the single-atom contact and its conductance value arises from a single mode almost perfectly transmitted attributable to s valence electrons. The lowest conductance peak in the conductance histograms of *transition metals* is found instead well above $1\,G_0$ in the majority of experiments, and it cannot be identified with an integer conductance value [3]. This feature is clearly visible in experiments performed at very low temperatures and in UHV conditions, which often show a main peak between $1.5\,G_0$ and $2.5\,G_0$ in the conductance histograms for Ni, Rh, Pd, Ir and

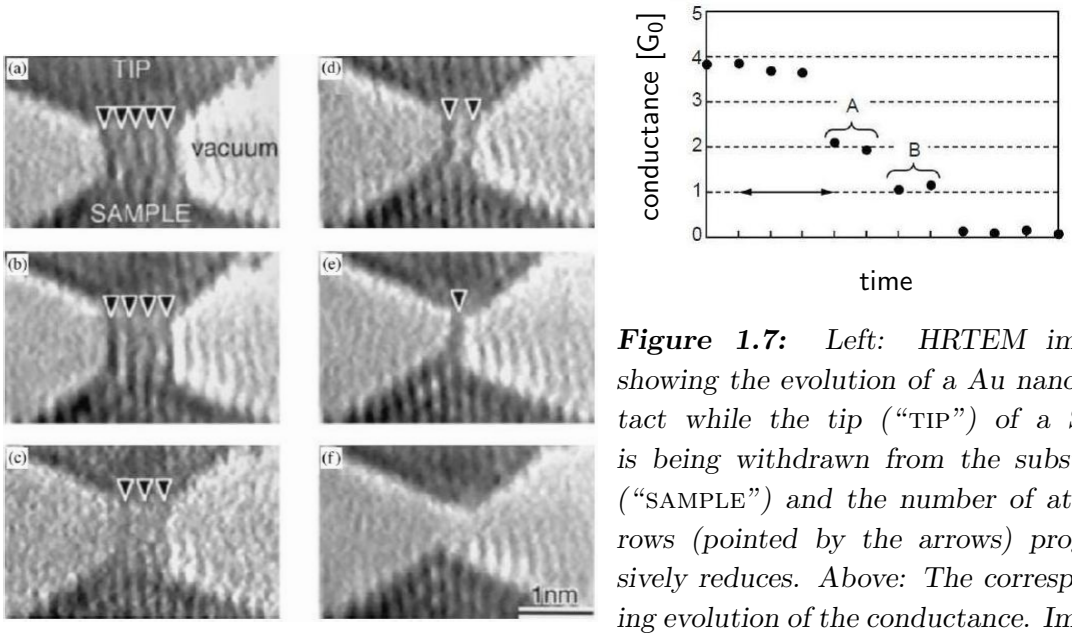

Figure 1.7: *Left: HRTEM images showing the evolution of a Au nanocontact while the tip ("*TIP*") of a STM is being withdrawn from the substrate ("*SAMPLE*") and the number of atomic rows (pointed by the arrows) progressively reduces. Above: The corresponding evolution of the conductance. Images reprinted from Ref. 4.*

Pt [6, 8, 25, 26], and is usually rationalized assuming that electrons belonging to the partially-filled valence *d* shell give rise up to five partially-transmitted additional channels in the one-atom contact. On the other hand, experiments performed at room temperature do not show a reproducible distribution of peaks: the lack of regularity in this kind of measurements has been attributed to the accidental presence of contaminants next to the junction, which could be responsible for changes in the conductance properties of the nanocontact [3, 25, 26] (see also Sec. 1.5 and Sec. 1.6).

1.4 Formation and conductance properties of monatomic chains

In October 1998, two reports appeared on the same review issue of *Nature* announcing simultaneously that one-atom-thick chains (or "monatomic chains") could be produced by progressively reducing the cross section of a gold nanocontact and that these chains could be maintained stable for several minutes at very low temperatures [4, 5]. The striking discovery was achieved by two independent experiments using very different techniques. Ohnishi and coworkers [4] recorded a sequence of HRTEM images showing the formation process of monatomic chains within a miniaturized STM placed at the specimen position of the HRTEM. The high resolution snapshots of the nanocontact taken during the withdrawal of the STM tip from the sample after contact making show with an atomic resolution the shrinking of the atomic junction

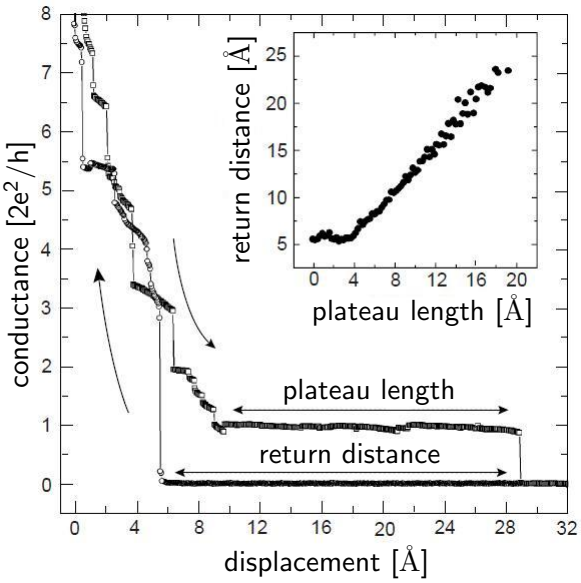

Figure 1.8: *Conductance trace recorded as a function of the displacement in a MCBJ experiment: the conductance trace begins at the top left corner (squares). The inset shows the average return distance against the plateau length (from STM measurements): there is a linear correspondence to a good level of approximation. Reprinted from Ref. 5.*

between the tip and the sample and eventually the formation of an atomic bridge a few atoms thick. In some occasions, just before rupture they could observe a single strand of atoms suspended between the metallic tips, as shown by the sequence of images in Fig. 1.7 on the left side. The number of atomic rows is seen to decrease by one unit at a time as the STM tip is withdrawn from the surface and, correspondingly, the conductance displays a stepwise behaviour, reaching values very close to 1 G_0 for the single strand (as in the two measurements labeled with "B" on the right side of the same figure).

The other article issued by Nature reported about the formation of monatomic chains in gold nanocontacts produced using a STM and a MCBJ at very low temperatures (4.2 K). In that experiment, Yanson et al. [5] did not image directly the chains, but rather they inferred that free-standing linear strands made of several gold atoms in a row had formed inside the nanocontact from the presence of exceptionally long plateaus in the conductance traces. Indeed, they observed that the last conductance plateau before going to tunneling regime always exhibits a conductance value very close to $1\,G_0$ and often extends for distances much longer than an atomic diameter, as it can be seen in Fig. 1.8, where a 2 nm long plateau obtained while pulling the tips apart is shown. They gave a confirmation of this hypothesis by measuring the so-called "return distance", the length by which the tips need to be displaced from their position at the moment of the rupture in order to bring them back into contact. If a tiny linear structure, such as a monatomic chain, is connecting the tips, then the atoms of the chain would re-adsorb on the surfaces soon after rupture, leaving between the tips an empty space of the same length of the former chain. Hence, the return distance must be approximately equal to the chain length and a linear

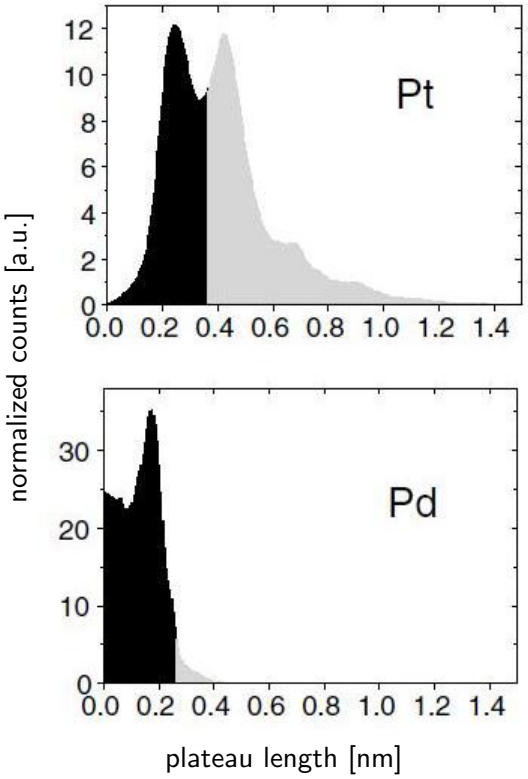

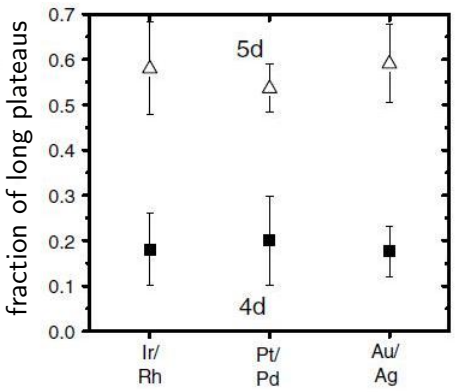

Figure 1.9: *Left: plateau length distribution for Pt and Pd nanocontacts formed in a MCBJ: the grey area corresponds to events in which a long plateau is formed (see text). Above: fraction of long plateaus over the total number of contacts formed for the 6 transition metals studied in [6].*

relationship should hold between them; this one-to-one correspondence, apart from an offset due to the elastic response of the tips, is clearly shown by the plot in the inset of Fig. 1.8.

The existence of monatomic chains has been substantiated also for metals other than gold, either directly through HRTEM imaging, or indirectly from the analysis of conductance measurements. Rodrigues et al. [8], for instance, reported HRTEM snapshots of Co, Pd and Pt nanowires produced by performing two nearby holes on a ultra-thin metallic film. Smit et al. [6] studied the formation of monatomic chains in transition metal nanocontacts analyzing a large number of conductance traces (similar to those reported in Fig. 1.8) produced in a MCBJ experiment at low temperatures. For a series of three $5d$ metals (Ir, Pt e Au) and the corresponding $4d$ series (Rh, Pd, Ag), the length of the last plateau (the one corresponding to the conductance of the atomic point contact) has been used to build histograms for the length distribution of the atomic chains formed as the contact was pulled apart. The length distribution histograms for Pt and Pd are shown in Fig. 1.9 on the left side: the histogram for Pt (as well as those for the other $5d$ metals) has several regularly spaced peaks, with a splitting between the peaks comparable to the atomic diameter in the bulk. In the histograms for Pd (and in those for the other $4d$ metals), instead, only one peak

is found: the peak corresponds to a plateau length smaller than the bulk atomic diameter and only a minuscule tail of events with longer plateaus is present. This difference in the histograms shows that, while Ir, Pt and Au have a strong tendency to form spontaneously monatomic chains in the last stage prior to the rupture of the contact, in the case of Rh, Pd and Ag there is a very high probability that the monatomic contact breaks at a shorter length, comparable to a single atomic diameter or even lower.

Smit and coworkers have also estimated the interatomic distance in the chains of these $5d$ elements from the separation between the peaks in the histograms: they obtained 2.2 ± 0.2 Å in Ir, 2.3 ± 0.2 Å in Pt, and 2.5 ± 0.3 Å in Au [6]. These values are actually smaller than the nearest neighbours distances in the corresponding bulk phase (which are, respectively, 2.71 Å, 2.77 Å and 2.88 Å), hence, at least for these three materials, bond lengths shorten when moving to low-dimensional systems such as monatomic chains. The tendency of forming monatomic chains has been quantified by Smit et al. [6] in the same experiment using the data from the length distribution histograms to compute the fraction of "long" plateaus[4] with respect to the total number of contacts formed. By comparing this ratio for the six transition metals considered (see right plot in Fig. 1.9) it is evident that $5d$ metals have a much stronger probability (about 3 times higher) than $4d$ metals to form long suspended monatomic chains in this kind of experiments.

1.5 Pt and Au nanocontacts in presence of CO: experiments

The effect of light impurities on the conductance properties of Pt and Au nanocontacts has been studied in several experiments. Different kinds of impurities have been considered, such as molecular hydrogen [19–23], molecular oxygen [27], carbon monoxide [25, 26], and others. However in this section we will focus mainly on the case of CO.

A MCBJ experiment performed at room temperature in UHV conditions by Rodrigues et al. [8] explored the conductance properties of nanocontacts made of ferromagnetic (Fe, Co, Ni), "quasi-magnetic" (Pd), and non-magnetic (Pt) transition metals. In the conductance histograms for all these three classes of metals they found unexpected peaks at fractional values of conductance (i.e. around $e^2/h = G_0/2$), which they explained with the possibility of spin-polarized electron transport through

[4] In Ref. Smit et al. [6] a plateau has been defined as "long" if it is at least one and a half times longer than the chain length associated to the lowest lying peak in the histogram. In Fig. 1.9 the fraction of long plateaus is represented by the ratio between the grey shaded area and the total area obtained by integrating the histogram curve over the whole range of lengths.

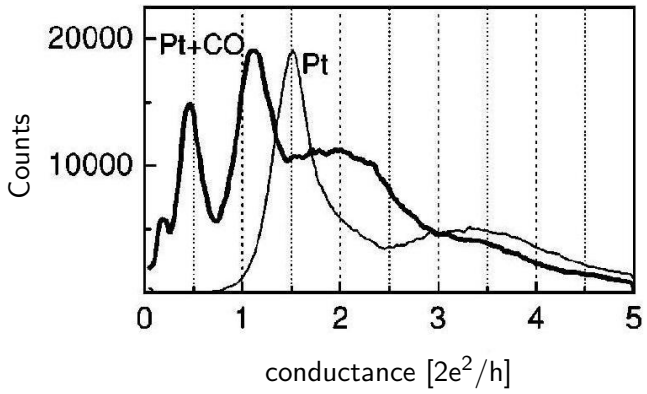

Figure 1.10: *Conductance histogram for a Pt nanocontact before (thin line) and after (thick line) intentional contamination by CO gas. Reprinted from Ref. 25.*

a spontaneously magnetized nanowire or point-contact. Also the histogram for Pt, which has a non-magnetic bulk phase, has such a peak at about $0.5\,G_0$, although it is much smaller than the main peak at $1.5\,G_0$.

Soon later, Untiedt et al. [25] studied Fe, Co, Ni, and Pt nanocontacts with a low-temperature MCBJ experiment in UHV conditions, which allow to produce perfectly clean contacts. At difference with Rodrigues et al., they didn't find any fractional peak in the histograms for the clean metals, both in absence and in presence of an external magnetic field, and thus ruled out spin-polarized transport as a possible explanation for those peaks. They showed instead that the conductance histograms of Fe, Co, and Ni are subject to large changes when the experiment is performed in a hydrogen-enriched atmosphere. The principal histogram peak, which is above $1\,G_0$ for the clean nanocontacts, moves very close to $1\,G_0$ for these three ferromagnetic metals after exposition to H_2, however no fractional peak emerges in the histograms. Noting that in the case of Pt a stable configuration of H_2 between the metal electrodes had been previously identified [19] and that it gives a $1\,G_0$ conductance, they deduce that also in the case of Fe, Co and Ni the molecule could stick next or in the middle of the contact and modify its conductance.

They also showed that the fractional peak of Pt seen by Rodrigues et al. can be attributed to carbon-monoxide (CO) adsorption on the nanocontact. Conductance histograms for the clean Pt nanocontact are characterized by a main peak at about $1.5\,G_0$ and a much broader peak above $3\,G_0$ (see Fig. 1.10, thin line). After contaminating the contact with a small addition of CO, a fractional peak at about $0.5\ G_0$ appears in the histogram. The main peak at $1.5\ G_0$ disappears and in its place a large peak slightly above $1\ G_0$ becomes visible after CO adsorption (see Fig. 1.10, thick line). According to the authors, these new peaks should be attributed to the formation of stable configuration of CO between the Pt electrodes, while magnetism does not play any role in this case.

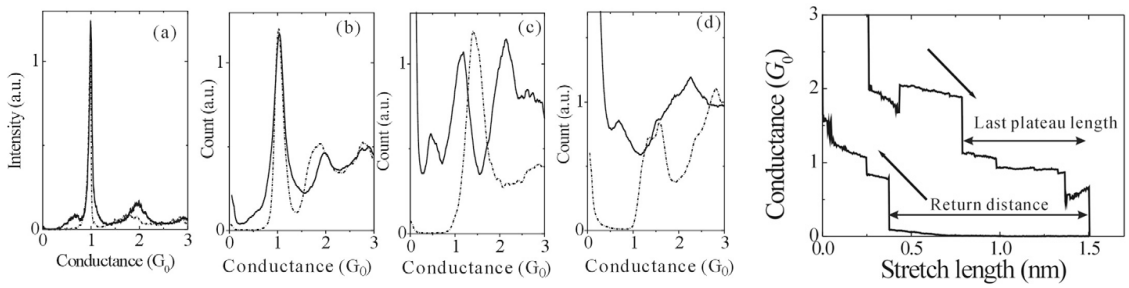

Figure 1.11: *Left: Conductance histograms of (a) Au, (b) Cu, (c) Pt, and (d) Ni nanocontacts before (thin dotted lines) and after admitting CO gas (thick lines). Right: Typical conductance traces measured for Au in presence of CO during contact breaking and restoring. Pictures reprinted from Ref. 26.*

Kiguchi et al. [26] studied the effect of CO on the conductance of nanocontacts made of different metals, namely Au, Cu, Pt, and Ni. Using the same experimental technique employed by Untiedt et al. [25], they compared the conductance histograms before and after the admission of the impurity in the environment where the MCBJ apparatus operates. Before admission of CO (see thin dotted lines in the histograms reported in Fig. 1.11), the conductance histograms are in agreement with previous experimental results for the clean metals: Au and Cu have a prominent peak centered near 1 G_0 and smaller peaks at higher conductance values (around 2 G_0 and 3 G_0), while Pt and Ni have a main peak at about $1.5\,G_0$ and broader features at larger conductances. After admitting CO gas in proximity of the nanocontact and repeating the conductance measurements (thick lines in the same figure), the conductance histograms are modified for all these elements. However, only slight changes are visible in the histograms of Au and Cu (first two from the left), such as a small fractional peak in the histogram of Au and a low conductance tail in that of Cu. The main peak at $1\,G_0$ is only slightly broadened, while the higher conductance peaks are slightly shifted towards larger values of conductance. The histograms of Pt and Ni (third and fourth from the left, respectively), instead, display much larger changes after CO admission and the original distribution of peaks is completely altered. In Pt, the peak at about $1\,G_0$ and the smaller peak at about $0.5\,G_0$ seen by Untiedt et al. [25] are well reproduced by this experiment (compare Fig. 1.10 with Fig. 1.11), while in place of the broad feature centered around $2\,G_0$ an additional strong peak is visible here. In Ni, it is not possible to distinguish a clear sequence of peaks, but only two broad features, one above $0.5\,G_0$ and another above $2\,G_0$. Both the histogram of Ni and that of Pt after contamination are characterized by a large low-conductance tail, which is instead much smaller in the histogram of Cu and completely absent in that of Au.

In the same experiment they have also focused on the small peak slightly above $0.5\,G_0$ observed in the histogram of Au after contamination. A typical conductance trace associated to the formation of the fractional peak is reported in Fig. 1.11 on the right side. After the monatomic Au chain has been formed between the electrodes (as witnessed by the length of the last conductance plateau), an abrupt change of the conductance from the monatomic chain value (around $1.0\,G_0$) down to about $0.5\,G_0$ is observed and the contact breaks after a small additional stretching (of 1.5 Å, approximately). This feature was found to be quite reproducible and has been imputed to the adsorption of a CO molecule on the Au nanowire or to the incorporation of a CO into the Au wire. The structure with fractional conductance thus formed destabilizes the Au nanowire and causes its sudden rupture after a small additional pulling of the contact [26]. The increasing slope of the fractional trace has been tentatively interpreted as an effect of a change in the molecular orientation of CO. In analogy to the conductance switching mechanism predicted from density-functional theory (DFT) calculations for the Au/H_2 nano-junction [18], Kiguchi and coworkers infer that also in the case of Au/CO junctions the change of the molecular orientation with respect to the contact axis, from a perpendicular to a longitudinal position, may be responsible for the increased conductance.

1.6 Pt and Au nanocontacts and chains with CO: simulations

Many *ab-initio* studies have addressed so far the interaction of Au nanowires with impurities such as light atoms or small molecules [13, 18, 23, 28, 37–41], focusing on the formation, stability and rupture mechanisms of the chain structures. Only a few first-principles calculations of CO on Pt and Au monatomic chains and nanocontacts have appeared to date [13, 29, 48, 49, 51] and, to our knowledge, no comparative study between the two metals exists.

1.6.1 CO adsorbed on a Pt point contact

Strange et al. [29] simulated within DFT the breaking cycle of a model Pt point-contact with a CO molecule initially adsorbed in an upright position bridging the two Pt apex atoms of the junction. The nanocontact is modeled with two pyramidal tips placed on facing Pt(111) surfaces and the pulling process has been simulated by gradually separating the surfaces and relaxing the atomic structure in the junction after each displacement. They find that, when the contact in stretched, at some point a configuration with a tilted CO bridging the two Pt tips becomes energetically convenient (see the snapshots of the atomic configuration and the total energy curve in Fig. 1.12). Correspondingly, the ballistic conductance of the Pt point contact,

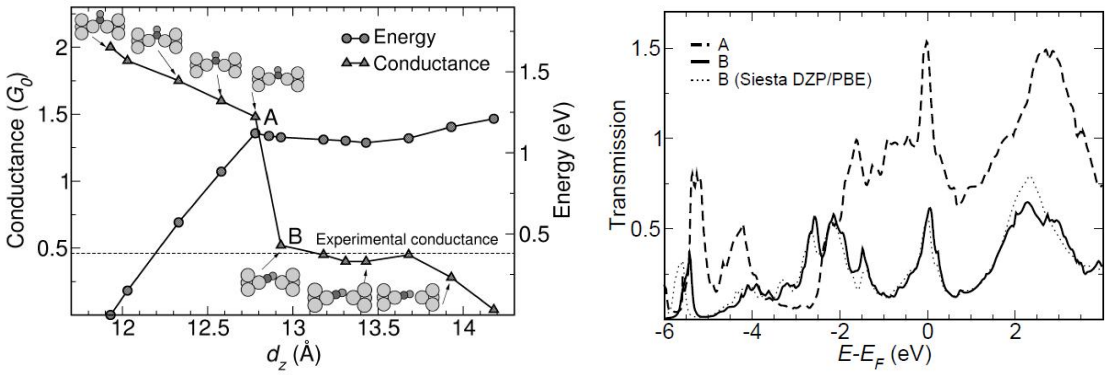

Figure 1.12: *Left: Conductance (triangles) and total energy (circles) as a function of the tips displacement, d_z, for a Pt-CO-Pt junction. A and B indicate atomic configurations where CO is upright and tilted, respectively (see also the atomic configurations of the junction reported in the insets). Right: Transmission for the A and B configurations calculated with two different methods. Pictures reprinted from Ref. 29.*

which is only slightly lowered by CO in the initial upright bridge position, has an abrupt jump and decreases to about 0.5 G_0, a value quite close to the position of the fractional peak seen in the conductance histograms of Pt [25, 26]. The transmission function for the "tilted bridge" configuration is peaked at the Fermi energy, E_F (see right side plot in Fig. 1.12). Strange and colleagues identified the nature of this resonance with a strong hybridization between the d bands at the Pt apex and the $2\pi^\star$ molecular orbital of CO characterized by a strongly asymmetric coupling with the Pt atoms, much stronger on the C side with respect to the O side.

1.6.2 CO adsorbed on Au monatomic chains and nanocontacts

Until now the adsorption of CO on monatomic Au chains has been studied only for a limited number of configurations. Bahn et al. [13] studied infinite chains with small impurities adsorbed at high coverages in order to investigate possible modifications in the structure and stability of the chains in presence of adsorbates. For a stretched chain (at a spacing of about 2.8 Å) they found an adsorption energy of almost 2 eV per molecule of CO at 1/2 of coverage (one CO every two Au atoms). They also addressed the dependence of adsorption energies on the local atomic coordination of the Au atoms close to the adsorption site: by correlating the interaction strength of CO (and O) on different gold structures (surfaces, clusters, and chains) with the atomic coordination number of the metal atoms, they showed that the reactivity of Au increases steadily as the coordination number decreases [13] (in accordance with previous results by Mavrikakis et al. [16] for CO on stepped Au surfaces).

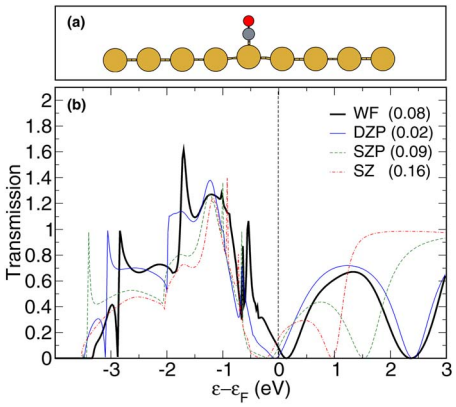

Figure 1.13: *Transmission function for an unsupported infinite Au chain with CO ontop calculated with different methods. The localized-basis method results (thin lines) approach the Wannier-function result (thick line) as the quality of the basis is improved. Reprinted from Ref. 50.*

Kochetov and Mikhaylushkin [48] studied a single CO molecule on a straight monatomic Au chain and found that CO can adsorb on the chain with the C atom (at a distance of about 1.8 Å from the chain), but is repelled if it approaches the chain with the O atom. They also excluded the possibility of CO dissociation in the vicinity of the gold nanowire, hence CO adsorption cannot be regarded as a source of contamination by atomic carbon in that systems.

The effect of CO adsorption on the electronic structure and ballistic conductance of infinite monatomic Au chains has been studied only for a particular configuration (CO in an ontop position on a strained chain, in Ref. 49), chosen in order to match the experimental geometry of short Au chains deposited on a NiAl substrate [31]. Both the experiment and the calculations show that the CO molecule attached ontop of a gold atom in the middle of a short chain breaks the electronic delocalization of some metallic states in the chain. Thus, CO should act as a "chemical scissor" for the coherent electron transport along the gold chain, as confirmed by ballistic transport calculations for an unsupported infinite chain: the transmission function displays a depression around E_{F} when CO is adsorbed ontop [49].

The same geometry has been used by Strange et al. [50] as a benchmark for two different ballistic transport methods within DFT-PBE, one based on a localized basis set and the other on plane waves (PWs) and Wannier functions (WFs). A schematic picture of the atomic geometry and a plot of the transmission function obtained with the different methods are reported in Fig. 1.13. The localized-basis method solution converges to the PW+WF solution as the quality of the localized basis is improved. Although the two independent calculations [49, 50] use exactly the same geometry and DFT approximation (PBE) and both methods are based on PW and WF, the shape of the transmission curves appears slightly different: the transmission in Ref. 49 is less smooth below E_{F}, and has a more wide depression around E_{F}.

Xu et al. [51] simulated a 3-atom-long Au chain between Au(111) surfaces; they

have reported that the geometry with CO at the bridge position is energetically favored and that the presence of CO does not influence much the conductance of the Au chain, which remains very close to $1\,G_0$. In their calculation, the main effect on the conductance is given by the structural changes of the Au chain induced by CO adsorption (namely, the elongation of the Au-Au bond below CO).

CHAPTER 2

Methodological background

In this chapter we will discuss the theoretical framework, the approximations and the computational methodologies that have been employed in this thesis. After introducing the density-functional theory and the Kohn-Sham (KS) equations for periodic solids, we will describe the pseudopotential (PP) technique, needed to treat efficiently large systems with a plane wave basis set, and explain briefly how the spin-orbit coupling (SOC) can be included in the KS equations for two-component spinors through ultrasoft pseudopotentials (USPPs). We will then report the formulas used to compute the density of states and projected-density of states in the two cases (with and without SOC). In the last two sections of the chapter we will describe the scattering-based approach for calculating the ballistic transmission developed by Choi and Ihm (for norm-conserving PPs) and its subsequent extensions to USPPs and then discuss a method for calculating the ballistic transmission within DFT+U.

2.1 Density functional theory

Within the *adiabatic approximation*[1] a physical system composed of atomic nuclei and electrons is described by a many-body wavefunction which has an explicit dependence on the electronic degrees of freedom, while the positions of the nuclei enter as external parameters. The quantum mechanical properties of a system of $N_{\rm el}$ interacting electrons in the external potential of the nuclei can be obtained by solving the many-body Schrödinger equation:

$$\hat{H}\psi(\mathbf{r}_1,\ldots,\mathbf{r}_{N_{\rm el}}) = E\psi(\mathbf{r}_1,\ldots,\mathbf{r}_{N_{\rm el}}) \tag{2.1}$$

with the following Hamiltonian:

$$\hat{H} = -\sum_{i=1}^{N_{\rm el}} \frac{\hbar^2}{2m}\nabla_i^2 + \sum_{i=1}^{N_{\rm el}} V_{\rm ext}(\mathbf{r}_i) + \frac{e^2}{2}\sum_{i\neq j}\frac{1}{|\mathbf{r}_i-\mathbf{r}_j|}\ , \tag{2.2}$$

where $\mathbf{r}_i$ is the position of electron i, ∇_i^2 indicates the laplacian taken with respect to the coordinate $\mathbf{r}_i$, while $V_{\rm ext}(\mathbf{r}_i)$ is the external potential acting on the electrons and depends parametrically on the nuclear positions. In the remaining of this chapter, we will always make use of atomic units and hence the lengths will be expressed in units of Bohr radii (a.u.) and the energies in hartree units (Ha). With this choice, in Eq. (2.2) we can make the substitutions: $e^2 = 1$, for the square of the electron charge, and $m = 1$, for the electron mass. In many cases, finding an exact general solution for Eq. (2.1) is an extremely complex problem, essentially because of the Coulomb repulsion term between the electrons which couples all the electronic degrees of freedom. Even searching for a numerical solution is a formidable task and the problem cannot be tackled without making any simplification in the many-body equation. It is then mandatory to find a suitable approximation which allows to find efficiently a numerical solution to the problem: a common and often successful approach, which will be adopted throughout this thesis, is density-functional theory (DFT).

DFT was introduced in 1964 by Hohenberg and Kohn [70], who proved a one-to-one correspondence between the ground-state electronic charge density $\rho(\mathbf{r})$ and the external potential $V_{\rm ext}(\mathbf{r})$. Therefore, since the external potential determines also the many-body wavefunction of the ground state, every physical quantity of the system in its ground state can be expressed as a *functional* of the electronic charge density. A central role is played by the ground-state total energy of the system, which can be

[1] The *Born-Oppenheimer* (or adiabatic) approximation exploits the fact that the ratio between electron and nuclear masses is sufficiently small to study the electronic degrees of freedom independently from those of the nuclei [69]. Furthermore, for our purposes, the atomic nuclei can be treated as classical particles.

written as the expectation value of the Hamiltonian on the ground state Ψ_0. If we express the total energy as a functional of the electronic density, it will read:

$$E[\rho(\mathbf{r})] = \langle \Psi_0 | \, \hat{H} \, | \Psi_0 \rangle = F[\rho(\mathbf{r})] + \int_V V_{\text{ext}}(\mathbf{r}) \rho(\mathbf{r}) \, \mathrm{d}^3 r \ , \tag{2.3}$$

where the integral is done over the whole volume V of the system. In this equation, $F[\rho(\mathbf{r})]$ is a universal functional of the density and it is given by the expectation value of the kinetic energy and of electrostatic electron repulsion terms on the ground state. The minimization of the functional $E[\rho(\mathbf{r})]$ with respect to the electronic density, with the constraint that the number of electrons N_{el} is fixed,

$$\int_V \rho(\mathbf{r}) \, \mathrm{d}^3 r = N_{\text{el}} \ , \tag{2.4}$$

gives the ground-state total energy and electronic density.

Since the exact form of the universal functional $F[\rho(\mathbf{r})]$ is not known, in 1965 Kohn and Sham [71] introduced a new functional by mapping the many-body problem into a non-interacting electrons problem with the same ground-state electronic density. The new functional can be obtained by subtracting to F some terms of the energy calculated for the non-interacting electrons problem. If we call $\psi_i(\mathbf{r})$ the single-particle wavefunctions, then the kinetic energy of a non-interacting electrons system is:

$$T_0 = \sum_i f_i \, \langle \psi_i | \, -\frac{1}{2} \nabla^2 \, | \, \psi_i \rangle \ , \tag{2.5}$$

where f_i is the occupation factor for state i. The density can be written as:

$$\rho(\mathbf{r}) = \sum_i f_i \, |\psi_i(\mathbf{r})|^2 \tag{2.6}$$

and is chosen equal to the ground-state electronic density of the interacting electrons system. From $F[\rho(\mathbf{r})]$ we can subtract a Hartree-like energy term, which accounts for the classical Coulomb interaction of a spatial charge distribution $\rho(\mathbf{r})$:

$$E_H = \frac{1}{2} \iint_V \frac{\rho(\mathbf{r}_1)\rho(\mathbf{r}_2)}{|\mathbf{r}_1 - \mathbf{r}_2|} \, \mathrm{d}^3 r_1 \, \mathrm{d}^3 r_2 \ , \tag{2.7}$$

and thus rewrite the universal functional as:

$$F[\rho(\mathbf{r})] = T_0 + E_H + E_{\text{xc}}[\rho(\mathbf{r})] \ , \tag{2.8}$$

where E_{xc} is the so-called "exchange-correlation" functional, which contains all the many-body interaction effects not included in the other energy terms. Using the

expression of the density given in Eq. (2.6), the interaction energy associated to the external potential can be rewritten as:

$$E_{\text{ext}} = \int_V V_{\text{ext}}(\mathbf{r})\rho(\mathbf{r})\,\mathrm{d}^3r = \sum_i f_i \langle\psi_i|\, V_{\text{ext}}\,|\,\psi_i\rangle \ , \tag{2.9}$$

and hence it becomes convenient to minimize the total energy functional,

$$E[\rho(\mathbf{r})] = T_0 + E_H + E_{\text{xc}}[\rho(\mathbf{r})] + E_{\text{ext}} \ , \tag{2.10}$$

with respect to the single-particle wavefunctions $\psi_i(\mathbf{r})$. The wavefunctions are normalized to one and satisfy the orthogonality constraint,

$$\langle\psi_i|\,\psi_j\rangle = \delta_{i,j} \ , \tag{2.11}$$

so that the minimization of the total energy functional can be performed through the Lagrange multiplier technique. The solution leads straightforwardly to the KS equations [71], which read:

$$\left[-\frac{1}{2}\nabla^2 + V_{\text{KS}}(\mathbf{r})\right]\psi_i(\mathbf{r}) = \epsilon_i\,\psi_i(\mathbf{r}) \ , \tag{2.12}$$

where the KS potential has been defined as

$$V_{\text{KS}}(\mathbf{r}) = V_H(\mathbf{r}) + V_{\text{xc}}(\mathbf{r}) + V_{\text{ext}}(\mathbf{r}) \tag{2.13}$$

and contains, besides the external potential, the Hartree potential,

$$V_H(\mathbf{r}) = \int_V \frac{\rho(\mathbf{r}')}{|\mathbf{r}-\mathbf{r}'|}\,\mathrm{d}^3r' \ , \tag{2.14}$$

and the exchange-correlation potential,

$$V_{\text{xc}}(\mathbf{r}) = \left.\frac{\delta E_{\text{xc}}[\rho]}{\delta\rho}\right|_{\rho=\rho(\mathbf{r})} . \tag{2.15}$$

From the solution of the KS equations one obtains the auxiliary single-particle wavefunctions, ψ_i, that give the ground-state electronic density through Eq. (2.6).

The natural interpretation of the KS scheme is that of a mean-field theory: the one-body KS Hamiltonian, given in Eq. (2.12), describes an electron moving in a potential generated by the nuclei and by the other electrons through their charge density. Since the ground-state charge density depends on the solution itself, in order to solve the problem it is necessary to utilize a self-consistent iterative procedure: an initial guess for the charge density, $\rho_{\text{in}}^{(0)}(\mathbf{r})$, is used to compute the KS potential, V_{KS}, which is needed to diagonalize the KS Hamiltonian and get a new estimate of the

density, $\rho^{(0)}_{\text{out}}(\mathbf{r})$, through the set of single-particle wavefunctions $\{\psi_i\}$. From a linear combination of the densities $\rho^{(0)}_{\text{in}}(\mathbf{r})$ and $\rho^{(0)}_{\text{out}}(\mathbf{r})$, a new trial density $\rho^{(1)}_{\text{in}}(\mathbf{r})$ for the next iteration is built. The potential V_{KS} is recomputed from $\rho^{(1)}_{\text{in}}(\mathbf{r})$, the KS Hamiltonian is diagonalized again to obtain $\rho^{(1)}_{\text{out}}(\mathbf{r})$, and the iteration step is repeated until the distance between the solutions of two consecutive iterations, which can be defined for instance as

$$\int_V |\rho^{(n)}_{\text{out}}(\mathbf{r}) - \rho^{(n)}_{\text{in}}(\mathbf{r})|^2 \, \mathrm{d}^3 r \, , \tag{2.16}$$

gets below a chosen threshold of accuracy.

Formally, DFT is an exact theory, but it does not say anything about the analytic form of the exchange-correlation functional E_{xc}; it would not be of much practical use without any suitable approximation for E_{xc}. A simple and widely adopted approach is the local density approximation (LDA), which has allowed to describe successfully a large number of systems [71, 72]. In the LDA, the exchange-correlation energy of the electrons system, which in general has a ground state with a *non-uniform* electron charge density, is approximated by:

$$E_{\text{xc}}[\rho(\mathbf{r})] = \int_V \varepsilon^{\text{hom}}_{\text{xc}}\big(\rho(\mathbf{r})\big) \, \rho(\mathbf{r}) \, \mathrm{d}^3 r \, , \tag{2.17}$$

where $\varepsilon^{\text{hom}}_{\text{xc}}(\rho)$ is the exchange-correlation energy density for a *homogeneous* gas of interacting electrons with constant charge density ρ and, for each point $\mathbf{r}$, the function $\varepsilon^{\text{hom}}_{\text{xc}}$ is evaluated at the local charge density of the non-uniform system, $\rho(\mathbf{r})$. In 1980, the value of $\varepsilon^{\text{hom}}_{\text{xc}}(\rho)$ has been computed by Monte Carlo methods for some values of the density ρ [73]. Successively, several theoretical works suggested various interpolation formulae for $\varepsilon^{\text{hom}}_{\text{xc}}(\rho)$: in our calculations we use the interpolation formula proposed by Perdew and Zunger [55].

A straightforward and commonly used extension of the LDA is the generalized gradient approximation (GGA), where the exchange-correlation energy depends locally not only on the charge density $\rho(\mathbf{r})$, but also on its gradient, $\nabla\rho(\mathbf{r})$. In this approximation, the exchange-correlation energy can be written as:[2]

$$E_{\text{xc}}[\rho(\mathbf{r})] = \int_V \varepsilon^{\text{GGA}}_{\text{xc}}\big(\rho(\mathbf{r}), \nabla\rho(\mathbf{r})\big) \, \rho(\mathbf{r}) \, \mathrm{d}^3 r \, . \tag{2.18}$$

In our work we used a popular gradient-corrected functional proposed by Perdew, Burke, and Ernzerhof [75], which is simple to implement and still widely adopted in many solid state applications.

[2] See Ref. 74. Since the gradient introduces a non-local dependence on the charge density, the exchange-correlation functionals falling within this approximation are often called "semi-local".

2.2 Kohn-Sham equations for periodic solids

The equilibrium positions of the nuclei in a crystalline solid can be described through a Bravais lattice, which consist of a set of points in space:

$$\mathbf{R} = n_1\mathbf{a}_1 + n_2\mathbf{a}_2 + n_3\mathbf{a}_3 \ , \tag{2.19}$$

where n_1, n_2 and n_3 are three integer indexes which univocally identify a lattice site. The three linearly independent vectors $\mathbf{a}_1$, $\mathbf{a}_2$, and $\mathbf{a}_3$ are the basis vectors of the direct[3] Bravais lattice and specify the unit-cell volume,

$$\Omega = \mathbf{a}_1 \cdot (\mathbf{a}_2 \times \mathbf{a}_3) \ , \tag{2.20}$$

and the periodicity of the crystal. We assume that our solid contains $N = N_1 \times N_2 \times N_3$ unit cells, so that its volume is given by $V = N\,\Omega$. The limit of an infinite periodic solid corresponds to $N \to \infty$, but can be obtained to a good accuracy with a finite number of unit cells by adopting appropriate boundary conditions (see later). If the unit cell of the crystal contains more than one atom (let us indicate with $N_{\rm at}$ the number of atoms per unit cell), then we need to introduce, in addition to the basis vectors of the lattice, other $N_{\rm at}$ vectors $\{\mathbf{d}_s;\ s = 1, 2, \ldots, N_{\rm at}\}$, with $\mathbf{d}_s$ corresponding to the position of the atom labeled with s of species $\gamma(s)$ in the unit cell centered at the origin (hence with $n_1 = n_2 = n_3 = 0$). With this choice the equilibrium positions of the nuclei are given by $\mathbf{R} + \mathbf{d}_s$, where $\mathbf{R}$ can be any vector of the direct Bravais lattice.

Using this notation, the external potential $V_{\rm ext}(\mathbf{r})$ generated by the nuclear charges has the same periodicity of the Bravais lattice associated to the crystal, since for every direct lattice vector $\mathbf{R}$ the following equality holds:

$$V_{\rm ext}(\mathbf{r} + \mathbf{R}) = V_{\rm ext}(\mathbf{r}) \ . \tag{2.21}$$

If the electronic density, $\rho(\mathbf{r})$, is invariant with respect to translations of a direct lattice vector $\mathbf{R}$, also the KS potential $V_{\rm KS}$ and the whole Hamiltonian have the same periodicity of the lattice. Therefore we can apply the Bloch theorem and write the single-particle wavefunctions in the following form:

$$\psi_{\mathbf{k},v}(\mathbf{r}) = \mathrm{e}^{\,\mathrm{i}\,\mathbf{k}\cdot\mathbf{r}} u_{\mathbf{k},v}(\mathbf{r}) \ , \tag{2.22}$$

where the lattice-periodic functions $u_{\mathbf{k},v}(\mathbf{r})$ are multiplied by a complex phase factor. The three-dimensional index $\mathbf{k}$ is related to the translational properties of the electronic wavefunctions and, for a fixed KS potential, the solutions at different $\mathbf{k}$ points

[3]The term "direct" is usually added to distinguish the Bravais lattice used to describe the nuclear positions $\mathbf{R}$ in real space from the corresponding "reciprocal" lattice, which is the set of $\mathbf{G}$ vectors satisfying $\mathrm{e}^{\,\mathrm{i}\,\mathbf{G}\cdot\mathbf{R}} = 1$, for all $\mathbf{R}$ in the direct lattice [69].

are independent. In the case of periodic boundary conditions (PBCs) of the Born-von Kármán type, $\mathbf{k}$ is a real vector and can be confined inside the first Brillouin zone (BZ) by introducing a band index v. The number of $\mathbf{k}$ points inside the first BZ coincides with the number of unit cells N included in the simulation volume V, while the number of occupied bands which must be calculated for each $\mathbf{k}$ depends on N_{el}, the number of electrons per unit cell: $N_{\mathrm{el}}/2$ bands are sufficient for a non-magnetic insulator, while for metallic systems we need to compute more bands and to introduce a broadening in the occupation factors (see later).

Given their periodicity, the functions $u_{\mathbf{k},v}(\mathbf{r})$ can be expanded in a PW basis set and the Bloch states can be written as

$$\psi_{\mathbf{k},v}(\mathbf{r}) = \frac{1}{\sqrt{V}} \sum_{\mathbf{G}} c_{\mathbf{k}+\mathbf{G},v}\, \mathrm{e}^{\,\mathrm{i}\,(\mathbf{k}+\mathbf{G})\cdot\mathbf{r}}\ , \tag{2.23}$$

where $\mathbf{G}$ is a reciprocal lattice vector and the PW coefficients $c_{\mathbf{k}+\mathbf{G},v}$ are normalized such that

$$\sum_{\mathbf{G}} |c_{\mathbf{k}+\mathbf{G},v}|^2 = 1\ . \tag{2.24}$$

By inserting in Eq. (2.12) the $\psi_{\mathbf{k},v}(\mathbf{r})$ expressed as in Eq. (2.23), we obtain the following $\mathbf{k}$-dependent eigenvalue problem:

$$\sum_{\mathbf{G}'} \Big[|\mathbf{k}+\mathbf{G}|^2 \delta_{\mathbf{G},\mathbf{G}'} + V_H(\mathbf{G}-\mathbf{G}') + V_{\mathrm{xc}}(\mathbf{G}-\mathbf{G}') + \\ + V_{\mathrm{ext}}(\mathbf{k}+\mathbf{G},\mathbf{k}+\mathbf{G}') \Big] c_{\mathbf{k}+\mathbf{G}',v} = \epsilon_{\mathbf{k},v}\, c_{\mathbf{k}+\mathbf{G},v} \tag{2.25}$$

where the eigenstates give the coefficients $c_{\mathbf{k}+\mathbf{G},v}$ of the PW expansion of $\psi_{\mathbf{k},v}(\mathbf{r})$.

The reciprocal space representation of the Hartree potential is given by[4]

$$V_H(\mathbf{G}) = 4\pi\, \frac{\rho(\mathbf{G})}{|\mathbf{G}|^2}\ , \tag{2.26}$$

where $\rho(\mathbf{G})$ is the Fourier transform of the electronic density,

$$\rho(\mathbf{G}) = \frac{1}{\Omega} \int_{\Omega} \rho(\mathbf{r})\, \mathrm{e}^{\,\mathrm{i}\,\mathbf{G}\cdot\mathbf{r}}\ \mathrm{d}^3 r\ , \tag{2.27}$$

while $V_{\mathrm{xc}}(\mathbf{G})$ is obtained by Fourier-transforming the exchange-correlation potential of Eq. (2.15). The matrix element of the external potential between two PWs reads

$$V_{\mathrm{ext}}(\mathbf{k}+\mathbf{G},\mathbf{k}+\mathbf{G}') = \frac{1}{V} \int_{V} \mathrm{e}^{-\,\mathrm{i}\,(\mathbf{k}+\mathbf{G})\mathbf{r}}\, V_{\mathrm{ext}}(\mathbf{r})\, \mathrm{e}^{\,\mathrm{i}\,(\mathbf{k}+\mathbf{G}')\mathbf{r}}\ \mathrm{d}^3 r\ , \tag{2.28}$$

[4]This expression for $V_H(\mathbf{G})$ is formally divergent at $|\mathbf{G}| = 0$. However, that component of the potential can be set to zero without changing the physical properties of the system [76].

thus it depends on $\mathbf{k}$ only if $V_{\text{ext}}(\mathbf{r})$ is replaced by a non-local potential (see Sec. 2.3). An infinite number of $\mathbf{G}$ vectors should be considered in order to represent exactly the Bloch states $\psi_{\mathbf{k},v}(\mathbf{r})$, but only a finite set of vectors can be used in practical calculations. Typically, the $\mathbf{G}$ vectors are selected by including all the PWs having a kinetic energy below a fixed cut-off:

$$\frac{1}{2}|\mathbf{k}+\mathbf{G}|^2 < E_{\text{cut},\psi} \ . \tag{2.29}$$

The degree of approximation due to the incompleteness of the basis set can be controlled quite easily by increasing the kinetic energy cut-off until the desired accuracy in the representation of the wavefunctions is reached.

Many physical quantities of the system can be written in terms of a summation over electronic states (which usually reads as $\sum_{\mathbf{k}\in BZ,v}$), but the space symmetry properties of the crystal allow to rewrite this kind of summations including only $\mathbf{k}$ vectors belonging to the so-called irreducible Brillouin zone (IBZ), which can be considerably smaller than the BZ if the crystal is symmetric. The set of $\mathbf{k}$ points used to sample the IBZ determines the accuracy of the summation: at a fixed number of points, the best approximation to the exact result (which, we remember, corresponds to a summation over an infinite number of $\mathbf{k}$) can be obtained by using particular sets of $\mathbf{k}$ points, called "special" $\mathbf{k}$ point sets. In our work, in order to sample the IBZ we use a modified version of the technique proposed by Monkhorst and Pack [77].

The occupations of the electronic states $\psi_{\mathbf{k},v}$ are given by the occupation factors $f_{\mathbf{k},v}$, which at zero temperature are given by the step function $f_{\mathbf{k},v} = \theta(E_{\text{F}} - \epsilon_{\mathbf{k},v})$, and hence are equal to one if the eigenvalue $\epsilon_{\mathbf{k}v}$ associated to $\psi_{\mathbf{k},v}$ is lower than the Fermi energy E_{F}, zero otherwise. For metallic systems, since one or more electronic bands cross the Fermi energy at some $\mathbf{k}$ points in the BZ, during the self-consistent iterative procedure the occupation factor of a state with $\epsilon_{\mathbf{k},v} \simeq E_{\text{F}}$ belonging to one of these bands can change from one to zero (or viceversa) from one iteration to the next. Because the electronic charge density is built from a summation over all the occupied states, the exclusion of a state which was included in the summation at the previous step can induced large variations between the charge densities at two successive iterations and the self-consistency procedure may become unstable and never reach convergence. To overcome this problem, it is common practice to utilize occupations $f_{\mathbf{k},v}$ without any discontinuity at $\epsilon_{\mathbf{k},v} = E_{\text{F}}$, a technique which is commonly called "broadening" or "smearing" of the occupation numbers. The "smoothness" of the occupation function in the region around E_{F} can be controlled by a smearing parameter σ, in such a way that the step function must be recovered in the limit $\sigma \to 0$. A larger value of σ corresponds to a smoother occupation function $f_{\mathbf{k},v}$, which allows one to decrease the number of $\mathbf{k}$ points needed to obtain a sufficiently accurate sampling of the Fermi surface. The main disadvantage of this

technique consists in the introduction of a non-physical dependence on the smearing parameter σ in the total energy, $E(\sigma)$, and also in the other physical quantities that can be computed. The exact (zero-smearing) value of the energy, $E(0)$, could be obtained to a high precision by extrapolating several values of $E(\sigma)$ computed by progressively decreasing σ towards zero. In practice we use the largest value of σ corresponding to a total energy value $E(\sigma)$ which is close enough to $E(0)$. In our calculations we used the occupation broadening technique introduced by Methfessel and Paxton [78], which ensures a quadratic convergence of $E(\sigma)$ towards the desired value $E(0)$ as the smearing σ goes to zero.

2.3 Notes on the pseudopotential method

The PW expansion of Eq. (2.23) represents the electronic wavefunctions with the same accuracy in all regions of space, hence a very large number of PWs is required in order to describe accurately all the wavefunctions of the system, including those of the inner shells (the *core* electrons). A possible solution to this problem is represented by the pseudopotential (PP) technique, which is based on the assumption that the main physical properties of the chemical bond are determined by the valence electrons of the atoms, while the core electrons can be considered frozen in their atomic ground state. The number of electronic states which actually need to be explicitly calculated is then reduced to the total number of valence electrons and the screening of the nuclear charges by the core electrons is included in the Hamiltonian through an effective potential. The first rigorous techniques for obtaining a successful form of PP were based on the so-called norm-conserving constraint [79]. In order to satisfy this constraint, it is necessary to introduce a distinct potential $\Delta V_l(r)$ for every angular momentum l of the valence electronic wavefunctions. For each l, the potential is computed by requiring that the atomic pseudo-wavefunction $\phi_l^{\rm PS}(r)$, solution of the PP-KS equation,

$$[\,T_l + V_{\rm eff}(r) + \Delta V_l(r)]\,\phi_l^{\rm PS}(r) = \epsilon_l\,\phi_l^{\rm PS}(r)\ , \tag{2.30}$$

and the corresponding atomic wavefunction $\phi_l^{\rm AE}(r)$, solution of the original KS equation (which keeps into account both core and valence electrons) at the same energy eigenvalue ϵ_l,

$$[\,T_l + V_{\rm KS}(r)]\,\phi_l^{\rm AE}(r) = \epsilon_l\,\phi_l^{\rm AE}(r)\ , \tag{2.31}$$

coincide for $r > r_{{\rm c},l}$ (where $r_{{\rm c},l}$ is called the "core radius"). In Eq. (2.30) and Eq. (2.31), the kinetic energy operator reads

$$T_l = -\frac{1}{2}\frac{{\rm d}^2}{{\rm d}r^2} + \frac{l(l+1)}{2\,r^2}\ , \tag{2.32}$$

while the effective potential in Eq. (2.30) is

$$V_{\rm eff}(r) = V_{\rm loc}(r) + V_H(r) + V_{\rm xc}(r) \tag{2.33}$$

and the all-electron KS potential, $V_{\rm KS}(r)$, has been defined in Eq. (2.13). If the pseudo-wavefunction $\phi_l^{\rm PS}(r)$ does not have any node inside the core region ($r < r_{{\rm c},l}$), then the non-local potential $\Delta V_l(r)$ can be obtained by inverting the PP-KS equation:

$$\Delta V_l(r) = \frac{1}{\phi_l^{\rm PS}(r)} \left[\epsilon_l - T_l - V_{\rm eff}(r)\right] \phi_l^{\rm PS}(r) \ . \tag{2.34}$$

An additional requirement for this kind of PP is that the norm of $\phi_l^{\rm PS}(r)$ inside the core region satisfies the following constraint:

$$\int_0^{r_{{\rm c},l}} \left|\phi_l^{\rm PS}(r)\right|^2 {\rm d}r = \int_0^{r_{{\rm c},l}} \left|\phi_l^{\rm AE}(r)\right|^2 {\rm d}r \ . \tag{2.35}$$

The local potential $V_{\rm eff}(r)$ is the same for every value of l and must coincide with $V_{\rm KS}(r)$ for $r > r_{\rm loc}$, while it can be chosen arbitrarily inside the core region.

In order to utilize this PP in a solid, the KS states of the valence electrons have to be separated into the different components of angular momentum l which have been included in the PP for each specific atom. The projector onto the angular momentum l can be written in terms of spherical harmonics:

$$\widehat{P}_l^I(\mathbf{r},\mathbf{r}') = \sum_{m_l=-l}^{l} Y_{l,m_l}(\Omega_{\mathbf{r}-\mathbf{R}_I}) Y_{l,m_l}(\Omega_{\mathbf{r}'-\mathbf{R}_I}) \ , \tag{2.36}$$

where I indicates an atom in the unit cell of the crystal and $\mathbf{R}_I$ its position. When used in the calculations for the solid, the PP becomes:

$$\begin{aligned} V^{\rm HSC}(\mathbf{r},\mathbf{r}') &= V_{\rm loc}(\mathbf{r})\delta(\mathbf{r}-\mathbf{r}') \\ &+ \sum_I \sum_{l=0}^{l_{\rm max}} \Delta V_l^{\gamma(I)}(|\mathbf{r}-\mathbf{R}_I|)\, \delta(|\mathbf{r}-\mathbf{R}_I| - |\mathbf{r}'-\mathbf{R}_I|)\, \widehat{P}_l^I(\mathbf{r},\mathbf{r}') \ , \end{aligned} \tag{2.37}$$

where $\gamma(I)$ specifies the chemical species of atom I, while the first term,

$$V_{\rm loc}(\mathbf{r}) = \sum_I V_{\rm loc}^{\gamma(I)}(|\mathbf{r}-\mathbf{R}_I|) \ , \tag{2.38}$$

and the second term on the right hand side of Eq. (2.37) are, respectively, the local and semi-local parts of the PP. The semi-local part of $V^{\rm HSC}$ is written in a form which does not lend itself for an efficient usage together with a PW basis, since it requires the calculation of a matrix $V^{HSC}(\mathbf{k}+\mathbf{G},\mathbf{k}+\mathbf{G}')$ containing a number of elements which scales as the square of the number of PWs.

This issue has been solved by Kleinman and Bylander [80], who devised a new type of norm-conserving PP which is completely non-local and fully separable. In this method, for every angular momentum l, the non-local term of the potential is written in the form:

$$\widehat{V}_{\rm L} = \frac{|\,\chi_l\rangle\langle\chi_l\,|}{\langle\chi_l|\,\phi_l^{\rm PS}\rangle}\ , \tag{2.39}$$

where the $\chi_l(r)$ must be determined such that $\widehat{V}_{\rm L}$ reproduces the effect of the potential $\Delta V_l(r)$ on the radial atomic pseudo-wavefunction $\phi_l^{\rm PS}(r)$, namely

$$\widehat{V}_{\rm L}|\,\phi_l^{\rm PS}\rangle = \Delta V_l(r)|\,\phi_l^{\rm PS}\rangle\ , \tag{2.40}$$

for instance by inverting the atomic KS equation:

$$|\,\chi_l\rangle = [\epsilon_l - T_l - V_{\rm eff}(r)]|\,\phi_l^{\rm PS}\rangle \quad . \tag{2.41}$$

As in the case of a semi-local PP, also with this new kind of PP we need to project onto spherical harmonics, but the semi-local part of Eq. (2.37) has been replaced by a fully non-local part:

$$V^{\rm KB}(\mathbf{r},\mathbf{r}') = V_{\rm loc}(\mathbf{r})\delta(\mathbf{r}-\mathbf{r}') + \sum_I \sum_{l,m_l} \frac{|\,\chi_l^I Y_{l,m_l}^I\rangle\langle\chi_l^I Y_{l,m_l}^I\,|}{\langle\chi_l|\,\phi_l^{\rm PS}\rangle}\ , \tag{2.42}$$

where χ_l^I is the $\chi_l(r)$ function associated to species $\gamma(I)$ and centered on atom I and Y_{l,m_l}^I are the spherical harmonics centered on atom I, while the $\langle\chi_l|\,\phi_l^{\rm PS}\rangle$ coefficients depend only on the atomic species $\gamma(I)$. The matrix element of the non-local part of the potential between two plane waves $\mathbf{G}$ and $\mathbf{G}'$ can be now separated in two independent integrals, one depending on $\mathbf{k}+\mathbf{G}$ and the other on $\mathbf{k}+\mathbf{G}'$.

A further and important progress in the PP technique is due to Vanderbilt [81], who introduced the so-called ultrasoft pseudopotential (USPP) technique. His scheme generalizes Kleinman and Bylander's PP generation procedure requiring that, for each channel l, the PP reproduces correctly the scattering properties of $V_{\rm KS}$ in the atom for a number N_ϵ of energy eigenvalues ϵ_i (usually two or more). If we fix the angular momentum l, which we indicate explicitly only in $\Delta V_l^i(r)$, the pseudo-wavefunctions $\phi_i^{\rm PS}(r)$ are the solutions of Eq. (2.30) at the different energies $\epsilon_1, \epsilon_2, \ldots$,

$$\begin{aligned}
\left[T_l + V_{\rm eff}(r) + \Delta V_l^1(r)\right]\phi_1^{\rm PS}(r) &= \epsilon_1\phi_1^{\rm PS}(r) \\
\left[T_l + V_{\rm eff}(r) + \Delta V_l^2(r)\right]\phi_2^{\rm PS}(r) &= \epsilon_2\phi_2^{\rm PS}(r) \\
\ldots \qquad\qquad \ldots \qquad\quad .
\end{aligned} \tag{2.43}$$

For $r > r_c$, each of the $\phi_i^{\rm PS}(r)$ must coincide with the corresponding $\phi_i^{\rm AE}(r)$, solution of the all-electron radial KS equation at the same energy ϵ_i,

$$\begin{aligned}
\left[T_l + V_{\rm KS}(r)\right]\phi_1^{\rm AE}(r) &= \epsilon_1\phi_1^{\rm AE}(r) \\
\left[T_l + V_{\rm KS}(r)\right]\phi_2^{\rm AE}(r) &= \epsilon_2\phi_2^{\rm AE}(r) \\
\ldots \qquad\qquad \ldots \qquad\quad .
\end{aligned} \tag{2.44}$$

For each angular momentum l, a set of N_ϵ functions $\chi_i(r)$ is computed starting from the pseudo-wavefunctions $\phi_i^{\mathrm{PS}}(r)$ through the methodology described above and, as a consequence, the PP term associated to l must be written in a more general form:

$$\widehat{V}_{\mathrm{L}} = \sum_{ij} A_{ij} |\, \chi_i\rangle\langle\chi_j \,| \;, \tag{2.45}$$

where the indexes i and j indicate the different energies used for that l. By introducing the coefficients

$$B_{ij} = \langle \phi_i^{\mathrm{PS}} |\, \chi_j\rangle \;, \tag{2.46}$$

it can be proved that the action of $\widehat{V}_{\mathrm{L}}$ on the $\phi_i^{\mathrm{PS}}(r)$ leads to the equalities written in Eqs. (2.43) if we choose $A_{ij} = (B^{-1})_{j\,i}$. The potential in Eq. (2.45) is customarily rewritten as

$$\widehat{V}_{\mathrm{L}} = \sum_{ij} B_{ij} |\, \beta_i\rangle\langle\beta_j \,| \;, \tag{2.47}$$

where the functions $|\, \beta_i\rangle$ are defined as

$$|\, \beta_i\rangle = \sum_j (B^{-1})_{j\,i} |\, \chi_j\rangle \;. \tag{2.48}$$

In order to ensure that the operator $\widehat{V}_{\mathrm{L}}$ is always Hermitian, the coefficients B_{ij} in Eq. (2.47) must be modified as follows:

$$D_{ij} = B_{ij} + \epsilon_j \, q_{ij} \;, \tag{2.49}$$

where q_{ij} are the integrals of the augmentation terms $Q_{ij}(r)$,

$$Q_{ij}(r) = [\phi_i^{\mathrm{AE}}(r)]^* \phi_j^{\mathrm{AE}}(r) - [\phi_i^{\mathrm{PS}}(r)]^* \phi_j^{\mathrm{PS}}(r) \tag{2.50a}$$

$$q_{ij} = \int_0^{r_c} Q_{ij}(r)\, \mathrm{d}r \;, \tag{2.50b}$$

and generally do not vanish when the norm-conserving constraint is released. Having substituted the B_{ij} coefficients with the D_{ij} coefficients given in Eq. (2.47), in order to reobtain Eqs. (2.43) through the action of $\widehat{V}_{\mathrm{L}}$ on the $\phi_i^{\mathrm{PS}}(r)$ the non-local potential $\widehat{V}_{\mathrm{L}}$ must be used inside a generalized eigenvalue problem,

$$\left[T_l + V_{\mathrm{eff}}(r) + \widehat{V}_L\right] \phi_i^{\mathrm{PS}}(r) = \epsilon_i \widehat{S} \phi_i^{\mathrm{PS}}(r) \;, \tag{2.51}$$

where an overlap operator appears on the left-hand side:

$$\widehat{S} = \mathbb{1} + \sum_{ij} q_{ij} |\, \beta_i\rangle\langle\beta_j \,| \;. \tag{2.52}$$

A further consequence is that the pseudo-wavefunctions are now orthogonal in the norm defined by the overlap operator,

$$\langle \phi_i^{\mathrm{PS}} | \, \widehat{S} \, | \, \phi_j^{\mathrm{PS}} \rangle = \delta_{i,j} \; , \tag{2.53}$$

and hence the electronic charge density must be augmented by a term which keeps into account the non-conservation of the norm inside the core regions,

$$\rho(r) = \sum_k f_k \left[\left| \phi_k^{\mathrm{PS}}(r) \right|^2 + \sum_{ij} Q_{ij}(r) \langle \phi_k^{\mathrm{PS}} | \, \beta_i \rangle \langle \beta_j | \, \phi_k^{\mathrm{PS}} \rangle \right] \; . \tag{2.54}$$

In this way we can ensure that actually the integral of the radial charge density on the real axis gives the correct total number of valence electrons in the system.

The three-dimensional charge density $\rho(\mathbf{r})$ in the solid can be rewritten by analogy with Eq. (2.54), summing up the augmentation terms associated to all the atoms described with an USPP:

$$\rho(\mathbf{r}) = \sum_{\mathbf{k},v} f_{\mathbf{k},v} \left[\left| \psi_{\mathbf{k},v}(\mathbf{r}) \right|^2 + \sum_{mn} Q_{mn}^I(\mathbf{r}) \langle \psi_{\mathbf{k},v} | \, \beta_m^I \rangle \langle \beta_n^I | \, \psi_{\mathbf{k},v} \rangle \right] \; . \tag{2.55}$$

In this equation we adopted a compact index notation, using the composite indexes $m = \tau, l, m_l$ and $n = \tau', l', m_l'$, where τ and τ' specify the energies. The angular momentum projector functions $| \, \beta_{\tau,l,m_l}^I \rangle$ are centered on $\mathbf{R}_I$ and can be written in real space representation as

$$\langle \mathbf{r} | \, \beta_{\tau,l,m_l}^I \rangle = \frac{1}{r} \, \beta_{\tau,l}^{\gamma(I)}(|\mathbf{r} - \mathbf{R}_I|) \, Y_{l,m_l}^I(\vartheta, \varphi) \; , \tag{2.56}$$

namely as the product of a radial part $\beta_{\tau,l}^{\gamma(I)}(r)$, which depends on the atomic species of atom I, on the energy τ, and on the angular momentum l, with the spherical harmonic $Y_{l,m_l}^I(\vartheta, \varphi)$, which gives the angular dependence. The radial augmentation functions are extended to the three-dimensional case in the same way:

$$Q_{\tau,l,m_l;\tau',l',m_l'}^I(\mathbf{r}) = \frac{1}{r^2} \left([\phi_{I,\tau,l}^{\mathrm{AE}}(r)]^* \phi_{I,\tau',l'}^{\mathrm{AE}}(r) - [\phi_{I,\tau,l}^{\mathrm{PS}}(r)]^* \phi_{I,\tau',l'}^{\mathrm{PS}}(r) \right) Y_{lm_l}^I(\vartheta, \varphi) \, Y_{l'm_l'}^I(\vartheta, \varphi) \; , \tag{2.57}$$

where $\phi_{I,\tau,l}^{\mathrm{AE}}(r)$ and $\phi_{I,\tau,l}^{\mathrm{PS}}(r)$ are, respectively, the radial all-electron wavefunction and pseudo-wavefunction with energy ϵ_τ and angular momentum l for the atomic species $\gamma(I)$ and are both centered on $\mathbf{R}_I$.

The charge density written as in Eq. (2.55) must be described using a number of PWs which is larger than that used in the norm-conserving PP scheme. While in the norm-conserving case the charge density and the wavefunctions can be described with the same accuracy using a kinetic energy cut-off as small as $E_{\mathrm{cut},\rho} = 4 \cdot E_{\mathrm{cut},\psi}$,

in the ultrasoft case a much larger $E_{\mathrm{cut},\rho}$ is needed in order to represent the augmentation functions $Q^I_{mn}(\mathbf{r})$ with a sufficient accuracy inside the core regions [82]. This additional computational cost is limited to the calculation of the charge density and does not increase the size of the matrices that have to be diagonalized, which is instead fixed by the wavefunction cut-off $E_{\mathrm{cut},\psi}$. Normally, the disadvantage is largely compensated by a conspicuous reduction of the wavefunction cut-offs (and hence of the size of the eigenvalue problem) with respect to those usually employed for norm-conserving PPs. Indeed, the relaxation of the norm-conservation constraint allows to obtain pseudo-wavefunctions which are much smoother in the core regions and also to choose larger core radii when building the PP.

When used in the solid, the USPP becomes:

$$V^{\mathrm{US}}(\mathbf{r},\mathbf{r}') = V_{\mathrm{loc}}(\mathbf{r})\,\delta(\mathbf{r}-\mathbf{r}') + \sum_{I,mn} \widetilde{D}^I_{mn} |\,\beta^I_m\rangle\langle\beta^I_n\,|\;, \tag{2.58}$$

and can be regarded as a more general form of the Kleinman-Bylander type of PP given in Eq. (2.42). The local part of the potential, $V_{\mathrm{loc}}(\mathbf{r})$, is still given by Eq. (2.38), while the screened coefficients of the non-local part have been defined as:

$$\widetilde{D}^I_{mn} = \bar{D}^{\gamma(I)}_{mn} + \int_V V_{\mathrm{eff}}(\mathbf{r})\, Q^I_{mn}(\mathbf{r}-\mathbf{R}_I)\,\mathrm{d}^3r\;, \tag{2.59}$$

where $V_{\mathrm{eff}}(\mathbf{r}) = V_{\mathrm{loc}}(\mathbf{r}) + V_H(\mathbf{r}) + V_{\mathrm{xc}}(\mathbf{r})$ is the local screened potential. The $\bar{D}^{\gamma(I)}_{mn}$ can be obtained by unscreening the $D^{l,\gamma(I)}_{\tau,\tau'}$ of the generating atomic configuration, through:

$$\bar{D}^{\gamma(I)}_{mn} \equiv \bar{D}^{\gamma(I)}_{\tau,l,m_l;\tau',l',m'_l} = \delta_{l,l'}\delta_{m_l,m'_l}\left(D^{l,\gamma(I)}_{\tau,\tau'} - \int_0^{r_c} V^{\gamma(I)}_{\mathrm{eff}}(r)\, Q^{l,\gamma(I)}_{\tau,\tau'}(r)\,\mathrm{d}r\right)\;, \tag{2.60}$$

where $D^{l,\gamma(I)}_{\tau,\tau'}$ and $Q^{l,\gamma(I)}_{\tau,\tau'}(r)$ are given by Eq. (2.49) and in Eq. (2.50a), respectively, and are written now with the explicit dependence on the angular momentum l and on the atomic species $\gamma(I)$. By looking at Eq. (2.59), it can be easily understood that in the ultrasoft scheme the $\widetilde{D}^I_{mn}$ coefficients must be updated at each iteration of the self-consistency cycle, since $V_{\mathrm{eff}}(\mathbf{r})$ depends on the electronic charge density $\rho(\mathbf{r})$. Inserting the USPP of Eq. (2.58) in the KS equations for the solid, we obtain a generalized eigenvalue problem [81]:

$$\left[-\frac{1}{2}\nabla^2 + V_{\mathrm{eff}}(\mathbf{r}) + \sum_{I,mn} \widetilde{D}^I_{mn} |\,\beta^I_m\rangle\langle\beta^I_n\,|\right] |\,\psi_{\mathbf{k},v}\rangle = \epsilon_{\mathbf{k},v}\,\widehat{S}\,|\,\psi_{\mathbf{k},v}\rangle\;, \tag{2.61}$$

where and the overlap matrix $\widehat{S}$ given by Eq. (2.52) has to be generalized using the three-dimensional form of the projectors, Eq. (2.56).

In the following we will refer to Eq. (2.61) as the *scalar-relativistic* (SR) pseudopotential KS equation and all the physical quantities that are computed from its solution will be labeled with SR.

2.4 Inclusion of spin-orbit coupling through the USPPs

All the scalar-relativistic corrections can be included in the KS equation through the PP technique just described, while the SOC effect is not included in this formulation. The largest contribution of the SOC to the energy of valence electrons originates from the regions close to the nuclei, hence SOC effects are suitable to be described through PPs. The PPs which include these effects can be generated by imposing that, for each channel, the scattering properties of the radial all-electron Dirac equation are well reproduced by the PP. Since the large component solutions are at the same time eigenstates of the total angular momentum squared, J^2, and of the orbital angular momentum squared, L^2, for each $l > 0$ the two channels $j = l + 1/2$ and $j = l - 1/2$ must be included in the non-local part of the PP, while for $l = 0$ only one channel with $j = l + 1/2$ is needed. In order to utilize this kind of PP in the solid, for each couple (l, j), the components with total and orbital angular momentum equal to, respectively, to j and l have to be separated: this can be done by using projectors written in terms of the spin-angle functions[5], $\tilde{Y}_{l,j,m_j}$ $(-j \leqslant m_j \leqslant j)$, centered on the individual atoms.

Since the spin-angle functions are two-component spinors, a SOC-including PP requires a two-component spinor DFT formalism such as that used to deal with a non-collinear magnetization [83, 84]. Within the non-collinear framework, the *spin-density* matrix $n_{\sigma\sigma'}(\mathbf{r})$ plays the same role played by the charge density $\rho(\mathbf{r})$ in the usual collinear formulation of DFT. The spin-density can be written in terms of the auxiliary two-component spinor single-particle wavefunctions, $\Psi_i(\mathbf{r})$, as

$$n_{\sigma\sigma'}(\mathbf{r}) = \sum_i f_i \, \bar{\Psi}_i^{\sigma}(\mathbf{r}) \Psi_i^{\sigma'}(\mathbf{r}) \, , \tag{2.62}$$

where $\Psi_i^{\sigma}(\mathbf{r})$ are the two spinor components

$$\Psi_i(\mathbf{r}) = \begin{pmatrix} \Psi_i^{\uparrow}(\mathbf{r}) \\ \Psi_i^{\downarrow}(\mathbf{r}) \end{pmatrix} \quad . \tag{2.63}$$

Two important quantities are derived from the spin-density: the charge density $n(\mathbf{r})$, which corresponds to the trace of $n_{\sigma\sigma'}(\mathbf{r})$, and the magnetization density $\mathbf{m}(\mathbf{r})$, which has three components given by

$$m_\alpha(\mathbf{r}) = \mu_B \sum_i \sum_{\sigma\sigma'} f_i \, [\Psi_i^{\sigma}(\mathbf{r})]^* \, \sigma_\alpha^{\sigma\sigma'} \Psi_i^{\sigma'}(\mathbf{r}) \, , \tag{2.64}$$

[5]The spin-angle function $\tilde{Y}_{l,j,m_j}$ is a two-component spinor (see later) which is at the same time an eigenstate of J^2, J_z, L^2, and S^2 (the spin angular momentum squared); m_j indicates the eigenvalues of the projection of J along a fixed quantization axis. An explicit formula for $\tilde{Y}_{l,j,m_j}$ can be found in Ref [63].

where σ_α are the Pauli matrices. The total energy of the system is a functional of the spin-density, but if we use the *local spin density approximation* (LSDA), which assumes that the exchange-correlation energy $E_{\rm xc}[n_{\sigma\sigma'}(\mathbf{r})]$ depends only upon the charge density $n(\mathbf{r})$ and the absolute value of the magnetization density $|\mathbf{m}(\mathbf{r})|$, the constrained minimization of the functional with respect to $\Psi_i(\mathbf{r})$ can be done using the expression of $n(\mathbf{r})$ and $|\mathbf{m}(\mathbf{r})|$ in terms of the $\Psi_i(\mathbf{r})$.

Dal Corso and Mosca Conte [63] have shown how to incorporate SOC effects in PPs of the Vanderbilt-ultrasoft type. With SOC, the non-local part of the USPP becomes:

$$\widehat{V}_{NL}^{\sigma\sigma'} = \sum_I \sum_{\tau,l,j,m_j} \sum_{\tau',l',j',m'_j} \widetilde{D}^I_{\tau,l,j,m_j;\tau',l',j',m'_j} |\, \beta^I_{\tau,l,j} \tilde{Y}^{I,\sigma}_{l,j,m_j} \rangle\langle \beta^I_{\tau',l',j'} \tilde{Y}^{I,\sigma'}_{l',j',m'_j} \,| \;, \tag{2.65}$$

where the radial components of the N_ϵ projectors, $\beta^I_{\tau,l,j}$, and the corresponding unscreened coefficients,

$$\bar{D}^{\gamma(I)}_{\tau,l,j,m_j;\tau',l',j',m'_j} = \bar{D}^{\gamma(I),l,j}_{\tau,\tau'}\, \delta_{l,l'}\delta_{j,j'}\delta_{m_j,m'_j} \;, \tag{2.66}$$

here depend on both l and j. The operator projecting onto the subspace with fixed l and j is a 2×2 matrix in the spin index σ.

By rewriting in a convenient way the spin-angle functions, it is possible to recast the non-local part of the USPP in a form similar to that reported in Eq. (2.58) for scalar wavefunctions [63]. The coefficients of the non local part are expressed as 2×2 matrices which depend on the two composite indexes $m = \tau, l, j, m_l$ and $n = \tau', l', j', m'_l$,

$$\bar{D}^{\gamma(I),\sigma\sigma'}_{\tau,l,j,m_l;\tau',l',j',m'_l} = \bar{D}^{\gamma(I),l,j}_{\tau,\tau'} f^{\sigma\sigma'}_{l,j,m_l;l',j',m'_l}\, \delta_{l,l'}\delta_{j,j'} \;, \tag{2.67}$$

where the expression for the $f^{\sigma\sigma'}_{l,j,m_l;l',j',m'_l}$ and the formula for the screened $\widetilde{D}^{I,\sigma\sigma'}_{mn}$ coefficients can be found in Ref. 63. The projector functions can be defined in terms of the functions $|\,\beta^I_m\rangle$, which can be written in real space representation as

$$\langle \mathbf{r}|\, \beta^I_{\tau,l,j,m_l}\rangle = \beta^I_{\tau,l,j}(r)\, Y^I_{l,m_l}(\vartheta,\varphi) \;. \tag{2.68}$$

The number of projectors for each $l > 0$ is therefore the double with respect to the SR case, but there is no more the need to project directly onto the spin-angle functions; indeed, the projectors in Eq. (2.68) do not contain anymore the spinors $\tilde{Y}^I_{l,j,m_j}$ of Eq. (2.65), but only the usual spherical harmonics $Y^I_{l,m_l}(\vartheta,\varphi)$ of the SR case.

The resulting two-component spinor KS equation including the USPP with SOC effects can be written in the following form [85]:

$$\sum_{\sigma'} \left[-\nabla^2\delta_{\sigma\sigma'} + V^{\sigma\sigma'}_{\rm LOC}(\mathbf{r}) + \sum_{I,mn} \widetilde{D}^{I,\sigma\sigma'}_{mn} |\, \beta^I_m\rangle\langle \beta^I_n \,| \right] |\, \Psi^{\sigma'}_{\mathbf{k}v}\rangle = \epsilon_{\mathbf{k}v}\, \widehat{S}^{\sigma\sigma'} |\, \Psi^{\sigma}_{\mathbf{k}v}\rangle \;, \tag{2.69}$$

where the local potential has been defined as

$$V_{\mathrm{LOC}}^{\sigma\sigma'}(\mathbf{r}) = V_{\mathrm{eff}}(\mathbf{r})\,\delta_{\sigma\sigma'} + \mu_B\,\mathbf{B}_{\mathrm{xc}}(\mathbf{r})\cdot\boldsymbol{\sigma}^{\sigma\sigma'}\ , \tag{2.70}$$

and contains the screened effective potential $V_{\mathrm{eff}}(\mathbf{r})$ and the products between the Pauli matrices $\boldsymbol{\sigma}$ and the components of the exchange-correlation magnetic field,

$$B_{\mathrm{xc},\alpha}(\mathbf{r}) = \frac{\partial E_{\mathrm{xc}}}{\partial|\mathbf{m}|}\frac{\partial|\mathbf{m}|}{\partial m_\alpha}\ . \tag{2.71}$$

In the following of this thesis, we will identify Eq. (2.69) as the *fully-relativistic* (FR) KS equation and all quantities computed through it will be marked as FR.

2.5 Density of states

The dispersion relations $(\mathbf{k}, \epsilon_{\mathbf{k}v})$ obtained by solving the KS equation (either in their SR or FR form) for the solid at different values of $\mathbf{k}$ it is possible to compute the density of states (DOS)

$$\rho(E) = \sum_{\mathbf{k},v}\delta(E-\epsilon_{\mathbf{k}v})\ , \tag{2.72}$$

which is here defined as a sum of Dirac delta functions centered at energy values corresponding to the eigenvalues of the KS equation. In practice this summation is performed by substituting $\delta(\epsilon)$ with a regular and continuous function $\tilde{\delta}(\epsilon)$ which has the same normalization as $\delta(\epsilon)$. In this thesis we used gaussian functions with a spread controlled by a smearing parameter s,

$$\tilde{\delta}(\epsilon) = \frac{1}{\sqrt{2\pi}s}\mathrm{e}^{-(\epsilon/2s)^2}\ . \tag{2.73}$$

In order to reach a good approximation of the exact limit of the DOS, given by Eq. (2.72) and corresponding to the limit $s \to 0$, a small enough value of the smearing has to be chosen. However, since the number of $\mathbf{k}$ points needed to converge the DOS increases very fast as s is decreased, in practical calculations one makes a trade-off between the desired accuracy (essentially, how much fine structures can be resolved in the DOS) and the computational cost given by the number of $\mathbf{k}$ points.[6]

Another quantity of interest that can be computed from the dispersion relations and from the pseudo-wavefunctions $\psi^{\mathrm{PS}}_{\mathbf{k}v}(\mathbf{r})$, eigenstates of the KS equation, is the projected-density of states (PDOS). For each atomic wavefunction $\psi^{\mathrm{PS}}_{I,\alpha}(\mathbf{r})$ associated to atom I (centered on $\mathbf{R}_I$), we can define the PDOS, $\rho_{I,\alpha}(E)$, as the DOS projected

[6]Since we mainly compute DOS for one-dimensional systems in this thesis we don't make use of the tetrahedron method, which is very efficient for a rapid converge of the DOS in 3D systems.

onto that atomic wavefunction. In the SR case, the quantum numbers of the atomic wavefunction have the form $\alpha = l, m_l$, where l and m_l are the indexes associated to the eigenstate $\psi^{\mathrm{PS}}_{I,l}(r)$ of the radial atomic SR equation and to the spherical harmonic Y^I_{l,m_l}, and the PDOS can be written as:

$$\rho_{I,\alpha}(E) = \sum_{\mathbf{k},v} \left| \langle \psi^{\mathrm{PS}}_{\mathbf{k}v} | \, \widehat{S} \, | \, \psi^{\mathrm{PS}}_{I,\alpha} \rangle \right|^2 \tilde{\delta}(E - \epsilon_{\mathbf{k}v}) \; , \tag{2.74}$$

where the overlap operator is needed in the ultrasoft case (for the norm-conserving case it has to be replaced by the identity operator). In the FR case, the KS eigenstates are projected onto atomic spinors $\Psi^{\mathrm{PS}}_{I,\alpha}(\mathbf{r})$, with $\alpha = l, j, m_j$, which are the eigenstates of the atomic FR equations with quantum numbers l, j, and m_j. Hence the PDOS can be written as

$$\rho_{I,\alpha}(E) = \sum_{\mathbf{k},v} \sum_{\sigma} \left| \langle \Psi^{\sigma}_{\mathbf{k}v} | \, \widehat{S} \, | \, \Psi^{\sigma}_{I,\alpha} \rangle \right|^2 \tilde{\delta}(E - \epsilon_{\mathbf{k}v}) \; , \tag{2.75}$$

where we omitted the PS label for simplicity of notation.

2.6 Ballistic transport calculations

In this section we will briefly describe the method we used to compute the scattering matrix $\mathbf{S}$ for an open quantum system (depicted schematically in Fig. 1.5 of Sec. 1.2). The coefficients of this matrix, which allow to compute the ballistic conductance through Eq. (1.11), can be obtained by solving the scattering problem for a system composed by a scattering region sandwiched between a left and a right lead. The scattering region can contain any kind of defect and all the reflection and transmission processes take place inside it, while the left (right) lead has a perfectly periodic crystalline structure and extends infinitely on the left (right) direction. The method is due to Choi and Ihm [62] and was originally formulated for the case of non-local PPs of the Kleinman-Bylander type defined in Eq. (2.42). In the work by Smogunov et al. [86], the method has been extended to the case of the USPPs written as in Eq. (2.58), thus making it suitable for studying the ballistic electron transport in systems with localized d valence electrons.

Within the DFT+USPP framework described in the previous sections, a scattering state Ψ at an energy E is the solution of the single-particle KS problem given by Eq. (2.61). Since the energy E is fixed and can be considered as an input parameter of the scattering equation, the coefficients $\widetilde{D}^I_{mn}$ appearing in the non-local term of the USPP,

$$\widehat{V}_{\mathrm{NL}} = \sum_{I,mn} \widetilde{D}^I_{mn} | \, \beta^I_m \rangle \langle \beta^I_n \, | \; , \tag{2.76}$$

can be conveniently replaced with $\bar{D}^I_{mn} = \widetilde{D}^I_{mn} - Eq^I_{mn}$, so that Eq. (2.61) can be rewritten in the following form:

$$\big[-\frac{1}{2}\nabla^2 + V_{\text{eff}} + \widehat{V}'_{\text{NL}} \big] | \Psi \rangle = E | \Psi \rangle \ , \tag{2.77}$$

without the overlap operator on the right hand side and with $\widehat{V}'_{\text{NL}}$ written as Eq. (2.76), but using the new coefficients.

We assume that the electron transport is along the z direction and we restrict the scattering region within $0 < z < L$, while the semi-infinite left and right leads occupy the regions of space defined by $z < 0$ and by $z > L$, respectively. The effective potential V_{eff}, the screened USPP coefficients $\widetilde{D}^I_{mn}$, and the q^I_{mn} coefficients can be obtained from a previous self-consistent calculation for a supercell which contains the resistive region in the middle and a portion of the leads on both sides. The system is repeated periodically in the xy plane, therefore along these two directions the scattering states can be written in the usual Bloch form:

$$\Psi(\mathbf{r}_\perp + \mathbf{R}_\perp, z) = \mathrm{e}^{\,\mathrm{i}\,\mathbf{k}_\perp \cdot \mathbf{R}_\perp} \Psi(\mathbf{r}_\perp, z) \ , \tag{2.78}$$

where $\mathbf{r}_\perp = (x, y)$ and $\mathbf{R}_\perp = n_1\mathbf{a}_1 + n_2\mathbf{a}_2$. At a fixed energy E, the scattering states can be classified according to the value of $\mathbf{k}_\perp$ and are independent. In the implementation of the method used in this thesis, the scattering states are expanded in PWs along the perpendicular directions x and y:

$$\Psi_{\mathbf{k}_\perp}(\mathbf{r}_\perp, z) = \sum_{\mathbf{G}_\perp} \Psi_{\mathbf{k}_\perp}(\mathbf{G}_\perp, z)\, e^{\,\mathrm{i}\,(\mathbf{G}_\perp + \mathbf{k}_\perp)\cdot \mathbf{r}_\perp} \ , \tag{2.79}$$

where the sum on the $\mathbf{G}_\perp$ vectors includes all the PWs comprised in the 2D basis set and counts N_{2D} elements.

If the vectors $\mathbf{R}$ of the direct lattice are written separating the component on the perpendicular 2D-lattice:

$$\mathbf{R} = \mathbf{R}_\perp + \mathbf{d}_s \ , \tag{2.80}$$

where $\mathbf{d}_s$ is the position of nucleus s within the supercell, we can rewrite the non-local part of the potential as

$$\widehat{V}_{\text{NL}} | \Psi_{\mathbf{k}_\perp} \rangle = \sum_{s,mn} \bar{D}^s_{mn} \langle \beta^s_n | \Psi_{\mathbf{k}_\perp} \rangle \left(\sum_{\mathbf{R}_\perp} \mathrm{e}^{\,\mathrm{i}\,\mathbf{k}_\perp \cdot \mathbf{R}_\perp} \beta^s_m(\mathbf{r} - \mathbf{R}_\perp - \mathbf{d}_s) \right) \ , \tag{2.81}$$

because the following relationship holds

$$\langle \beta^I_n | \Psi_{\mathbf{k}_\perp} \rangle = \mathrm{e}^{\,\mathrm{i}\,\mathbf{k}_\perp \cdot \mathbf{R}_\perp} \langle \beta^s_n | \Psi_{\mathbf{k}_\perp} \rangle \tag{2.82}$$

and the coefficients $\bar{D}^s_{mn}$ are independent of $\mathbf{R}_\perp$ thanks to the periodicity of $V_{\text{eff}}(\mathbf{r})$. If we make the following definitions:

$$\begin{aligned} P_{sm}(\mathbf{r}) &\equiv \sum_{\mathbf{R}_\perp} \mathrm{e}^{\,\mathrm{i}\,\mathbf{k}_\perp\cdot\mathbf{R}_\perp}\beta^s_m(\mathbf{r}-\mathbf{R}_\perp-\mathbf{d}_s)\ , \\ C^{\mathbf{k}_\perp}_{sm} &\equiv \sum_n \bar{D}^s_{mn}\langle\beta^s_n|\,\Psi_{\mathbf{k}_\perp}\rangle\ , \end{aligned} \tag{2.83}$$

then Eq. (2.77) acquires the form of an integral-differential equation:

$$\big[-\frac{1}{2}\nabla^2+V_{\text{eff}}-E\big]|\,\Psi_{\mathbf{k}_\perp}\rangle+\sum_{sm}P_{sm}(\mathbf{r})C^{\mathbf{k}_\perp}_{sm}=0\ , \tag{2.84}$$

where the summation on sm now includes only the N projectors associated to the atomic centers inside the supercell.

At a fixed $\mathbf{k}_\perp$-point, the scattering state $\Psi_{\mathbf{k}_\perp}$ with energy E which originates from a right-moving Bloch state ψ_k incoming from $z=-\infty$ can be written as [62]:

$$\Psi_{\mathbf{k}_\perp}=\begin{cases}\psi_k+\sum_{k'\in\mathcal{L}}r_{k'k}\,\psi_{k'}\ , & z\leqslant 0\\ \sum_n c_n\phi_n(\mathbf{r})+\sum_{sm}c_{sm}\phi_{sm}(\mathbf{r})\ , & 0\leqslant z\leqslant L\\ \sum_{k'\in\mathcal{R}}t_{k'k}\,\psi_{k'}\ , & z\geqslant L\ ,\end{cases} \tag{2.85}$$

where the sum over $k'\in\mathcal{L}$ ($k'\in\mathcal{R}$) includes all the generalized Bloch waves $\psi_{k'}$ propagating or decaying to the left (to the right) in the left lead (in the right lead).

Within the leads ($z<0$ and $z>L$), the generalized Bloch waves satisfy

$$\psi_k(\mathbf{r}_\perp,z+d)=\mathrm{e}^{\,\mathrm{i}\,kd}\psi_k(\mathbf{r}_\perp,z)\ , \tag{2.86}$$

where d is the lattice periodicity of the leads. The wavenumber k can be in general a complex number (since the PBCs have been removed along z) and the dispersion relations (k,E) represent the so-called complex band structure (CBS) of the leads. The ψ_k can be obtained from the general solution of Eq. (2.84) inside a unit cell of the leads (i.e., for $z_0<z<z_0+d$) and can be described as a linear combination of two kind of terms [62]:

$$\psi_k(\mathbf{r})=\sum_n c_{n,k}\phi_n(\mathbf{r})+\sum_{sm}c_{sm,k}\phi_{sm}(\mathbf{r})\ . \tag{2.87}$$

The first kind of terms contain the ϕ_n, which are linearly independent solutions of the homogeneous equation associated to Eq. (2.84):

$$\big[-\frac{1}{2}\nabla^2+V_{\text{eff}}-E\big]|\,\phi_n\rangle=0\ , \tag{2.88}$$

while the second kind contain the ϕ_{sm}, which are the particular solutions of the non-homogeneous equations:

$$\big[-\frac{1}{2}\nabla^2 + V_{\text{eff}} - E\big]\,|\,\phi_{sm}\rangle + P_{sm} = 0\ . \tag{2.89}$$

The number of states ϕ_{sm} that have to be computed is equal to the number N of projectors within the unit cell of the lead.

Given an energy E, in order to find the possible values of k we impose that both the solutions and their derivatives with respect to z satisfy the condition in Eq. (2.86)

$$\psi_k(\mathbf{r}_\perp, z+d) = \mathrm{e}^{\mathrm{i}kd}\psi_k(\mathbf{r}_\perp, z) \tag{2.90}$$

$$\psi'_k(\mathbf{r}_\perp, z+d) = \mathrm{e}^{\mathrm{i}kd}\psi'_k(\mathbf{r}_\perp, z)\ . \tag{2.90$'$}$$

Furthermore, the function ψ_k in Eq. (2.87) can be a solution to Eq. (2.84) only if the coefficients $c_{sm,k}$ satisfy

$$c_{sm,k} = \sum_n \bar{D}^s_{mn}\langle\beta^s_n|\,\psi_k\rangle\ . \tag{2.91}$$

By inserting the expansion (2.87) in Eq. (2.90), (2.90$'$) and (2.91) we can obtain a generalized eigenvalue problem [62]:

$$AX = \mathrm{e}^{\mathrm{i}kd}BX\ , \tag{2.92}$$

where A and B are two general complex matrices. The solutions of Eq. (2.92) give the CBS and the generalized Bloch states ψ_k. The size of the A and B matrices in Eq. (2.92) is equal to $N_{2D} \times N_{2D}$ and by solving the eigenvalue problem we get N_{2D} complex eigenvalues k and eigenstates $X = \{c_{n,k}, c_{sm,k}\}$, which contain the coefficients needed to compute the scattering state $\psi_k(\mathbf{r})$ through Eq. (2.87). Among the eigenvalues, some are real and correspond to propagating Bloch states which can also be obtained with 3D periodic boundary conditions, while the remaining have a non-null imaginary part, $\Im k \neq 0$, and correspond to exponentially decaying or growing states.

Inside the scattering region ($0 < z < L$), the scattering state can be expressed as a linear combination similar to that in Eq. (2.87):

$$\Psi_{\mathbf{k}_\perp}(\mathbf{r}) = \sum_n c_n\phi_n(\mathbf{r}) + \sum_{sm} c_{sm}\phi_{sm}(\mathbf{r})\ , \tag{2.93}$$

where the functions ϕ_n and ϕ_{sm} are the solutions of Eq. (2.88) and Eq. (2.89), respectively, in the region $0 < z < L$ and the sum over sm includes all the projectors in the scattering region, while the coefficients c_{sm} must satisfy:

$$c_{sm} = \sum_n \bar{D}^s_{mn}\langle\beta^s_n|\,\Psi_{\mathbf{k}_\perp}\rangle\ . \tag{2.94}$$

If the atomic spheres[7] of the projectors $|\,\beta_n^s\rangle$ centered on atom s cross the $z = 0$ plane, the c_{sm} coefficients must fulfil an additional set of conditions involving the $c_{sm,k}$ coefficients obtained previously,

$$c_{sm,k} + \sum_{k'} r_{k'k} c_{sm,k'} = c_{sm} \ , \tag{2.95}$$

while for atomic spheres crossing the $z = L$ plane, the coefficients must satisfy

$$\sum_{k'} t_{k'k} c_{sm,k'} = c_{sm} \ . \tag{2.96}$$

The last three equations, together with the boundary conditions for $\Psi_{\mathbf{k}_\perp}(\mathbf{r})$ and for its derivatives at $z = 0$ and $z = L$, give an algebraic system of linear equations. The unknown coefficients $\{c_n, c_{sm}, r_{kk'}, t_{kk'}\}$ can be obtained by solving the linear system and allow to determine the scattering state and the transmission matrix.

In order to fulfil the unitary condition of Eq. (1.12), the $t_{kk'}$ coefficients must be renormalized according to Eq. (1.13), giving $t'_{kk'} = \sqrt{v_k/v_{k'}}\, t_{kk'}$, where v_k is the velocity associated to the Bloch state ψ_k. Equivalently, the transmission coefficients can be renormalized with $t'_{kk'} = \sqrt{I_k/I_{k'}}\, t_{kk'}$, where I_k is the quantum-mechanical probability current associated to ψ_k. In the USPP case, the usual formula for the current flowing through a plane S perpendicular to the z axis and located at z_0,

$$I_k^0 = 2\,\Im\left[\int_S \mathrm{d}\mathbf{r}_\perp^2\ \psi_k^*(\mathbf{r}_\perp, z_0) \frac{\partial \psi_k(\mathbf{r}_\perp, z)}{\partial z}\bigg|_{z=z_0}\right] , \tag{2.97}$$

where $\Im$ denotes the imaginary part, is valid only when the plane does dot cross any atomic sphere of the PP. A more general formula, valid for any z_0, has been put forward by Smogunov et al. [86]:

$$I_k = I_k^0 - 2\,\Im\left[\sum_{I,mn} \widetilde{D}^I_{mn} \langle \beta_n^I |\, \psi_k\rangle \int_{-\infty}^{z_0} \mathrm{d}z \int_S \mathrm{d}\mathbf{r}_\perp^2\ \beta_m^I(\mathbf{r} - \mathbf{R}_I) \psi_k^*(\mathbf{r})\right] , \tag{2.98}$$

and keeps properly into account the augmentation terms localized within the atomic spheres. The normalized coefficients are then used to build the $\mathbf{t}^\dagger\mathbf{t}$ matrix, which can be diagonalized to give the eigenvalues τ_i and, finally, the ballistic conductance of the system through Eq. (1.14).

A recent work by Dal Corso et al. [85] has extended further this method to include SOC effects in the transmission matrix calculation by using the FR-USPPs described

[7] For a projector associated to an atomic center I inside the scattering region, the atomic spheres are the regions with $|\mathbf{r} - \mathbf{R}_I| < r_{c,l}$, where $r_{c,l}$ are the core radii of the PP described in Sec. 2.3.

in Sec. 2.4. Also in the FR case, the non-local part of the USPP can be rewritten by replacing the screened $\widetilde{D}^{I,\sigma\sigma'}_{mn}$ with:[8]

$$\bar{D}^{I,\sigma\sigma'}_{mn} = \widetilde{D}^{I,\sigma\sigma'}_{mn} - E q^{I\sigma\sigma'}_{mn} \ , \tag{2.99}$$

so that the overlap matrix does not appear anymore on the right side of Eq. (2.69). The resulting FR scattering equation can be solved with a procedure analogous to that outlined here above for the SR case and the transmission coefficients can be normalized using the probability current formula extended to the FR case [85].

If the leads represent 1D-structures of finite cross-section (such as a monatomic chain, a thicker nanowire or a nanotube, for instance), the transmission does not depend on $\mathbf{k}_\perp$, as long as the supercell size along the perpendicular dimensions is large enough to avoid spurious interactions with the periodic replicas. When solving the scattering problem for tipless chains (see Sec. 3.3 and Sec. 4.3), we have used supercells which are large enough along x and y so that the transmission can be evaluated to a good accuracy by using only the Γ point in the two-dimensional BZ. If instead the leads represent extended 2D-structures (such as semi-infinite bulk regions terminated by a surface, see Chap. 5), the $\mathbf{k}_\perp$-dependent transmission can display large variations at different points of the 2D-BZ (see, for instance, Refs. 87 and 88). It is therefore necessary to sample of the 2D-BZ with an appropriate set of points: in this work we have chosen a two-dimensional grid of uniformly-spaced $\mathbf{k}_\perp$-points, in analogy with the 3D grids used to sample the BZ in the electronic structure calculations, and the accuracy of the results has been checked by increasing systematically the number of points in the grid.

All the ballistic transport calculations presented in this thesis have been performed using the implementation of the method contained in the `PWcond` code, included in the Quantum ESPRESSO distribution [47].

[8] The reader can refer to [63] for the definition of $q^{I\sigma\sigma'}_{mn}$ in the FR framework.

2.7 A scheme for ballistic transport within DFT+U

A shortcoming of common local and semi-local exchange-correlation functionals of widespread use in DFT calculations is the inexact cancellation of the self-interaction energy in the Hartree and exchange terms. This approximate treatment of the exchange energy leads to what is commonly known as the self-interaction error (SIE) in the description of the electronic structure. The effects of the SIE are enhanced in structures characterized by a low dimensionality (such as 1D-chains) because the electron localization is higher. For a fully occupied state, for instance, the incomplete cancellation of the Hartree energy by the exchange term results in a one particle energy level which is less bound (thus it moves towards higher energies with respect to E_{F}). Various solutions have been proposed to cure this problem, such as self-interaction correction (SIC) schemes or hybrid functionals techniques, also known under the name of exact exchange (EE).

Also the so-called DFT+U method, although more aimed at introducing electron-electron correlations, can be regarded as a possible strategy to cope with the SIE, since it originates from a mean-field treatment of an Hartree-Fock Hamiltonian on a set of localized orbitals (the atomic functions of d electrons, for instance). The method has already been applied to study monatomic chains made of $3d$ and $4d$ transition metals and it has been demonstrated that a SIC has the same qualitative effect of a +U correction at small values of U (in the range $U = 2 \div 3\,\mathrm{eV}$) [57]. While SIC and EE methods introduce substantial complications or a non-negligible computational overload (or both) with respect to standard DFT, the DFT+U method represents a minimal extension which retains the computational efficiency of DFT in treating large systems from first principles and, despites its simplicity, it can improve the physical description of several problematic cases [58–60]. Our aim here is to select a formulation of DFT+U that could be easily integrated inside the scattering-state formalism for ballistic transport outlined in the previous section, in order to allow the calculation of the ballistic transmission for an Hamiltonian including the Hubbard U correction. As it will explained soon in more detail, we found quite suitable to use a simple rotationally-invariant formulation of the Hubbard Hamiltonian, already implemented in the `PWscf` code [58], and modify the procedure of computing the local occupations. Instead of projecting KS states onto atomic wavefunctions, we choose to build the occupations from the overlaps between KS states and the USPP projectors (which are localized inside the core regions), following what has been proposed by Bengone et al. [60] in the projector augmented-wave (PAW) framework.

The DFT+U approach involves the following steps: (i) a localized basis set is selected in order to project onto a manifold of electronic states which are not described with a sufficient accuracy within LDA/GGA (for instance states which give rise to very

narrow bands, such as $3d$ electrons in third row transition elements), or which conserve a strong atomic-like character also in the solid (such as $4f$ electrons in lanthanides); (ii) electrons populating these states are described with a model Hamiltonian, usually derived from a mean-field unrestricted Hartree-Fock treatment of the on-site many-body Coulomb interaction among the localized electronic manifold associated to each atomic center. Various formulations of the DFT+U method have been developed since its earlier proposals [89–91]; in this work we use a simplified version [58, 59], where only the main effect of the on-site Coulomb repulsion is taken into account by keeping the F_0 term in the multipolar expansion of the Coulomb interaction and disregarding the contribution of the higher order terms $F_2, F_4, \ldots$ [58]. The resulting formula has the advantage of being rotationally-invariant with respect to the choice of the local basis set and it uses a single external parameter U [59]. In this simplified formulation, the additional term which is added to the total energy DFT functional reads [58]:

$$E_U = E_{\mathrm{Hub}} - E_{\mathrm{DC}} = \frac{U}{2} \sum_{I\sigma} \sum_{m} \left[n^{I\sigma}_{mm} - \sum_{m'} n^{I\sigma}_{mm'} n^{I\sigma}_{m'm} \right] , \tag{2.100}$$

where a double counting term E_{DC} is subtracted to the Hubbard energy E_{Hub} in order to avoid adding to the total energy those terms which can be accounted for in standard DFT and are actually already included in the original functional. In Eq. (2.100), the $n^{I\sigma}_{mm'}$ are the local occupation matrices and can be written in a quite general form [58]:

$$n^{I\sigma}_{mm'} = \sum_{\mathbf{k}v} f_{\mathbf{k}v} \langle \psi^{\sigma}_{\mathbf{k}v} | \, P^{I}_{mm'} \, | \psi^{\sigma}_{\mathbf{k}v} \rangle , \tag{2.101}$$

where the generalized projection operators $P^{I}_{mm'}$ are applied to the wavefunctions $\psi^{\sigma}_{\mathbf{k}v}$, solutions of the KS equation in the solid for the spin component σ at a point $\mathbf{k}$ in the IBZ. The definition of Eq. (2.101) can be used in any implementation of the spin-polarized collinear DFT framework, i.e. it is not formulated only for a particular basis set employed to solve the KS equations.

The $n^{I\sigma}_{mm'}$ matrices are diagonal in the spin index and in spin unpolarized calculations they are also spin-independent (that is to say, $n^{I,-\sigma}_{mm'} = n^{I,\sigma}_{mm'}$). The Hubbard energy and double counting term in Eq. (2.100) can be rewritten using a Kronecker delta as:

$$E_U = \frac{U}{2} \sum_{I\sigma} \sum_{mm'} n^{I\sigma}_{mm'} \left[\delta_{m,m'} - n^{I\sigma}_{m'm} \right] , \tag{2.102}$$

so that the Hubbard correction to the KS potential can be derived straightforwardly from the expression of E_U by taking its functional derivative with respect to the KS

states (through the dependence on the local occupations):

$$V_U^\sigma |\, \psi_{\mathbf{k}v}^\sigma \rangle = \frac{\delta E_U}{\delta \langle \psi_{\mathbf{k}v}^\sigma \,|} = \sum_I \sum_{mm'} \frac{\partial E_U}{\partial n_{mm'}^{I\sigma}} \, \frac{\delta n_{mm'}^{I\sigma}}{\delta \langle \psi_{\mathbf{k}v}^\sigma \,|} \, . \tag{2.103}$$

Working out the first term in the products we get

$$\frac{\partial E_U}{\partial n_{mm'}^{I\sigma}} = \frac{U}{2}(\delta_{m'm} - 2n_{m'm}^{I\sigma}) \, , \tag{2.104}$$

while from the second, using Eq. (2.101), we get

$$\frac{\delta n_{mm'}^{I\sigma}}{\delta \langle \psi_{\mathbf{k}v}^\sigma \,|} = P_{mm'}^I |\, \psi_{\mathbf{k}v}^\sigma \rangle \, , \tag{2.105}$$

and hence the correction to the potential reads:

$$V_U^\sigma = \sum_I \sum_{mm'} V_{mm'}^{I\sigma} \, P_{mm'}^I \, , \tag{2.106}$$

where the $V_{mm'}^{I\sigma}$ have been defined as:

$$V_{mm'}^{I\sigma} = \frac{\partial E_U}{\partial n_{mm'}^{I\sigma}} = \frac{U}{2}(\delta_{m'm} - 2\, n_{m'm}^{I\sigma}) \, . \tag{2.107}$$

Once we have selected the manifold of valence electrons which need to be treated within the DFT+U scheme (usually it corresponds to an electronic shell of the atoms with the Hubbard correction, such as the d shell for transitional elements or the f shell for rare earths), a possible choice for the projectors might be:

$$P_{mm'}^I = |\, \varphi_m^I \rangle \langle \varphi_{m'}^I \,|, \tag{2.108}$$

where $|\, \varphi_m^I \rangle$ is the atomic pseudo-wavefunction with orbital quantum numbers (l, m) for the atom sitting at site I (the angular momentum is fixed by the choice of the shell: $l = 2$ for the d shell, $l = 3$ for the f shell, ...). The radial part of these atomic wavefunctions usually comes together with the PP files (or PAW datasets), since they are used to build an initial guess for the charge density. In order to be used in the solid, the atomic wavefunctions are written as a Bloch state (as in a tight binding formalism) and contain a structure factor which gives a dependence upon $\mathbf{k}$, hence the projectors themselves are $\mathbf{k}$-dependent. We notice here that the form in Eq. (2.108) is fully separable and thus very convenient to be used in a PW code, as explained in Sec. 2.3 for the Kleinman-Bylander's type of PP. In the USPP formalism, in Eq. (2.108) the pseudo-wavefunctions $|\, \varphi_m^I \rangle$ have to be replaced by $|\, \widehat{S} \varphi_m^I \rangle$ (and, analogously, $\langle \varphi_{m'}^I \,|$ with $\langle \varphi_{m'}^I \widehat{S} \,|$), where $\widehat{S}$ is the overlap operator introduced in Eq. (2.52) of Sec. 2.3.

For our purposes, the main disadvantage of choosing the projectors as in Eq. (2.108) is that, although the atomic wavefunction $\langle \mathbf{r}| \varphi_m^I \rangle$ goes rapidly to zero in the unit cell when moving away from the atomic center $\mathbf{R}_I$, it is in principle defined on a non-limited support and this would cause difficulties in the calculation of the CBS with the method described in Sec. 2.6. Therefore, we propose an alternative approach to compute local occupations which makes use of the overlap between KS states and PP projectors in place of atomic wavefunctions. Our idea was inspired by a DFT+U formulation devised for the PAW scheme by Bengone et al. [60], who used an approximate count for the local occupations obtained by integrating the local charge density only inside the atomic core regions. Thanks to the similarity between the USPP method and the PAW formalism, we can apply a PAW-like transformation [92] to the all-electron (AE) version of the projection operator, $P_{mm'}^{\mathrm{AE},I} = | \phi_m^{\mathrm{AE},I} \rangle \langle \phi_{m'}^{\mathrm{AE},I} |$, to obtain the corresponding pseudo (PS) version[9] as in Ref. 60:

$$\begin{aligned} \langle \psi_{\mathbf{k}v}^{\mathrm{AE}} | \, P_{mm'}^{\mathrm{AE},I} \, | \, \psi_{\mathbf{k}v}^{\mathrm{AE}} \rangle = \langle \psi_{\mathbf{k}v} | \, P_{mm'}^{\mathrm{AE},I} \, | \, \psi_{\mathbf{k}v} \rangle + \\ \sum_{ij} \langle \psi_{\mathbf{k}v} | \, \beta_i \rangle \left[\langle \phi_i^{\mathrm{AE}} | \, P_{mm'}^{\mathrm{AE},I} \, | \, \phi_j^{\mathrm{AE}} \rangle - \langle \phi_i^{\mathrm{PS}} | \, P_{mm'}^{\mathrm{AE},I} \, | \, \phi_j^{\mathrm{PS}} \rangle \right] \langle \beta_j | \, \psi_{\mathbf{k}v} \rangle \end{aligned} \tag{2.109}$$

where ϕ_i^{AE} (ϕ_i^{PS}) is the AE (PS) partial wave corresponding to the PP projector β_i, and $\psi_{\mathbf{k}v}$ are the PS wavefunctions which are obtained from the solution of the USPP-KS equation. The integrals needed for the AE and PS matrix elements between square brackets can be performed within the augmentation spheres around each atom, since AE and PS partial waves coincide outside the spheres by construction. Notice that the index i is a shortcut for a composite index $i = \{I, \tau, l, m_l\}$ which runs over atoms, energy and orbital angular quantum numbers (the same applies to $j = \{J, \tau', l', m_l'\}$).

Assuming that the projection operators $P_{mm'}^{\mathrm{AE},I}$ are sufficiently localized within the atomic spheres and that partial waves and projectors form a complete basis inside these regions, we can apply to $P_{mm'}^{\mathrm{AE},I}$ the following equality (valid for an arbitrary operator $\hat{B}$ entirely localized within the atomic spheres):

$$0 = \langle \psi_{\mathbf{k}v} | \, \hat{B} \, | \, \psi_{\mathbf{k}v} \rangle - \sum_{ij} \langle \psi_{\mathbf{k}v} | \, \beta_i \rangle \langle \phi_i^{\mathrm{PS}} | \, \hat{B} \, | \, \phi_j^{\mathrm{PS}} \rangle \langle \beta_j | \, \psi_{\mathbf{k}v} \rangle \tag{2.110}$$

and substitute in Eq. (2.109) to obtain an approximate expression for the projection operators:

$$\langle \psi_{\mathbf{k}v}^{\mathrm{AE}} | \, P_{mm'}^{\mathrm{AE},I} \, | \, \psi_{\mathbf{k}v}^{\mathrm{AE}} \rangle \simeq \sum_{ij} \langle \psi_{\mathbf{k}v} | \, \beta_i \rangle \langle \phi_i^{\mathrm{AE}} | \, P_{mm'}^{\mathrm{AE},I} \, | \, \phi_j^{\mathrm{AE}} \rangle \langle \beta_j | \, \psi_{\mathbf{k}v} \rangle \quad . \tag{2.111}$$

[9] This expansion holds only for "quasilocal" operators; for truly nonlocal operators there is an additional term, given by Eq. 12 of Ref. 92, which is neglected in this formula. Anyway it is formally zero for operators which vanish outside the spheres.

With this choice, the Hubbard potential can be rewritten in a form which will be then easily incorporated in the non-local part of the PP. Indeed, by inserting in Eq. (2.106) this expression for the projection operators we obtain:

$$V_U^\sigma = \sum_{ij} \left[\sum_I \sum_{mm'} V^{I\sigma}_{mm'} \langle \phi_i^{\mathrm{AE}} | \, P^{\mathrm{AE},I}_{mm'} \, | \, \phi_j^{\mathrm{AE}} \rangle \right] | \, \beta_i \rangle \langle \beta_j \, | = \sum_{ij} \Delta^\sigma_{ij} | \, \beta_i \rangle \langle \beta_j \, | \, , \tag{2.112}$$

where in the last passage we assigned to Δ^σ_{ij} the quantity in square brackets. Now the Hubbard potential can be included straightforwardly in the non-local part V^σ_{NL} of the USPP appearing in Eq. (2.61), simply by adding these new coefficients to the usual Vanderbilt screened coefficients:

$$V^\sigma_{\mathrm{NL+U}} \equiv V^\sigma_{\mathrm{NL}} + V^\sigma_U = \sum_{ij} \left(\widetilde{D}^\sigma_{ij} + \Delta^\sigma_{ij} \right) | \, \beta_i \rangle \langle \beta_j \, | \, , \tag{2.113}$$

where we have set $\widetilde{D}^\sigma_{ij} \equiv \widetilde{D}^{\gamma(I),\sigma}_{\tau,l,m_l;\tau',l',m'_l} \cdot \delta_{I,J}$ and $\beta_i \equiv \beta^I_{\tau,l,m_l}$ for shortness of notation.

The following observations about the methodology described here above can be made: (i) it is of straightforward implementation in any existing USPP code, since there is no need to introduce any additional projector other than those of the PP; (ii) the method can also be employed with norm-conserving Kleinman-Bylander's PPs dropping the τ dependence in the projector index i and adding the Hubbard contribution to the bare coefficients of the non-local potential; (iii) although $\langle \phi_i^{\mathrm{AE}} | \, P^{\mathrm{AE},I}_{mm'} \, | \, \phi_j^{\mathrm{AE}} \rangle$ can be computed only once at the beginning of the self-consistent calculation, the Δ^σ_{ij} coefficients need to be updated at each iteration (similarly to the screened coefficients $\widetilde{D}^\sigma_{ij}$) because the local occupations $n^{I\sigma}_{mm'}$ may change while reaching self-consistency; (iv) there is no need to compute additional corrections to Hellmann-Feynmann forces or to the stress tensor, since these will be automatically included when computing contributions from the nonlocal part of the USPP; (v) the Hubbard potential is now localized inside the atomic spheres (since the β_i functions vanish outside).

The last point is particularly important for what concerns the inclusion of the Hubbard potential in the scattering problem, see Eq. (2.77) at page 59. Indeed, all the theoretical details and the technical difficulties arising when using a pseudopotential with a non-local term have already been discussed and solved [62, 86]. Because the Hubbard contribution to the KS potential now consist merely in a renormalization of the coefficients in the non-local part of the PP, as we have shown in Eq. (2.113), the only additional step consists in redefining the coefficients which multiply the β projectors in the non-local potential V'_{NL} of Eq. (2.77) using $\bar{D}^\sigma_{ij} = \widetilde{D}^\sigma_{ij} + \Delta^\sigma_{ij} - Eq_{ij}$. Similarly to the $\widetilde{D}^\sigma_{ij}$ coefficients, the Δ^σ_{ij} are obtained from a previous self-consistent electronic structure calculation at convergence. From a practical point of view, no further coding is required if the subroutines which initialize and update the screened

PP coefficients are shared between the electronic structure module and the ballistic transport module (and this is the case for the `PWscf` and `PWcond` codes in the QUANTUM ESPRESSO distribution).

The degree of approximation introduced by assuming a localized projection operator can be estimated by writing the complete formula in Eq. (2.109) in a form more suitable to be used in a USPP calculation: after rewriting the AE operator as a sum of a "soft" operator, $P^{\mathrm{PS},I}_{mm'} = |\,\phi^{\mathrm{PS},I}_{m}\rangle\langle\phi^{\mathrm{PS},I}_{m'}\,|$, and an additional term $\Delta P^{I}_{mm'}$ localized within the atomic augmentation spheres, we can substitute $P^{\mathrm{AE},I}_{mm'} = P^{\mathrm{PS},I}_{mm'} + \Delta P^{I}_{mm'}$ inside Eq. (2.109). Using the relationship in Eq. (2.110) for $\Delta P^{I}_{mm'}$ we arrive at the following equation

$$\begin{aligned}\langle\psi^{\mathrm{AE}}_{\mathbf{k}v}|\, P^{\mathrm{AE},I}_{mm'}\,|\,\psi^{\mathrm{AE}}_{\mathbf{k}v}\rangle = \langle\psi_{\mathbf{k}v}|\, P^{\mathrm{PS},I}_{mm'}\,|\,\psi_{\mathbf{k}v}\rangle + \\ \sum_{ij}\langle\psi_{\mathbf{k}v}|\,\beta_i\rangle\left[\langle\phi^{\mathrm{AE}}_{i}|\, P^{\mathrm{AE},I}_{mm'}\,|\,\phi^{\mathrm{AE}}_{j}\rangle - \langle\phi^{\mathrm{PS}}_{i}|\, P^{\mathrm{PS},I}_{mm'}\,|\,\phi^{\mathrm{PS}}_{j}\rangle\right]\langle\beta_j|\,\psi_{\mathbf{k}v}\rangle\end{aligned} \tag{2.114}$$

which can be evaluated on the smooth pseudo wavefunctions. Although we will not use this formula, we point out that it could be used as an alternative to that involving the overlap operator $\widehat{S}$.

In Sec. 4.5 the method outlined in Eqs. (2.111) through (2.113) will be used to compute the band structure and CBS of the infinite monatomic Au chain within LDA+U. A necessary condition for this approach to work is that the real part of the CBS obtained by solving the scattering equation at different values of E matches (within the numerical accuracy) the band structure of the underlying electronic structure calculation: this will be verified in the case of the Au chain. In the same section, we will then compare the LDA+U transmission of the Au chain at equilibrium spacing with a single CO adsorbed ontop and at the bridge.

CHAPTER 3

CO adsorption on monatomic platinum chains

In this chapter we study the interaction of a single CO molecule with a free-standing, infinitely long monatomic Pt chain within the framework of DFT (see Sec. 2.1 and Sec. 2.2). We mainly consider three adsorption geometries: a CO perpendicular to the chain and bridging two Pt atoms (with the C atom closest to the chain), a perpendicular CO standing atop of one Pt, and a longitudinal CO in a substitutional position forming a linear structure (see Fig. 3.1). When discussing the energetics we also consider the possibility of a tilted geometry, since it has been proposed recently in the literature [29]. The results on the ontop geometry were reported in Refs. 93 and 94, while the bridge, tilted bridge, and substitutional configurations were presented in Ref. 95. The purpose of this chapter is to survey these previous works, giving the fundamental details of the interaction between CO and Pt chains, but also highlighting common points and differences between the individual adsorption geometries, and to prepare the ground for an easier comparison with the case of Au chains (which will be discussed in the two following chapters). After describing the energetics in Sec. 3.1, we will analyze the electronic structure in Sec. 3.2 discussing the adsorption mechanism of CO. Finally, in Sec. 3.3 the ballistic transport properties are studied and correlated with the electronic structure features of the system. Two kind of

calculations have been performed, scalar-relativistic (SR) and fully-relativistic (FR) ones (see Sec. 2.3 and Sec. 2.4 for the methodological details), and the results are compared to highlight how the electronic structure and the ballistic transmission of the system are modified by the introduction of SOC effects.

3.1 Geometry and energetics

We performed DFT electronic structure calculations using the `PWscf` code contained in the open-source QUANTUM ESPRESSO package [47]. The total energy has been computed both in the LDA using the Perdew-Zunger exchange-correlation functional [55] and in the GGA using the PBE functional [75], so that equilibrium distances and adsorption energies obtained with the two approximations can be compared. The interaction of the nuclei and core electrons with the valence electrons is described by SR and FR ultrasoft pseudopotentials [81]. The parameters of the pseudopotentials used in the calculations are reported in App. B together with the kinetic energy cut-offs used to describe the wavefunctions and the charge density.

In order to simulate the ideal case of *one* molecule interacting with a monatomic Pt chain using periodic boundary conditions, we consider N_{Pt} platinum atoms and a CO molecule inside a tetragonal supercell (represented in Fig. 3.1 for the bridge, ontop and substitutional geometries). The wire is placed along the z axis and the size of the cell along the x and y directions has been chosen as $d_{\perp} = 18$ a.u.. For the "tilted bridge" configuration, where the CO axis lies on the xz plane but is not aligned with the x axis or with the z axis, we used a similar supercell. The SR (FR) chemisorption energies and optimized distances reported in this section have been calculated with $N_{\mathrm{Pt}} = 15$ ($N_{\mathrm{Pt}} = 7$) Pt atoms per cell [93], while bigger cells have been used for the PDOS (see next section). As for the pristine Pt chain (see Sec. B.2 in the Appendix), the perpendicular direction of the BZ is sampled with the Γ point only, while in the longitudinal direction we reduce the number of k-points according to the number of Pt atoms in the cell (for $N_{\mathrm{Pt}} = 15$ we used 13 uniformly spaced points). The orbital occupations are broadened using the smearing technique of Methfessel and Paxton [78], with a smearing parameter $\sigma = 0.01$ Ry. With this choice of parameters, the error on the calculated chemisorption energies is lower than a few tens of meV (see Ref. 93), while the optimized distances are converged within 0.01 Å (0.05 Å for $d_{\text{O-Pt}}$ in the FR substitutional case).

We partially optimized the geometry of the system (see Fig. 3.1) by moving only

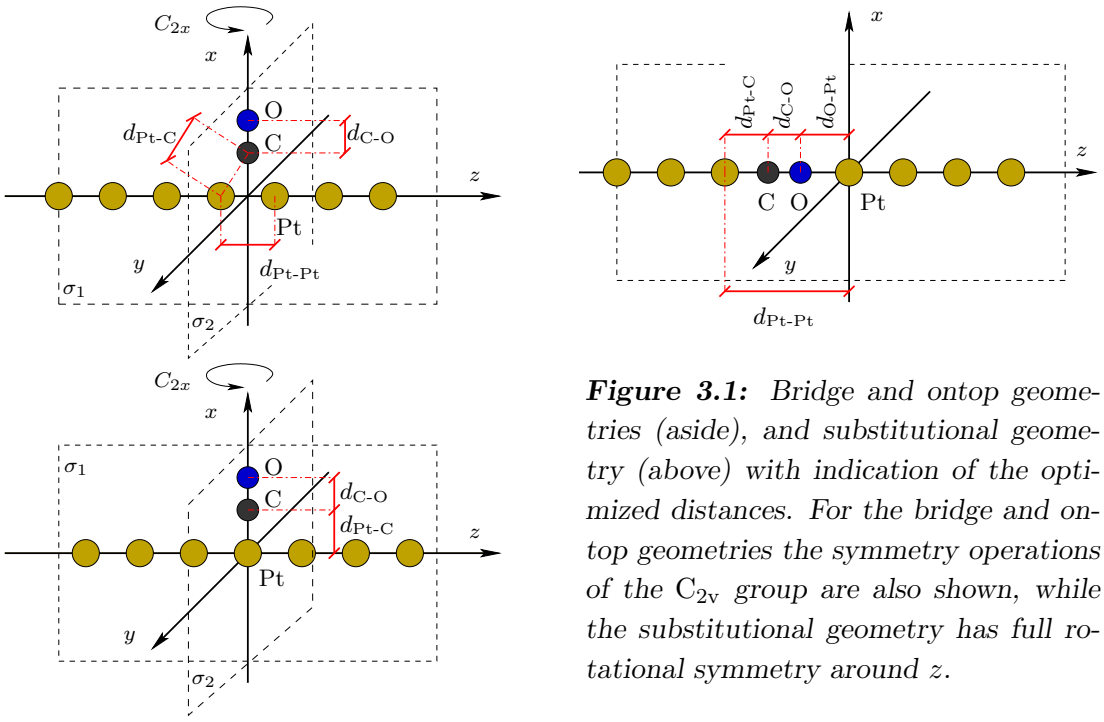

Figure 3.1: *Bridge and ontop geometries (aside), and substitutional geometry (above) with indication of the optimized distances. For the bridge and ontop geometries the symmetry operations of the C_{2v} group are also shown, while the substitutional geometry has full rotational symmetry around z.*

the C and O atoms,[1] while keeping the Pt atoms fixed on the z axis. In the bridge and substitutional configurations, this optimization has been repeated for different values of the distance ($d_{\text{Pt-Pt}}$) between the two Pt atoms in contact with CO while all the other Pt atoms are kept at the theoretical equilibrium distance in the isolated chain ($d_{\text{chain}} = 2.34$ Å with LDA, $d_{\text{chain}} = 2.39$ Å with GGA). In the ontop case, only the configuration with all Pt atoms equally spaced by the theoretical equilibrium distance has been considered. The LDA and GGA total energy of the optimized configurations is shown as a function of $d_{\text{Pt-Pt}}$ on the left and on the right side in Fig. 3.2, respectively. The zero of the energy has been chosen as the sum of the energies of the isolated CO and of the isolated Pt chain at equilibrium spacing (i.e. without broken bonds). In the same plot we report also the sum of the energies of the isolated CO and of a Pt chain with one bond stretched to $d_{\text{Pt-Pt}}$.

In Tab. 3.1 we report the chemisorption energies, E_{chem}, and geometrical parameters calculated for three selected configurations: the ontop geometry, the bridge geometry with all Pt atoms equally spaced ($d_{\text{Pt-Pt}} = d_{\text{chain}}$), and the substitutional geometry at

[1] In the structural optimizations we require that each component of the force on the C and O atoms gets lower than 1 mRy/a.u. . In the bridge and ontop geometries the C and O atoms are constrained to move on the axis perpendicular to the wire (x axis), while in the substitutional case we keep them aligned with the wire (hence on the z axis). In the tilted bridge configuration, the C and O atoms can move on the xz plane.

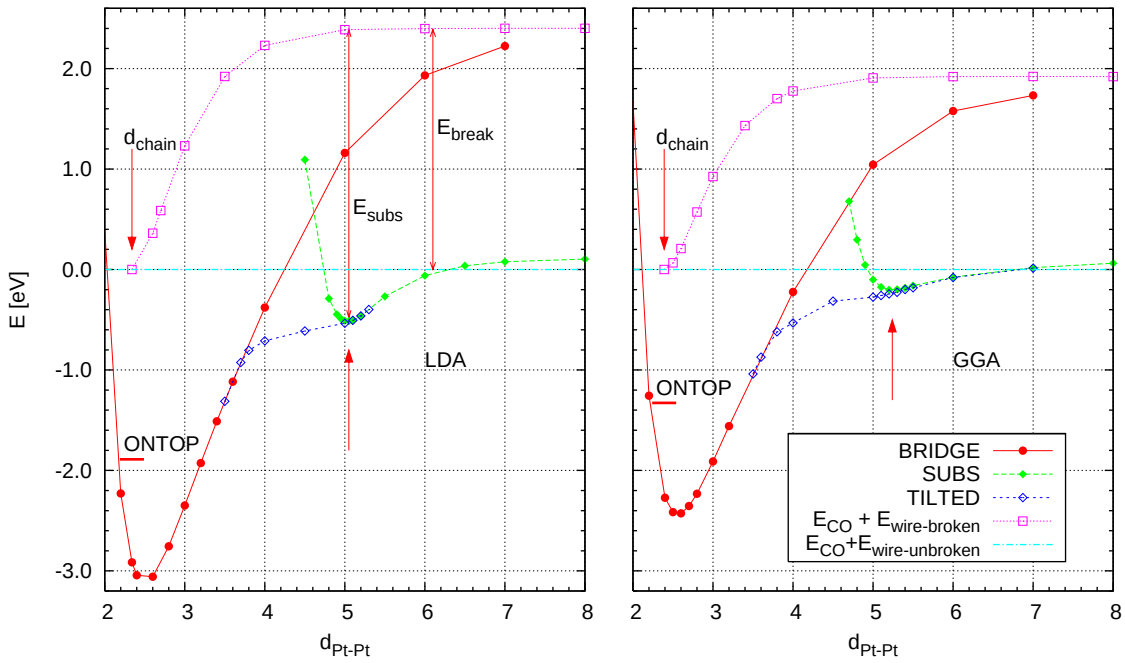

Figure 3.2: *Optimized energy (with respect to the C and O positions) for different geometries as a function of the Pt-Pt distance, $d_{\text{Pt-Pt}}$ (see text and Fig. 3.1). In the* BRIDGE *(*SUBS*) geometry, indicated with solid (dashed) line, the C and O atoms are constrained to be on the x (z) axis, while in the* TILTED *geometry (short-dashed line) they can move on the whole xz plane. The optimized energy of the* TOP *geometry (only at $d_{\text{Pt-Pt}} = d_{chain}$) is indicated with an horizontal thick line. The zero of the energy is set as the sum of the energies of an isolated CO and an isolated Pt chain (with the same N_{Pt} and $d_{\text{Pt-Pt}} = d_{chain}$). This energy has been calculated also for some values of $d_{\text{Pt-Pt}} \geqslant d_{chain}$ (squares), and at a large enough $d_{\text{Pt-Pt}}$ it equals E_{break}. The energy gain of placing substitutionally the CO at an already broken Pt-Pt bond is then given by E_{subs} and is comparable to the E_{chem} of CO at the bridge site of an unbroken wire.*

the optimal $d_{\text{Pt-Pt}}$. The chemisorption energies are calculated by subtracting to the total energy of the optimized interacting system (CO plus Pt chain) the sum of the total energy of the isolated CO molecule at the equilibrium distance and the total energy of the isolated wire with the same N_{Pt}:

$$E_{\text{chem}} = E_{\text{CO+wire}} - E_{\text{CO}} - E_{\text{wire}} \ . \tag{3.1}$$

For the bridge and substitutional cases, the values of E_{chem} reported in the table correspond to the energy of the "BRIDGE" and "SUBS" curves in Fig. 3.1, at the values of $d_{\text{Pt-Pt}}$ pointed by the arrows, while the ontop E_{chem} is indicated by a horizontal dash in the same plot.

	Bridge			Ontop			Substitutional				
	$d_{\text{Pt-C}}$	$d_{\text{C-O}}$	E_{chem}	$d_{\text{Pt-C}}$	$d_{\text{C-O}}$	E_{chem}	$d_{\text{Pt-C}}$	$d_{\text{C-O}}$	$d_{\text{O-Pt}}$	E_{chem}	E_{break}
SR-LDA	1.95	1.16	-2.9	1.82	1.14	-1.9	1.82	1.17	2.05	-0.5	2.5
FR-LDA	1.95	1.16	-3.0	1.81	1.14	-2.0	1.82	1.17	2.06	-0.6	2.4
SR-GGA	1.98	1.17	-2.3	1.84	1.15	-1.4	1.85	1.17	2.22	-0.2	1.9

Table 3.1: *Relaxed distances (in Å) and chemisorption energies (in eV) for the three geometries. In the substitutional case, the energy cost for breaking the wire (calculated as described in the text) is also shown.*

If the bond is not stretched ($d_{\text{Pt-Pt}} \simeq d_{\text{chain}}$), the bridge configuration is favored with respect to the ontop position,[2] the adsorption energy being about 1 eV smaller for the ontop configuration within both LDA and GGA. The energy of the bridge geometry as a function of $d_{\text{Pt-Pt}}$ has a minimum at a distance slightly longer than d_{chain} ($d_{\text{Pt-Pt}} =$ 2.56 Å with GGA and $d_{\text{Pt-Pt}} = 2.50$ Å with LDA). The substitutional geometry has an energy minimum at a much longer distance ($d_{\text{Pt-Pt}} = 5.24$ Å and $d_{\text{Pt-Pt}} = 5.05$ Å, respectively). In this hyper-stretched configuration the substitutional geometry is favored with respect to the bridge. However, here a "tilted bridge" configuration, where the CO axis lies on the xz plane but is in not aligned with the x axis or with the z axis, still has an energy slightly lower than the substitutional minimum. While this tilted configuration does not reveal an energy minimum with respect to $d_{\text{Pt-Pt}}$, it is anyway preferred to the bridge and substitutional configurations at intermediate distances (about 3.7 Å $\leqslant d_{\text{Pt-Pt}} \leqslant$ 5.3 Å with GGA and 3.8 Å $\leqslant d_{\text{Pt-Pt}} \leqslant$ 5.1 Å with LDA). We notice here that both in LDA and GGA curves the total energy is always increasing when going from the bridge minimum toward larger $d_{\text{Pt-Pt}}$ values, hence a pulling tension must be applied to the chain throughout all process to obtain a transition from the bridge to the substitutional positions passing through a tilted bridge configuration. We will see in Sec. 4.1 that Au chains behave differently in this respect.

If compared to the bridge and ontop geometries, the substitutional configuration has a much lower E_{chem}, because in this case we have to pay an energy cost E_{break} for breaking a Pt-Pt bond in the middle of the chain. In Tab. 3.1 we also report E_{break} calculated as the difference between the total energy of the Pt cluster obtained by removing C and O and the total energy of the unbroken chain with the same N_{Pt}: it

[2] Although assessing correct binding energies of CO on close-packed Pt surfaces, as the Pt(111) surface and vicinals to it, can be difficult in DFT with many of the commonly used exchange and correlation functionals, potentially resulting in a wrong predicted site preference [96], in the monatomic chain case the calculated energy difference between bridge and top sites (about 1 eV) is sensibly larger than the potential energy corrugation of that problematic surface case ($\sim 0.1 \div 0.2$ eV).

is about 1.9 eV within GGA and 2.4 eV within LDA (as can be additionally inferred from Fig. 3.2). Note that the chemisorption energy of substitutional CO on a broken wire (indicated by E_{subs} in the same figure) is comparable to the chemisorption energy in the bridge configuration.

In all geometries the optimized C-O bond distance is slightly longer than the value $d_{\text{C-O,eq}}$ calculated for the isolated molecule, ($d_{\text{C-O,eq}} = 1.13$ Å and $d_{\text{C-O,eq}} = 1.14$ Å within the LDA and GGA, respectively, see Sec. B.1). The calculated optimal distance between the C atom and the nearest neighbour Pt atoms, $d_{\text{Pt-C}}$, is about 1.95 Å (1.98 Å) in the bridge geometry within LDA (GGA); it is longer than the C-Pt distance found in the ontop geometry, $d_{\text{Pt-C}} = 1.82$ Å (1.85 Å). This increase of $d_{\text{Pt-C}}$ with the coordination number of C is in agreement with the experimental and theoretical values found for CO adsorbed on Pt(111) surfaces. For instance, LEED experiments report $d_{\text{Pt-C}} \simeq 1.85$ Å for atop CO and $d_{\text{Pt-C}} \simeq 2.08$ Å for CO at the bridge site and DFT calculations at the GGA level are quite close to these values (see Ref. 97 and references therein). In the substitutional case, $d_{\text{Pt-C}}$ is quite similar to the ontop case, while the C-O bond is slightly longer than in the other two geometries. As a general remark we can say that LDA and GGA give qualitatively the same picture of the interaction between CO and the Pt chain, although the former method gives larger binding energies and slightly shorter bonds lengths (as one could have expected from the general trends seen for these families of exchange-correlation functionals). Finally we note that in LDA bonding distances and chemisorption energies do not change significantly in presence of SOC. This result is in line with the general observation, supported by results in the next Section, that while Fermi-level related properties, including transport, may be heavily and directly influenced by SOC through band splittings, the overall energetics, involving charge distributions obtained by integration over the complex of these bands rather than just those at E_F, is much less altered by SOC.

3.2 Electronic structure

In this section we present the electronic structure of the bridge, ontop, and substitutional geometries (calculated within LDA), for the specific configurations pointed by the arrows in Fig. 3.2 ($d_{\text{Pt-Pt}} = d_{\text{chain}} = 2.34$ Å for the bridge and ontop geometries, $d_{\text{Pt-Pt}} = 5.05$ Å for the substitutional). The substitutional geometry preserves the rotational symmetry of the infinite chain (see Sec. B.2), and that allows a classification of SR (FR) states according to the quantum number m (m_j) — the projection of the orbital (total) angular momentum along the wire axis. In the bridge and ontop geometries, where the symmetry point group reduces to C_{2v}, this is no longer the case.

The C_{2v} symmetry group contains the elements illustrated in Fig. 3.1 (the identity E, the rotation of π radians about the x axis C_{2x} and the mirror symmetries σ_1 and σ_2), but no rotation along z.

We will analyze the PDOS (defined in Sec. 2.5) projected on the atomic orbitals of C and O atoms and of the Pt atoms next to the molecule. The peaks in the PDOSs projected on the orbitals of C and O will allow us to identify the energy position of those states with high projections on the molecular orbitals of CO. In the absence of interaction between the molecule and the chain, we would expect to find peaks at energies below or above the Fermi energy in correspondence of, respectively, the occupied and the empty molecular levels (which are shown in Sec. B.1). In the interacting system these molecular levels can shift and also broaden; moreover additional peaks can appear in the C and O PDOS because of the hybridization with Pt states. The comparison between the PDOS of Pt in the presence of CO with the PDOS of the Pt pristine chain will show which states of the metal are involved in the hybridization with the levels of CO.

In order to reduce the effects of the periodic CO replicas on the bands (which are visible as small artificial gaps in the PDOS), we used supercells having a longitudinal size much bigger than that needed to converge chemisorption energies and bond lengths. We utilized cells with $N_{\mathrm{Pt}} = 50$ for the FR PDOS, and up to $N_{\mathrm{Pt}} = 105$ in the SR case. The KS-eigenstates used to build the PDOS have been calculated for a uniform mesh of $(1050/N_{\mathrm{Pt}})$ **k**-points along z, since the size of the BZ reduces linearly with N_{Pt}.

3.2.1 CO adsorbed at the bridge site

We start by discussing the SR electronic structure of the monatomic Pt chain with CO adsorbed at the bridge site when all Pt atoms are equally spaced. For an arbitrary k_z the small group of k_z is $C_s = \{E, \sigma_1\}$, thus we can divide the states into "even" and "odd" with respect to the xz mirror plane (σ_1 symmetry in Fig. 3.1). The $m = 0$ states of the chain are even, while $|m| = 1$ and $|m| = 2$ states split into even states (derived from d_{xz} and $d_{x^2-y^2}$ atomic orbitals, respectively) and odd states (from d_{yz} and d_{xy}). Since the molecule is placed with its axis along x, all σ states will be of even symmetry, while the two-fold degenerate π states split into even states (from p_z) and odd states (from p_y).

We report in Fig. 3.3 (left side) the electronic PDOS projected on the *even* atomic orbitals of C and O and on the even atomic orbitals of one of the two Pt atoms in

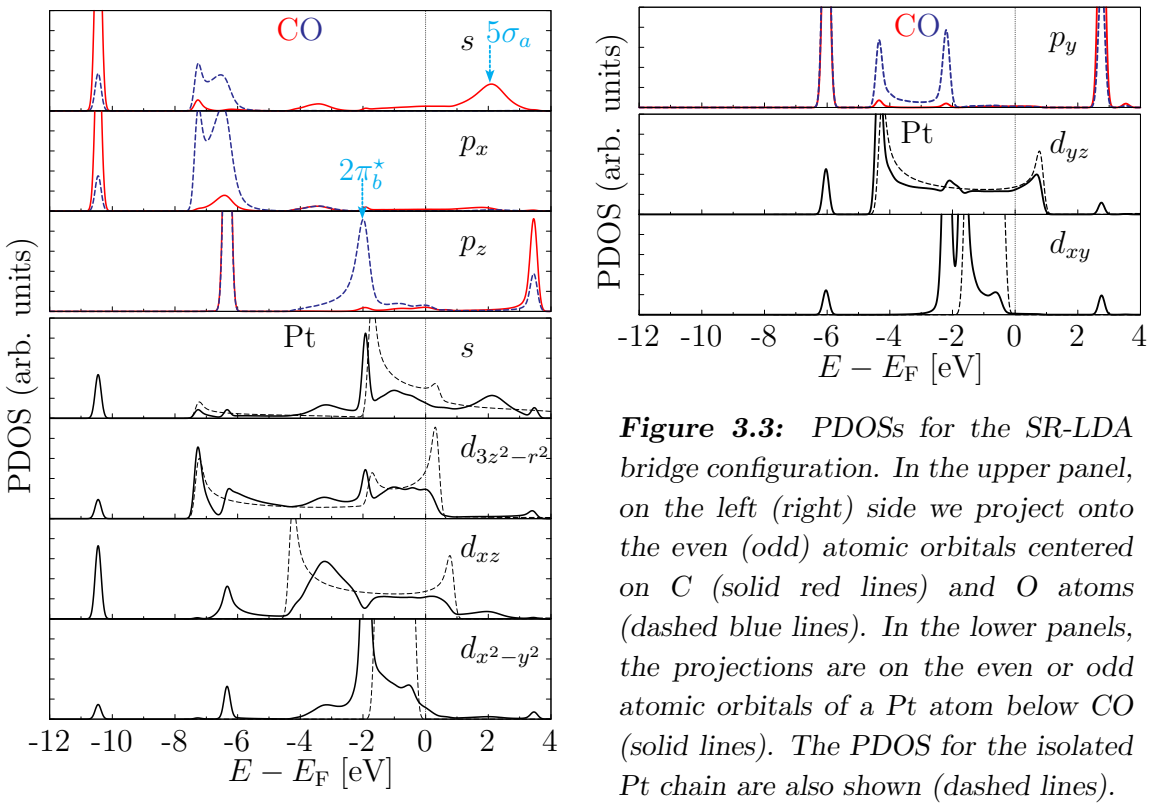

Figure 3.3: *PDOSs for the SR-LDA bridge configuration. In the upper panel, on the left (right) side we project onto the even (odd) atomic orbitals centered on C (solid red lines) and O atoms (dashed blue lines). In the lower panels, the projections are on the even or odd atomic orbitals of a Pt atom below CO (solid lines). The PDOS for the isolated Pt chain are also shown (dashed lines).*

contact with the molecule.[3] The PDOSs are decomposed into the projections on the s, p_x or p_z orbitals of C and O and into those on the s, $d_{3z^2-r^2}$, d_{xz} or $d_{x^2-y^2}$ orbitals of Pt. Some of the peaks correspond to the even levels of the molecule. The 3σ and 4σ molecular states are in the C and O s and p_x PDOS, at -22.5 eV (not shown) and at -10.4 eV, respectively, while peaks corresponding to the 1π and to the $2\pi^\star$ states are at about -6.3 eV and at 3.3 eV in the C and O p_z PDOS. The 4σ state is moderately hybridized with the even Pt orbitals, while the 3σ state is not directly involved in the Pt-CO interaction.

The broadening of molecular features and the presence of several additional peaks indicate a chemical interaction between the molecule and the wire. Interaction between the σ orbitals and Pt states is visible in the projections on the s and p_x orbitals of C and O from -7.5 eV up to 3 eV. In two energy regions, at about 2.1 eV and between -7.5 eV and -6.0 eV there are several large peaks in the s projection and in both the s and p_x projections, respectively, whereas at other energies the projections are smaller while not completely vanishing. The broad peak centered at about 2.1 eV in the PDOS projected on the C s orbital is due to the 5σ orbital and shows that

[3]Because of the σ_2 mirror symmetry, the two atoms which form the bridge site accommodating the molecule are equivalent, hence we show the projections for one of them only.

there is a depopulation of the HOMO of CO (donation), since the 6σ level of the molecule is much higher in energy (not shown here). These states are antibonding Pt-CO states while the corresponding bonding states show up as the double-peak feature below E_F, between about -7.5 eV and -6.0 eV. Thus the 5σ orbital is broadened and generates a set of occupied bonding states $5\sigma_{\rm b}$ below $E_{\rm F}$ and a set of empty antibonding states $5\sigma_{\rm a}$ above $E_{\rm F}$. Some of the KS-eigenstates associated to these peaks are shown in Fig. 3.4. In the upper panel of this figure we draw a contour plot of the charge density of a $5\sigma_{\rm b}$ state at -6.1 eV and of a $5\sigma_{\rm a}$ state at 2.1 eV in the xz plane (which contains both the molecule and the wire). The former clearly displays a Pt-C bonding character, since the σ charge lobe on the C side is shared between the molecule and the two nearest Pt atoms, while the latter (above $E_{\rm F}$) is antibonding. In the $5\sigma_{\rm b}$ state the presence of the Pt-C bonding charge slightly pushes away the Pt-Pt bonding charge from the z axis towards the opposite side with respect to the C atom.

We note that the interaction brings part of the 5σ orbitals below the 1π level, and that there is an orbital mixing between 4σ and 5σ levels. As a consequence, the projections of $5\sigma_{\rm b}$ states on the s and p_x orbitals of O are higher than those on the s and p_x orbitals of C (at variance with the 5σ level in the free molecule). These are the same features which characterize the absorption of CO on transition metal surfaces, well described in the literature [54]. The hybridization of the 5σ orbital is mainly with the $m = 0$ bands of the Pt wire, which have predominant $d_{3z^2-r^2}$ character at low energies and s character at energies higher than 0.4 eV. Moreover a smaller, but relevant, hybridization of $5\sigma_{\rm a}$ states with the d_{xz} ($|m| = 1$) Pt orbital is present. The hybridization of the 4σ orbital is instead stronger with the d_{xz} orbital.

Additional peaks and broad features due to the hybridization are present also in the p_z PDOS. Moreover some hybridization of π levels with Pt states occurs also at -6.3 eV, which is the position of the 1π states. The strong peak at about -2 eV and the weaker features above and below -2 eV are due to bonding hybridization between the even $2\pi^\star$ orbital and the Pt states. The presence of these new states, which we may call $2\pi^\star_{\rm b}$, shows that the $2\pi^\star$ orbital of CO is partially occupied corresponding to back-donation. The $2\pi^\star$ level broadens between 3.2 eV and 3.6 eV and forms the antibonding $2\pi^\star_{\rm a}$ states. A contour plot of the charge density associated to the $2\pi^\star$-derived states is shown in Fig. 3.4 (lower panels), a bonding orbital at -2.0 eV on the left and an antibonding orbital at 3.5 eV on the right. The $2\pi^\star_{\rm b}$ states have a large contribution from oxygen p_z orbitals, with very low projections on the carbon atom (see also the PDOS, Fig. 3.3). This is caused by a mixing between the 1π and $2\pi^\star$ orbitals of the molecule due to its interaction with the wire, and has been well characterized for CO adsorbed on metal surfaces [54]. The $2\pi^\star_{\rm b}$ hybridization

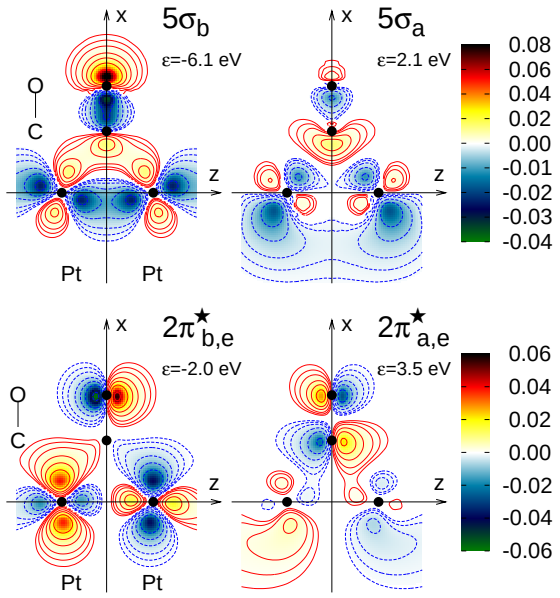

Figure 3.4: *Two dimensional contour plot of the charge density of even KS-eigenstates (calculated at $k_z = 0$) corresponding to σ-derived and π-derived states. In the upper panel we show the $5\sigma_b$ (left) and $5\sigma_a$ (right) states, while in the lower panel the bonding (left) and antibonding (right) between even $2\pi^\star$ and even Pt states. Dots mark the positions of atoms, while solid red (dashed blue) lines are positive (negative) isolevels with the following values of density:* ± 0.0005 ± 0.001, ± 0.002, ± 0.005, ± 0.01, ± 0.02, ± 0.05 electrons/$(a.u.)^3$.

at -2 eV involves both $m = 0$ (s and $d_{3z^2-r^2}$) and $|m| = 2$ ($d_{x^2-y^2}$) Pt states, and because of this interaction a relevant portion of the $d_{x^2-y^2}$ PDOS moves outside the energy range of the $|m| = 2$ band of the pristine wire. The $|m| = 1$ (d_{xz}) states instead give a much smaller contribution at -2 eV and interact in a wider energy range between -4 eV and -2 eV.

In Fig. 3.3 (right side) we also show the PDOS projected on the *odd* atomic orbitals. As found in the even π interaction, in the PDOS projected onto the p_y orbitals of C and O two peaks correspond to the odd 1π molecular level at -6 eV and to the odd $2\pi^\star_a$ state at 2.8 eV, while additional peaks are caused by interaction. Here we find two new peaks below E_F, one at -4.3 eV and the other at -2.2 eV. They correspond to the odd $2\pi^\star_b$ levels and their splitting reflects the different hybridization of the $2\pi^\star$ orbital with distinct bands of the wire. The peak at -4.3 eV is present only in the PDOS projected on d_{yz}, while the peak at -2.2 eV is essentially due to an hybridization with the $|m| = 2$ band, since the corresponding d_{xy} peak is much stronger than that in the d_{yz} PDOS. As noticed in the even PDOS, this strong interaction brings some charge in the $2\pi^\star$ molecular state and perturbs the PDOS of the wire, especially the $|m| = 2$ component (d_{xy} in the odd case) where a lot of states are now outside the energy range of the pristine wire $|m| = 2$ band.

With addition of SOC in the FR case this donation/back-donation picture does not change. Now states fall into the two irreducible representations Γ^3 and Γ^4 of the double group C^D_s and it is not possible to separate even and odd states. In the isolated wire the representations $\Gamma^{1/2}$, $\Gamma^{3/2}$, etc. of $C^D_{\infty v}$ are two-dimensional and the FR bands are two-fold degenerate. With each couple of bands we can form

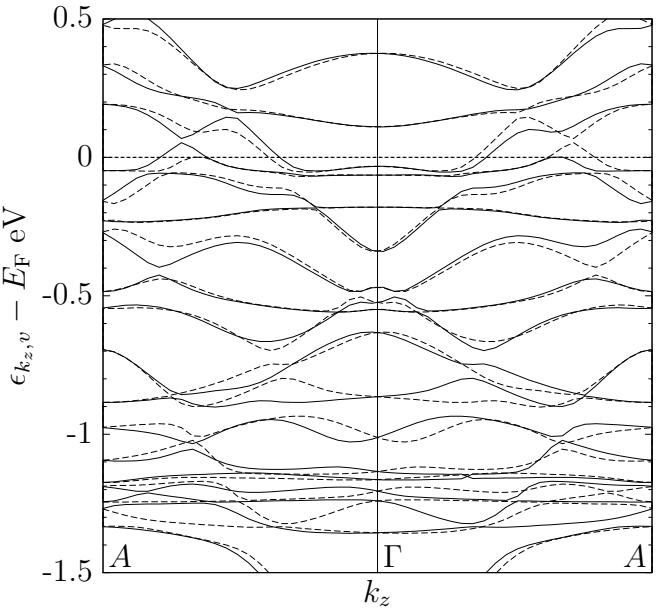

Figure 3.5: *FR electronic band structure calculated for CO at the bridge of a Pt chain with $N_{Pt} = 7$. Bands have been separated according the irreducible representations of C_s^D double group: Γ^3 (solid lines) and Γ^4 (dashed lines).*

linear combinations which transform as Γ^3 and Γ^4 and these remain degenerate. In presence of CO this degeneracy is broken, thus each couple of bands splits. Since in the absence of magnetization time reversal symmetry holds, there is a (Kramers) degeneracy between the Γ^3 band at k_z and the Γ^4 band at $-k_z$. This degeneracy can be clearly seen in the FR band structure reported in Fig. 3.5, where the electronic bands are separated according to their symmetry. Therefore we can analyze the CO-Pt nanowire system by focusing on bands belonging to one of the two symmetries, for instance the Γ^3 bands.[4] In C or in O there are four FR atomic orbitals that transform according to Γ^3, one derived from the s ($l = 0$) state, with $(j, j_y) = (1/2, 1/2)$ and three derived from the p ($l = 1$) states, with $(j, j_y) = (1/2, -1/2)$, $(3/2, -1/2)$, and $(3/2, 3/2)$.

In Fig. 3.6 we show the PDOS projected onto these four Γ^3 atomic orbitals. The molecular levels can be easily identified. At lower energies two sharp peaks are at -22.4 eV (not shown) and at -10.5 eV in all the four PDOS and correspond to the 3σ and 4σ SR states, respectively. Two other peaks are close together (-6.3 eV and -6.0 eV) and are both present in the PDOS projected onto the two states with $l = 1$ and $j_y = -1/2$, but only the low energy peak is evident in the PDOS projected onto the $j_y = 3/2$ state. The position of these two peaks coincides with the even and

[4]The atomic orbitals suited for the projection of states with Γ^3 symmetry can be chosen among spinors which are eigenstates of the total angular momentum J^2, (with eigenvalue $j(j+1)$) and of its projection along y, J_y (with eigenvalue j_y). These states, labeled with (j, j_y), transform according to the Γ^3 or Γ^4 irreducible representations.

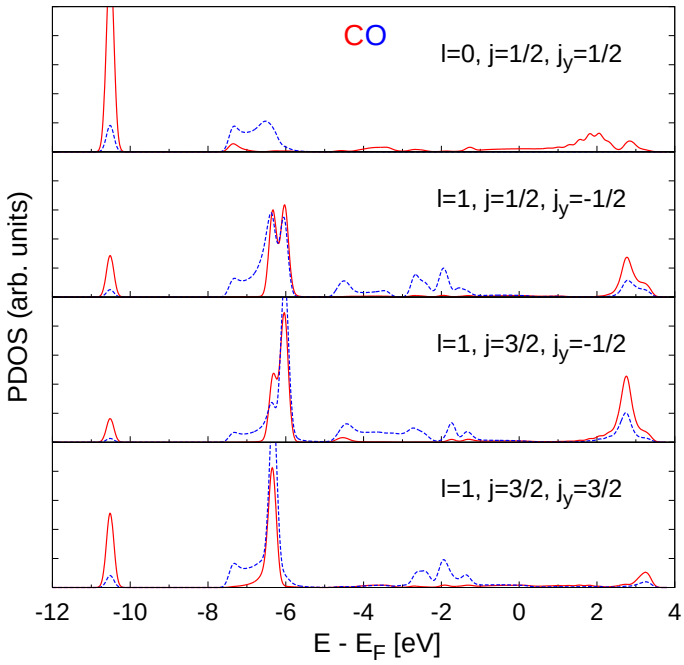

Figure 3.6: *PDOS for the bridge configuration calculated with the FR-LDA (wire along y, see text). The projections are on the Γ^3 symmetry FR atomic orbitals of C (solid red lines) and O (dashed blue lines). Atomic orbitals are labelled according to the eigenvalues of the angular momentum (l), of the total and angular momentum (j) and of its projection along y (j_y).*

odd 1π states observed in the SR PDOS. The odd 1π state (-6.0 eV) has very low projection onto the $j_y = 3/2$ state since the former is oriented along the xy direction, while the latter is made up of $m = 1$ orbitals, that are oriented in the xz plane (the quantization axis is y). The broad feature between -7.3 eV and -6.2 eV, which is present in all four PDOS, can be distinguished from the neighbouring 1π peaks since it has much more weight on the O atom rather than on the C atom, similar to the $5\sigma_{\mathrm{b}}$ SR states (see PDOS on even SR states in Fig. 3.3). Therefore we can recognize this feature as the FR analog of the $5\sigma_{\mathrm{b}}$ states, which are in the same energy range in the PDOS projected on the s and p_x orbitals. Above the Fermi energy, we can identify the empty $5\sigma_{\mathrm{a}}$ antibonding states which give rise to the broad peak at about 2 eV in the $j_y = 1/2$ PDOS.

In the energy range between -4.3 eV and -1.1 eV we find some features which are more evident in the $l = 1$ components of the PDOS, and have very low weight on the C orbitals. In the SR case the energy range of the $2\pi^\star_{\mathrm{b}}$ states goes from -4.4 eV (lowest peak in the p_y PDOS, see Fig. 3.3) to about -1 eV (tail of the even $2\pi^\star_{\mathrm{b}}$ peak in the p_z PDOS) and they have very low projections on the carbon, thus we can identify these features in the FR PDOS as the FR analog of those states. The corresponding even and odd $2\pi^\star$ antibonding states are responsible for the peaks at 3.2 eV and 2.8 eV, respectively. Although their splitting is too small to be resolved in a single PDOS with this value of the smearing, only the even peak (such as the even 1π) is evident in the $j_y = 3/2$ PDOS, while both are present in the $l = 1$, $j_y = -1/2$ PDOS and both have much smaller weight in the $l = 0$ component. We can therefore

conclude that although SOC changes the symmetry of the orbitals, the mechanism of donation and back-donation still describes well the bonding between the molecule and the wire.

3.2.2 CO adsorbed ontop

The ontop geometry has the same space group symmetry as that of the bridge geometry discussed here above, thus we can divide electronic states into even and odd also in this case. However, since it has been shown that the hybridization of the Pt states with both the σ and the π levels of CO can be described through the even PDOS and that the odd PDOS does not add important information, in the following we will focus on the former, although the PDOSs of both symmetries will be shown. On the left (right) side of Fig. 3.7 we report the PDOS projected on the even (odd) atomic orbitals of C and O atoms and of the Pt atom below CO (see the ontop geometry in Fig. 3.1, page 73). The projections have been decomposed as for the bridge geometry (Fig. 3.3 in the previous section).

By comparing the ontop even PDOS with the bridge even PDOS (left side of Fig. 3.3), we can see that the interaction mechanism of CO is the same in the two geometries, although some features specific to one or the other geometry can be recognized. It is worth noticing here that, although mixing among σ and π molecular states is allowed because the rotational symmetry of the molecule is broken and all among the even Pt states could in principle participate in both σ- and π-derived states, in the ontop geometry this mixing is almost absent and only the $|m| = 1$ (d_{xz}) orbital of Pt hybridize with the π levels (and only with those). This can be understood from the geometrical disposition of the atoms in the ontop geometry (being the Pt aligned with the C-O axis) and from the spatial charge distribution of the atomic orbitals of Pt and of the molecular levels: the d_{xz} orbital changes sign when crossing the x axis, hence it has a greater overlap with the π levels of CO along x and no overlap with the σ levels, while for the other even orbitals of Pt (which all have a maximum of density on the x axis) the opposite is true.

In the ontop geometry, the interaction of the molecule σ orbitals with the Pt states is characterized by the same series of peaks in the s and p_x PDOS of C and O: 4σ, $5\sigma_\mathrm{b}$, and $5\sigma_\mathrm{a}$ (as usual, the 3σ orbital does not take part in the Pt-CO interaction). The 4σ orbital hybridizes with Pt states (mainly $d_{x^2-y^2}$) more strongly than in the bridge geometry, while the bonding $5\sigma_\mathrm{b}$ state appears as a single narrow peak (instead of the broader double peak feature of the bridge case) and matches the small peaks at $-7.7\,\mathrm{eV}$ in the PDOS projected on s, $d_{3z^2-r^2}$, and $d_{x^2-y^2}$ states of Pt. The second $5\sigma_\mathrm{b}$ peak, which results from an hybridization with (mainly) $d_{3z^2-r^2}$ states, has not completely disappeared but is present as a little shoulder above the $5\sigma_\mathrm{b}$ peak (while

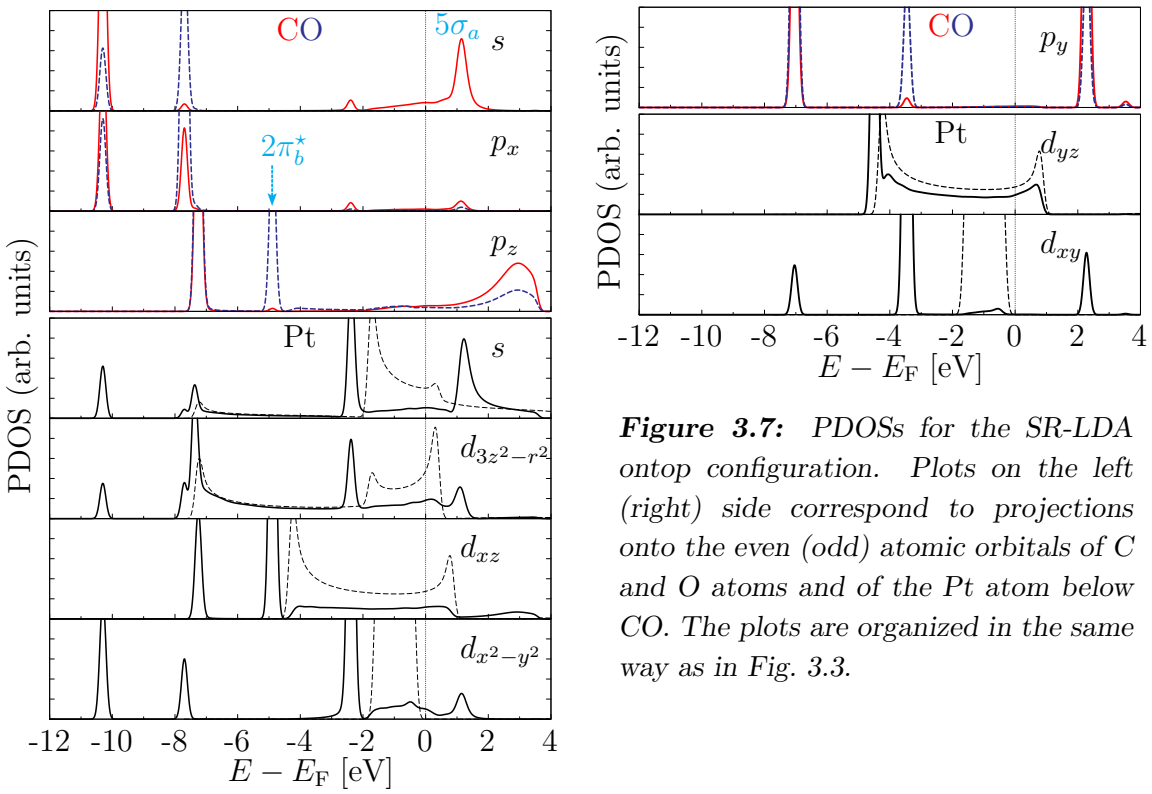

Figure 3.7: *PDOSs for the SR-LDA ontop configuration. Plots on the left (right) side correspond to projections onto the even (odd) atomic orbitals of C and O atoms and of the Pt atom below CO. The plots are organized in the same way as in Fig. 3.3.*

in the bridge geometry it is found below the $5\sigma_b$-$d_{3z^2-r^2}$ peak) and matches the strong $d_{3z^2-r^2}$ peak at $-7.4\,\text{eV}$. Notice that here the $5\sigma_b$ states are almost entirely below the even 1π level of the molecule (which is visible in the p_z PDOS at $-7.2\,\text{eV}$). Also the antibonding $5\sigma_a$ peak is not as broad as in the bridge case and moreover it is centered at a lower energy (at about 1.1 eV instead of 2.1 eV).

The interaction of π states is still characterized by the $2\pi_b^\star/2\pi_a^\star$ couple of bonding/antibonding states, plus the additional hybridization of the 1π molecular level. With respect to the bridge geometry, the $2\pi_b^\star$ state is at lower energies and consists mainly of a single peak at $-4.9\,\text{eV}$ in the p_z PDOS (plus very weak features at higher energies), while the $2\pi_a^\star$ state is much broader and has its maximum at slightly lower energies than in the bridge geometry (at about 2.9 eV instead of 3.5 eV). Peaks corresponding to the $2\pi_b^\star$ and $2\pi_a^\star$ states can be found in the PDOS projected on the d_{xz} orbital of Pt which, as was said above, is the only one having a good overlap with π states of CO in the ontop position. Although there is no direct hybridization between even π states and Pt states other than the d_{xz}, a strong peak in the $d_{x^2-y^2}$, s, and $d_{3z^2-r^2}$ PDOS is present at about $-2.4\,\text{eV}$, much similar to that associated to the hybridization with $2\pi_b^\star$ states in the bridge geometry. However, in the C and O PDOS only a very small peak in the s and p_x projections is found at that energy. This strong peak in the PDOS of Pt perturbs the $d_{x^2-y^2}$ density of states and the

amount of states which moves outside of the range of the $|m| = 2$ band (dashed lines) is even larger than what found in the bridge geometry.

3.2.3 Substitutional CO

The substitutional configuration (see Fig. 3.1) has a different space group symmetry with respect to the previous two. In this linear geometry the rotational symmetry is preserved, hence SR states with different m cannot hybridize. Therefore we can study the interaction by focusing on the PDOS projected on $m = 0$ and $|m| = 1$ orbitals only (reported, respectively, on the left and right sides in Fig. 3.8), disregarding $|m| = 2$ states that are not present in the molecular levels of CO. The 4σ and 5σ molecular levels give rise to two peaks at -11.0 eV and at -8.5 eV in the C and O s and p_z PDOS. As in the ontop configuration, the $5\sigma_\mathrm{b}$ level is lower than the 1π derived level (see later in the text). We do not find here isolated peaks above E_F which correspond to the antibonding $5\sigma_\mathrm{a}$ states, but an almost flat plateau which extends in the whole energy range of the $m = 0$ bands of Pt. The hybridization between the 5σ CO orbital and the Pt states is different on the two sides of the molecule, as can be seen comparing the PDOS projected onto the $m = 0$ orbitals centered on the two opposite Pt atoms. At -8.5 eV the 5σ CO orbital is more coupled to the Pt on the C side (especially via $d_{3z^2-r^2}$ states), and this causes a higher depopulation of $m = 0$

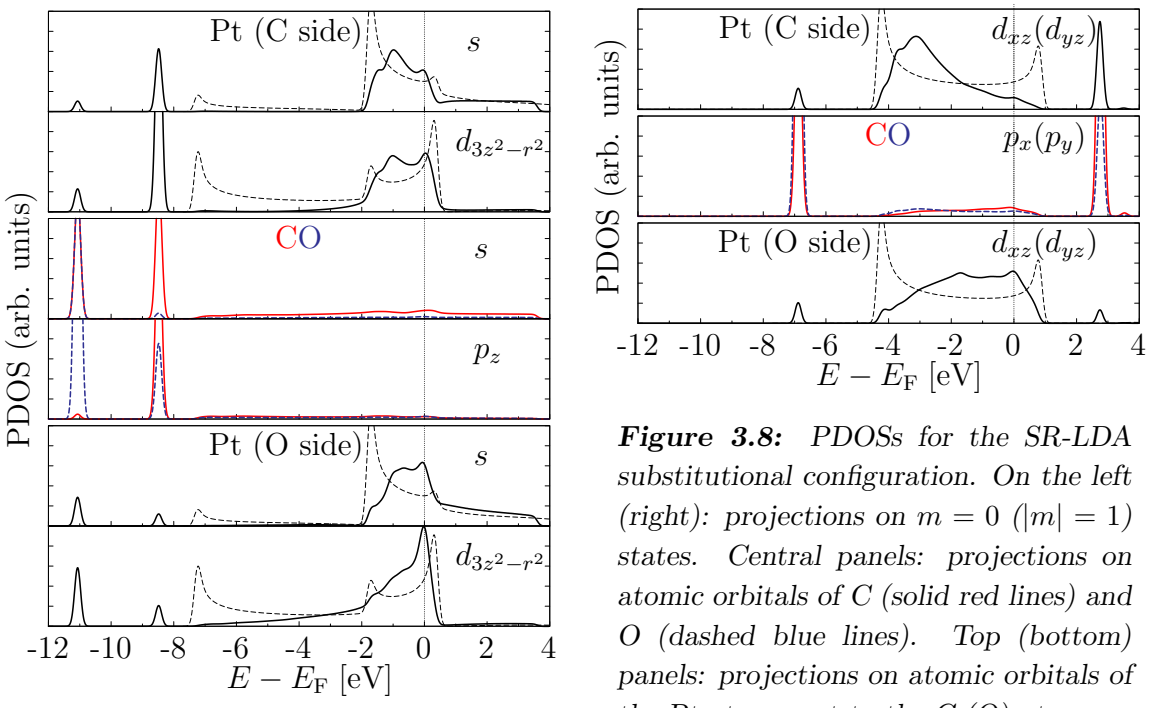

Figure 3.8: *PDOSs for the SR-LDA substitutional configuration. On the left (right): projections on $m = 0$ ($|m| = 1$) states. Central panels: projections on atomic orbitals of C (solid red lines) and O (dashed blue lines). Top (bottom) panels: projections on atomic orbitals of the Pt atom next to the C (O) atom.*

states between -7.3 eV and -2 eV on the Pt next to the C atom with respect to the Pt on the O side.

The PDOS projected onto the $|m| = 1$ (p_x or p_y) orbitals of C and O (see right side of Fig. 3.8) displays two peaks due to the π molecular states, one at -6.8 eV (1π) and another at 2.8 eV ($2\pi^\star$). However, in contrast with the bridge and ontop cases, instead of new intense peaks below the Fermi energy, we find in the substitutional case a plateau which spans the whole energy range of the Pt wire $|m| = 1$ band. Although the hybridization with Pt states is different from the bridge and ontop geometries, donation/back-donation is present here too. In fact a portion of the plateau in the $m = 0$ PDOS extends above E_{F}, while the plateau on the $|m| = 1$ PDOS lies mainly below E_{F}. In order to have an estimate of the donation we can consider the integral (from $-\infty$ to E_{F}) of the PDOS on the C and O orbitals forming σ states in the molecule (s plus p_x in the bridge geometry, s plus p_z in the substitutional). This integral gives 5.3 both in the substitutional and bridge geometries, while in the isolated molecule it gives about 5.9. Estimating in the same way the amount of back-donation, by integrating the PDOS on the orbitals which form the π states (p_z plus p_y in the bridge geometry, p_x plus p_y in the substitutional), we find 4.7 electrons both in the substitutional and in the bridge geometry, to be compared to the value of 3.9 obtained with the isolated CO (see also Sec. 4.2).

In the FR case we can label states according to the total angular momentum m_j, and hybridization occurs only among states with the same m_j. In Fig. 3.9 we report the PDOS projected onto the FR atomic orbitals of C and O separated according to the values of l and m_j of the spin-angle function. The peaks in these figures can be easily identified and their position compared with that of the SR case. In addition to the molecular σ levels present only in the PDOS on the $|m_j| = 1/2$ states at -23.7 eV (not shown), -11.2 eV and -8.6 eV, there are two peaks in the $l = 1$, $|m_j| = 1/2$ PDOS, one at -7 eV and another at 2.4 eV. They can be matched with the two peaks at -6.9 eV and at 2.8 eV in the $l = 1$, $|m_j| = 3/2$ PDOS, and correspond to the SOC split 1π and $2\pi^*$ states of the molecule (see Sec. B.1 in the Appendix). With respect to the isolated molecule, the 1/2-3/2 splitting of the π states is enhanced by the interaction with the Pt states, especially for the $2\pi^\star$ states.

As in the SR case, the interaction between the molecule and the wire is visible here as a plateau which extends in a wide energy range. In the PDOS projected onto the $l = 0$, $|m_j| = 1/2$ states the plateau extends between -7 eV and 3 eV, and is due to the hybridization between the 5σ orbital with the $|m_j| = 1/2$ bands of the Pt nanowire. The small peak at about -3.3 eV and the gap just above it are due to an anticrossing of the $|m_j| = 1/2$ bands [85], which generates new peaks and gaps in the FR-DOS of the Pt nanowire (see Sec. B.2 in the Appendix). In

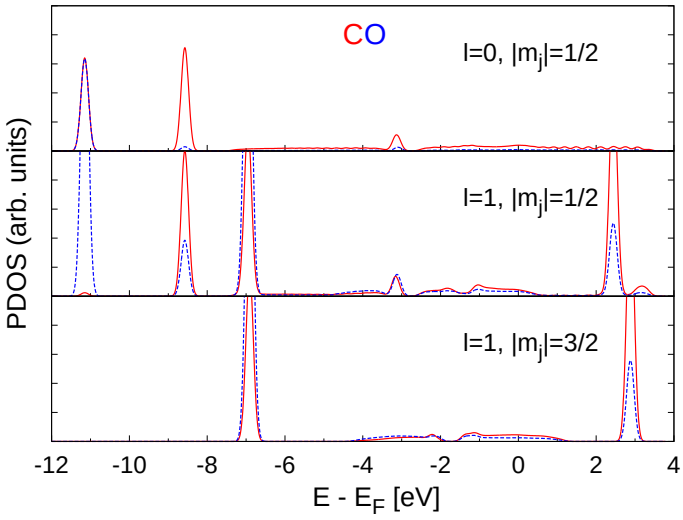

Figure 3.9: *PDOS for the substitutional configuration calculated within the FR-LDA. The projections are on the $|m_j| = 1/2$ and $|m_j| = 3/2$ FR atomic orbitals of C (solid red lines) and O (dashed blue lines). In the case $l = 1$, $|m_j| = 1/2$ the PDOS projected onto states of different j^2 have been added.*

the PDOS projected on the $l = 1$, $|m_j| = 3/2$ states there is a plateau between -4.2 eV and 0.8 eV due to the hybridization between π-derived states and $|m_j| = 3/2$ states of Pt. This plateau is localized in the same energy range as that of the SR π-$|m| = 1$ bands, slightly increased by the spin-orbit splitting of the $|m| = 1$ band. A hybridization gap of the $|m_j| = 3/2$ band of Pt is visible just above -2 eV. In the PDOS projected on $l = 1$, $|m_j| = 1/2$ states we find contributions from both σ-derived an π-derived states. In summary, also in the substitutional geometry we can conclude that the donation/back-donation model gives a good description of both the SR and FR electronic structure. Near the Fermi level the changes caused by SOC are not large in extent, but still quite visible in the electronic structure. This will reflect on the ballistic transport properties, which are discussed in the next Section.

3.3 Ballistic transmission of tipless chains

In this section we present the transmission of an infinite ideal Pt chain as a function of energy, for the three CO adsorption geometries discussed above, purposely without tips but with the adsorbed molecule as the sole scatterer. This idealized transmission measures the amount of obstacle posed by the molecule to electron free propagation, in addition to that, molecule-independent, caused by the tip-wire contacts – which as was said are left out here. This latter kind of effects will be addressed in the case of monatomic Au chains with CO (see Sec. 5.2). The transmission is calculated with the methods developed in Refs. 85, 86 (for the SR case), and in Ref. 62 (for the FR case), which have been briefly outlined in Sec. 2.6. The ballistic conductance has been calculated with the Landauer-Büttiker formalism, evaluating the total transmission at the Fermi energy.

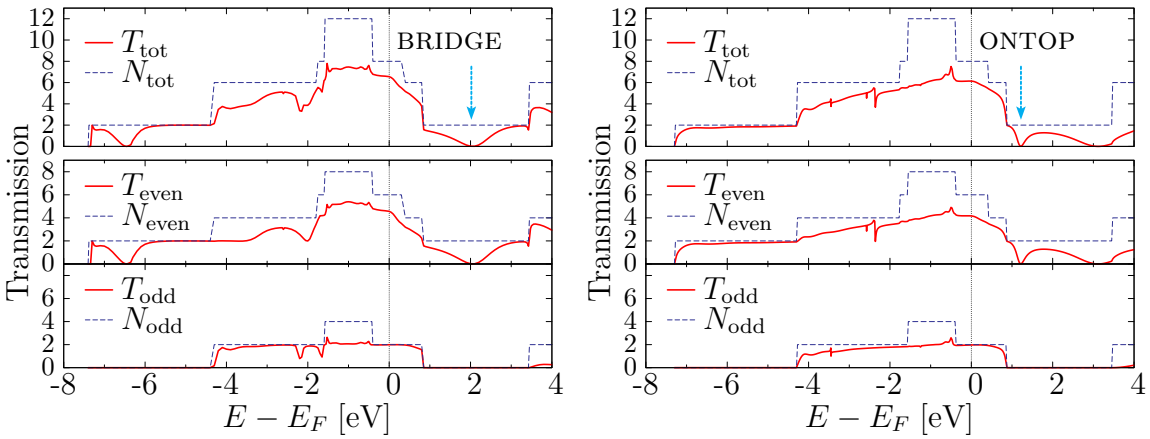

Figure 3.10: *Total and symmetry-separated SR-LDA transmission (solid red lines) and number of channels (dashed blue lines) for a tipless monatomic Pt chain with CO adsorbed at the bridge or ontop (left and right side, respectively)*

We report in the upper panel of Fig. 3.10 the SR transmission as a function of energy for the bridge and ontop geometries (left and right side, respectively). The total transmission, $T_{\rm tot}$, is shown in the upper panels, while the contribution of even and odd states to the transmission, $T_{\rm even}$ and $T_{\rm odd}$, are reported separately in the central and bottom panels, respectively. The total number of transmission channels, $N_{\rm tot}$, and the number of channels available for each symmetry, $N_{\rm even}$ and $N_{\rm odd}$, are indicated with dashed lines in the corresponding plots. At the Fermi level four (spin-degenerate) SR channels are available, three even and one odd. The $|m| = 2$ bands do not cross $E_{\rm F}$, hence they do not contribute to the conductance. The transmission properties of the Pt chain next to $E_{\rm F}$ are similar in the bridge and ontop CO adsorption geometries. In both geometries, the odd $|m| = 1$ band is almost perfectly transmitted, while the even $|m| = 1$ band and the two $m = 0$ bands are partially reflected. The resulting SR conductance is $G_{SR} = 6.6\ e^2/h$ in the bridge geometry and $G = 6.1\ e^2/h$ in the ontop, to be compared with the value $8\ e^2/h$ of the clean wire.

The energy dependent transmission shows instead more pronounced differences between the bridge geometry and the ontop geometry. We discuss first the *even* contribution to the transmission trying to establish a connection with the features in the PDOS projected on the corresponding atomic orbitals, shown previously in Sec. 3.2 for the bridge geometry (Fig. 3.3) and for the ontop geometry (Fig. 3.7). For energies between -5.8 eV and -4.3 eV there is only one $m = 0$ channel, which is almost perfectly transmitted in both geometries. Below -5.8 eV this channel is only slightly reflected when CO is ontop, but it is much more reflected when CO is at the bridge (and totally reflected at about -6.4 eV). In the PDOS of the bridge geometry, this range of energies ($-7.5\,\text{eV} < E < -5.8\,\text{eV}$) contains the peaks of the even 1π and $5\sigma_{\rm b}$ states. The presence of these peaks perturbs the $m = 0$ PDOS of the two Pt

atoms in contact with CO (compare solid and dashed lines in the s and $d_{3z^2-r^2}$ PDOS) and modify correspondingly the transmission in this energy range. In the ontop case instead, the $5\sigma_{\mathrm{b}}$ peak is at lower energies (below $-7.2\,\mathrm{eV}$) and influences the $m = 0$ PDOS only very close to the lower band edge, while the even 1π does not perturb the $|m| = 0$ PDOS, but only the $|m| = 1$ PDOS (d_{xz} orbitals). At higher energies (up to $-1.8\,\mathrm{eV}$), where in principle a new even channel (with $|m| = 1$) becomes available, the even contribution to the transmission grows only moderately and it is much larger in the ontop geometry. Actually, in the bridge geometry the even $|m| = 1$ states are directly involved in the $2\pi^{\star}_{\mathrm{b}}$ hybridization between -4.2 eV and -2.1 eV, therefore they do not transmit well (compare the PDOS projected on the d_{xz} orbital with that projected on $d_{3z^2-r^2}$: in this energy range, the matching with the PDOS of the Pt distant from CO is better in the case of $d_{3z^2-r^2}$ orbitals rather than d_{xz} orbitals).

In the ontop geometry instead, the d_{xz} PDOS shows that, although there is a depletion of the density which moves below and above the range of the $|m| = 1$ bands to form the $2\pi^{\star}_{\mathrm{b}}$ and $2\pi^{\star}_{\mathrm{a}}$ states, no direct hybridization with the $2\pi^{\star}$ is present within that range, resulting in a better transmission of $|m| = 1$ states with respect to the bridge case. The availability of the $|m| = 2$ channels between -1.6 eV and -0.4 eV leads only to a very small increase of the transmission, more pronounced in the bridge case with respect to the ontop. The fact that $|m| = 2$ states are badly transmitted can be easily related to the large mismatch between the $d_{x^2-y^2}$ PDOS of the two Pt atoms next to the molecule and that of a Pt atom distant from CO: the mismatch in the ontop case (Fig. 3.7) is larger than in the bridge case (Fig. 3.3).

Above 0.8 eV only the $m = 0$ channel with predominant s character is present: its transmission is strikingly different in the bridge and ontop geometries. In the former the transmission completely vanishes at 2.1 eV and it shows a dip about that energy, while in the latter there are two dips at about 1.2 eV and 3.1 eV. The position of the lowest dip in the ontop geometry and of the single dip in the bridge geometry (see arrows in Fig. 3.10) coincides with the position of the $5\sigma_{\mathrm{a}}$ resonance (see the PDOS projected onto the s orbitals in Fig. 3.7 and Fig. 3.3, respectively), which is located at two different energies in these two geometries. The dip at higher energies, visible only in the ontop case, can be attributed instead to the presence of the $2\pi^{\star}_{\mathrm{a}}$ states at that energy. In the bridge case they are higher in energy and their effect on the transmission is hidden by the onset of the well-transmitted $|m| = 1$ channels of p type.

The *odd* channels are available and can contribute to the transmission between -4.3 eV and 0.8 eV. The odd $|m| = 1$ channel is generally well transmitted in the whole energy span except for some localized energy ranges: in the bridge geometry there are two small dips near $-2\,\mathrm{eV}$ and a decrease of the transmission next to the lower band edge, while in the ontop geometry there is a very sharp antiresonance at

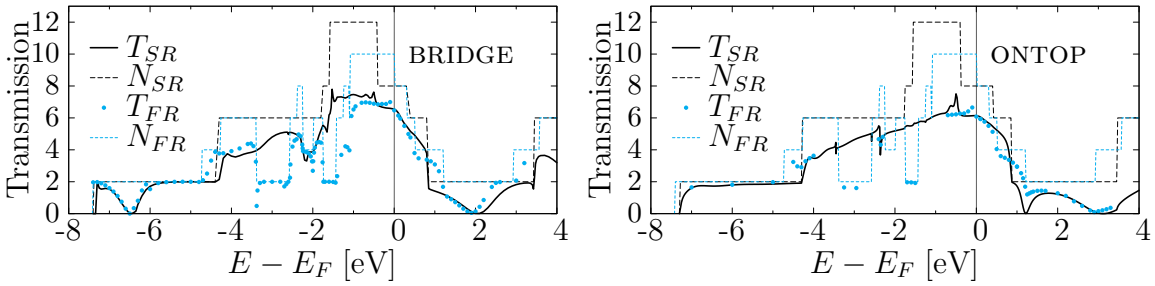

Figure 3.11: *Total SR and FR transmission (black solid lines and cyan dots, respectively) for a tipless Pt monatomic wire with CO adsorbed at the bridge or ontop (right and left side, respectively). The corresponding number of channels is indicated with dashed lines. The number of SR (black dashed lines) and FR (cyan short dashed lines) channels available at each energy is also indicated.*

−3.4 eV and a moderate reflection below −2.5 eV. The lowest dip in the bridge case and the sharp antiresonance in the ontop case correspond to the odd $2\pi_b^\star$ peak present at those energies in the respective PDOS (see Fig. 3.3 and Fig. 3.7, plots on the right side), while the position of the highest dip in the bridge case can be matched with the energy of a strong peak in the PDOS projected on the d_{xy} states of Pt (which does not correspond to any peak in the PDOS of C or O). As was noticed for the even $|m| = 2$ channel, also the odd $|m| = 2$ channel is almost blocked, since the corresponding Pt states are more perturbed by the interaction with the $2\pi^\star$ orbitals of CO, and the reflection is larger in the ontop case with respect to the bridge. This difference in the transmission properties between $|m| = 1$ and $|m| = 2$ odd channels could be predicted from the PDOSs: indeed the d_{yz} PDOSs looks similar to that of a Pt atom of the pristine nanowire, while the d_{xy} PDOS does not match at all the original PDOS of the wire.

The effect of SOC on the transmission properties of the bridge and ontop geometries is shown in Fig. 3.11 (left and right side, respectively), where we report the FR transmission, T_{FR} (dots), for selected energies and the number of FR channels, N_{FR} (short dashed lines). The SR transmission and number of SR channels shown previously are reported here again (solid lines and dashed lines, respectively) for a better comparison with the FR result. Since in the FR case states belonging to the Γ_3 or to the Γ_4 representations have the same transmission, we do not show their separate contributions but only their sum.

In the FR calculation, the SOC splitting of the $|m| = 2$ bands brings one channel (with $m_j = 5/2$) close to E_F, but actually this additional channel is poorly transmitted (in both bridge and ontop geometries) and hence the calculated conductances do not differ substantially from the corresponding SR value. The FR value of the

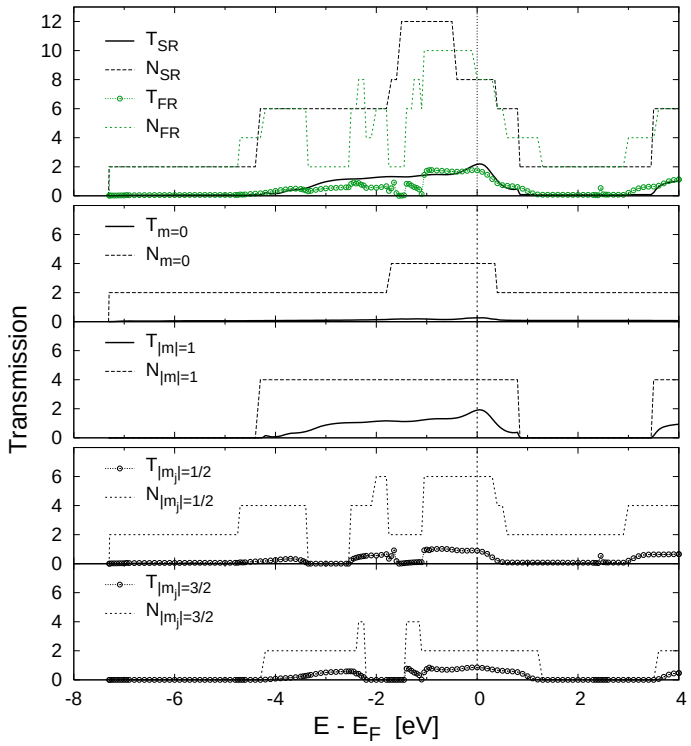

Figure 3.12: *Electron transmission for the substitutional geometry. In the top panel the SR (FR) transmission T_{SR} (T_{FR}) is shown with solid lines (green circles), while the number of channels N_{SR} (N_{FR}), is shown with dashed lines (short-dashed green lines). In the middle (bottom) panel we separate the SR (FR) transmission and number of channels according to the angular momentum $|m|$ ($|m_j|$). The contribution from $|m| = 2$ ($|m_j| = 5/2$) channels to the total SR (FR) transmission is practically zero, hence it is not shown (see text).*

conductance is $G_{FR} = 6.5\ e^2/h$ for the bridge geometry [95] and $G_{FR} = 6.1\ e^2/h$ for the ontop [94]. The largest differences between SR and FR transmissions are in correspondence of SOC-induced anticrossings of Pt bands of the wire (below E_{F}, see also Fig. B.6). The anticrossing of $|m_j| = 1/2$ bands between -4.4 eV and -2.6 eV and two anticrossings (one of $|m_j| = 1/2$ bands and the other of $|m_j| = 3/2$ bands) which overlap between -1.7 eV and -1.5 eV remove several channels from those energy regions decreasing the FR transmission. Above E_{F}, the $5\sigma_{\mathrm{a}}$ dip is still present in the FR transmission of the bridge geometry, although it is slightly shifted towards lower energies, but it disappears in the ontop geometry.

The SR and FR total transmissions as a function of energy for the substitutional geometry are shown in the top panel of Fig. 3.12. In this geometry we find a conductance of about $2.2\ e^2/h$, much smaller than in the bridge geometry. Actually at the Fermi level the transmission of the two degenerate $|m| = 1$ channels is about one half and that of the $m = 0$ channels is quite small (slightly above 0.1). In the other energy regions the transmission is even lower, since the $m = 0$ channels are almost totally blocked and the transmission of the $|m| = 1$ channels remains always below one half. The 5σ-derived states could in principle transmit because they hybridize with Pt states, but actually this is not the case since the coupling of the left Pt to CO is quite different from that of right Pt, as noted before in Sec. 3.2. Moreover, the

transmission due to the $|m| = 2$ bands of Pt (not shown here) is close to zero, since the CO has no states with matching symmetry. Thus the SR and FR calculations give similar results also for the substitutional geometry; the calculated FR value of the conductance is 1.7 e^2/h to be compared with $G = 6.5\ e^2/h$ for the upright bridge.

In the substitutional case the contributions from the $|m_j| = 1/2$ and the $|m_j| = 3/2$ channels are almost equal, in agreement with the fact that in the SR case only the $|m| = 1$ channels contribute to transmission. We can pinpoint some dips specific to the FR energy dependent transmission, that are due to the SOC-induced splittings of the bands. They are evident if we look separately at the $|m_j| = 1/2$ and $|m_j| = 3/2$ contributions to the total number of available channels: the former goes to zero between -3.4 eV and -2.5 eV, while the latter vanishes between -2.2 eV and -1.4 eV. The $|m_j| = 5/2$ contribution to the transmission (not shown) is almost zero, since the $|m_j| = 5/2$ channels have $|m| = 2$ orbital components that are completely blocked by the CO.

It should be pointed out here that the details of all channels will be modified by the onset of magnetism [98, 99], and this could in principle modify the ballistic conductance of our system. However, although a finite magnetization lifts the $\pm|m_j|$ degeneracy and consequently splits each pair of bands, the nature of the Pt states will not change dramatically and we can make a reasonable guess on what effect could have magnetism on the conductance. As an example, here we consider only the case of bridge and ontop geometries (which have very similar conductance properties) when with a finite magnetic moment parallel to the wire axis is present on Pt atoms. Smogunov et al. [99] have shown that in this magnetic configuration the number of conductance channels of the infinite monatomic wire decreases from $N_{\mathrm{ch}} = 10$ to $N_{\mathrm{ch}} = 7$ for a moderately strained wire ($d_{\mathrm{Pt\text{-}Pt}} = 2.66$). This drop in the number of channels is caused by three bands being shifted below E_{F}: one of these bands has $m_j = +5/2$ and is similar to the non-magnetic $|m_j| = 5/2$ band, while the other two have $m_j = +1/2$ and $m_j = -1/2$ and derive from mixing of the $m = 0$ and $|m| = 1$ SR bands. Therefore, we can expect a decrease of about $1 \div 2\, e^2/h$ for the bridge and ontop conductances in presence of a longitudinal magnetic moment, since in the non-magnetic FR case the $|m_j| = 5/2$ channel gives only a very small contribution to the conductance, while the other two channels are partially transmitted and their removal from E_{F} would certainly lower the conductance.

Although as was said above our conductance values cannot be directly compared with experimental data because they do not include the effect of the tips [29], they do indicate that in the substitutional configuration the conductance is about 3 times lower than in the ontop and upright bridge configurations, where at difference with the substitutional the $m = 0$ channels are not so strongly reflected. The Pt states with angular momentum $|m| = 2$ are (more or less strongly) blocked in all the geometries

examined here, but for different reasons: in the bridge and ontop cases they interact more with CO and this perturbs a lot the $|m| = 2$ PDOS on the neighbouring Pt; in the substitutional there is no CO orbital with the matching symmetry and thus the $|m| = 2$ channel is totally blocked by the molecule. Anyway, since these states fall below the Fermi level, their interaction with the molecule does not influence the conductance. The FR conductance does not differ substantially from the SR value because the $|m_j| = 5/2$ channels (which could in principle give rise to an increased conductance, since the corresponding FR band approaches the Fermi level) are almost completely blocked both by CO adsorbed in an upright position and by the substitutional CO, and because there are no SOC-induced gaps near the Fermi level.

In summary, in this chapter we characterized theoretically the adsorption of a CO molecule on a Pt monatomic chain in three selected geometries. We have found that in the bridge and ontop geometries the so called "donation/backdonation" process [52], which has proved useful in explaining the adsorption of CO on transition metal surfaces, gives a correct description of the electronic structure. The HOMO (5σ) and LUMO ($2\pi^\star$) of CO (often called "frontier orbitals") are mainly involved in the Pt-CO bond and strongly hybridize with Pt states forming localized bonding/antibonding pairs. As a consequence, some charge of the 5σ molecular orbital is donated to the wire, which in turn back-donates some charge partially filling the empty $2\pi^\star$ orbitals of the molecule. We also pointed out some additional features, such as the adsorption-induced mixing between 4σ and 5σ and between 1π and $2\pi^\star$ molecular levels, which indicate that the successive refinements [54] to the frontier orbitals model for surface adsorption are appropriate also in this quasi-1D case. When the chain is equally spaced, the bridge is much favored with respect to the other two configurations, but a substitutional CO could be conveniently accommodated at a highly stretched Pt-Pt bond, thus becoming a plausible configuration only in the case of a wire under high strain or near rupture. Also in the substitutional case there is a hybridization between Pt states and CO orbitals giving rise to donation and backdonation, but the π hybridization is weaker with respect to the bridge and ontop cases.

The calculated transmission shows that CO adsorption at the bridge or ontop does not lead to a big reduction in the conductance of the (tipless) Pt chain, while the substitutional CO poses a great barrier to the electron transmission along the chain and causes a much bigger reduction of the conductance. In this latter geometry, only $|m| = 1$ channels are partially transmitted through the molecule thanks to the hybridization with its π levels, while all the other channels are essentially blocked. In the other two geometries, where the transmission takes place prevalently through the wire, channels corresponding to those Pt states which are more involved in the interaction with CO are reflected the most. At some specific scattering energies we

identified some transmission "dips" (principally in the $m = 0$ channels) which can be ascribed to specific hybridizations between Pt and CO states and can be identified from peaks at the same energies in the PDOS. Finally, we showed that the inclusion of SOC, although modifying heavily the electronic structure of the Pt chain, does not change the qualitative features of the Pt-CO interaction. Also the ballistic conductance is not much influenced by SOC effects, since the largest differences between the SR and FR results are restricted to energy regions well below E_{F}.

CHAPTER 4

CO ADSORBED ON MONATOMIC GOLD CHAINS

In this chapter we study the interaction of a CO molecule with monatomic Au chains at different levels of complexity. We start from the simplest model, a straight infinite chain at the equilibrium spacing, examining the same adsorption configurations considered in Chap. 3 for CO on Pt chains, namely bridge, ontop, and substitutional. We will describe and discuss the energetics of CO, the electronic structure and the ballistic transport, making a comparison with the case of Pt chains. Then, in order to catch the strain-related effects on these properties, that might be observed, for instance, when chains are kept under tension by the pulling tip of a STM, we consider regularly-spaced stretched chains for several values of the Au-Au distance above the equilibrium one. Since the tipless conductance obtained from these geometries is quite sensitive to the details of the band structure (due to the presence of d band edges very close to the Fermi level), we find significant to check the stability of LDA or GGA results against misplacements of d bands driven, for instance, by the self-interaction error. For this purpose we apply the DFT+U scheme described in Sec. 2.7 to the electronic structure and ballistic conductance of Au chains (with or without CO) exploring several values of U. Finally, in Chap. 5, we will move to more realistic short free-standing monatomic chains hanging between two Au(001) surfaces.

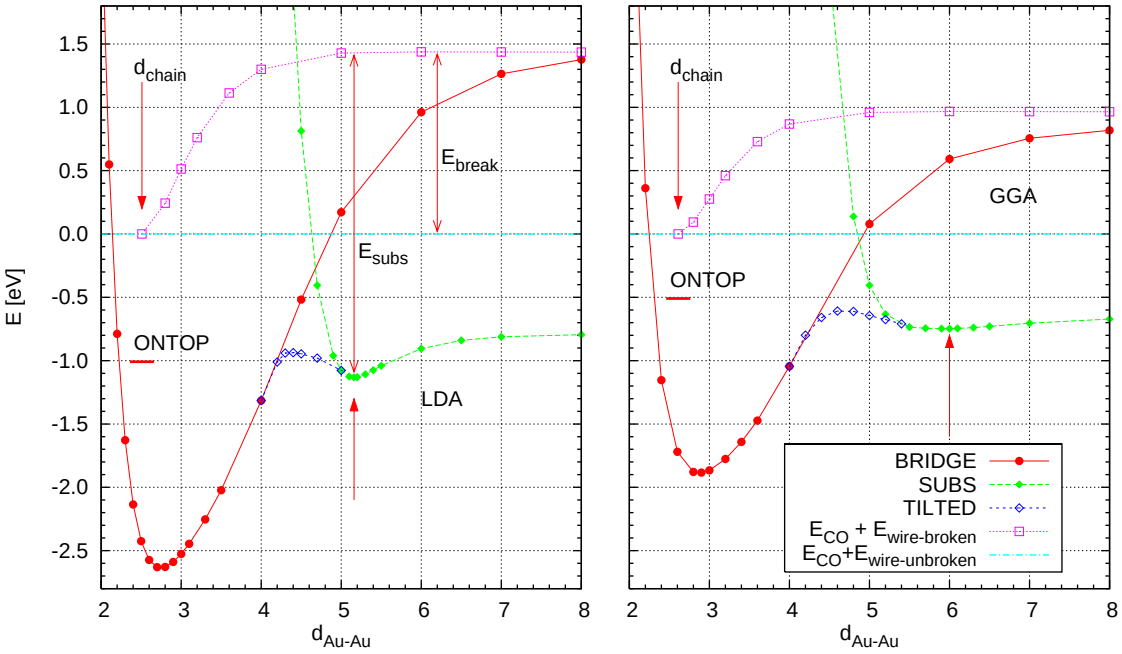

Figure 4.1: *Optimized energy (with respect to the C and O positions) for different geometries as a function of the Au-Au distance, $d_{Au\text{-}Au}$ (see text in this section and caption of Fig. 3.2 at page 74).*

4.1 Geometry and energetics

The atomic configurations of CO adsorbed on monatomic Au chains are the same as those already considered for CO on Pt chains (Fig. 3.1). We use the same supercell dimensions, number of metal atoms, and **k**-point samplings, while the kinetic energy cut-offs are discussed in Sec. B.2 in the Appendix. The structural optimizations have been performed following the criteria described in Sec. 3.1 for Pt chains: we optimized the positions of C and O along x for the bridge and ontop geometries, along z for the substitutional, and in the xz plane for the tilted bridge, while keeping all Au atoms aligned along z at the equilibrium spacing ($d_{\rm chain} = 2.51$ Å with LDA, $d_{\rm chain} = 2.61$ Å with GGA). For the bridge, substitutional, and tilted bridge geometries we repeated the relaxation of the atomic positions for different values of the Au-Au distance $d_{\rm Au\text{-}Au}$ between the two Au atoms in contact with the molecule.

The LDA (GGA) total energy of the optimized geometries is reported as a function of $d_{\rm Au\text{-}Au}$ on the left (right) side of Fig. 4.1, respectively (the zero of the energy is the sum of the energies of the isolated CO and of the isolated Au chain at equilibrium spacing). If we compare the LDA or GGA data for Au in Fig. 4.1 with that for Pt

	Bridge						Ontop					
	SR-LDA			SR-GGA			SR-LDA			SR-GGA		
M	$d_{\text{M-C}}$	$d_{\text{C-O}}$	E_{chem}	$d_{\text{M-C}}$	$d_{\text{C-O}}$	E_{chem}	$d_{\text{M-C}}$	$d_{\text{C-O}}$	E_{chem}	$d_{\text{M-C}}$	$d_{\text{C-O}}$	E_{chem}
Pt	1.95	1.16	−2.9	1.98	1.17	−2.3	1.82	1.14	−1.9	1.84	1.15	−1.4
Au	1.95	1.16	−2.4	1.99	1.17	−1.7	1.89	1.14	−1.0	1.96	1.14	−0.5

Table 4.1: *Comparison of the optimized distances (in Å) and chemisorption energies (in eV) for the ontop and bridge adsorption geometries of CO on Pt and Au chains. The metal-carbon distance $d_{M\text{-}C}$ is $d_{Pt\text{-}C}$ for Pt (see Fig. 3.1), and $d_{Au\text{-}C}$ for Au.*

in Fig. 3.2, we can identify the same three ranges of Au-Au bond distances that were discussed for CO on Pt chains: (i) when $d_{\text{Au-Au}}$ is close or slightly larger than the equilibrium spacing of the isolated chain, only the ontop and bridge configurations are possible; (ii) when $d_{\text{Au-Au}}$ is very large, corresponding to a highly stretched Au-Au bond, a substitutional CO in a linear configuration is favored;[1] (iii) at intermediate values of $d_{\text{Au-Au}}$, a tilted bridge configuration is the most stable one. We will now discuss some differences and similarities between Pt and Au in these three ranges of $d_{\text{Au-Au}}$, separately.

As in Pt, when the Au-Au bond is not stretched ($d_{\text{Au-Au}} \simeq d_{\text{chain}}$) the bridge configuration is much favored with respect to the ontop. In Tab. 4.1 we compare the optimized bond lengths and the chemisorption energy computed as in Eq. (3.1) for the two configurations. We report LDA and GGA data for both Pt chains (from the previous chapter) and Au chains at the respective equilibrium atomic spacings ($d_{\text{M-M}} = d_{\text{chain}}$, M being either Pt or Au, corresponding to the configurations pointed by the "d_{chain}" arrows in Fig. 3.2 and in Fig. 4.1). As one could have expected, being gold a "noble" metal, the adsorption energy of CO in Au is smaller than in Pt. In the bridge geometry the chemisorption energies are not very different, since E_{chem} in Au is only about $0.5 \div 0.6$ eV smaller than in Pt, while in the ontop geometry the difference is more pronounced, being E_{chem} about 0.9 eV smaller in Au. Therefore, the preference for the bridge adsorption site in Au chains is more marked than in Pt chains, as shown by the difference in E_{chem} between the two adsorption geometries (in Au, 1.4 eV and 1.2 eV within LDA and GGA respectively; in Pt, about 1.0 eV and 0.9 eV).

The C-O distance is always larger when the molecule binds to the chain in the

[1] Notice that the Au-Au spacing needed to host a substitutional CO (see also later in the text) is much larger than the theoretical breaking distance of a pristine Au chain (about 3.1 Å with LDA and 3.0 Å with GGA, see for instance Ref. 100), hence this geometric configuration should be regarded as a possible evolution from a perpendicular CO adsorbed at the bridge or ontop.

bridge configuration, where the chemisorption energies are larger, and it has almost the same values in Pt and Au. In the GGA ontop configuration, instead, there is a larger difference in $d_{\text{C-O}}$ between Pt and Au. This difference is compatible with the smaller value of E_{chem} found in Au for this geometry. In the bridge geometry, $d_{\text{Au-C}}$ is quite similar to $d_{\text{Pt-C}}$ being only slightly larger in Au, but in the ontop geometry there is instead a significant difference between Pt and Au, since $d_{\text{Au-C}}$ is about 7% larger than $d_{\text{Pt-C}}$ within GGA (4% larger within LDA). As was already noticed for Pt (see Sec. 3.1 and Ref. 95), the carbon-metal bond length ($d_{\text{Au-C}}$ for Au and $d_{\text{Pt-C}}$ for Pt) is larger in the bridge geometry than in the ontop geometry, since the C atom binds to two atoms of the chain instead of one. In the case of Au chains we did not reoptimize our geometries using the FR-USPP because in the previous chapter we have seen that the SOC corrections to the chemisorption energies of CO are of the order of 0.1 eV or smaller in Pt, and they are not expected to be larger in Au. Finally, the data for Au chains confirm again the general trend of larger adsorption energies and slightly shorter bond lengths in the LDA compared to the GGA.

The energy minimum of the bridge configuration is found at a distance ($d_{\text{Au-Au}}$) larger than d_{chain}, as seen also in Pt chains. Within GGA, for instance, the optimal distance of the Au-Au bond below CO is $d_{\text{Au-Au}} = 2.87$ Å, corresponding to an energy gain of about 0.15 eV with respect to the uniformly spaced configuration ($d_{\text{Au-Au}} = d_{\text{chain}}$). The optimal $d_{\text{Au-Au}}$ is however much larger than the optimal $d_{\text{Pt-Pt}}$ in Pt (see Fig. 3.2): this could be explained with the larger equilibrium spacing in Au chains or with a larger stiffness of M-M bonds in Pt chains with respect to Au chains. This can be understood by comparing the "$E_{\text{CO}} + E_{\text{wire-broken}}$" curves of Pt and Au (indicated by squares in Fig. 3.2 and Fig. 4.1, respectively): for instance, the GGA energy cost to stretch by 10% a Au-Au bond (that is to say, from $d_{\text{Au-Au}} = 2.61$ Å to $d_{\text{Au-Au}} = 2.87$ Å) is about 0.16 eV, much smaller than the corresponding value for a Pt chain (about 0.26 eV to stretch a Pt-Pt bond from $d_{\text{Pt-Pt}} = 2.39$ Å to $d_{\text{Pt-Pt}} = 2.63$ Å).

In the region with a hyper-stretched Au-Au bond, corresponding to $d_{\text{Au-Au}}$ above 5.0 Å (above 5.5 Å) in the LDA (GGA) plot of Fig. 4.1, the substitutional configuration is favored and has an energy minimum at about $d_{\text{Au-Au}} = 5.16$ Å (at $d_{\text{Au-Au}} \simeq 6.0$ Å). The comparison between the Pt and Au substitutional configurations is strikingly different in the LDA and GGA pictures. Indeed, within LDA the Au-Au distance of the substitutional energy minimum in Au is just 2% larger than in Pt ($d_{\text{Pt-Pt}} = 5.05$ Å), while the GGA Au-Au distance at the minimum is about 14% larger than the GGA Pt-Pt distance ($d_{\text{Pt-Pt}} = 5.24$ Å). Moreover, in Au the GGA energy curve is much more shallow around its minimum with respect to the LDA energy curve. We calculated the depth of the minimum using as a reference energy the substitutional energy at $d_{\text{Au-Au}} \to \infty$ and found that within GGA it is less than 0.1 eV, while in the LDA it is about 0.3 eV (i.e. more than three times deeper). In the

substitutional configuration of Pt there was also a large difference between GGA and LDA, but the LDA minimum was only two times deeper than the GGA minimum (about 0.6 eV against 0.3 eV). Despite this discrepancy between the LDA and GGA descriptions of the O-Au bond in the substitutional geometry, both approximations give the same conclusion when comparing Au with Pt: once CO is in the substitutional position, the Au-CO-Au junction would break more easily than the Pt-CO-Pt junction. This conclusion will become useful to provide some interpretation of the conductance histograms of Au and it will be recalled in Sec. 5.3.

The substitutional configuration seems to be energetically more stable in Au than in Pt, since the substitutional energy curve lies at lower energies in Au. This depends on the different energy cost needed to break a metal-metal bond of the chain (E_{break} shown in Fig. 3.2 for Pt and in Fig. 4.1 for Au), which is much larger for Pt chains. Instead, in Pt the energy gain of placing CO substitutionally at the broken bond (E_{subs}) is only slightly larger than in Au, resulting in a smaller chemisorption energy (given by $E_{\text{subs}} - E_{\text{break}}$). This apparent inconsistency can be solved once we understand that the linear structure (either Au-CO-Au or Pt-CO-Pt) will break at its weakest point when a longitudinal tension is applied to the opposite ends. This point corresponds to the metal-oxygen bond, because the M-CO configuration is much lower in energy than the CO-M configuration as $d_{\text{M-M}} \to \infty$ (see Ref. 95), and the CO-Au bond is weaker than the CO-Pt bond.

In a short range of intermediate distances (4.1 Å $< d_{\text{Au-Au}} <$ 5.0 Å within LDA, 4.3 Å $< d_{\text{Au-Au}} <$ 5.4 Å within GGA), a tilted bridge configuration ("TILTED" curve in Fig. 4.1) is preferred to the upright bridge and substitutional positions. In Pt chains, the CO passes from the upright bridge to the tilted bridge position at a much smaller length of the Pt-Pt bond (about 3.7 Å). This difference can be attributed mainly to the position of the inflection point in the energy curve of the bridge geometry (which marks a kind of structural instability), which is at larger distances in Au chains compared to Pt chains (respectively, slightly above 4.1 Å and at about 3.4 Å). The tilted-bridge to linear-substitutional transition within Au chains takes place at $d_{\text{Au-Au}}$ smaller than the distance of the substitutional energy minimum, while in Pt chains the tilted-bridge geometry is preferred also at $d_{\text{Pt-Pt}}$ values close or slightly larger than the substitutional energy minimum position (although the two configurations are almost degenerate when $d_{\text{Pt-Pt}}$ is greater than that distance). As a consequence, the tilted bridge is preferred in a range of distances which is larger in Pt than in Au. We also notice that when moving from the optimal bridge configuration to the optimal substitutional configuration by increasing $d_{\text{M-M}}$, so that the CO axis tilts gradually from perpendicular to longitudinal, an energy maximum is encountered at about $d_{\text{Au-Au}} = 4.4$ Å with LDA ($d_{\text{Au-Au}} = 4.6$ Å with GGA), while in Pt chains there is no such a maximum in the energy of the tilted bridge geometry.

4.2 Electronic structure

We have seen in the previous section that, according to our LDA or GGA calculations, CO can adsorb on monatomic Au chains, although the chemisorption energies are smaller than in Pt chains. The bridge geometry is the most stable configuration. The ontop has a much smaller chemisorption energy and the substitutional, stable at larger $d_{\text{Au-Au}}$, could be easily broken by applying a tiny external pulling force. However, in addition to the bridge geometry, in this section we will discuss the electronic structure properties also for the other two configurations, for different reasons. The ontop site is studied because it has been reported experimentally as the preferred adsorption site of CO on short Au chains deposited on a NiAl substrate [31] and it has in part already been studied from first principles (though only in a strained geometry, see Ref. 49). The same configuration has also been used as a benchmark for different methodologies of ballistic transport calculation [50], thus it could be a useful test case for our transmission calculations. The substitutional geometry is studied because it has been hypothesized by Kiguchi et al. [26] as a possible meta-stable intermediate configuration to explain the raise in the conductance observed while pulling a Au nanocontact after a CO has been adsorbed on it (see Sec. 1.5 and Sec. 5.3 for more details).

In the previous chapter we have seen that the details of the electronic structure (like the positions of peaks, or their broadening, for instance) depend strongly on the adsorption geometry and have a non-negligible influence on the ballistic transmission of the Pt chain. We can expect that these details depend considerably on the material of the chain as well. Since Au has one more valence electron than Pt, in Au chains the d bands are completely filled and are lower in energy than in Pt chains (see Fig. B.6 in the Appendix). Nonetheless, the d bands of Au are still very close to E_{F} and can participate in the bonding with the molecule, hence we do not expect a completely different adsorption mechanism from that seen in Pt. Another difference between the band structures of Pt and Au chains are the band widths, which are sensibly reduced in Au because of the larger interatomic equilibrium distance (within LDA: 2.51 Å in Au, against 2.34 Å in Pt). Therefore we can expect that in Au chains the metal states are more perturbed than in Pt chains by the presence of CO, since, as shown for Pt in the previous chapter, states with smaller bandwidths (such as the $|m| = 2$ bands) are subject to stronger modifications upon CO adsorption.

In the following of this section we will analyze the density of states projected on the atomic orbitals of C, O and of the Au atom(s) in contact with the molecule. The PDOSs for CO on Au chains presented in this section have been obtained with the same computational parameters used for Pt (number of atoms in the supercell, smearing width, and **k**-point sampling).

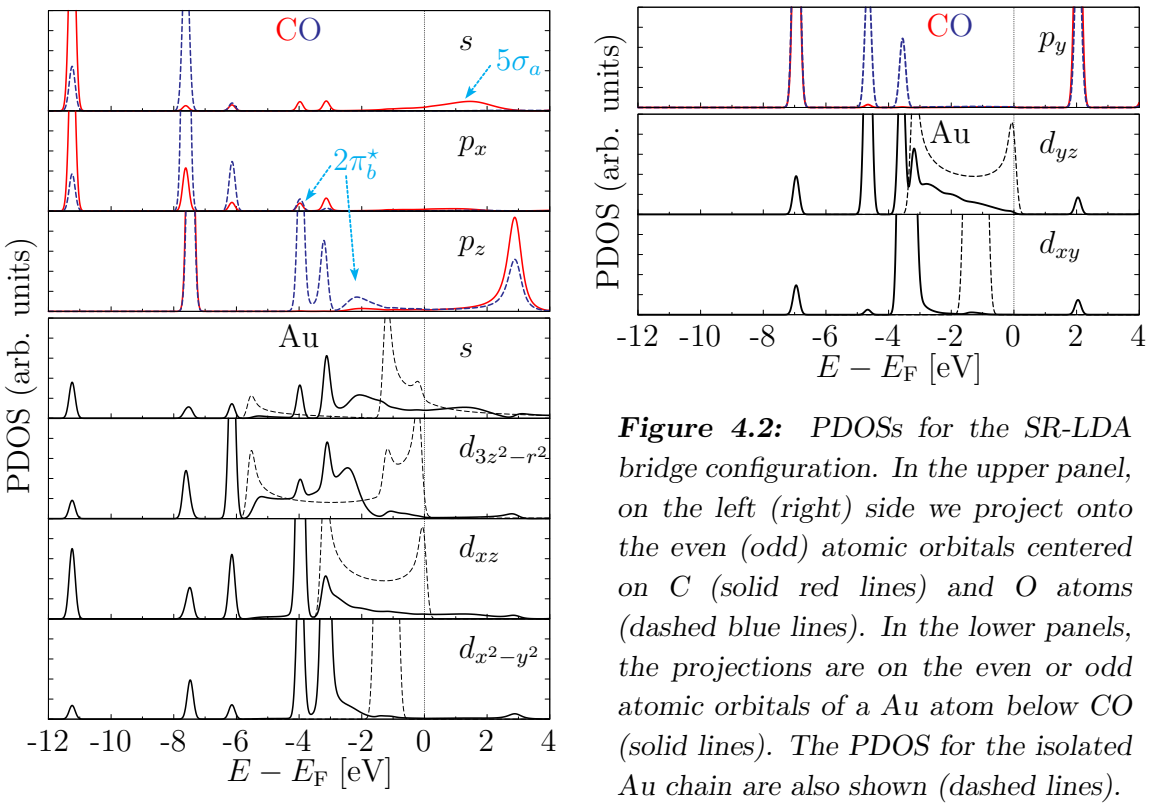

Figure 4.2: *PDOSs for the SR-LDA bridge configuration. In the upper panel, on the left (right) side we project onto the even (odd) atomic orbitals centered on C (solid red lines) and O atoms (dashed blue lines). In the lower panels, the projections are on the even or odd atomic orbitals of a Au atom below CO (solid lines). The PDOS for the isolated Au chain are also shown (dashed lines).*

4.2.1 CO adsorbed at the bridge site

The PDOSs for the LDA bridge geometry are shown in Fig. 4.2, separated according to the even/odd symmetry and reported on the left (right) part of the figure for the projections on the even (odd) states. From a first glance at the PDOS projected onto the even orbitals of C and O we can argue that a donation/backdonation process takes place between the molecule and the metal, as seen in Pt. In the PDOS projected onto s and p_x atomic orbitals of C and O there is a broad feature above the Fermi energy, centered at about 1.5 eV, which corresponds to the $5\sigma_\mathrm{a}$ states arising from the σ donation. The backdonation is instead visible in the PDOS projected onto p_z orbitals as the three separate peaks, lying between -4 eV and -2 eV, which represent the $2\pi_\mathrm{b}^\star$ states.

There are however some differences with respect to the electronic structure of CO adsorbed on a Pt chain in the same geometry (see the PDOS in Fig. 3.3, page 78). The $5\sigma_\mathrm{a}$ peak above the Fermi level is much broader in Au and it is positioned slightly lower in energy. This peak is mainly coupled with the metal s states, hence we may expect that it will cause the same drastic reduction of the s channel transmission at the energy of the peak as that observed in Pt chains. Below E_F, the double peaked

$5\sigma_{\mathrm{b}}$ feature present in Pt between $-7.5\,\mathrm{eV}$ and $-6\,\mathrm{eV}$, in Au is split into two peaks spaced by about $1.6\,\mathrm{eV}$, a principal peak at $-7.7\,\mathrm{eV}$ and a secondary peak at smaller binding energies. With respect to the $5\sigma_{\mathrm{b}}$ peaks of Pt, these two peaks are less broadened by the interaction with the metal, since they lie below the bottom of the $m = 0$ Au bands. These two bonding $5\sigma_{\mathrm{b}}$ states are more strongly coupled to $d_{3z^2-r^2}$ Au bands, although all the PDOSs projected on even orbitals of Au have two distinct peaks at $-7.7\,\mathrm{eV}$ and $-6.1\,\mathrm{eV}$ which match the $5\sigma_{\mathrm{b}}$ peaks in the C and O PDOS. The shape of the 4σ peak in Au is instead much more similar to that in Pt, although it is found at larger binding energy (at about $-11.2\,\mathrm{eV}$, instead of $-10.5\,\mathrm{eV}$).

Among π-derived states, visible in the p_z projections, the molecular 1π and $2\pi^\star_{\mathrm{a}}$ states (at $-7.4\,\mathrm{eV}$ below E_{F} and at $2.9\,\mathrm{eV}$ above E_{F}, respectively) have a small hybridization with Au states and correspond to small peaks in the metal PDOS. These two states are shifted to larger binding energies with respect to the corresponding states in Pt (the former shifts down of more than $1\,\mathrm{eV}$, the latter of about $0.6\,\mathrm{eV}$). Between the 1π and $2\pi^\star_{\mathrm{a}}$ peaks, we find the bonding $2\pi^\star_{\mathrm{b}}$ states, which present more differences with respect to the $2\pi^\star_{\mathrm{b}}$ of the Pt chain. In Pt these states merge in a single broad peak, originating from the coupling with mainly $d_{x^2-y^2}$ states, with a shoulder at lower energies corresponding to a broad feature in the d_{xz} PDOS and a tail at higher energies matching with a bump in the s PDOS (see Sec. 3.2). In Au, we can still recognize these three contributions to the $2\pi^\star_{\mathrm{b}}$ DOS, but they are less broadened and result in three peaks which are more separate in energy. At larger binding energies there is the d_{xz} contribution, represented by a single narrow peak at $-4.0\,\mathrm{eV}$ (thus below the bottom of the $|m| = 1$ Au bands, while in Pt this coupling takes place within the energy range of those bands). The hybridizations of the $2\pi^\star$ with the $d_{x^2-y^2}$ and s states are also visible in the PDOS (see the peak at $-3.2\,\mathrm{eV}$ and the bump at $-2.1\,\mathrm{eV}$), but do not merge in a single feature, as instead happens for Pt. The contribution of the $d_{3z^2-r^2}$ states in the two latter peaks is larger here than in Pt.

Among *odd* states, in the PDOS projected on the p_y orbitals of C and O we find the same four peaks that we have identified in the case of Pt chains. Between the odd 1π peak and the odd antibonding $2\pi^\star_{\mathrm{o,a}}$ peak there are two bonding $2\pi^\star_{\mathrm{o,b}}$ peaks, one lower in energy which matches a strong peak in the d_{yz} PDOS of Au, and the other, higher in energy, matching a strong peak in the d_{xy} PDOS. At variance with Pt chains, here the d_{yz} PDOS is quite perturbed by the presence of CO, hence we might expect a sizeable transmission reduction also for the odd $|m| = 1$ channel, which was instead well transmitted in Pt.

As seen for Pt chains, the onset of these new localized states brought by the interaction with CO perturbs strongly the overall density distribution in the PDOS of the metal atoms in contact with the molecule, especially for states having a more

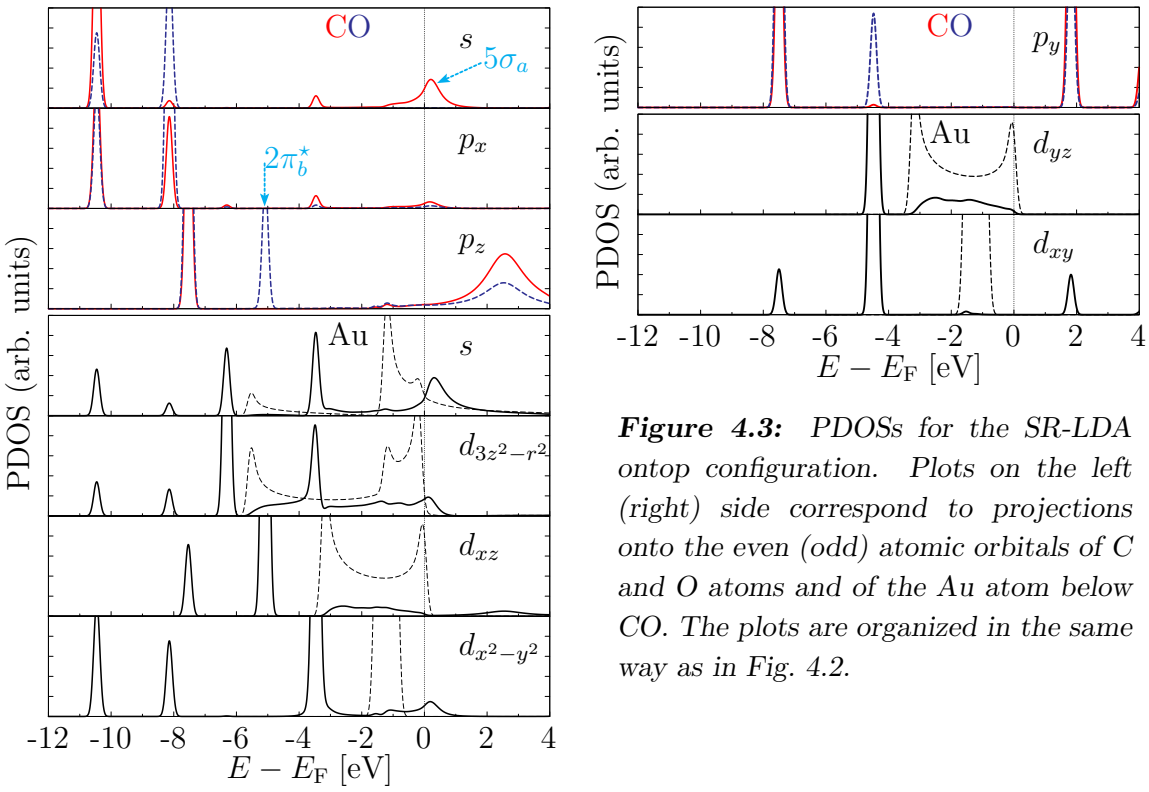

Figure 4.3: *PDOSs for the SR-LDA ontop configuration. Plots on the left (right) side correspond to projections onto the even (odd) atomic orbitals of C and O atoms and of the Au atom below CO. The plots are organized in the same way as in Fig. 4.2.*

pronounced spatial localization (narrower bandwidth), such as $d_{x^2-y^2}$ and d_{xy}. In Au chains the width of $|m| = 1$ and $|m| = 2$ bands is visibly reduced with respect to Pt chains (up to about one half for the $|m| = 2$ band), and, as a consequence, the depletion of density cause by CO adsorption in Pt is enhanced in Au. Notably, in the $d_{x^2-y^2}$ and d_{xy} PDOSs the greatest part of electronic density present in the pristine Au chain within the energy span of the $|m| = 2$ bands (from $-1.6\,\text{eV}$ to $-0.8\,\text{eV}$) has moved to different energies, but also the d_{xz} and d_{yz} PDOSs from $-3.3\,\text{eV}$ to E_F and the $d_{3z^2-r^2}$ PDOS from to $-1.2\,\text{eV}$ to $-0.1\,\text{eV}$ suffer a great reduction of the density, much bigger than in Pt. Therefore, for electron scattering energies between $-3.3\,\text{eV}$ and E_F we could expect a greater reduction in the transmission of Au chains (examined in Sec. 4.3) with respect to Pt.

4.2.2 CO adsorbed ontop

The PDOSs for the LDA ontop geometry are reported in Fig. 4.3, the projections onto even (odd) atomic orbitals of C, O, and Au being on the left (right) side. With respect to the PDOSs for CO ontop of a Pt chain (see Fig. 3.7, page 84), the main changes are in the position of the peaks, while the number of peaks is the same and their appearance (broadening, height,...) is unchanged for most of them.

In the s and p_x PDOS of C and O and in the s, $d_{3z^2-r^2}$, and $d_{x^2-y^2}$ PDOS of Au, the 4σ and $5\sigma_\mathrm{b}$ peaks are almost identical to those of Pt; they are only shifted down of about 0.2 eV with respect to E_F. A state with a strong peak in the s, $d_{3z^2-r^2}$, and $d_{x^2-y^2}$ PDOS of Au and a much smaller projection on the orbitals of C and O is present also in Au (at -3.5 eV, while in Pt it was found at -2.4 eV). Both position and height of the $5\sigma_\mathrm{a}$ peak above E_F are instead different with respect to Pt, since in Au the peak is smaller and is positioned at lower energies. While in Pt it was found at about 1.1 eV above E_F, in Au it moves much closer to the Fermi level (just 0.2 eV above E_F). It is still coupled with a peak in the s PDOS of the metal, which is now more perturbed in the energy region around E_F. This fact could have a noticeable impact on the conductance, since we have seen that in Pt the $5\sigma_\mathrm{a}$ peaks are responsible for the s transmission dips above E_F.

Among π-derived even states, the distribution of peaks in the p_z PDOS of Au is pretty similar to that of Pt, with the narrow 1π and $2\pi^\star_\mathrm{b}$ peaks below E_F and the broader $2\pi^\star_\mathrm{a}$ feature above E_F. The PDOS projected onto the odd states is also very similar to that of Pt, the only difference being a downshift of the peaks (about -0.5 eV for the 1π, -1.1 eV for the $2\pi^\star_\mathrm{b}$, and -0.3 eV for the $2\pi^\star_\mathrm{a}$). Although in the ontop geometry the interaction with CO can be characterized by similar peaks in Pt and Au, the changes in the PDOS projected on the metal atom in contact with the molecule are larger in Au (the same has been noticed for the bridge geometry). For instance, among odd states, in both metals the d_{xy} PDOS is totally different from the original shape of the $|m| = 2$ PDOS, but the d_{yz} PDOS, which was not much perturbed in Pt, is subject to larger modifications in Au. This holds also for the even states between -5.8 eV and E_F, thus we expect that the overall reduction of the pristine chain transmission in Au is larger than in Pt for the ontop geometry too.

The details of the even π interaction depend more on the geometry rather than on the metal. Indeed, in the ontop geometry, even π states couple prevalently with d_{xz} orbitals of the metal (compare Pt, Fig. 3.7, and Au, Fig. 4.3), essentially for geometrical reasons and orbital overlaps, while in the bridge geometry there is a stronger hybridization with all the orbitals (see Fig. 3.3 and Fig. 4.2). As a consequence, in the ontop geometry the $2\pi^\star_\mathrm{b}$ states consist of a single peak (matching a d_{xz} peak), while in the bridge geometry there are three contributions (which however merge in a single feature in Pt), corresponding to the couplings to the individual metal orbitals (d_{xz}, $d_{x^2-y^2}$, or s) with different strengths. Also the odd π interaction has a similar feature: in the ontop geometry, the odd π orbitals of CO hybridize only with the d_{yz} states of the chain, resulting in a single $2\pi^\star_\mathrm{b}$ peak, while in the bridge geometry there are two $2\pi^\star_\mathrm{b}$ peaks, one mostly d_{yz} and the other mostly d_{xy}.

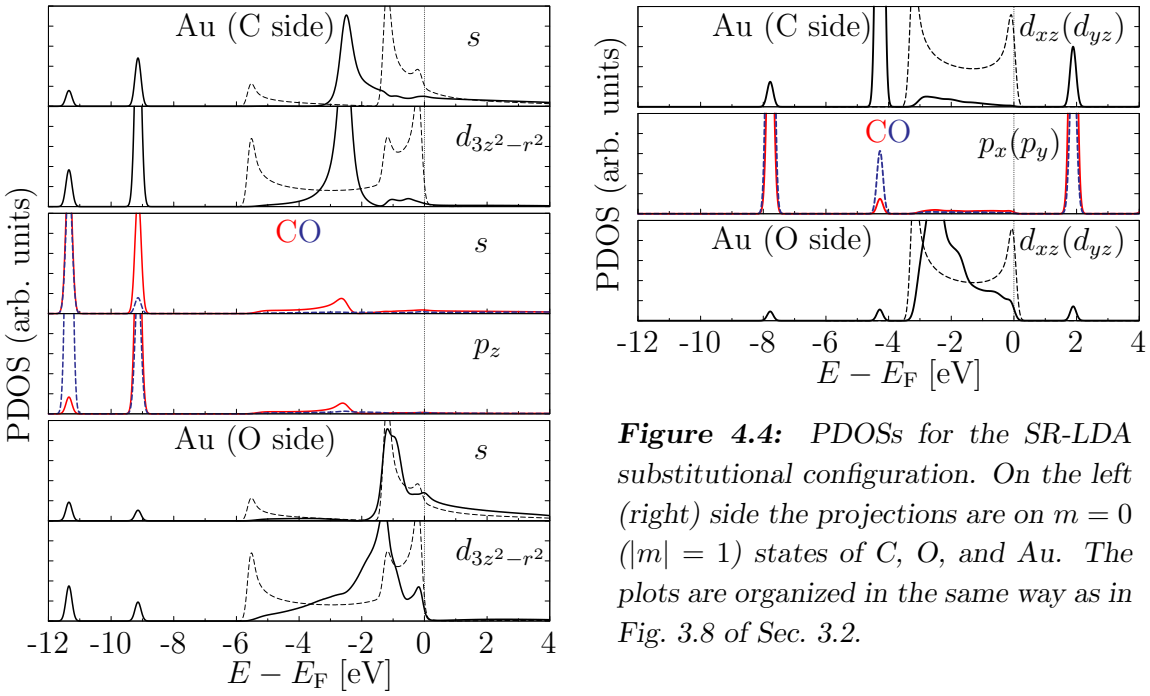

Figure 4.4: *PDOSs for the SR-LDA substitutional configuration. On the left (right) side the projections are on $m = 0$ ($|m| = 1$) states of C, O, and Au. The plots are organized in the same way as in Fig. 3.8 of Sec. 3.2.*

4.2.3 Substitutional CO

The LDA-PDOS for the substitutional configuration corresponding to the energy minimum of the "SUBS" curve in Fig. 4.1 is reported in the left (right) part of Fig. 4.4 for the projections on $m = 0$ ($|m| = 1$) atomic orbitals. As done for Pt chains, in addition to the PDOS projected on C and O orbitals (central panels), we report the PDOS for both the Au atom next to the C (upper panels) and the Au atom next to the O (lower panels).

At large binding energies, the PDOS projected onto $m = 0$ atomic orbitals of C and O (central panel on the left side of Fig. 4.4) are characterized by the 3σ peak (not shown), which is not involved in the interaction, and by the 4σ and $5\sigma_b$ peaks (centered at $-11.3\,\text{eV}$ and at $-9.2\,\text{eV}$, respectively), which are visible at the same energies also in the $m = 0$ PDOS of the Au atom on the C side (see the projections onto s and $d_{3z^2-r^2}$ orbitals in the upper panel). Similar peaks are found also in the $m = 0$ PDOS of the Au atom on the O side, although the peak matching the $5\sigma_b$ state is much weaker. At smaller binding energies, the σ interaction is visible in the PDOS of CO as a more broad density distribution extending across the whole energy range of the $m = 0$ bands of Au (from about $-5.5\,\text{eV}$ to $4.8\,\text{eV}$). It has a small peak in the PDOS of C (red solid curve) which matches a strong resonance at about $-2.6\,\text{eV}$ in the PDOS of the Au atom next to the C atom, while a correspondent resonance for the Au on the O side is absent. Looking at the PDOS for energies equal or higher than E_F, we notice that the donation is not characterized by a dominant peak, unlike

in the bridge and ontop cases, but the density is spread in a much larger range and it stays almost constant up to 4.8 eV. For energies below E_F the shape of PDOS projected onto $m = 0$ states of Au is more similar to the PDOS of the pristine wire (dashed lines) for the Au atom next to O than for the Au next to C; this already suggests that the hybridization between σ states of CO and Au states involves mainly orbitals of the Au atom on the C side.

The interaction of π states can be described by the PDOS projected onto $|m| = 1$ orbitals of C and O (see right side of Fig. 4.4). Besides the 1π and $2\pi^\star$ peaks associated to the molecular orbitals (at about -7.8 eV and 1.9 eV, respectively), we find a broad and weak density feature in the energy range of the $|m| = 1$ bands of Au (i.e. between -2.2 eV and 0.0 eV) plus a small peak at about -4.3 eV signaling the occurrence of backdonation. The $2\pi^\star_b$ bonding state at -4.3 eV matches with a very strong peak in the PDOS of the Au atom on the C side, while at that energy the PDOS of the Au atom next to O has only a very small peak. As a consequence, while the PDOS of the Au next to O is still within the energy range of the $|m| = 1$ bands of the pristine Au chain, the PDOS of the Au next to C has moved almost completely to lower energies to form the $2\pi^\star_b$ state.

In the substitutional configuration, a striking difference between Pt and Au is found: only in Au the $2\pi^\star_b$ peak is present in the $|m| = 1$ PDOS (see PDOS projected on C and O orbitals in Fig. 4.4), while in Pt the PDOS displays only broad features between the original peaks of the molecule (see Fig. 3.8). The resulting large density redistribution in the $|m| = 1$ PDOS of the Au atom in contact with C, not observed in Pt, is expected to have strong consequences on the transmission of $|m| = 1$ states in the Au chain.

4.2.4 Estimate of charge donation and backdonation from the PDOS

In order to have an estimate of the amount of *donation* we can consider the integral (from $-\infty$ to E_F) of the PDOS on the C and O orbitals forming σ states in the molecule (s plus p_x in the bridge and ontop geometries, s plus p_z in the substitutional). Due to the incompleteness of the basis set formed by the atomic orbitals of C and O, this integral gives about 5.88 electrons for the isolated CO molecule (within LDA), instead of 6 electrons, as the number of σ valence electrons in CO. We then chose to estimate the donation as the difference $\Delta\rho_\sigma$ between the PDOS integral computed for the isolated CO and the PDOS integral for CO adsorbed on the chain. The amount of *backdonation* can be estimated in the same way, by integrating the PDOS on the orbitals which form the π states of CO (p_z plus p_y in the bridge and ontop geometries, p_x plus p_y in the substitutional). In the isolated CO the integral gives 3.93 (while the number of π valence electrons is 4 in CO); by subtracting to this value the same integral computed for the adsorbed CO we obtain our backdo-

	Bridge		Ontop		Subst.	
	$\Delta\rho_\sigma$	$\Delta\rho_\pi$	$\Delta\rho_\sigma$	$\Delta\rho_\pi$	$\Delta\rho_\sigma$	$\Delta\rho_\pi$
Pt	0.59	−0.77	0.54	−0.53	0.55	−0.72
Au	0.75	−0.67	0.63	−0.36	0.66	−0.49

Table 4.2: *LDA estimates of σ charge donated from CO to the metal (either Pt or Au), $\Delta\rho_\sigma$, and of π charge back-donated to CO, $\Delta\rho_\pi$, for the three adsorption geometries of CO on Pt and Au chains discussed in Sec. 3.2 and in this section, respectively.*

nation estimate $\Delta\rho_\pi$. Within our notation, a positive number represent a transfer of charge from the molecule to the metal and viceversa for negative numbers, hence the donation/backdonation model is valid here if $\Delta\rho_\sigma > 0$ and $\Delta\rho_\pi < 0$.

In Tab. 4.2 we report $\Delta\rho_\sigma$ and $\Delta\rho_\pi$ for the three adsorption sites, bridge, ontop and substitutional. Since $\Delta\rho_\sigma$ is always positive and $\Delta\rho_\pi$ always negative, we conclude that both donation and backdonation occur at the same time, hence the Blyholder picture of CO adsorption is valid both in Pt and in Au. Among the three adsorption sites the smallest backdonation is present in the ontop configuration (both in Pt and in Au), in agreement with the smaller E_{chem} and smaller CO bond elongations of that geometry.

It is generally difficult to estimate the charge transfer in the case of covalent bonds or strong chemisorption processes. The charge transfer estimation from differences of charge densities, as that reported in Ref. 93 for the ontop CO on the Pt chain, shows that there is a very small net transfer between CO and the chain. We believe that such a tiny transfer cannot be estimated in a reliable way through the integrals of the PDOS, since there might be large overlaps between CO molecular orbitals and states of the chain (especially for the 5σ orbital, which has an extended charge lobe pointing from C towards the chain).

4.3 Ballistic transmission of the tipless chains

In this section we report the results of ballistic transport calculations for the three geometries described in the previous section and make a connection between their electronic structure and transmission. We will first discuss together the transmissions of the bridge and ontop geometries, which have the same symmetry, while the transmission of the substitutional configuration, which exhibits a different symmetry, will be discussed later.

According to our LDA calculations, the Au monatomic chain at equilibrium distance ($d_{\text{chain}} = 2.51\,\text{Å}$) has a d band edge very close to the Fermi level, which increases considerably the number of conductance channels (leading to a theoretical conductance of $3\,G_0$ in the pristine chain) and moreover is responsible for a magnetic instability. Both these features have never been observed in nanocontact experiments. The non-magnetic Au chain with $1\,G_0$ conductance can be recovered by including atomic tips in transport calculations (see Sec. 5.2), or by considering an interatomic Au-Au spacing well above the theoretical equilibrium value [101] (because the width of d bands decreases with strain, see also next section). Another way to remove this problem is to include electronic correlations effects beyond LDA or GGA, for instance through the DFT+U method (the results of its application to our systems will be discussed in Sec. 4.5). Because of this, in the present section we will focus on the qualitative features induced by CO on the transmission function, rather than on the precise ballistic conductance values given by this tipless model, which cannot represent the situations typically realized in STM or MCBJ experiments.

4.3.1 Bridge and ontop geometries

The two plots in Fig. 4.5 show the transmission function (total and separated in the contributions from even and odd states) as a function of energy for the bridge and ontop geometries. The same general conclusions drawn in Pt chains hold here as well: the molecule causes a partial reflection of the electrons propagating along the chain and the reflection is stronger for electronic states belonging to the more localized d bands, while the broader s-$d_{3z^2-r^2}$ states are generally transmitted better, except for a few energy regions where the transmission function displays some dips.

In the *even* contribution to the transmission (T_{even}), in both geometries the transmission of the only channel present below $-3.3\,\text{eV}$ ($m = 0$, mostly $d_{3z^2-r^2}$) is reduced for energies close to the lower band edge and in correspondence of a narrow dip. This dip is at $-3.9\,\text{eV}$ in the bridge geometry and at $-3.5\,\text{eV}$ in the ontop and matches the energy of the previously noticed s-$d_{3z^2-r^2}$-$d_{x^2-y^2}$ peak in the corresponding PDOS (Fig. 4.2 and Fig. 4.3, respectively). In this energy region the transmission is higher

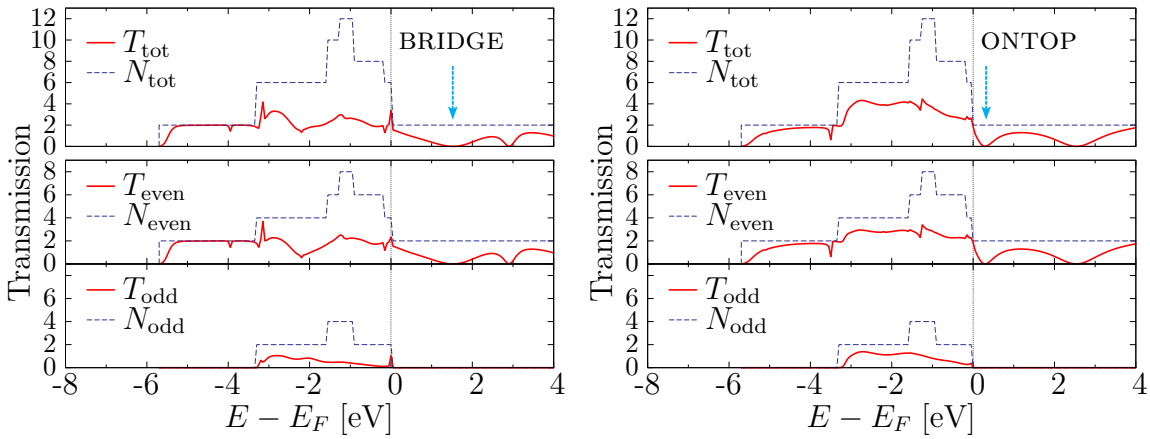

Figure 4.5: *Total (upper panel) and symmetry-separated (lower panels) SR-LDA transmission (solid red lines) and number of channels (dashed blue lines) for a tipless Au monatomic wire with CO adsorbed at the bridge (left) or ontop (right).*

when CO is at the bridge, and, indeed, the $d_{3z^2-r^2}$ PDOS in the bridge geometry is less perturbed than in the ontop geometry, except for the lower band edge region. On the contrary, at higher energies, in the whole energy range of the $|m| = 1$ band ($-3.3 < E < 0.0\,\text{eV}$) the bridge transmission is lower than the ontop transmission, especially for energies around $-2.2\,\text{eV}$. The wide depression centered at that point in the bridge transmission can be associated with the broader peak among the $2\pi^\star_{\text{e,b}}$ series of peaks visible in the p_z PDOS of the bridge geometry (Fig. 4.2), which is more coupled to s and $d_{3z^2-r^2}$ states and is absent when CO is ontop because of different orbital overlaps (as discussed in the previous section). The $|m| = 2$ even states (available between $-1.7\,\text{eV}$ and $-0.9\,\text{eV}$) are completely blocked by the presence of CO in both geometries. In the previous section we have seen that, both in the bridge and in the ontop geometry, the $d_{x^2-y^2}$ density of states of the Au atoms in contact with CO is completely detuned from the density of the narrow $|m| = 2$ band of the chain, because of a depletion of density from the $|m| = 2$ band range to different energies corresponding to hybridization peaks. Above the Fermi level, and up to at least 4 eV, only one spin-degenerate $m = 0$ channel (mostly s) is available for transmission. In this energy region the electronic transport is characterized by the presence of wide dips leading to a decrease in the transmission and, in some points, to the complete suppression of the transport. Both the bridge and ontop transmission curves have these dips. Their position depends on the adsorption site and can be matched with that of the $5\sigma_{\text{a}}$ peak (at lower energy) and that of the $2\pi^\star_{\text{e,b}}$ peak (at higher energies) in the PDOS of the bridge and ontop geometries.

The transmission of the *odd* channels, T_{odd}, shows a marked difference from what observed in Pt chains (see Fig. 3.10, page 88): although the $|m| = 2$ odd state is almost completely blocked by CO both in Pt and Au, the transmission of the $|m| = 1$

odd state is quite reduced in Au, while in Pt, except for a few narrow dips, it is close to the ideal value everywhere. Moreover, while in Pt the bridge and ontop T_{odd} are quite similar, in Au the bridge T_{odd} is visibly lower than the ontop T_{odd}. Finally, we notice that the reduction of the total transmission, $T_{\mathrm{tot}} = T_{\mathrm{odd}} + T_{\mathrm{even}}$, due to the interaction with CO is overall more marked in Au, especially for the bridge geometry and in those energy regions where the number of d channels is larger.

The above discussed $5\sigma_{\mathrm{a}}$ transmission dip, pointed by the arrows in Fig. 4.5, might have important effects in the ontop conductance because it falls close to the Fermi level in that geometry (just 0.2 eV above E_{F}), while in the bridge geometry it is located much higher in energy (at about 1.6 eV). Although in these simplified tipless geometries the presence of that dip has no big effect on the theoretical ontop conductance (because of the presence of a sizeable contribution from d channels, as mentioned before), it might have an impact if the modeling of the geometry is improved (for instance with the introduction of strain or tips, discussed later in Sec. 4.4 and Sec. 5.2, respectively), or when electron correlations are included in the electronic structure (see Sec. 2.7), since the energy position and transmission properties of d channels are quite sensitive to these factors.

4.3.2 Substitutional geometry

Kiguchi and coworkers [26] have argued that the slight increase in the conductance seen at small conductances while stretching the contact prior to breaking might be due to a geometrical rearrangement of the absorbed CO, which should pass from a perpendicular configuration to a longitudinal one (much in the same way as H_2 does in Pt nanocontacts). We will show that this cannot be the case, since the substitutional CO causes a much bigger reduction of the transmission over the whole energy range.

In Fig. 4.6, we report separately the $m = 0$ and $|m| = 1$ contributions to the LDA transmission and their sum for the substitutional configuration at $d_{\text{Au-Au}} = 5.16$ Å. As seen in Pt, a longitudinal CO cannot support the transmission of $|m| = 2$ channels; the same is valid also in Au. The $m = 0$ states are rather badly transmitted also in the Au chain, since they suffer from a strong reflection at the weak O-Au bond, and only $|m| = 1$ states are able to partially propagate across the barrier offered by CO, via a hybridization with the π states of the molecule. Comparing Fig. 4.6 with Fig. 3.12, we notice that the $|m| = 1$ channels in Au are restricted to a smaller energy range and their transmission is visibly reduced with respect to Pt. Moreover, while in Pt the $|m| = 1$ transmission ($T_{m=1}$) has a maximum at the Fermi energy, in Au the maximum is positioned well below E_{F} (at about -2.6 eV) and $T_{m=1}$ is much smaller at all other energies (below 0.2 per spin), resulting in a much lower conductance.

In Au, excluding the energies of the dips, where the T_{tot} goes to zero, the bridge

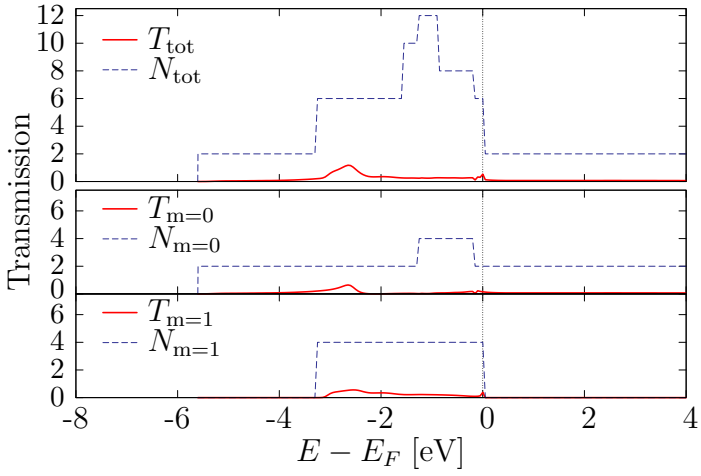

Figure 4.6: *Total (upper panel) and symmetry-separated (lower panels) SR-LDA transmission (solid red lines) and number of channels (dashed blue lines) for a tipless monatomic wire with a substitutional CO between two Au atoms separated by* $d_{Au\text{-}Au} = 5.16\,\text{Å}$ *(see arrow in Fig. 4.1).*

geometry has always a much larger total transmission than the substitutional geometry. Since the dips in the bridge transmission are distant from $E_{\rm F}$, the conductance cannot increase when CO gets tilted from an upright bridge position towards a longitudinal position for a substitutional inclusion in the chain. Effects associated to strain or addition of self-interaction error (SIE) corrections, that will be discussed in the next sections, move the d channels lower in energy and leave at $E_{\rm F}$ only the s-like channel, which is transmitted much better in the bridge configuration than in the substitutional. This conclusion would not be modified either by the addition of tips either, since, as we will see in the next chapter, the surface/wire interfaces introduce an additional strong scattering of d states, but a much smaller scattering of s states.

4.4 Effects of the strain on the energetics and transmission

In this section, we study the effects of strain by considering chains with tunable spacing, $d_{\rm chain}$. We assume that the strain is homogeneously distributed along the chain. This may not be the case for short chains attached to bulk tips, but this simple treatment is already able to catch very important features, that will be later contrasted to the less idealized case of a fully-relaxed short chain attached to bulk surfaces or tips (see next chapter). Actually the infinite wire model is relevant to the problem of atomic-sized contacts because the gross value of the nanocontact conductance is limited by the conductance of its narrowest part (an atom or a monatomic chain) and hence the modifications of the atomistic configuration are likely to have a bigger impact on the transport properties when they are localized in this region, rather than in other places (as in the tips).

4.4.1 Strain dependence of the energetics: bridge and ontop geometries

We start analysing how much the chemisorption energy and the bonding distances of CO on Au chains are influenced by the strain. This can help to understand if the adsorption site preference may vary during different stages in the pulling process of the monatomic chain. As noted in Sec. 4.1, a substitutional CO can only be hosted between two very largely spaced Au atoms, hence we consider here CO in the bridge and ontop positions only.

We optimized C and O positions along x while keeping all Au atoms fixed on the z axis and spaced by d_{chain}, which has been varied between 2.5 Å and 2.9 Å to simulate a wire at different levels of strain. From the total energy of the relaxed structure, $E_{\text{CO+wire}}$, we computed the chemisorption energy E_{chem} using Eq. (3.1), where now the reference energy E_{wire} is the energy of an isolated Au chain at an interatomic spacing equal to d_{chain}. In Tab. 4.3 the optimized distances and chemisoption energies are reported for a chosen set of d_{chain}values. The first two rows ($d_{\text{chain}} = 2.50$ Å and $d_{\text{chain}} = 2.60$ Å) correspond to Au-Au distances around the equilibrium lattice spacings obtained for the pristine wire with LDA (2.51 Å) and GGA (2.61 Å), respectively, while the third ($d_{\text{chain}} = 2.70$ Å) and the fourth ($d_{\text{chain}} = 2.90$ Å) describe a wire under moderate strain or near rupture, respectively.

The chemisorption energies reported in the table give evidence that the bridge site is preferred in stretched chains too. An increase of strain results in larger binding energies for both ontop and bridge geometries, but the site preference ordering is reinforced when going to larger values of d_{chain}. For instance, around the equilibrium value of d_{chain}, the bridge site E_{chem} is about 1.43 eV (1.22 eV) higher than the ontop site E_{chem} within LDA (GGA), while it is 1.65 eV (1.31 eV) higher when $d_{\text{chain}} = 2.9$ Å. In the bridge geometry the increase of E_{chem} with strain can be ascribed to the adjustment of the Au-C-Au angle towards the optimal value. The angle depends

	Ontop			Bridge			
d_{chain}	$d_{\text{Au-C}}$	$d_{\text{C-O}}$	E_{chem}	$d_{\text{C-axis}}$	$d_{\text{Au-C}}$	$d_{\text{C-O}}$	E_{chem}
2.50	1.89(1.96)	1.14(1.14)	-0.99(-0.36)	1.50(1.55)	1.95(1.99)	1.16(1.16)	-2.42(-1.53)
2.60	1.89(1.96)	1.14(1.14)	-1.14(-0.50)	1.45(1.51)	1.95(1.99)	1.16(1.17)	-2.64(-1.72)
2.70	1.90(1.96)	1.14(1.14)	-1.22(-0.58)	1.41(1.47)	1.95(2.00)	1.16(1.17)	-2.78(-1.83)
2.90	1.90(1.97)	1.13(1.14)	-1.26(-0.62)	1.31(1.38)	1.95(2.00)	1.16(1.17)	-2.91(-1.93)

Table 4.3: *Relaxed distances (in Å) and chemisorption energies (in eV) of CO adsorbed ontop or at the bridge of an infinite and straight Au chain computed in the LDA (GGA values in parenthesis) for selected values of the inter-atomic spacing in the chain (d_{chain}).*

on the Au-C bond length, $d_{\text{Au-C}}$, and on the distance between the two Au atoms in contact with CO, $d_{\text{Au-Au}}$; in Sec. 4.1, we have seen that the optimal bond angle is reached at $d_{\text{Au-Au}}$ values larger than the equilibrium d_{chain} (namely, at $d_{\text{Au-Au}} \simeq 2.8\,\text{Å}$ in LDA and at $d_{\text{Au-Au}} \simeq 2.9\,\text{Å}$ in GGA, as shown by Fig. 4.1). As a consequence, since $d_{\text{Au-C}}$ has a very slight dependence on d_{chain} (for instance, when d_{chain} is increased from 2.50 Å to 2.90 Å, changes in $d_{\text{Au-C}}$ are well below 1%), when the chain is strained CO moves towards the wire axis (see $d_{\text{C-axis}}$, the distance between the C atom and the z axis) and correspondingly the bond angle increases towards the optimal value.

If the chain is kept straight, also the ontop E_{chem} increases with strain, but at low/moderate strains there is a pronounced tendency for the Au atom below the molecule to move towards the C atom (visible from the residual force acting on the Au atom after having optimized the positions of C and O). We then repeated the structural relaxations (within GGA only) optimizing also the x coordinate of that Au atom and we have found that it gets displaced by 0.95 Å with respect to the wire axis when starting from a configuration with $d_{\text{chain}} = 2.60\,\text{Å}$, but only by less than 0.27 Å in a strained configuration (at $d_{\text{chain}} = 2.90\,\text{Å}$, in fair agreement with Ref. 49). Using $E_{\text{CO+wire}}$ from these optimized structures to recompute the chemisorption energies (while E_{wire} is still that from the isolated straight chain), we got $E_{\text{chem}} = -0.93\,\text{eV}$ at $d_{\text{chain}} = 2.50$ and $E_{\text{chem}} = -0.72\,\text{eV}$ at $d_{\text{chain}} = 2.60$ (respectively, 0.57 eV and 0.22 eV more stable than CO on a straight wire), while E_{chem} is almost stationary between $-0.65\,\text{eV}$ and $-0.64\,\text{eV}$ for $2.70 \leqslant d_{\text{chain}} \leqslant 2.90$. Actually, taking into account this additional degree of freedom, the variation of the ontop E_{chem} with strain is opposite with respect to that of the bridge E_{chem}. We can argue that at lower strains the chemisorption energy is larger because the structure is more close to the optimized geometry of the neutral Au_3CO cluster, where the gold atoms form a nearly equilateral triangle with Au-Au distances of about 2.74 Å [102].

At this point it is interesting to compare our GGA data for CO adsorbed on 1D-chains with recent DFT calculations of CO adsorbed on Au surfaces [103]. Although the surface calculations in Ref. 103 are at a much higher CO coverage and adopt a slightly different exchange-correlation functional (PW91 instead of PBE), the following conclusion can be drawn from the comparison:[2] (i) distances and chemisorption energies for CO ontop of step edge atoms in the Au(211) surface are not much different from those in the monatomic chain (surface: $d_{\text{Au-C}} = 1.99\,\text{Å}$, $E_{\text{chem}} = -0.54\,\text{eV}$; chain: $d_{\text{Au-C}} = 1.97\,\text{Å}$, $E_{\text{chem}} = -0.62\,\text{eV}$); (ii) for CO adsorbed at the bridge the differences are larger, especially in E_{chem} (surface: $d_{\text{C-surf}} = 1.46\,\text{Å}$, $E_{\text{chem}} = -0.65$; chain: $d_{\text{C-axis}} = 1.38\,\text{Å}$, $E_{\text{chem}} = -1.93$) (iii) larger chemisorption energies in the chain are attributable to different coordination numbers of Au atoms, much smaller

[2]The theoretical nearest neighbour distance in bulk Au is around 2.94 Å, so that we should compare the (211) surface data with the data for the chain at $d_{\text{chain}} = 2.90\,\text{Å}$.

in the chain, since the comparative study of the different Au surfaces shows that a decrease in the local coordination of surface atoms leads to higher binding energies of CO [10, 16, 103]; (iv) the increase in E_{chem} with respect to the surface case is much higher for CO at the bridge than for CO ontop, and hence the preference for the bridge site in the monatomic chain is much more marked than in the stepped surface (where the two sites are separated by only 0.11 eV); (v) the C-O bond elongation in the surface case ($d_{\text{C-O}} = 1.17$ Å for CO ontop and $d_{\text{C-O}} = 1.15$ Å for CO at the bridge) is comparable to the values obtained for the 1D chain.

4.4.2 Strain dependence of the transmission

The band structure of the isolated infinite Au chain is subject to some changes upon stretching, namely: (i) the bandwidth is progressively reduced as the Au-Au spacing increases; (ii) d bands edges move in energy with respect to the Fermi level and, as a consequence, the number of electronic channels available at a certain scattering energy can vary with strain (in particular, the number of open conductance channels changes as a function of the bond length, see Ref. 56). For instance, the d channels move below the Fermi level already at moderate strains ($d_{\mathrm{chain}} = 2.70$ Å), but going to higher strains does not change the number of channels anymore (only one s band is present). Therefore in the ideal (defectless) monatomic chain alone, the tipless conductance does not change anymore with strain above a critical d_{chain}.

We computed the total transmission as a function of energy for straight Au chains at three different values of d_{chain} and CO ontop or at bridge site, using the optimized distances reported in Tab. 4.3. The results are shown in Fig. 4.7 on the left (right) side for the bridge (ontop) geometry: for each geometry, the strain increases going from top to bottom. The first panel at the top corresponds to the equilibrium Au-Au spacing, which has been discussed in Sec. 4.3 and is reported here again for comparison. In the bridge geometry, a moderate strain ($d_{\mathrm{chain}} = 2.70$ Å) introduces many dips in the transmission of $m = 0$ states below -2.3 eV and enhances the depression due to $2\pi^{\star}_{\mathrm{e,b}}$ states, which is still centered at about -2.1 eV. Around the Fermi energy the d band edge resonance is removed and the transmission looks smoother now. Above E_{F}, the $5\sigma_{\mathrm{a}}$ dip moves at higher energies (from 1.6 eV to 2.2 eV) and merges with the $2\pi^{\star}_{\mathrm{e,b}}$ dip, which instead moves at slightly lower energies, forming a wide region where the transmission is strongly suppressed. At higher strains ($d_{\mathrm{chain}} = 2.90$ Å) the transmission at energies below -0.6 eV degrades further, while above that energy it actually increases. There is still a depression at energies above 2 eV, but the $5\sigma_{\mathrm{a}}$ and $2\pi^{\star}_{\mathrm{e,b}}$ dips have disappeared and so the transmission does not vanish anymore above E_{F}. In the ontop geometry a moderate strain does not produce such a reduction of the transmission at energies below -2.3 eV, but instead it does in the energy range between -1.2 eV and -0.1 eV. This tendency is confirmed also at higher strains, since

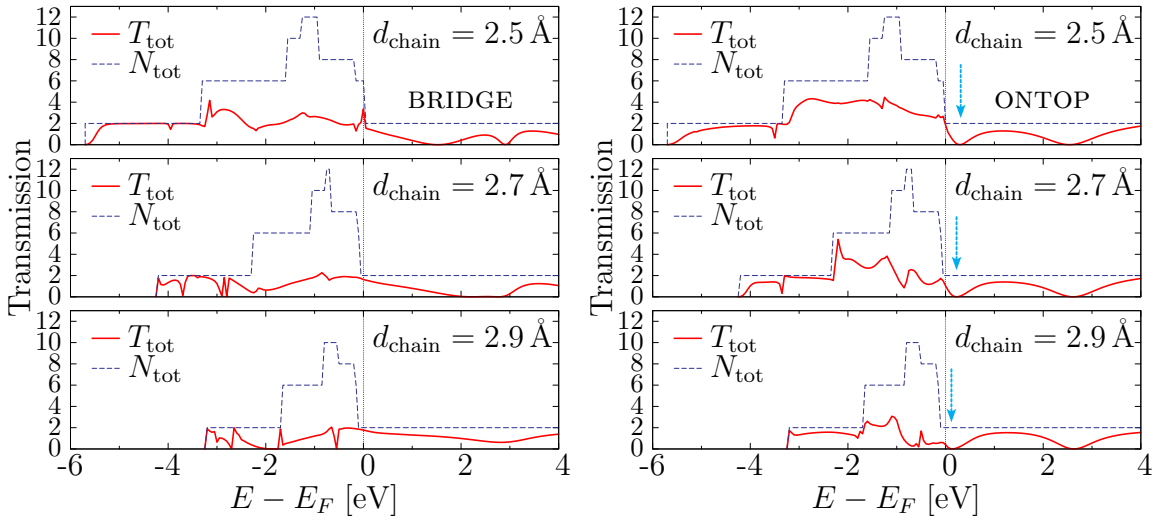

Figure 4.7: *Total SR transmission for a tipless Au monatomic wire with CO adsorbed at the bridge (left) or ontop (right). The interatomic spacing of Au atoms, d_{chain}, and the GGA (LDA) $E_{\rm chem}$ are reported on each plot.*

the reduction of the transmission is more marked in that energy range. Above $E_{\rm F}$ the presence of dips persists even at high strains. The $2\pi^{\star}_{\rm e,b}$ dip moves a little higher in energy while the $5\sigma_{\rm a}$ dip gradually approaches $E_{\rm F}$, causing a progressive reduction of the conductance when increasing the strain.

If we now compare the evolution of the conductance with strain, we notice a very different behaviour in the two geometries. In fact, once the d channels have been removed from the Fermi level (i.e., for $d_{\rm chain} \geqslant 2.7$ Å), if CO is ontop the conductance is subject to a drastic reduction caused by the dip associated to $5\sigma_a$ states moving towards $E_{\rm F}$ as the chain is stretched (see arrows in Fig. 4.7), while if CO is at the bridge there are no dips close to $E_{\rm F}$ and the conductance increases slightly with strain. This observation, together with the energetics discussed in Sec. 4.1 and the conductance value of the substitutional geometry reported in Sec. 4.3, supports our hypothesis that the fractional conductance feature seen by Kiguchi et al. [26] in their experiment can be assigned to a monatomic Au chain with a CO molecule at the bridge, and that the increase of the conductance upon stretching has probably to be attributed to the stretching of the chain rather than to a tilting of the molecule. However, the conductance values obtained for the bridge geometry are slightly too high to match exactly the fractional peak seen in the conductance histograms. In order to find a more realistic estimate of the conductance we need to model the effects of tips in our ballistic transport calculations, but this point will be addressed in Chap. 5.

4.5 Transmission properties within DFT+U

In the present section, the LDA+U method described in Sec. 2.7 is applied to the electronic structure of the monatomic Au chain in order to study the effects of the Hubbard U on the electron transport properties of the pristine chain and of the chain with CO adsorbed on it. Since the $5d$ wavefunctions of Au suffer from a large SIE because of their strong localization in the 1D chain, we apply the Hubbard U correction to the d manifold and we compute the local occupation using local projectors derived from the atomic d orbitals. We will show that the main effect of the Hubbard potential is to push down in energy the $|m| = 2$ and $|m| = 1$ bands, which are, respectively, completely-filled and almost-filled in the (plain) LDA (or GGA) electronic band structure of the Au chain at the equilibrium spacing. For instance, the upper $|m| = 1$ band edge, which is slightly above E_F in LDA is pushed below E_F by using a large enough value of U. This has two main effects: (i) the magnetic instability of the Au chain at equilibrium spacing is suppressed and a non-magnetic ground state is obtained already at small values of U; and (ii) the spurious d conductance channels with $|m| = 1$ are removed from E_F, thus restoring a more realistic single s-like channel conductance.

Band structure modifications similar to those observed when computing the overlap with full atomic wavefunctions (which have a non-limited support) can be obtained by computing the overlap with the PP projector functions (which are instead localized inside the atomic-spheres), although a larger value of U is required to achieve comparable effects. The use of PP projections allows an easier extension of the complex

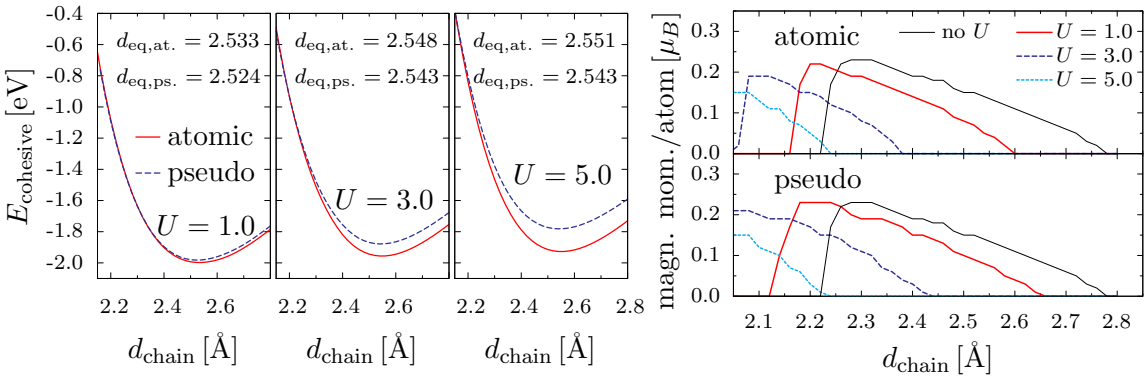

Figure 4.8: *Binding energy curve (left side) and magnetic moment per atom (right side) of the pristine Au chain within LDA+U for a range of d_{chain} around the equilibrium value (indicated in the insets, in Å). The two methods of computing the local occupations ("atomic" and "pseudo", see text) are compared for several values of U (given in eV).*

band structure (CBS) and transmission calculations, hence it will be adopted in order to compute the effects of the Hubbard potential on the ballistic transport properties. In this section we start by discussing how the structural, magnetic, and electronic structure properties of the infinite Au chain are modified by the inclusion of the Hubbard U. We then show that the CBS at real k_z actually reproduces the band structure of the infinite chain computed with PBCs along z. Then we will compare again the transmission curves for the bridge and ontop geometries at the equilibrium Au-Au spacing for one value of U (the smallest value that removes the magnetic instability of the pristine chain). Finally, we will plot the ballistic conductance of these two geometries for several values of U and compare it with the plain LDA conductance, thus testing its reliability in this critical case.

4.5.1 Band structure and magnetization of Au chains within LDA+U

In Fig. 4.8 we report the ground state total energy (left side) and magnetic moment per atom (right side) of the pristine infinite Au chain as a function of the chain spacing d_{chain} in a range of values around the energy minimum and we study how these properties change when increasing the Hubbard U (here we show the results for three values, $U = 1.0\,\text{eV}$, $U = 3.0\,\text{eV}$, and $U = 5.0\,\text{eV}$). The "atomic" and "pseudo" labels in the plots indicate the two different methods of calculating the local occupations, either from the overlap with the atomic wavefunctions or with the PP projectors. The zero of energy has been chosen as the total energy of the isolated Au atom computed consistently (i.e., with the same U and projectors), hence the plots show the cohesive energy of the chain as U is increased. The equilibrium spacing of the Au chain slightly grows from the plain LDA value ($d_{\text{Au-Au}} = 2.51\,\text{Å}$), until it saturates at about 2.55 Å in the "atomic" method and at about 2.54 Å in the "pseudo" method for $U \geqslant 3.0$. The changes in the cohesive energy are instead sizably different in the two methods: in both cases the cohesive energy decreases at larger values of U, but much more rapidly in the "pseudo" method.

The total ground state magnetic moment per atom has been computed for spacings $1.9\,\text{Å} \leqslant d_{\text{chain}} \leqslant 2.8\,\text{Å}$ within LDA (black line) and within LDA+U using the atomic occupations (upper panel) or the pseudo occupations (lower panel) for the same three values of U. The plain LDA result shows that for $2.22\,\text{Å} \leqslant d_{\text{chain}} \leqslant 2.78\,\text{Å}$ the ground state has a finite magnetization. The maximum value of the magnetic moment per atom ($m_{\text{max}} = 0.23\,\mu_{\text{B}}$) is reached at $d_{\text{chain}} = 2.3\,\text{Å}$, while at the equilibrium distance it is $m_{\text{eq}} = 0.15\,\mu_{\text{B}}$. The main effect of the Hubbard potential on the magnetization of the chain is to shift the magnetic instability region toward lower Au-Au spacings. Both the width of the magnetic region and the maximum magnetic moment are reduced by increasing the value of U and these two effects are more pronounced in the atomic method. Notwithstanding the quantitative difference, both methods give

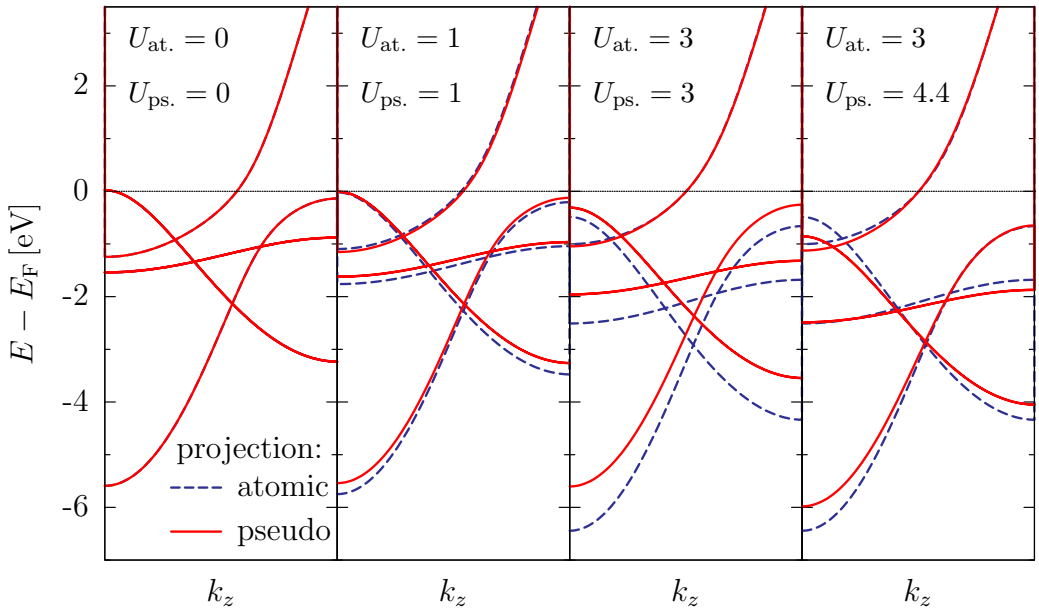

Figure 4.9: *Electronic band structure of a monatomic Au chain at the LDA equilibrium spacing for different values of the U parameter (in eV). In the leftmost panel the band structure without U is reported for comparison, while in the rightmost panel two different values of U have been used for the two different projection methods.*

the same qualitative picture, namely the spurious magnetic instability of the chain at its equilibrium spacing can be completely suppressed for large enough values of U.

The magnetic instability depends on the large electronic density of states at E_{F}, due to the presence of the $|m| = 1$ band edge, and both methods are effective in removing this band edge from E_{F}. In Fig. 4.9 we report the electronic band structure of a Au chain (at the LDA equilibrium distance) computed without (leftmost plot) or with the Hubbard correction. By looking at the position of d bands for increasing values of U (plots from the left to the right) we can see that the qualitative effect of the Hubbard correction is the same for both ways of computing the local occupations: filled d bands are pushed down in energy. For small values of U (around 1.0 eV), the changes in the band structure are quite small: the flat $|m| = 2$ bands shift down in energy and the lower $|m| = 1$ band edge slightly moves to lower energies, but the upper $|m| = 1$ band edge at Γ is still pinned at E_{F}. For larger values of U (for instance, $U \simeq 3.0$ eV), instead, the three bands with larger weights onto the d orbitals of Au are visibly shifted down in energy and the upper $|m| = 1$ band edge goes below E_{F}. The downshift of the d bands is stronger when using the "atomic" method, but a comparable downward shift can be obtained also with the "pseudo" method for a larger value of U (see rightmost plot in the figure). This behaviour

can be easily understood by looking at the Hubbard correction to the KS potential in Eq. (2.107): if a KS orbital has a perfect overlap with one of the wavefunctions used to compute the occupations and it is fully occupied, that orbital gets pushed down in energy by $-U/2$ (substitute $n^{I\sigma}_{m'm} = 1$ in that expression). In a monatomic chain the electronic states bear a strong resemblance to the corresponding atomic wavefunctions, especially for states belonging to flat bands (e.g. $|m| = 2$ bands), or equivalently with low hybridization. Hence, d-like electronic states of the chain will have a perfect overlap (i.e., close to one) with the full atomic wavefunctions used for the projections in the "atomic" method, but a smaller overlap with the truncated projectors in the "pseudo" method (since the charge outside the atomic sphere is not included): consequently, smaller energy corrections will arise in the latter case (since $n^{I\sigma}_{m'm} < 1$ leads to a potential energy gain smaller than $U/2$).

Besides downshifting the position of the center of d bands, the Hubbard potential introduces a broadening effect of their bandwidths. Hence it is not possible to obtain bands which exactly match each other with the two different methods, even if using two different values of U. However, both methods remove the $|m| = 1$ band edge from E_{F} already at U as small as 3 eV and a single channel (of s character) is left at the Fermi level. This is expected to have a big effect in the estimated conductance of Au chains, either clean or with an adsorbed impurity, at spacings around the equilibrium value.

4.5.2 Complex band structures of Au chains within LDA+U

In order to compute the ballistic conductance we must be able to calculate the complex band structure with the same accuracy of the self consistent electronic structure calculation. We test the method for the monatomic Au chain with $U = 3.0\,\mathrm{eV}$ and compare the bands at real k_z of the CBS obtained by solving Eq. (2.92) in Sec. 2.6 with the bands obtained by diagonalizing the $\mathbf{k}$-dependent Hamiltonian. From the plot in Fig. 4.10 we see that, on the energy scale used in the figure, the two band structures are undistinguishable. The only electronic band, of mainly s-character, which still crosses the Fermi level gives a single (spin-degenerate) conductance channel in the ballistic transport calculation.

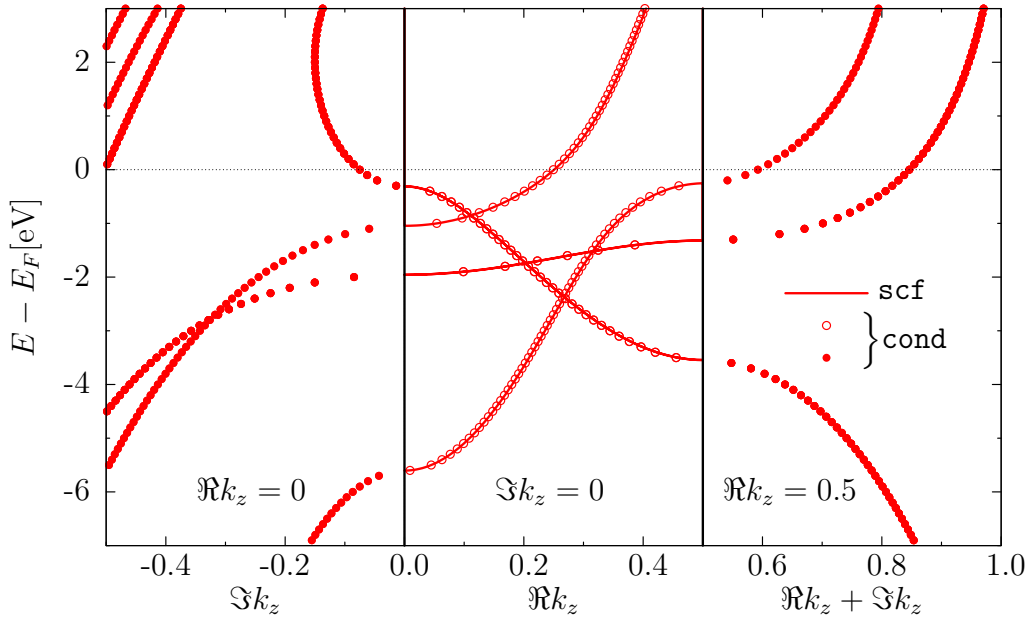

Figure 4.10: *Complex band structure of the monatomic Au chain within LDA+U (using $U = 3\,eV$) computed with the ballistic transport code* `PWcond` *(red circles and points). Eigenvalues at real k_z (red circles) match perfectly with bands computed with the electronic structure code* `PWscf` *(solid red lines).*

4.5.3 Comparison of bridge and ontop transmission within LDA+U

In this part we present the LDA+U ballistic transport properties of the monatomic Au chain with CO adsorbed at the bridge or ontop. We first show how the transmission function changes in the two geometries at a selected value of U, and then we study how the tipless conductance changes when increasing the Hubbard U. The Hubbard potential is applied to the d electrons of all the Au atoms in the cell and the occupations are calculated with the "pseudo" method. For the bridge (ontop) adsorption geometry, we considered a supercell with a single CO and a Au chain of 18 (17) atoms at the equilibrium spacing. As in the plain LDA transmission calculations, the CBS is computed using the leftmost region of the supercell, which has been chosen large enough so that the resulting CBS matches that of the pristine wire (Fig. 4.10) within a few tens of a meV.

The ballistic transmission and the number of channels as a function of the scattering energy are reported in Fig. 4.11 for the two adsorption geometries. The results obtained with $U = 3.0\,eV$ (red lines) are compared with the plain LDA results. The number of channels available at each energy changes according to the energy shifts induced by U in the band structure of the Au chain. This can be seen by comparing

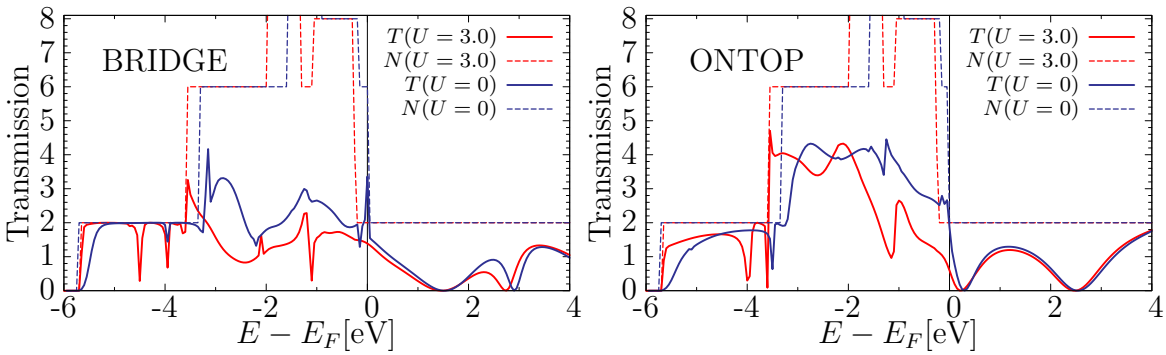

Figure 4.11: *Transmission (solid red lines) and number of channels (dashed red lines) for the bridge and ontop geometries (left and right hand side, respectively) within LDA+U ($U = 3.0\,eV$). The transmission and the number of channels computed at $U = 0$ are reported again for comparison (solid and dashed blues lines, respectively).*

the blue and red dashed lines in any of the two plots of Fig. 4.11: the major changes in the number of channels take place at energies between $-3.5\,\text{eV}$ and the Fermi level. The range of energies where $|m| = 1$ and $|m| = 2$ channels are available is shifted downwards of about $0.2 \div 0.4\,\text{eV}$. At the Fermi energy the number of channels undergoes a big reduction (from 3 to 1 spin-degenerate channels), since the $|m| = 1$ band edges have moved to lower energies and a single s channel is left. The transmission of the bridge geometry around E_F is smoother in the LDA+U case because the resonance associated to the d band edge disappears, resulting in a lower conductance value $G \simeq 0.7\,G_0$. In the ontop geometry the removal of the d contribution to the transmission around E_F leads to a lowering of the conductance as well (down to about to $G \simeq 0.3\,G_0$), essentially for two reason: (i) because of the lower number of channels and (ii) because the $5\sigma_\text{a}$ dip is shifted down by about 0.1 eV towards E_F. Above the Fermi energy the transmission is due to s type electrons, which are not directly influenced by the Hubbard potential; however, since the d bands have been displaced because of the Hubbard correction, some of the states involved in the chemisorption process can move from their original energy. Besides the above mentioned $5\sigma_\text{a}$ resonance in the ontop geometry, this is clearly visible also for the $2\pi^\star_\text{e,b}$ resonance in the bridge geometry which moves to lower energies (from 2.9 eV to about 2.7 eV). Below E_F, the biggest changes in the transmission curves are within the energy range between $-3.5\,\text{eV}$ and $0.0\,\text{eV}$. In that range, the transmission of the bridge geometry is generally smaller within LDA+U, apart for a small range between $-3.6\,\text{eV}$ and $-3.3\,\text{eV}$ where more channels are available. In the ontop case the biggest reduction of the transmission is limited in the energy range between $-2.0\,\text{eV}$ and $0.0\,\text{eV}$, while at lower energies the transmissions are comparable. Since the $|m| = 1$ channels are present also at energies down to $-3.6\,\text{eV}$ within LDA+U, there is a actually a big

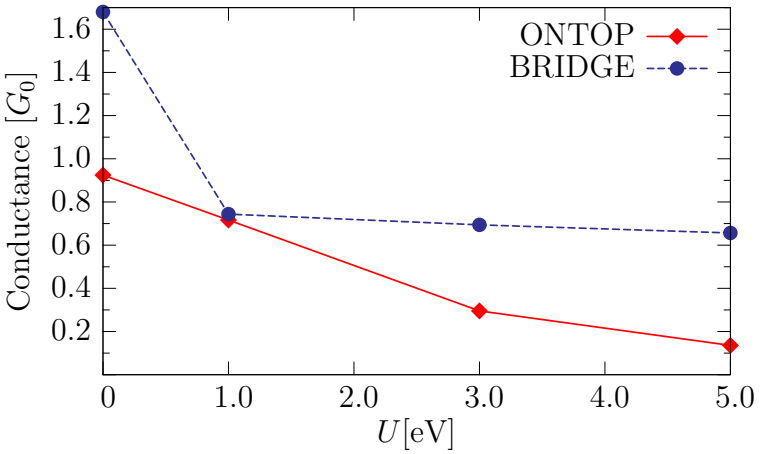

Figure 4.12: *Ballistic conductance for the bridge geometry (blue points) and for the ontop geometry (red diamonds) obtained for a selected set of U values.*

increase in the transmission between $-3.6\,\mathrm{eV}$ and $-3.2\,\mathrm{eV}$.

In Fig. 4.12, we plot the ballistic conductance of the bridge and ontop configurations computed for selected values of the Hubbard parameter between $U = 0$, corresponding to the plain LDA result, up to $U = 5$. At small values of U the conductance decreases with U more rapidly since the contribution of d channels to the LDA transmission at E_F is important in both the bridge and ontop geometries and the addition of the Hubbard potential progressively moves these channels away from E_F. We notice that for U equal or greater than 1 eV both geometries have a conductance lower than $1\,G_0$, a more realistic value given that the experimental conductance of a monatomic Au nanowire is slightly below $1\,G_0$ and the interaction with an impurity is expected to lower the conductance. Increasing the value of U above 1 eV changes very little the conductance of the bridge geometry, but leads to a further conductance decrease in the ontop geometry because the $5\sigma_\mathrm{a}$ dip moves closer to E_F as the position of the d bands is shifted down in energy. When U is greater than 3.0 eV the two geometries have well-separated conductance values and that of the bridge geometry is always the largest, hence the bridge adsorption site should be distinguishable from ontop site not only at high strains but also when the chains are unstretched.

CHAPTER 5

CO adsorption on gold model nanocontacts

Several aspects of monatomic chains as formed in nanocontact experiments are missing in the idealized infinite wire model, but in principle they can be described by *model nanocontact* geometries. For instance, Au atomic chains hanging between tips, as those routinely created through a STM or a MCBJ, have a *finite length*: the longest chains measured so far are made of at most 6 or 7 freely-suspended Au atoms. Moreover, these chains are not constrained to a regular spacing nor they are forced to be strictly linear. The apex atoms of a finite-length chain between tips have a different atomic coordination with respect to atoms in the inner part of the chain, since the edges are connected to the surfaces. Each of these aspects could influence to a different extent the physical properties of the system, such as the stability of the chain, its chemical reactivity, its transport properties, and others.

In this chapter we will model the nanocontact with a short Au chain suspended between two facing Au surfaces and address the main points examined in the previous chapter for the infinite chain model, namely the adsorption site preference of CO, the strain dependence of the chemisorption energy and of the ballistic conductance (especially the contrasting behaviour of the bridge and the ontop geometries). The energetics is treated in Sec. 5.1: by varying the inter-surface distance and re-optimizing

the atomic positions of the chain and of CO, we study the effect of strain on the bond lengths and on the chemisorption energy of CO. The conductance properties of the nanocontact are discussed in Sec. 5.2, where some of the atomic configurations obtained from the structural optimizations are used to compute the ballistic transmission. These calculations also aim at checking if the $5\sigma_a$ transmission dip, which is at the origin of the large difference between the bridge and ontop conductances, is a peculiarity of CO interacting with an infinite chain or, at the contrary, survives also in the model nanocontact. To validate the results obtained with this simple nanocontact geometry, for selected values of the inter-surface distance we compute the conductance of a short chain attached to the surfaces through smooth tips and with CO in the bridge and ontop positions. Finally, in Sec. 5.3 we will use the conclusions from the previous two sections to compare our results with the available experimental data and the interpretations that have been proposed. Our focus will be on the fractional conductance trace reproducibly observed in an experiment with Au nanocontacts contaminated with CO [26] and associated with the peak at $\simeq 0.6\,G_0$ in the conductance histogram.

5.1 Geometry and energetics

In our calculations we modeled the nanocontact as a row of Au atoms suspended between fcc bulk Au leads terminated by two facing (001) surfaces. The simulation supercells, shown in Fig. 5.1, consist of a slab geometry with 7 Au layers perpendicular to the [001] direction of the fcc lattice coinciding with the z axis (which is also the transport direction, see next section). The spacing between innermost layers corresponds to the theoretical equilibrium value in the bulk ($d_b = 2.029$ Å with LDA, $d_b = 2.082$ Å with GGA). The clean, unreconstructed Au (001) surface shows a significant inward relaxation just for outermost layer (about 1.8% with LDA, and about 1.5% with GGA, in agreement with recent DFT calculations [104]), while spacings between inner layers deviate from the bulk value by less than 0.4%. Therefore we keep into account the relaxation of the outermost layer on both sides of the junction by setting the first interlayer distance to $d_s = 1.992$ Å with LDA and to $d_s = 2.051$ Å with GGA (see also Fig. 5.1). The in-plane distances between gold atoms are those of the bulk.

A short monatomic Au chain (from 3 up to 7 atoms long) is suspended in the vacuum region between the slabs and the apex atoms of the chain are attached to the surfaces at a 4-fold coordinated hollow site. The symmetry group of the straight chain between the two (001) surfaces is D_{4h}, the same as in the clean surface case studied with a slab geometry having inversion symmetry. A single CO molecule is adsorbed

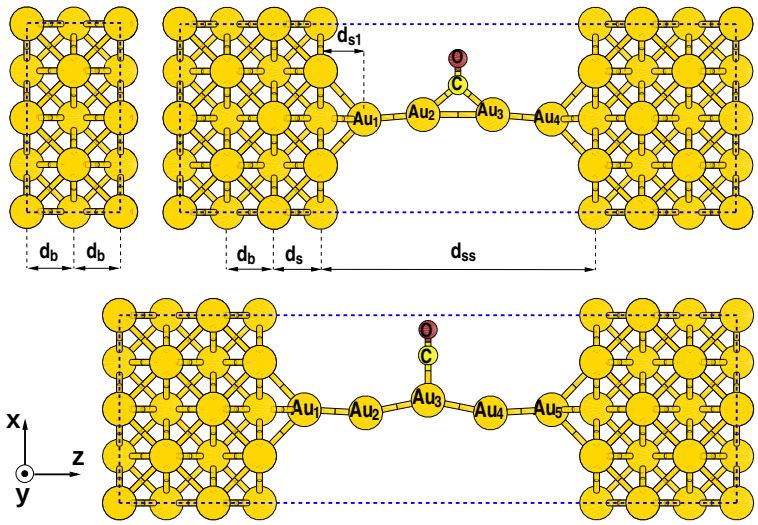

Figure 5.1: *Lateral view of the supercell used to simulate Au nanowires between Au(001) surfaces with CO at the bridge or CO ontop of the central atom(s) of the wire (in the drawings at the top and at the bottom, respectively). The smaller cell on the top left corner is used to compute the CBS of the leads (see later in the text).*

on the central site of the chain (hence the number of Au atoms in the chain is even for the bridge geometry and odd for the ontop geometry), as depicted in Fig. 5.1 for CO at the bridge of a 4Au wire and CO ontop of a 5Au wire. The symmetry group of the system in presence of CO is C_{2v}, as in the case of CO adsorbed at the bridge or ontop of infinite Au chains. The xy in-plane periodicity of the supercells corresponds to a $(2\sqrt{2} \times 2\sqrt{2})$R45° surface structure, which gives a wire-wire spacing of about 8.12 Å in the x and y directions between two adjacent replicas. We checked that optimized atomic positions obtained with this supercell result in atomic forces below 0.003 Ry/a.u. when utilized in a $(3\sqrt{2} \times 3\sqrt{2})$R45° supercell, which corresponds to a wire-wire spacing of about 12.18 Å.

For different values of the inter-surface distance, d_{ss} (see Fig. 5.1), the atomic positions along z of the N_{Au} atoms of a short, straight chain (without CO) have been optimized,[1] allowing for a variable interatomic spacing across the wire length, while all the other Au atoms are kept frozen in the layered structure described above (interlayer distances are also kept fixed).[2] The optimized distances between Au atoms of the wire (d_{1-2}, d_{2-3}, ...) and the distance between the surface plane and the apex atom of the wire (d_{s1}) are reported in the left part of Tab. 5.1 and Tab. 5.2 for a

[1] These short wires are kept straight and we do not explore zigzag or bent configurations, which are expected to become favored at low values of d_{ss} [9, 105, 106]. When CO is adsorbed, however, Au wires are not constrained to be straight.

[2] Here we mimic the pulling of the nanocontact by increasing the intersurface distance, so that we obtain a different level of strain on the chain. In principle also the Au surface layers on both sides should be allowed to relax, but this would require much bigger supercells. Anyway, since we are mostly interested in the local interaction between CO and Au, the strain level on the chain is the decisive factor. The elastic response of the banks is not considered directly, but it can be modeled through a linear differential equation as in Ref. 29 (see Sec. 5.3).

4-atom-long and a 5-atom-long wire, respectively. Each pair of rows in the tables show results from a LDA and a GGA calculation alternately.

The inter-surface distances, d_{ss}, in the first pair of rows correspond to chains with Au-Au distances close to the equilibrium value in the infinite chain (2.51 Å within LDA and 2.61 Å within GGA, see Sec. 4.1). The values of d_{ss} in the second pair of rows correspond to moderately strained chain geometries, while those in the third pair of rows give rise to highly stretched Au-Au bonds. At the lowest strain considered here, the atoms in the chain are almost equally spaced, but the bond length between atoms at the extremities of the chain, d_{1-2}, adjusts to a value slightly smaller than the others (only d_{2-3} in 4-atom and 5-atom chains, but we verified that this holds also for the inner bonds of longer chains). The difference between d_{1-2} and d_{2-3} distances becomes larger as the strain level on the chain grows up, since the ratio d_{2-3}/d_{1-2} is always larger than one and increases with d_{ss}. Excepted for the highly stretched 4-atom chain configuration, where the ratio is much larger in the GGA case, LDA and GGA give similar d_{2-3}/d_{1-2} values.

An early ab-initio theoretical work [107] studied Au chains of various lengths connected to pyramidal clusters at both ends and reported the optimized bond lengths (within the LDA) for chains made of n atoms between the apexes of the two pyramids (where n corresponds to $N_{\mathrm{Au}} - 2$ in our geometry, if we consider the apex atom of both pyramids as belonging to the chain). Their configurations correspond to highly stretched chains with an average bond length of 3.0 Å, thus larger than the largest value shown here in the tables (about 2.85 Å for the 5-Au-wire at $d_{\mathrm{ss}} = 15.36$ Å). For short chains (2 or 3 atoms between the pyramids, corresponding 4-atom-long and 5-atom-long chains, respectively) they obtain Au-Au spacings that increase from the extremities to the center of the chain, in agreement with our finding. For longer chains, instead, they report an oscillatory behaviour of the bond lengths, with alternating longer and shorter bonds, when the average Au-Au distance is larger than 2.8 Å, which eventually gives rise to a set of coupled Au dimers at average bond lengths of about 3.0 Å. We also studied longer chains (with $N_{\mathrm{Au}} = 6$ and $N_{\mathrm{Au}} = 7$, not reported here), and found that this behaviour (dimerization) is present only for average Au-Au bond lengths above 3.0 Å, while at lower strains the Au-Au bond lengths are always increasing when going from the ends toward the center of the chain.

Although the apex atoms of the chain (for instance the left-end atom, labelled $\mathrm{Au}_{(1)}$ in Fig. 5.1) are coordinated to 4 atoms of the surface and to only one atom of the chain, the distance between the surface plane and the apex atom (d_{s1} for the left apex) increases with strain at the same pace or higher than the intra-chain spacings, d_{1-2} and d_{2-3}, where the coordination number is equal to 2 (the same holds for $\mathrm{Au}_{(N_{\mathrm{Au}})}$ at the right extremity, since $d_{sN_{\mathrm{Au}}} = d_{s1}$ for our symmetric configurations). For instance,

	4-Au wire			CO at the bridge					
$d_{\rm ss}$	$d_{\rm s1}$	d_{1-2}	d_{2-3}	$d_{\rm s1}$	d_{1-2}	d_{2-3}	$d_{\rm Au\text{-}C}$	$d_{\rm C\text{-}O}$	$E_{\rm chem}$
11.16	1.79	2.52	2.53	1.83	2.53	2.74	1.99	1.16	−2.19
(11.56)	(1.87)	(2.61)	(2.61)	(1.90)	(2.59)	(2.86)	(2.03)	(1.17)	(−1.47)
11.76	1.91	2.64	2.66	1.87	2.56	2.93	1.98	1.16	−2.36
(12.16)	(1.99)	(2.72)	(2.74)	(1.93)	(2.61)	(3.09)	(2.02)	(1.17)	(−1.61)
12.36	2.00	2.77	2.81	1.92	2.62	3.30	2.00	1.17	−2.72
(12.76)	(2.09)	(2.82)	(2.94)	(1.99)	(2.67)	(3.44)	(2.06)	(1.18)	(−1.94)

Table 5.1: *Optimized distances (in Å) and chemisorption energies (in eV) obtained with LDA (GGA values in parenthesis) for CO adsorbed at the bridge site of a 4-atom-long chain for selected values of d_{ss} (see Fig. 5.1). Since we consider a symmetric configuration, $d_{3-4} = d_{1-2}$ and $d_{4s} = d_{s1}$.*

in the 4Au-wire case studied within GGA, $d_{\rm s1}$ increases of about 12% (12% within LDA, too) when $d_{\rm ss}$ spans from the minimum to the maximum of the values reported in Tab. 5.1, while d_{2-3} increases of about 13% and d_{1-2} of only 8% (respectively, 11% and 10% within LDA). The GGA data for the 5Au-wire in Tab. 5.2 gives again an increase of about 12% for $d_{\rm s1}$ (the same found with LDA), while d_{2-3} increases of 12% and d_{1-2} of 10% (13% and 11% within LDA). This agrees with the study of Bahn and Jacobsen [10] about relative bond strength of bulk-phase compared to monatomic chains, which showed that for Au a bond in the chain is much stiffer than a bond between two atoms in the bulk.

We have then placed an upright CO at the *bridge site* in the middle of a short suspended chain (between atoms $\rm Au_{(2)}$ and $\rm Au_{(3)}$ in the 4-atom-chain shown in Fig. 5.1) and we have optimized the atomic positions of C, O and of the Au atoms of the chain (while all the other Au atoms are kept frozen as above); the optimized distances are reported on the right side of Tab. 5.1 for CO adsorbed on a 4-atom-long wire for the same set of selected $d_{\rm ss}$ values. The carbon-oxygen bond length of the adsorbed molecule, $d_{\rm C\text{-}O}$, is equal or slightly larger (by less than 1%) than the value found for CO on the infinite chain (see Tab. 4.3 at page 112), while C-Au bond lengths, $d_{\rm Au\text{-}C}$, are 1% to 3% larger than those found in the infinite chain geometries. The bond length between the two Au atoms in contact with CO, d_{2-3}, is always longer than the other Au-Au bonds in the chain (compare d_{2-3} with $d_{1-2} = d_{3-4}$ in the table). At low strain (first pair of rows in the table), d_{2-3} adjusts to a value similar to or slightly larger than the Au-Au distance corresponding to the bridge energy minimum for the infinite chain geometry ($d_{\rm Au\text{-}Au} = 2.63$ Å with LDA and $d_{\rm Au\text{-}Au} = 2.87$ Å with GGA,

see Fig. 4.1). The other Au-Au bond lengths, instead, stay closer to the equilibrium spacing of the infinite chain. Since the length of the central Au-Au bond increases after CO adsorption, while the other Au-Au bonds do not shorten correspondingly, at low or moderate strains the resulting optimized geometries have a bend towards CO in the middle of the chain.

At larger strains the wire atoms get progressively more aligned along the z direction forming an almost linear strand with one overstretched Au-Au bond in correspondence of the CO adsorption site, while the other Au-Au distances are just slightly above the equilibrium spacing of the isolated chain. The flexibility of the Au-C-Au bond angle allows for very large Au-Au distances between the two atoms in contact with CO as d_{ss} is increased, but above a critical d_{ss} value the molecule will presumably prefer to tilt its axis from the perpendicular position towards a substitutional configuration, similar to that predicted theoretically for the Pt-CO-Pt nanocontact [29]. As discussed in Sec. 4.1, this structural change would probably lead to the rupture of the wire at the O-Au bond, since we have seen that the tilted bridge and substitutional configurations in Au correspond to a maximum and a very shallow minimum of the energy, respectively. However, in that section we have found that the transition from the upright bridge to the tilted bridge geometry takes place at a Au-Au distance above 4.0 Å (i.e. a distance longer than the largest d_{2-3} reported in Tab. 5.1), hence we can expect that the perpendicular position of CO is preferred for the values of d_{ss} considered here.

Additionally, we studied CO adsorption at the bridge of a 6-atom-long chain (within LDA only) and we have found that also for this longer chain the bond length between the two Au atoms in contact with CO is always the largest and increases significantly with strain. In this chain there are also Au atoms which are not in contact with CO or with the surface (we indicate those atoms with $\mathrm{Au}_{(2)}$ and $\mathrm{Au}_{(5)}$). We find that the bond length between these atoms and the nearest Au atom in contact with CO ($\mathrm{Au}_{(3)}$ and $\mathrm{Au}_{(4)}$, respectively) is much shorter than the bond length with the other neighbouring atom, ($\mathrm{Au}_{(1)}$ and $\mathrm{Au}_{(6)}$, respectively, which are in contact with the surface). Since in the 6-atom-long chain we always find that $d_{2-3} > d_{1-2}$, while after CO adsorption we have that $d_{2-3} < d_{1-2}$, we conclude that the weakening of the bond between $\mathrm{Au}_{(3)}$ and $\mathrm{Au}_{(4)}$ below CO leads to stronger bonds with the lateral atoms in the chain ($\mathrm{Au}_{(2)}$–$\mathrm{Au}_{(3)}$ and $\mathrm{Au}_{(4)}$–$\mathrm{Au}_{(5)}$ bonds). At lower strains we observe here as well a bend towards CO in the middle of the chain (involving the 4 central atoms $\mathrm{Au}_{(2)}$, $\mathrm{Au}_{(3)}$, $\mathrm{Au}_{(4)}$, and $\mathrm{Au}_{(5)}$), while a zigzag configuration appears at the edges of the wire.

In Tab. 5.2 we report the optimized distances for CO adsorbed *ontop* of the central atom of a 5-atom-long Au chain (indicated with $\mathrm{Au}_{(3)}$ in Fig. 5.1). With respect to

	5-Au wire			CO ontop					
$d_{\rm ss}$	$d_{\rm s1}$	d_{1-2}	d_{2-3}	$d_{\rm s1}$	d_{1-2}	d_{2-3}	$d_{\rm Au\text{-}C}$	$d_{\rm C\text{-}O}$	$E_{\rm chem}$
13.76	1.80	2.53	2.54	1.90	2.63	2.68	1.93	1.14	−1.17
(14.16)	(1.86)	(2.61)	(2.61)	(1.98)	(2.72)	(2.76)	(1.98)	(1.14)	(−0.78)
14.56	1.93	2.66	2.69	1.92	2.65	2.73	1.91	1.14	−1.06
(14.96)	(2.00)	(2.73)	(2.75)	(1.99)	(2.73)	(2.83)	(1.99)	(1.14)	(−0.55)
15.36	2.01	2.81	2.86	1.98	2.74	2.96	1.91	1.14	−1.16
(15.76)	(2.09)	(2.87)	(2.92)	(2.04)	(2.77)	(3.08)	(1.98)	(1.14)	(−0.63)

Table 5.2: *Optimized distances (in Å) and chemisorption energies (in eV) obtained with LDA (GGA values in parenthesis) for CO adsorbed the on-top of the central atom of the 5-atom long chain at selected values of $d_{\rm ss}$ (see Fig. 5.1). Owing to the symmetry, $d_{3-5} = d_{1-2}$, $d_{3-4} = d_{2-3}$, and $d_{5s} = d_{s1}$.*

CO adsorbed on the infinite chain, C-Au bond lengths are larger for CO on the short chain (compare with Tab. 4.3); the increase in $d_{\rm Au\text{-}C}$ is around 1% (thus smaller than that found for the bridge case), except for the LDA case at $d_{\rm ss} = 13.76\,$Å, where $d_{\rm Au\text{-}C}$ is about 2% larger than in the infinite chain geometry at equilibrium spacing. On the other hand, the carbon-oxygen bond distance is quite stable at the value found in the infinite wire case ($d_{\rm C\text{-}O} = 1.14\,$Å). CO adsorption in the ontop position distorts the chain more than in the bridge position (as visible in the sample geometries in Fig. 5.1); the Au atom right below the molecule moves upwards while the two lateral Au atoms ($\rm Au_{(2)}$ and $\rm Au_{(4)}$) slightly displace downwards, creating a zigzag geometry. By comparing d_{1-2} with d_{2-3}, we see that the bond established between C and $\rm Au_{(3)}$ weakens the binding of $\rm Au_{(3)}$ to the neighbouring atoms, $\rm Au_{(2)}$ and $\rm Au_{(4)}$. With CO adsorbed ontop, the ratio d_{2-3}/d_{1-2} is always larger than in the pristine 5Au-atom chain and grows more rapidly with strain.

Using the total energies of these partially relaxed atomic structures (short suspended wires with and without CO), together with the energy of an isolated CO molecule in the same supercell, through Eq. (3.1) we compute the *chemisorption energy* as a function of $d_{\rm ss}$ for CO in the bridge and ontop positions. We report $E_{\rm chem}(d_{\rm ss})$ in the rightmost column of Tab. 5.1 and Tab. 5.2, respectively, asides of the corresponding optimized distances. The clear-cut preference for the bridge adsorption site, encountered in the case of infinite chains, is confirmed here by the large difference between the bridge $E_{\rm chem}$ and the ontop $E_{\rm chem}$. The chemisorption energy in the bridge geometry increases with strain, hence it follows the trend detected for the infinite straight chain (see Sec. 4.4), while in the ontop geometry this is verified only for large enough values of $d_{\rm ss}$. Actually, in the ontop geometry the largest value

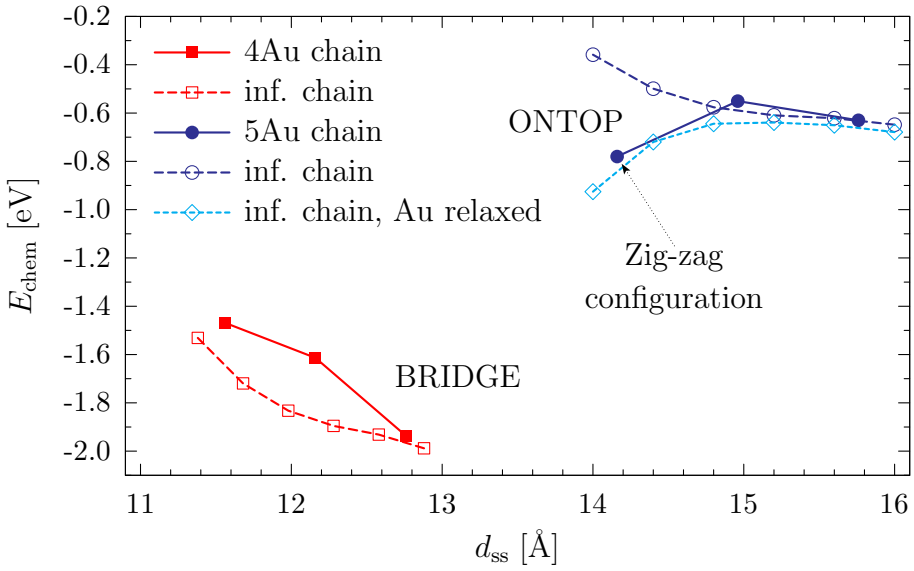

Figure 5.2: *Chemisorption energies (within GGA) for CO at the bridge of a 4Au-atom wire (red filled squares) and for CO ontop of a 5Au-atom wire (blue bullets) as a function of d_{ss}. The values of $E_{\rm chem}(d_{chain})$ for infinite straight chains are reported here as a function of $\tilde{d_{ss}}(d_{chain}) = 2 \cdot \langle d_{s1} \rangle + (N_{Au} - 1) \cdot d_{chain}$, where $N_{Au} = 4$ for the bridge geometry (red empty squares) and $N_{Au} = 5$ for the ontop geometry (blue circles), while $\langle d_{s1} \rangle$ is chosen as described in the text. For CO in the ontop position we also report $E_{\rm chem}(\tilde{d_{ss}})$ obtained by optimizing the x coordinate of the Au atom below CO in the infinite chain (cyan empty diamonds).*

of $E_{\rm chem}$ is obtained for the lowest $d_{\rm ss}$ considered here ($d_{\rm ss} = 13.76$ with LDA and $d_{\rm ss} = 14.16$ with GGA), the opposite of what predicted by the infinite straight chain model.

In order to compare more clearly the energetics of the infinite chain geometry with that of the short chain, we put in correspondence $E_{\rm chem}$ computed in the previous chapter as a function of the uniform spacing of the infinite chain, $d_{\rm chain}$, with $E_{\rm chem}$ computed for a suspended $N_{\rm Au}$-atom-long chain as a function of the inter-surface distance $d_{\rm ss}$. For this purpose, we report $E_{\rm chem}(d_{\rm chain})$ as a function of an equivalent inter-surface distance, $\tilde{d_{\rm ss}}(d_{\rm chain})$, which can be compared directly with $d_{\rm ss}$. We set $\tilde{d_{\rm ss}} = 2 \cdot \langle d_{\rm s1} \rangle + (N_{\rm Au} - 1) \cdot d_{\rm chain}$, where the Au-Au spacing $d_{\rm chain}$ is multiplied by the number of Au-Au bonds in the short chain, while $\langle d_{\rm s1} \rangle$ accounts for the distance between the surface plane and the apex atom of the chain (since it is included in $d_{\rm ss}$). This distance has been estimated by averaging the optimized values of $d_{\rm s1}$ reported in Tab. 5.1 for the bridge geometry and in Tab. 5.2 for the ontop geometry, resulting in $\langle d_{\rm s1} \rangle = 1.94$ Å and $\langle d_{\rm s1} \rangle = 2.00$ Å, respectively (from the GGA data).

In Fig. 5.2 we report $E_{\mathrm{chem}}(\tilde{d_{\mathrm{ss}}})$ for the infinite chain geometries with CO at the bridge or CO ontop (empty squares and circles, respectively) and $E_{\mathrm{chem}}(d_{\mathrm{ss}})$ for CO at the bridge or ontop of a short suspended chain with, respectively, $N_{\mathrm{Au}} = 4$ atoms (filled squares) or $N_{\mathrm{Au}} = 5$ atoms (filled circles). In the range of d_{ss} considered here there is only a qualitative agreement between E_{chem} for the short suspended chain and that for the infinite straight chain. As said above, the strain dependence of E_{chem} is the same in these two different model geometries (infinite chain and short chain) only for CO in the bridge position (compare empty and filled squares), while for CO in the ontop position (empty and filled circles) there is a discrepancy at low d_{ss} because of the appearance of zigzag geometries. If both the ontop CO and the Au atom below the molecule are allowed relax along x in the infinite chain geometry (empty diamonds in Fig. 5.2), then $E_{\mathrm{chem}}(\tilde{d_{\mathrm{ss}}})$ is in much better agreement with the results from the 5-atom-chain ontop geometry. As already mentioned in Sec. 4.4, the main geometrical distortion induced by CO adsorption is the upward displacement of the Au atom below the molecule and this displacement is more pronounced at low strains. Thus the displacement of that Au atom accounts for great part of the discrepancy in E_{chem} between the infinite straight chain and the short chain, while distortions of the chain further away from the adsorption site give smaller contributions to the chemisorption energy. The smaller discrepancies in the bridge geometry can be mainly imputed either to the shortness of the chain, or to the non-uniform Au-Au bond length across the chain, or to the bending of the chain (or a combined effect of these factors).

Another point that should be taken in consideration for a realistic estimate of the chemisorption energy is the chain geometry before CO adsorption, since it determines the reference energy E_{wire} used to compute E_{chem}. At lower strains, zigzag or bent configurations have been predicted for short monatomic chains between tips [9], while in our calculations we only consider straight geometries for the pristine chain. When d_{ss} is sufficiently small, allowing for zigzag geometries would lead to a lowering of the optimal energy E_{wire} in Eq. (3.1) and hence to a smaller E_{chem}. However, Häkkinen et al. [9] reported that the linear chain configuration is favored with respect to both zigzag and bent configurations (which correspond to local minima of the energy) when the average spacing between the atoms in the chain is equal or larger than approximately 2.65 Å, while the three configurations are nearly degenerate for slightly smaller spacings. Therefore we can expect that only the result at the smallest value of d_{ss} considered here (first pair of rows in Tab. 5.1 and Tab. 5.2) would be changed by recomputing E_{chem} with E_{wire} obtained from non-linear chain geometries.

In conclusion, chemisorption energies from a very simple model, such as the straight, equally-spaced infinite chain, do not account for several factors included in the short suspended chain geometry (the finite length of the chain, the irregular spacing, bent or zigzag configurations), nevertheless they can predict the same site preference given

by more realistic (and computationally expensive) geometrical configurations, at least if the two adsorption sites are enough separated in energy. Including a few additional degrees of freedom in the geometry optimizations of CO on the infinite chains (such as the Au atom displacement when CO is ontop, or a larger spacing between the two Au atoms in contact with CO in the bridge position), which can be inferred from the residual forces after a partial structural optimization, can be sufficient to give realistic estimates of E_{chem}.

5.2 Ballistic conductance

We have seen in the previous section that the intra-chain bonds next to the apexes of the short suspended chain are stiffer than those in the middle and that the atomic spacing increases significantly when going from the extremities to the center of a stretched chain. Moreover the presence of an adsorbed CO can generate a crooked chain geometry, which gradually disappears turning into a more straight configuration as the tension applied on the junction increases. These structural changes may have an influence on the electronic transport across the chain, therefore in this section we will study the transport properties of the short Au chains introduced in the previous section in order to obtain more realistic predictions on the nanocontact conductance.

Using the partially-optimized atomic configurations computed previously, we calculate the *ballistic transmission* for several values of the inter-surface distance d_{ss} to get the dependence of the conductance on the *contact stretching*. An "abrupt" junction is simulated using as the scattering region the supercells with $(2\sqrt{2}\times 2\sqrt{2})\mathrm{R}45^\circ$ in-plane periodicity shown in Fig. 5.1. In the same figure we also show the unit-cell for the left and right leads used to compute the CBS along the [001] direction of bulk Au. The unit-cell is composed of two bulk (001) layers with the same cross section of the scattering region (the third layer shown in the figure is the periodic repetition of the first and matches the leftmost layer of the scattering region). The transmission has been averaged on a 7×7 uniform mesh of $\mathbf{k}_\perp$-points in the 2D-BZ of the supercell[3] (in the plane perpendicular to the transport direction), corresponding to 10 and 16 $\mathbf{k}_\perp$-points in the irreducible 2D-BZs of the short straight chain and the short chain with CO adsorbed, respectively. We have checked that this sampling gives a well converged transmission value at the Fermi level and at scattering energies close to it, but result in larger errors for scattering energies more distant from E_{F}. However here we are more interested in the behaviour of the transmission close to E_{F} and we will not try to converge the full transmission curve to the same accuracy (i.e., errors below one percent) reached at the Fermi level.

[3]The importance of an accurate $\mathbf{k}_\perp$-point sampling of the ballistic transmission in model nanocontacts with extended leads has been discussed by Thygesen and Jacobsen [87].

We also investigate the influence of the *tip smoothness* by computing, for a couple of test configurations, the transmission of the short chain connected to the (001) surfaces through a junction less abrupt than that obtained attaching the apex atoms directly to the surface. A more "smooth" junction is simulated with (3×3) supercells; the scattering region, shown in the insets of Fig. 5.4, has pyramidal tips connecting the chain apexes to the Au(001) surfaces. This geometry is composed of a seven-layer slab with an interlayer spacing equal to the bulk value d_{b}, plus four additional Au atoms on each side in the positions of an additional layer at a distance d_{s} from the surface plane. The chain is attached at the 4-fold hollow site formed by these four additional atoms. The unit-cell for the leads in the (3×3) geometry (not shown) is built as above for the smaller scattering region. For this geometry a 5×5 uniform mesh of $\mathbf{k}_{\perp}$-points has been used to sample the transmission in the 2D-BZ.

5.2.1 Short pristine chains

We start discussing the ballistic transport of the short chain in the abrupt junction geometry. The transmission function of the 4Au-atom straight chain is shown in Fig. 5.3 on the left side (with blue lines and diamonds) for scattering energies from $-1.0\,\mathrm{eV}$ below to $1.0\,\mathrm{eV}$ above the Fermi level. We use the LDA geometries with the optimized interchain spacings given in the previous section (see Tab. 5.1) and we compare the transmission for two selected values of the intersurface distance, corresponding to a low/moderate strain or to a high strain (upper and lower panel in the figure, respectively). At low strain (configuration with $d_{\mathrm{ss}} = 11.76\,\text{Å}$) the 4Au-atom chain has a conductance value slightly above $0.9\,G_0$, attributable to a single well transmitted spin-degenerate channel of s character. This value is in fair agreement with the conductance of an unstretched 4-atom-chain (oriented in the [110] direction) between smooth tips reported by Häkkinen et al. [9].

Although the number of scattering channels increases with the cross-section of the supercell, for a long enough chain and a small charge transfer between the leads and the chain, the theoretical maximum of the transmission is given by the number of channels in the infinite tipless chain (see dashed lines in Fig. 4.7, page 115). Around the Fermi energy, E_{F}, the transmission curve is rather flat, while below E_{F} it is more structured due to the presence of poorly transmitted additional d channels of the chain and a higher reflection of the s channel, which is instead better transmitted next to E_{F} and at higher energies. This is in line with the common understanding that d states, which correspond to more directional bonds with respect to s states, are more reflected by the presence of an abrupt change in the atomic structure at the surface/wire interface.

When the strain is increased (configuration at $d_{\mathrm{ss}} = 12.36\,\text{Å}$) the conductance

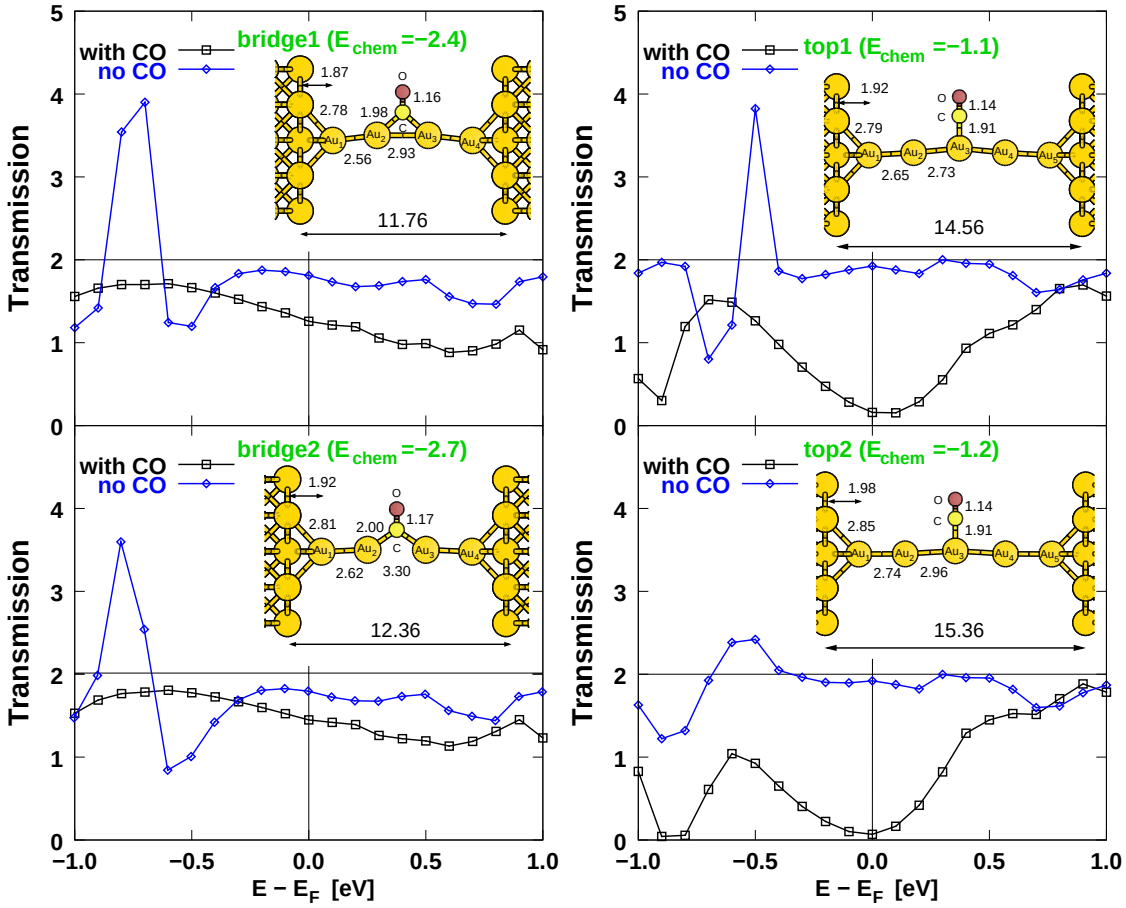

Figure 5.3: *Ballistic transmission for a short, straight wire with $N_{Au} = 4$ (panels on the left) or $N_{Au} = 5$ (panels on the right) between Au(001) surfaces at two selected values of d_{ss} (blue diamonds). The optimized Au-Au distances reported in Tab. 5.1 and in Tab. 5.2 have been used. For the same values of d_{ss}, the ballistic transmission of the optimized atomic configurations with CO adsorbed at the bridge of the 4Au-wire or ontop of the 5Au-wire are reported in the correspondent plot (black squares). The central part of the scattering region and the inter-surface distance d_{ss} (in Å) are shown in the insets. The optimal distances (in Å) and chemisorption energies of CO (in eV) are also reported in the insets.*

changes very little: it decreases of about 1 % only. Previous calculations [9, 107] have also found that the conductance decreases monotonically when the junction gets stretched and that at this level of stretching (average spacing around 2.80 Å) the conductance has not yet started to drop significantly, being still close to $1\,G_0$ [107], or slightly below [9]. Above E_F the shape of the transmission function is very similar to that obtained for the less-strained configuration, while below E_F the reflection slightly increases with the strain.

The transmission function for the 5-atom-long chain is shown in Fig. 5.3 on the right side (blue lines and diamonds) for two levels of strain, larger for the chain geometry in the lower panel ($d_{ss} = 15.36$ Å, see also distances in Tab. 5.2) with respect to that in the upper panel ($d_{ss} = 14.56$ Å). The conductance of the 5Au-atom chain (about $0.96\,G_0$ for both values of d_{ss} considered in the figure) is larger than that found for 4Au-atom chain, in agreement with the odd-even effect seen in experiments [108] and also in theoretical calculations [106, 109]. For instance, de la Vega et al. [109] have calculated the theoretical conductance of short chains between flat Au(111) surfaces and confirmed that chains with even number of atoms have lower conductance than those with an odd number. With respect to our results, they find larger conductances (about $0.96\,G_0$ and $0.99\,G_0$ for 4-atom and 5-atom long chains, respectively), probably because the chains are attached to the more compact Au(111) surface in their calculations. We find that also in this longer chain the conductance has a tiny dependence on strain, since it is almost unchanged when the average spacing in the chain increases from 2.74 Å to 2.90 Å (see d_{1-2} and d_{2-3} corresponding to $d_{ss} = 14.56$ Å and $d_{ss} = 15.36$ Å in Tab. 5.2). For the 5-atom-long chain between Au(111) surfaces, de la Vega and coworkers [109] have found that the conductance goes from $0.99\,G_0$ to about $1\,G_0$ when the spacing between atoms in the chain grows from 2.70 Å to 3.00 Å, while the conductance of the 4-atom-long chain does not change appreciably, as in the case of the Au(001) surface examined here.

From the comparison of the energy dependent transmissions of the 4Au-chain and of the 5Au-chain in this small range of energies around E_F, we notice that at lower strains (upper panels) the contribution of d channels appears in both cases as a peak below E_F, but it is positioned at different energies (at about -0.75 eV in the 4-atom-long chain and at -0.5 eV in the 5-atom-long chain). Above E_F the transmission is more similar and it is always larger in the 5-atom-long chain. At larger strains (lower panels) there are more differences between the 4Au chain and the 5Au chain transmissions below E_F: in the 5-atom-long chain the $5d$ peak is much more reduced and it is also slightly broadened.

5.2.2 Short chains with CO adsorbed

We will now discuss how the conductance changes when CO is adsorbed in the bridge position on the 4Au-atom chain or in the ontop position on the 5Au-atom chain. The optimized configurations presented in the previous section are used to define the scattering region (see distances in Tab. 5.1 and Tab. 5.2, respectively). For the reader's convenience, the central part of the scattering region is schematically depicted in the inset of each transmission plot in Fig. 5.3, with d_{ss} and the optimized distances also indicated. With CO at the bridge, the conductance of the chain at low/moderate strains (black lines and squares in the top left plot of Fig. 5.3) is reduced to about $0.63\,G_0$, a value close to the fractional conductance peak seen in a MCBJ experiment of Au nanocontacts in presence of CO gas [26]. The transmission curve has a small dependence on the scattering energy in the range shown and decreases monotonically. The $5d$ peak present below E_{F} in the transmission of the pristine chain is suppressed by CO-adsorption, but for some energy ranges the transmission is actually higher in the configuration with CO adsorbed, probably because of geometrical modifications of the chain structure that change the coupling of d states with the leads.

At a larger strain (see bottom left plot), the transmission curve for CO at the bridge retains its smooth shape as a function of energy, but has slightly higher values with respect to the transmission at lower strains. As a consequence the conductance increases with strain to about $0.72\,G_0$, probably because of the straightening of the chain. However the central Au-Au bond is very stretched with respect to the others and therefore the electron conduction takes place not only through the chain but also through the molecular states hybridizing with Au bands. When CO is adsorbed at the bridge, the strain-dependence of the chain conductance is compatible with the experimental fractional conductance trace [26], which has a positive slope (i.e., the conductance increases with strain, see also next section). With respect to the tipless transmission calculations for the infinite chain presented in the previous chapter (see Fig. 4.7, compare with the bridge geometry at $d_{\mathrm{chain}} = 2.70\,\text{Å}$), the transmission including the effect of the surface/wire interface is smaller by about 10 %, but it has a similar dependence on the scattering energy around E_{F}. Previous conductance calculations for a 3-atom chain between Au(111) leads and CO at the bridge have found a larger conductance (above $0.9\,G_0$, see Ref. 51) for a strain level which is intermediate to the two considered here (the Au-Au bond below CO is 3.02 Å long, while the other Au-Au bond in the chain is 2.60 Å). The discrepancy may be ascribed to the shorter chain length [11] or to the rather different functional used (B3LYP).

When CO is adsorbed ontop, the conductance is much more reduced (see black lines and squares in the right side plots of Fig. 5.3), marking a large difference with respect to the bridge case. In the low-strain configuration (upper panel), the transmission

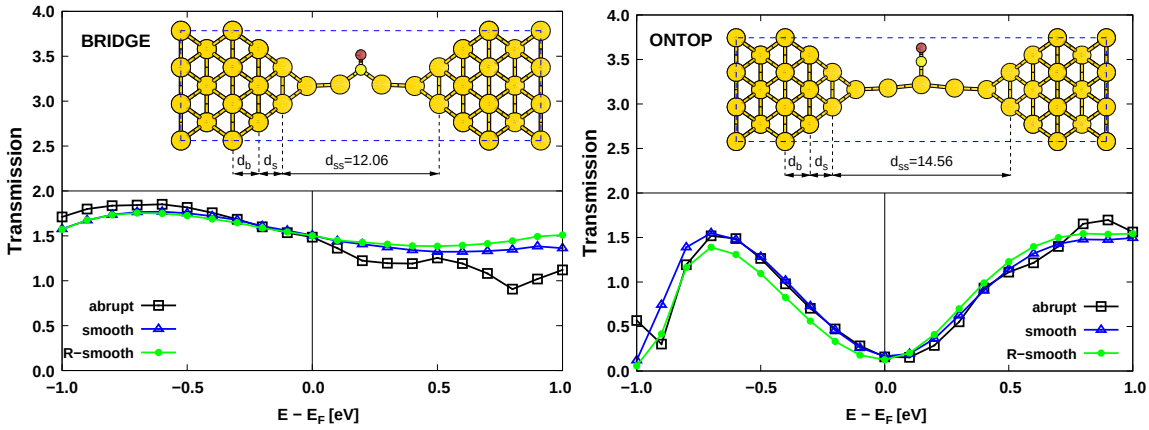

Figure 5.4: *Ballistic transmission of a short chain with CO adsorbed: dependence on the smoothness at the surface/chain interfaces. For both bridge and ontop adsorption geometries (left and right side, respectively) at a selected value of d_{ss}, the transmission computed using $(2\sqrt{2} \times 2\sqrt{2})R45°$ cells with abrupt interfaces (see Fig. 5.3) or using the (3×3) cells with smoother interfaces (see insets) are reported as a function of the scattering energy (black squares and blue triangles, respectively). The central region of the smooth junction is built from the atomic positions optimized for the smaller cell (blue triangles) or by relaxing again the atoms in the constriction (green circles).*

curve has a wide depression centered just above E_F and the conductance is about $0.08\,G_0$, more than ten times smaller with respect to the value obtained for the pristine 5Au-chain at the same value of d_{ss}. The d peak below E_F is suppressed as in the bridge geometry, while at energies higher than 0.5 eV the s channel is less reflected and has a transmission which approaches that of the pristine chain. Comparing the ontop transmission in Fig. 5.3 with the tipless transmission of the ontop geometry at $d_{chain} = 2.70$ Å in Fig. 4.7, we observe that the $5\sigma_a$ dip has moved closer to E_F in the short chain geometry, resulting in a greater reduction of the conductance at comparable strain levels. As in the case of infinite chains, the transmission dip moves closer to E_F at higher strains (see lower panel in Fig. 5.3) and hence the conductance drops down to about $0.03\,G_0$. Therefore, as already inferred from the transmission results in the tipless chain geometries, when CO is in the ontop position the strain dependence of the chain conductance is completely different from that found with CO in the bridge position. This point will be discussed further later, in the context of a comparison with experimental data.

The atomic configurations for the bridge and ontop geometry with smooth tips are shown in Fig. 5.4, in the left and in the right inset, respectively. For each geometry we select a value of d_{ss} and from the optimized structures computed previously we determine the atomic positions of CO and of the short chain between the two

terminal 4-atom square basal planes (which are spaced by d_{ss}). The transmission curves obtained with the sharp interface (labelled "abrupt" in Fig. 5.4) and with the corresponding smoother interface ("smooth") show generally a quite good agreement below E_F, while above E_F there are some differences, especially for the bridge geometry. However, the conductance values correspond almost perfectly and confirm the striking difference between bridge and ontop conductances, which cannot therefore be considered as an artifact due to the sharpness of the interface (and not even to the complete absence of tips). We further optimized part of the structure: more precisely, we let the 4 basal atoms on each side move along the longitudinal direction (z axis), while the Au atoms in the chain and the CO molecule are free to move in all directions. The structural changes are rather small and the total energy is lowered by 0.3 eV or less. The transmission curve for the relaxed geometries with smooth interfaces (labelled "R-smooth" in the same plots) does not change appreciably in the bridge geometry, while in the ontop geometry the $5\sigma_a$ transmission dip moves closer to E_F. In both cases the conductance value is very similar to that found with the initial atomic configuration, and hence also to that obtained with the more abrupt interface.

5.3 Discussion and comparison with experimental data

In this section we will try to explain some of the experimental data reported by Kiguchi et al. [26] regarding the fractional conductance trace observed in Au nanocontacts after admitting CO, because this could give some evidence on how the CO molecule is adsorbed on, or incorporated into, the Au nanowire. A reproducible feature observed in typical breaking traces for Au after admitting CO is an abrupt jump in the conductance just before rupture, followed by a slight increase of the conductance and the drop into the tunneling regime after a small further elongation [26]. We will use our theoretical conductances for the bridge and ontop geometries and their dependence on d_{ss} to simulate that part of the conductance trace obtained after CO adsorption, thus making a direct comparison with the experimental trace. First we discuss the differences between the two possible adsorption sites and contrast with other possibilities that have been proposed, then we will focus on the slope of this conductance trace and its dependence on the elastic response of the electrodes.

5.3.1 Evolution of the Au nanocontact after CO adsorption

In Fig. 5.5, we plot on the same graph the conductance of the bridge and ontop geometries as a function of the displacements between the surfaces, d_{ss}, and we compare with an experimental conductance trace associated to the fractional peak in the

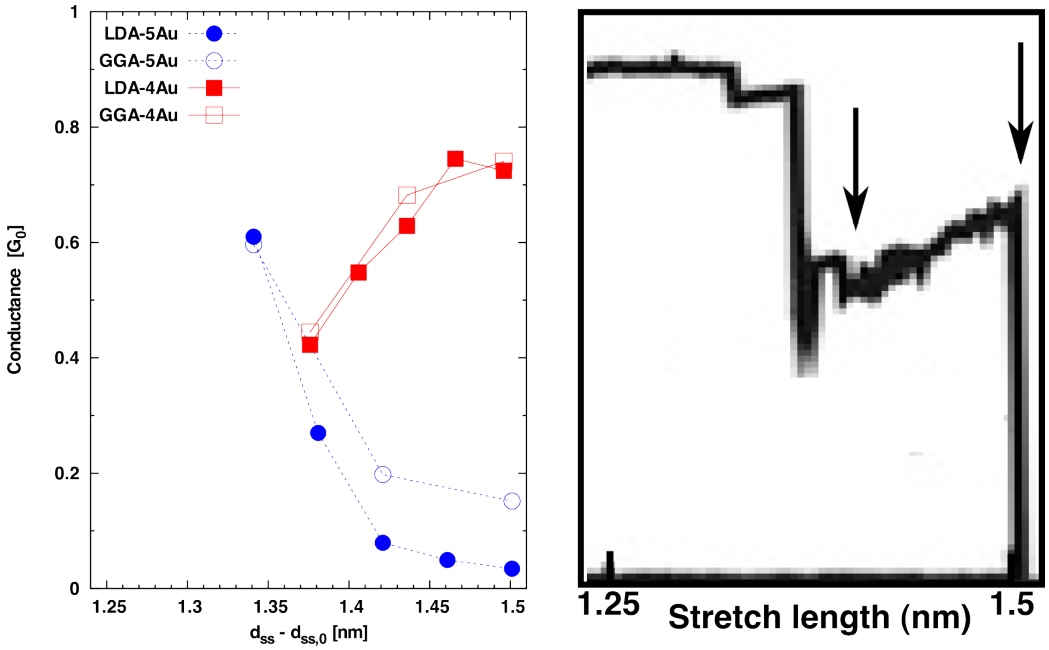

Figure 5.5: *Ballistic conductance as a function of the tips displacement from the theoretical simulations of the nanocontact (left side) and from an experiment measure (right side, adapted from Ref. 26). The same conductance scale is used in the two plots.*

conductance histogram of gold.[4] We imagine that at some point of the pulling cycle a CO molecule sticks to the Au wire (either in the bridge or in the ontop position), causing a conductance drop, and we study how the conductance of the two different geometries evolves while stretching further the nanocontact. Comparing these two simulated conductance traces with the experimental one given by Kiguchi et al. [26] we can see that only the bridge is compatible with the experimental evidence, while the ontop is too low and has an opposite behaviour with strain. This observation, together with the fact that the ontop geometry is energetically unfavored with respect to the bridge geometry (see E_{chem} in Fig. 4.7), might explain the presence of the fractional peak at about $0.6\,G_0$ (close to the conductance value of our bridge configurations) and the absence of a low conductance tail in the histogram (since the ontop configurations, which have a lower conductance, should be realized with very small probability). We notice however that the slope of the theoretical conductance for the bridge geometry does not match the slope of the experimental trace (the two plots in the figure are reported on the same scales for both the conductance axis and the length axis, hence the slopes can be compared directly from the graph visually). We are not aware if the experimental value of the conductance slope is a stable feature

[4] In order to keep into account the offset in the experimental measure of the displacement, in each set of calculations we shifted d_{ss} by a constant value $d_{\mathrm{ss},0}$.

of the Au/CO nanocontact, but we find interesting to explore further this point (see next subsection).

Our conductance calculations for the substitutional configuration (without the tips, see Sec. 4.3), showing that G is close to zero, also exclude the interpretation given by Kiguchi et al. [26] to the conductance increase seen while the nanocontact is stretched. They conjecture that the behaviour of the fractional conductance trace, first increasing upon stretching and then jumping abruptly to tunneling, could be explained by a CO bridging two atoms of the chain and passing from a perpendicular position to a longitudinal substitutional position before the nanocontact breaks. Our calculation instead show that this tilting of 90° would lead to a decrease in the conductance rather than an increase, while the latter could be obtained with CO staying upright during the pulling. Moreover, while in the case of case of Pt nanocontacts a "tilted bridge" configuration of the molecule corresponds to a local minimum of the energy in a Pt-CO-Pt junction [29], we expect that this might not be the case in a Au-CO-Au junction. From our theoretical picture of the energetics (Sec. 3.1 and Sec. 4.1), it is more probable that this junction breaks as soon as the CO axis starts to incline from the perpendicular direction, since once the energy maximum of the tilted bridge configuration is reached, the potential energy profile is too much shallow to realize another quasi-stable configuration which could sustain the external stress (see Fig. 4.1, page 96).

5.3.2 Modeling the elastic response of the electrodes

The slope of the conductance as a function of the contact stretching may not be well reproduced because up to now we have neglected the elastic response of the banks. In our simulations we control the inter-surface distance d_{ss}, but in order to model in a more realistic way the structural modifications of the junction during the pulling process one should optimize also the atomic position of the leads. This requires much larger supercells, which so far have been studied mainly with tight-binding potentials, either semi-empirical or fitted from ab-initio data. However, it is possible to keep into account the mechanical response of the leads to the external stress approximately by treating them as ideal springs with a finite spring constant k_s. Following the idea of Strange et al. [29], we assume that the position of the electrodes is controlled externally at two opposite points, far away from the junction, and we denote by L the separation between these two points. The force balance between the springs and the junction region can be expressed by the following equation [29]:

$$\frac{1}{2}k_s(L - d_{\mathrm{ss}}) = \frac{\partial E_{\mathrm{tot}}(d_{\mathrm{ss}})}{\partial d_{\mathrm{ss}}} \tag{5.1}$$

where d_{ss} is the distance between the Au surfaces and $E_{\mathrm{tot}}(d_{\mathrm{ss}})$ is the total energy of the optimized configuration at that inter-surface distance. The relation between L

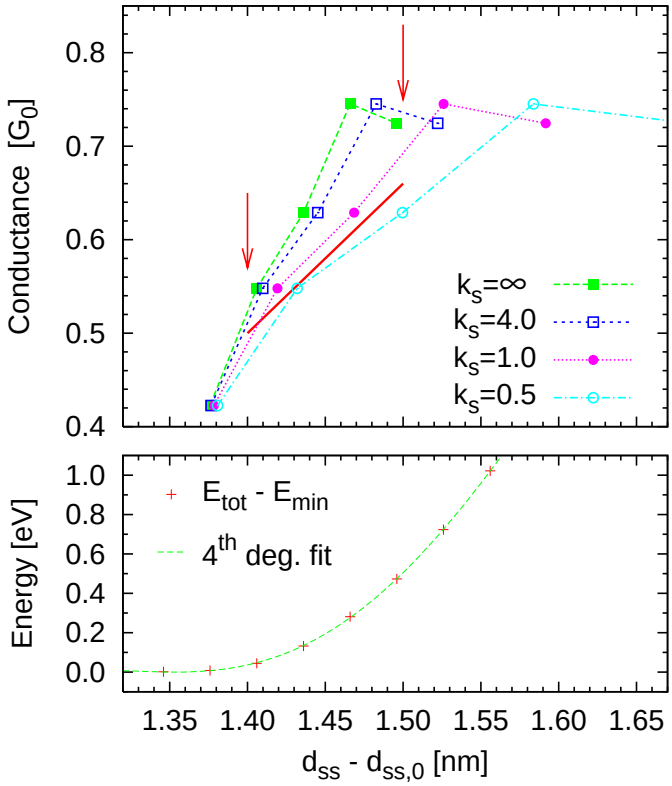

Figure 5.6: *In the upper panel: Ballistic conductance of the LDA 4Au-atom nanocontact with CO in the bridge position as a function of the equivalent tips displacement (see text) for different values of the electrode stiffness k_s (given in eV/Å^2). The arrows point the start and stop points indicated by the arrows in Fig. 5.5 and the solid red line approximates the experimental conductance trace from Ref. 26 as a straight line between those points. In the lower panel: total energy of the optimized nanocontact geometry as a function of the inter-surface distance d_{ss}.*

and the inter-surface distance can be obtained by solving for L in Eq. (5.1); this only requires the knowledge of the total energy of the simulation supercell as a function of d_{ss} and an estimate for the electrode stiffness k_s. Experimental estimates for k_s in Au electrodes have been reported by Rubio-Bollinger et al. [110], on the basis of the non-exponential dependence of the tunneling current on the distance: values in the range 0.3 eV/Å^2 to 3.7 eV/Å^2 have been found, depending on the junction realization.

We then consider the LDA bridge geometry, which we showed to reproduce a qualitatively correct variation of the conductance with strain, and fit $E_{\rm tot}(d_{ss})$ with a 4$^{\rm th}$ degree polynomial. In the lower panel of Fig. 5.6 we report the optimized total energy, $E_{\rm tot}$, computed for a selected set of d_{ss} values, and the corresponding fitting curve: the fit provides a good accuracy in the range of d_{ss} of our interest. From the analytical derivative of the fitted polynomial we estimate the derivative of the total energy with respect to the surface distance, which in turn is used to determine the relation $L(d_{ss}; k_s)$, containing a parametrical dependence on the electrode stiffness k_s. In the upper panel of Fig. 5.6 we plot the conductance as a function of the equivalent electrode distance L for several values of k_s. The case with $k_s = \infty$ is the theoretical conductance trace already shown in Fig. 5.3 and corresponds to infinitely stiff leads, hence the external stress is released totally in the narrowest part of the junction (the

short monatomic chain). This situation is not realistic and a finite stiffness of the leads should be considered. For stiffness value of $4.0\,\mathrm{eV/\AA^2}$, close to the upper limit of the experimental estimate, the slope does not change appreciably, but if we consider a smaller value ($0.5\,\mathrm{eV/\AA^2}$), slightly above the lower limit of the experimental estimate, the slope has a significant change and the conductance increases much more slowly with the contact stretching. The thick solid line in the same figure approximates the last part of the experimental conductance trace (from Ref. 26, also reported in Fig. 5.3) with a linearly increasing conductance. Its slope can be reproduced by our calculated conductance if we assume an electrode stiffness between $0.5\,\mathrm{eV/\AA^2}$ and $1.0\,\mathrm{eV/\AA^2}$, which is in a realistic range according to the experiment [110]. We can conclude that different slopes in the conductance trace obtained when pulling a monatomic Au junction with CO in the bridge position might be explained by assuming different values for the electrode stiffness, which in the experiment can be dependent on the particular nanocontact realization [110].

Conclusions

In this thesis we have studied the adsorption of CO on Pt and Au monatomic chains and on model Au nanocontacts, analyzing the consequences of the adsorption on the electronic structure and on the ballistic transport properties of the chains. Using an infinite chain geometry and a nanocontact geometry made of short chains between surfaces, we have described from first principles (within DFT) the energetics of CO in a few possible adsorption sites (bridge, ontop, and substitutional) and we have discussed the interplay between the electronic structure and the electron transmission across the chain. In particular, we have characterized the system by modeling different properties of the chain, such as the SOC or the geometrical strain, and studied their impact on the energetics of CO and on the transport properties. Moreover, we have discussed the effect of SIEs in the band structure and transmission of Au chains (also in presence of CO) and we have introduced a simple method to include the Hubbard U in the ballistic transport calculations.

In both Pt and Au, depending on the distance between the metal atoms in contact with the molecule, different adsorption geometries of CO are preferred. When the distance is comparable to the equilibrium spacing of the chain, the upright bridge position is energetically favoured; in this regime, chemisorption energies in Pt are sizably larger than in Au (at least 0.6 eV larger). At intermediate distances, a "tilted bridge" configuration has the lowest energy, although it does not correspond to a minimum of the energy. When the metal bond is highly stretched, in Au the preferred configuration is a linear substitutional geometry, corresponding to a very shallow minimum of the energy. In Pt, the energy minimum of the substitutional is less shallow than in Au, but the tilted bridge geometry is slightly lower in energy and the two configurations are almost degenerate for distances larger than the substitutional minimum. We have verified for Pt chains that the inclusion of SOC does not modify this picture of the energetics.

The binding of CO to Pt and Au chains has been characterized by the Blyholder model, in terms of electron donation and backdonation between the molecule and the metal. This picture of the interaction has been illustrated through the DOS projected on CO. As a consequence of the adsorption, new peaks appear in the DOS of CO, corresponding to the formation of bonding-antibonding pairs of 5σ and $2\pi^\star$ states:

the presence of antibonding $5\sigma_{\mathrm{a}}$ (bonding $2\pi^{\star}_{\mathrm{b}}$) states above E_{F} (below E_{F}) can be associated to electron donation (backdonation). The features of these new peaks (their position, intensity, and broadening) and their coupling to the metal states depend strongly on the adsorption site and on the metal.

In presence of CO, the modification of the electronic structure influences the transmission across the chain, which decreases in a site- and metal-dependent way: in the bridge and ontop geometries, d states of the chain which hybridize more strongly with CO are transmitted more poorly than the others (especially in Au), while s states are generally well transmitted except for some particular energies in correspondence of the hybridization peaks in the DOS. In the substitutional geometry instead, only $|m| = 1$ states are partially transmitted across the molecule, thanks to the hybridization with π states. SOC changes the band structure of Pt and Au chains and also their transmission; nevertheless, we have verified that it does not modify qualitatively the SR description of CO adsorption on Pt chains and the related effects on the ballistic conductance. In Pt, the theoretical tipless conductance is essentially the same in the bridge and ontop geometries and corresponds to a slight reduction of the pristine chain conductance, while a much larger reduction is found in the substitutional geometry. In Au, after having removed the spurious d channels from E_{F} by correcting their SIE through the DFT+U approach, a noticeable difference between the bridge and the ontop conductance is found: the ontop geometry has a much smaller conductance because of a ($5\sigma_{\mathrm{a}}$) transmission dip close to E_{F}. The substitutional conductance is still much smaller than the bridge and ontop conductances and is expected to decrease further with the addition of the Hubbard U correction.

The effect of strain has been analyzed considering Au chains at different spacings. We have shown that the site preference prediction towards the bridge site is reinforced in chains with stretched Au-Au bonds and that the transport properties in presence of CO are also sensitive to strain. The transmission of d channels degrades at larger strains, while that of the s channel is still characterized by the presence of dips which can appear, disappear or move in energy, depending on the strain and on the adsorption site. When the chain is stretched, the difference between the bridge and ontop conductances is enhanced: the former slightly increases with strain, while the latter is reduced further, because of the $5\sigma_{\mathrm{a}}$ dip moving closer to E_{F}.

In the model nanocontact, the strain has been studied by varying the distance between the two Au(001) surfaces: the optimized geometries of the short chain with CO adsorbed are not straight nor uniformly spaced. When CO is at the bridge site, at low strains the chain bends towards the molecule, while at larger strains the atoms of the chain are more aligned and the Au-Au bond below CO elongates much more rapidly than the others. When CO is ontop, the chain forms a zigzag geometry, more pronounced at lower strains, with the Au atom below CO displaced towards

the molecule. Nevertheless, the chemisorption energies of CO are comparable to those found in the infinite straight chains, and if the displacement of the Au atom below the ontop CO is allowed also in the infinite chain geometry, we get a fair agreement in the variation of E_{chem} with strain. The striking difference between the bridge and ontop conductance values and their dependence on the strain are stable with respect to the inclusion of the tips, using either abrupt interfaces or smoother junctions between the chain and the surfaces. The bridge geometry, besides being energetically favoured, has a conductance value which is compatible with the position of a peak in the conductance histogram of Au nanocontacts in presence of CO. While the theoretical ontop conductance decreases with strain, the bridge conductance has a positive slope which could explain the experimental increase of the conductance seen while stretching a Au nanocontact.

Acknowledgements

The research work presented in this thesis has been done during my PhD studies in the Condensed Matter Theory Sector at SISSA, under the constant supervision of Prof. Andrea Dal Corso. I wish to thank Andrea for having suggested an interesting topic and for having guided me all the way through this interesting trip inside the physics of nanocontacts and nanowires. I'm also grateful to him for having shared his scientific knowledge and research experience and for his care and patience in the manuscript correction. Alexander Smogunov and Prof. Erio Tosatti have also collaborated in this research project and I want to thank them for their precious help. The computational resources needed for this work have been provided (through SISSA, INFM and other grants) by CINECA in Bologna and by Democritos/SISSA eLab in Trieste.

Thanks to Prof. S. Baroni, for having involved me in the Quantum ESPRESSO team and especially in the School/"adventure" in Santa Barbara, and also to Prof. S. de Gironcoli and Prof. P. Giannozzi, for useful discussions and their help. Thanks to all the people at SISSA who dedicated to me part of their time: all the professors, the PhD students (in particular, Marco, Juan, Yanier, Armin, Giuseppe, Serena, Pilar, Angus, Emine), and postdocs (Baris, Davide R., Riccardo M.) of the Condensed Matter Theory Sector and from other sectors, and also the student secretariat and SIS staff. Giovanni Borghi and Lorenzo Paulatto deserve special thanks for useful and interesting conversations about physics, informatics, and "QE-technicalities".

Fare una lista completa di tutti le altre persone che che vorrei ringraziare per la loro amicizia e vicinanza in questi anni richiederebbe un altro capitolo, quindi, giunto spossato al termine della stesura della presente, mi sottraggo a tale difficile compito. Ricordo con affetto tutti gli ex-compagni di Università a Udine (in particolare Nicola "Re Conean" Tonello e Matteo "Cacit" Lostuzzo per i nostri mitici viaggi "alla garibaldina"), tutti gli altri amici di "vecchia data" e quelli conosciuti all'Oratorio/Associazione "Il Ponte" di Pavia di Udine, l'OraCoro e, non da ultimo, l'Emmaus Ensemble.

Al plui grand ringraciament al va a me mari e a gno pari, par ve crodût simpri in me e vêmi sostignût e volût ben in ducj chescj agns di studis. Un augûr a Daniele e Ilaria pe lôr (ma ancje nestre) piçule Angela.

APPENDIX A

Spin-orbit splitting in atoms: FR-USPP and perturbative results

The Dirac equation gives an accurate quantum-mechanical description of an atom including the relativistic effects, not present in the Schrödinger equation. Relativistic effects are more important close to the nucleus and are stronger for heavier elements.[1] Therefore, the relativistic description of the atomic levels is expected to modify more strongly the energy levels of the innermost shells. However, already in medium weight elements also the outermost shell levels can experience relativistic corrections in the order of 1 eV, which are in the energy scale of the chemical bond and hence might be relevant for the description of molecules and solids.

Instead of solving the computationally expensive Dirac equation for the solid, relativistic effects are customarily included in the non-relativistic equations for solids through the PPs. We have seen in Sec. 2.3 and Sec. 2.4 that scalar-relativistic effects can be included in the KS equation for scalar wavefunctions through the SR-PP, while SOC effects can be incorporated through the FR-PP. The latter kind of PP must be used within a two-component spinors equation, usually applied to describe

[1] Strictly speaking, the Dirac theory of the electron was formulated for one-electron systems. When dealing with many-electron systems, such as any atom with $Z > 1$, we are implicitly referring to the relativistic extension of DFT, see for instance Ref. 111 and 112.

non-collinear magnetism, which requires a considerably larger computational effort to be solved with respect to the standard KS equation, hence spin-orbit couplings are often computed within first-order perturbation theory from the scalar-relativistic solution. In this Appendix we compare the accuracy of these two methods, FR-PP calculations and first-order corrections within perturbation theory, in describing the spin-orbit splitting of the atomic valence orbitals. Our reference values are obtained from the all-electron solutions of the atomic Dirac equation.

A.1 FR-USPP versus perturbative treatment of SOC

As was said in Sec. 2.4, FR-USPPs are designed in such a way that they can reproduce the scattering properties of an atom starting from the large-components of the solutions of the all-electron radial Dirac equation. While the full solutions of the Dirac equation are not eigenstates of the orbital angular momentum L^2, the large and small components of the solutions taken separately are eigenstates both of the total angular momentum squared, J^2, and of L^2 (but with two different eigenvalues l and $l' = l \pm 1$). For each $l > 0$ we can get the spin-orbit splitting from the $j = l + 1/2$ and $j = l - 1/2$ eigenvalues of the Dirac equation (for $l = 0$ only $j = l + 1/2$ is possible and there is no splitting, obviously). If we consider for instance the valence electrons of Pt or Au, the atomic $5d$ level will be split in two levels, $j = 5/2$ and $j = 3/2$, while $6s$ electrons will result in a single, non-split $j = 1/2$ level.

An alternative way of getting spin-orbit splittings proceeds through the Pauli equation for two-component spinors, which can be derived by Taylor-expanding the Dirac equation in $Z\alpha$ (where $\alpha = 1/137.036$ is the fine structure constant and Z the atomic number). The spin-orbit term appears in the Pauli equation correct up to order $(Z\alpha)^2$ and hence we will stop the expansion at this order. For spherically symmetric external potentials, the Pauli equation including spin-orbit coupling can be written as:[2]

$$[H_0 + H_{\rm m} + H_{\rm D} + H_{\rm SO}]|\,\Psi_{l,j,m_j}\rangle = E_{l,j}\,|\,\Psi_{l,j,m_j}\rangle\,, \tag{A.1}$$

where H_0 is the non-relativistic Hamiltonian, $H_{\rm m}$ is the relativistic "mass-velocity" correction (which corresponds to the classical variation of the relativistic mass with velocity), $H_{\rm D}$ is the Darwin term (also called "relativistic s shift"), and $H_{\rm SO}$ is the spin-orbit operator:

$$H_{\rm SO} = \frac{\alpha^2}{2}\left(\frac{1}{r}\frac{{\rm d}V}{{\rm d}r}\right)\mathbf{L}\cdot\mathbf{S}\,. \tag{A.2}$$

[2]We omit here by purpose the dependency of the solution on the principal quantum number, since this does not change the conclusions of the present discussion.

Here the potential $V(r)$ is the radial one-electron potential which appears in the non-relativistic Hamiltonian (external plus Hartree and exchange-correlation potentials). We can separate the radial from the angular dependency by searching for a solution in the following form:

$$\langle \mathbf{r}| \, \Psi_{l,j,m_j} \rangle = R_{l,j}(r) \, \tilde{Y}_{l,j,m_j} \; , \tag{A.3}$$

where the radial part $R_{l,j}(r)$ is a scalar wavefunction which depends on both l and j, while the spin-angle function $\tilde{Y}_{l,j,m_j}$ is a two-component spinor, simultaneous eigenstate of J^2, J_z, L^2, and S^2 (m_j indicates the eigenvalues of J_z, the projection of J along a fixed quantization axis). With this choice we obtain the radial Pauli equation for $R_{l,j}(r)$, which has the same form as Eq. (A.1). The first three terms of the Hamiltonian become [113]:

$$\begin{aligned} H_0 &= -\frac{1}{r^2}\left[\frac{\mathrm{d}}{\mathrm{d}r}\left(r^2\frac{\mathrm{d}}{\mathrm{d}r}\right)\right] + V(r) + \frac{l(l+1)}{r^2} \\ H_{\mathrm{m}} &= -\frac{\alpha^2}{4}\left[E^{(0)} - V(r)\right]^2 \\ H_{\mathrm{D}} &= -\frac{\alpha^2}{4}\left(\frac{\mathrm{d}V}{\mathrm{d}r}\right)\frac{\mathrm{d}}{\mathrm{d}r} \; , \end{aligned}$$

where $E^{(0)}$ is the zero-order (non-relativistic) eigenvalue, while for $l > 0$ the spin-orbit term is given by:[3]

$$H_{\mathrm{SO}} = \begin{cases} -\dfrac{\alpha^2}{4}[\quad -l \quad]\dfrac{1}{r}\dfrac{\mathrm{d}V}{\mathrm{d}r}, & \text{if} \quad j = l + 1/2 \\ -\dfrac{\alpha^2}{4}[\quad l+1 \,]\dfrac{1}{r}\dfrac{\mathrm{d}V}{\mathrm{d}r}, & \text{if} \quad j = l - 1/2 \end{cases} \; .$$

Instead of solving directly the radial Pauli equation, we can proceed in the framework of first-order perturbation theory to get the energy eigenvalues (correct up to order $Z^2\alpha^2$) by computing the expectation value of $[H_{\mathrm{m}} + H_{\mathrm{D}} + H_{\mathrm{SO}}]$ on the eigenstates of the zero-order non-relativistic equation:

$$H_0(r) R_l^{(0)}(r) = E_l^{(0)} R_l^{(0)}(r) \; . \tag{A.4}$$

The first-order corrected eigenvalue for the case with $l = 0$ is then given by:

$$E^{(1)}_{l=0,j=1/2} = E_l^{(0)} + E_{\mathrm{m},l} + E_{\mathrm{D},l} \; , \tag{A.5}$$

[3]The operator $\mathbf{L}\cdot\mathbf{S}$ can be rewritten as $\frac{1}{2}(J^2 - L^2 - S^2)$ and commutes with J^2, L^2, and S^2. Therefore the spin-angle functions in Eq. (A.3) satisfy the following eigenvalue equation: $\mathbf{L}\cdot\mathbf{S}\,|\,\tilde{Y}_{l,j,m_j}\rangle = \frac{1}{2}\big(j(j+1) - l(l+1) - \frac{3}{4}\big)|\,\tilde{Y}_{l,j,m_j}\rangle$, where the eigenvalue equals $l/2$ or $-(l+1)/2$ when, respectively, $j = l + 1/2$ and $j = l - 1/2$.

while for $l > 0$ the spin-orbit split pair of eigenvalues is:

$$E^{(1)}_{l,j=l-1/2} = E^{(0)}_l + E_{\mathrm{m},l} + E_{\mathrm{D},l} - (\,l+1\,)E_{\mathrm{SO},l} \tag{A.6a}$$

$$E^{(1)}_{l,j=l+1/2} = E^{(0)}_l + E_{\mathrm{m},l} + E_{\mathrm{D},l} + (\quad l \quad)E_{\mathrm{SO},l}\ , \tag{A.6b}$$

where the separate contributions to the relativistic correction are given by:

$$E_{\mathrm{m},l} = -\frac{\alpha^2}{4}\int_0^\infty \mathrm{d}r\ r^2 |R^{(0)}_l(r)|^2 \left[E^{(0)}_l - V(r)\right]^2 \tag{A.7a}$$

$$E_{\mathrm{D},l} = -\frac{\alpha^2}{4}\int_0^\infty \mathrm{d}r\ r^2 R^{(0)}_l(r) \left(\frac{\mathrm{d}V}{\mathrm{d}r}\right) \frac{\mathrm{d}R^{(0)}_l}{\mathrm{d}r} \tag{A.7b}$$

$$E_{\mathrm{SO},l} = +\frac{\alpha^2}{4}\int_0^\infty \mathrm{d}r\ r^2 |R^{(0)}_l(r)|^2 \left(\frac{1}{r}\frac{\mathrm{d}V}{\mathrm{d}r}\right)\ . \tag{A.7c}$$

Since the mass-velocity and Darwin contributions do not depend on j, it is sufficient to evaluate $E_{\mathrm{SO},l}$ in order to obtain the spin-orbit splitting of the eigenvalues, ΔE, which is equal to:

$$\Delta E \equiv E^{(1)}_{l,j=l+1/2} - E^{(1)}_{l,j=l-1/2} = (\,2l+1\,)\ E_{\mathrm{SO},l}\ . \tag{A.8}$$

We implemented the relativistic corrections of Eqs. (A.7a-c) in the atomic code `ld1`, which is part of the QUANTUM ESPRESSO distribution [47]. This code already implements the AE and PP solutions of the non-relativistic radial Schrödinger equation and the AE solution of the relativistic radial Dirac equation. The calculation and printout of the first-order corrected eigenvalues, given by Eq. (A.5) and Eqs. (A.6a-b), can be now enabled by setting `relpert=.true.` in the input for a non-relativistic, spin-unpolarized AE calculation with `ld1`. The correction terms in Eqs. (A.7a-c) are written separately on output after the non-relativistic eigenvalue if `verbosity="high"` is set on input.

A.2 Comparison of spin-orbit splittings in isolated atoms

In this section we compare the accuracy of the spin-orbit splittings computed within first-order perturbation theory – given by ΔE in Eq. (A.8) – and the splittings obtained through the relativistic Dirac equation. As a test case we compare the splitting of the valence d electrons ($l = 2$) of the transition metal series of the 3rd row (from Sc, $Z = 21$, to Zn, $Z = 30$), of the 4th row (from Y, $Z = 39$, to Cd, $Z = 48$), and of the 5th row (from Hf, $Z = 72$, to Zn, $Z = 80$), which correspond to the filling of the $3d$, $4d$, and $5d$ shells, respectively. Within this selection of elements, covering a wide

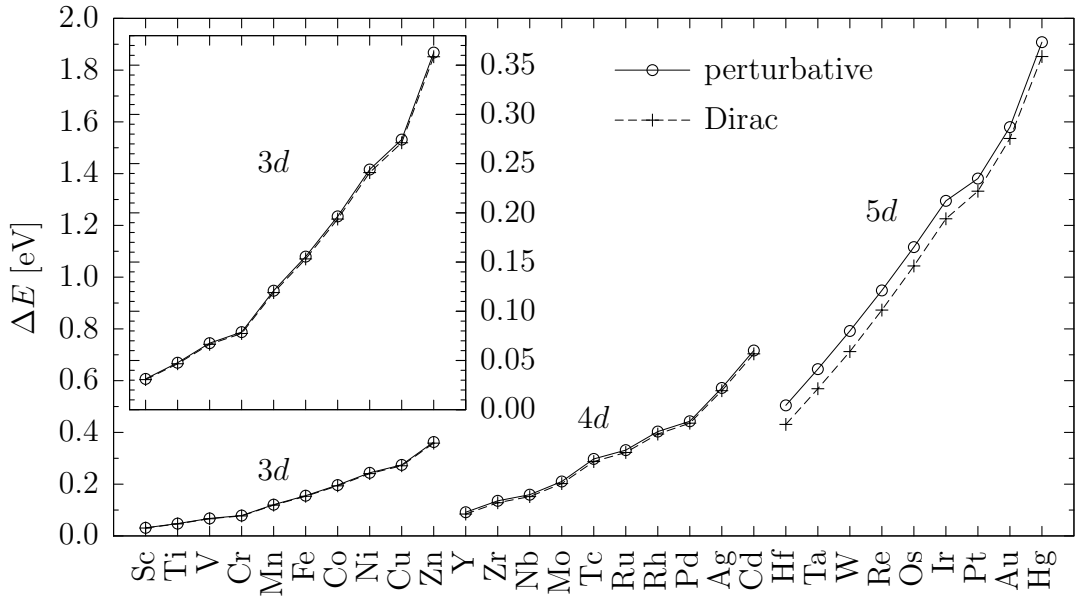

Figure A.1: *Spin-orbit splitting of the energy eigenvalues, ΔE, for the valence d electrons in elements belonging to $3d$, $4d$, or $5d$ transition metal series. Splittings obtained directly from the solution of the relativistic Dirac equation (crosses) or computed within first-order perturbation theory starting from the non-relativistic wavefunctions (circles) are compared. In the inset, ΔE is shown on a magnified scale for the $3d$ elements.*

range of atomic numbers (from $Z = 21$ up to $Z = 80$), the SOC gives rise to energy splittings which span two orders of magnitude.

The splittings of $3d$, $4d$, and $5d$ valence orbitals computed within LDA with the PZ functional [55] are shown in Fig. A.1 (GGA calculations are not reported here since they give very similar results). Within the same row the splitting increases monotonically with Z, while there is an initial drop of the splitting when passing from the last element of a row to the first element of the following (because a more external d shell is in valence). In $3d$ transition elements the splitting goes from about 0.031 eV in Sc to 0.359 eV in Zn and it is described with a reasonable accuracy by first-order perturbation theory (from the inset we can see that the error with respect to the Dirac-relativistic splitting is always below 5meV). The magnitude of relativistic effects in the elements of the $4d$ series is almost doubled with respect to those of the $3d$ series and the errors of the perturbation-theory estimate are about 3 times larger. When going from the $4d$ to the $5d$ series, the elements have much larger atomic numbers and the spin-orbit splittings become of the order of 1 eV (from about 0.43 eV in Hf, up to 1.85 eV in Hg). The error done by discarding higher-order terms in the perturbative expansion are quite significant here and can go up to 75 meV.

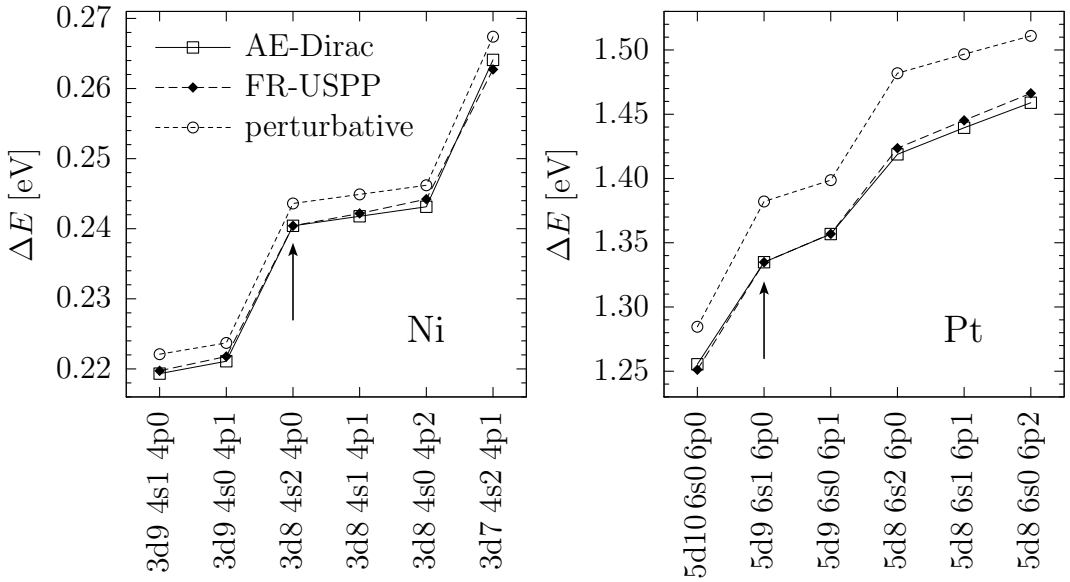

Figure A.2: *Spin-orbit splitting of 3d orbitals in Ni (left side) and 5d orbitals in Pt (right side). Splittings have been obtained either by solving directly the relativistic Dirac equation (squares) or the FR-USPP equation (diamonds), or from relativistic first-order perturbation corrections (circles). We test several electronic configurations with a different filling of the d shell (lines have the only purpose to guide the eye). The configuration pointed by the arrow corresponds to the experimental atomic ground state and was used to generate the PP.*

When using a FR-USPP, the spin-orbit splittings of the valence orbitals coincide with the AE splittings for an atom in the same electronic configuration used to built the PP (which may correspond or not to the ground state). However, the electronic states in the solid are usually different from those in the atom. A common technique to test the so-called "transferability" of the PP consists in comparing the energy eigenvalues of valence orbitals as obtained from PP and AE atomic calculations for a selected set of distinct electronic configurations. The more an electronic test configuration differs from that used to generate the PP the bigger the distance between AE and PP solutions will be.

In order to compare transferability errors of FR-USPPs with the error from the first-order perturbative treatment of relativistic effects, we calculate the spin-orbit splittings for a relatively light atom (Ni) belonging to the $3d$ series and for a much heavier one (Pt) belonging to the $5d$ series in several electronic configurations. Splittings of d valence orbitals are reported in Fig. A.2 (for Ni, on the left, and for Pt, on the right). The FR-PP for Ni exhibits a very good transferability and the largest error in the FR-PP splitting compared to the correct Dirac splitting is about $1.1 \div 1.3$ meV (in the $3d8\,4s0\,4p2$ and $3d7\,4s2\,4p1$ configurations). The errors in the splitting com-

puted from perturbation theory are also in the order of a few meV in Ni. The transferability errors of the FR-PP for Pt are instead larger (up to about 7.3 meV in the $5d8\,6s0\,6p2$ configuration), nevertheless they are of the same order of magnitude as in Ni. The error from the perturbative treatment of SOC, instead, grows considerably when moving from $3d$ elements to $5d$ elements (about one order of magnitude, see also Fig. A.1), therefore the relative accuracy of the spin-orbit splittings obtained from FR-USPPs with respect to those from first-order perturbation theory becomes overwhelming at large Z.

APPENDIX B

Reference calculations

In order to facilitate the description of the interaction of CO with monatomic Pt and Au chains (Chap. 3 and Chap. 4, respectively), in this chapter we briefly describe some equilibrium properties of the isolated CO molecule and of infinite isolated chains, making also a comparison bewteen SR and FR results. If not otherwise specified, the same USPPs and cut-off parameters reported in this section have been used also in the calculations for the CO adsorbed on Pt and Au infinite monatomic chains (Chap. 3 and Chap. 4) or on Au model nanocontacts (Chap. 5).

In all our LDA calculations we used the same PPs as in Ref. 64 for both Pt and Au, while for C and O we generated new USPP with the parameters reported in Ref. 95. Within GGA we generated new SR USPP for all the atoms; the parameters for Pt, C and O are reported in Ref. 95, while for Au we used the same reference configuration and cutoff radii of the LDA PP. In LDA calculations involving Pt and/or CO we describe the KS orbitals using a plane wave basis set with a kinetic energy cut-off of 29 Ry (32 Ry) for the wavefunctions in the SR (FR) case, while for the charge density we use a cut-off of 300 Ry. In LDA calculations for Au (with or without CO adsorbed) we use a cut-off of 32 Ry for the wavefunctions and of 320 Ry for the charge density. In all GGA calculations we always use 32 Ry and 320 Ry

for the wavefunctions and the charge density, respectively. The orbital occupations are broadened using the smearing technique of Methfessel and Paxton [78], with a smearing parameter $\sigma = 0.01$ Ry.

B.1 Isolated CO molecule

The isolated CO molecule has been described here using a cubic supercell of 20 a.u. and the Γ point sampling of the BZ. From the total energy $E_{\rm tot}$ of CO computed as a function of the C-O distance, $d_{\rm C\text{-}O}$, and interpolated with a third degree polynomial to obtain the curve $E_{\rm tot}(d_{\rm C\text{-}O})$, we calculated the equilibrium distance, $d_{\rm C\text{-}O,eq}$, and the intramolecular vibrational frequency, $\omega_{\rm C\text{-}O}$, as the C-O distance and as the second derivative of $E_{\rm tot}(d_{\rm C\text{-}O})$ at its minimum, respectively.

The equilibrium distance and vibrational frequency are reported in Fig. B.1 in the inset: the inclusion of SOC does not change significantly the equilibrium properties of CO, since both C and O are light atoms. LDA data are in good agreement with the experimental data reported in Ref. 114 ($d_{\rm C\text{-}O,eq} = 1.128$ a.u. and $\omega_{\rm C\text{-}O} = 2169.8$ cm^{-1}) and with recent DFT-LDA calculations (USPP calculations: $d_{\rm C\text{-}O,eq} = 1.136$ a.u. and $\omega_{\rm C\text{-}O} = 2169$ cm^{-1} [115]; all-electron: $d_{\rm C\text{-}O,eq} = 1.142$ a.u. and $\omega_{\rm C\text{-}O} = 2169$ cm^{-1} [116]). Within GGA the equilibrium distance slightly increases, while the vibrational frequency is shifted down (previous DFT works reported: $d_{\rm C\text{-}O,eq} = 1.151$ a.u. and $\omega_{\rm C\text{-}O} = 2118$ cm^{-1} [115]; $d_{\rm C\text{-}O,eq} = 1.150$ a.u. and $\omega_{\rm C\text{-}O} = 2105$ cm^{-1} [116]).

The atomization energy $E_{\rm at}$ is estimated by subtracting $E_{\rm tot}(d_{\rm C\text{-}O,eq})$ to the sum of the total energies of isolated C and O atoms[1]. Our SR-LDA result, $E_{\rm at} = 12.8$ eV, is in good agreement with previous DFT-LDA calculations (12.7 eV in Ref. 115 and 12.72 eV in Ref. 116), but overestimates the experimental value (11.24 eV, from Ref. 117). Within SR-GGA we obtain a smaller atomization energy, $E_{\rm at} = 11.8$ eV, a value much closer to the experimental one and still in fair agreement with previous DFT calculations (11.7 eV and 10.88 eV in Refs. 115 and 116, respectively).

The isolated CO molecule has full rotational symmetry around its axis, thus we can use the irreducible representations of the $C_{\infty v}$ symmetry group to label the molecular orbitals, or, equivalently, we can use the expectation value m (m_j) of the orbital angular momentum L (total angular momentum $J = L + S$) projected along the CO axis on the SR wavefunctions (FR spinor wavefunctions). In the SR case the lowest lying bound states have $m = 0$ (σ bonds) or $|m| = 1$ (π bonds), since C and

[1]The total energy of the isolated atoms were calculated in the same supercell and with the same cut-off used for the molecule. The atomic configurations were fixed with the following occupations: $2s^2\,2p^2$ and $2s^2\,2p^4$, for C and O, respectively.

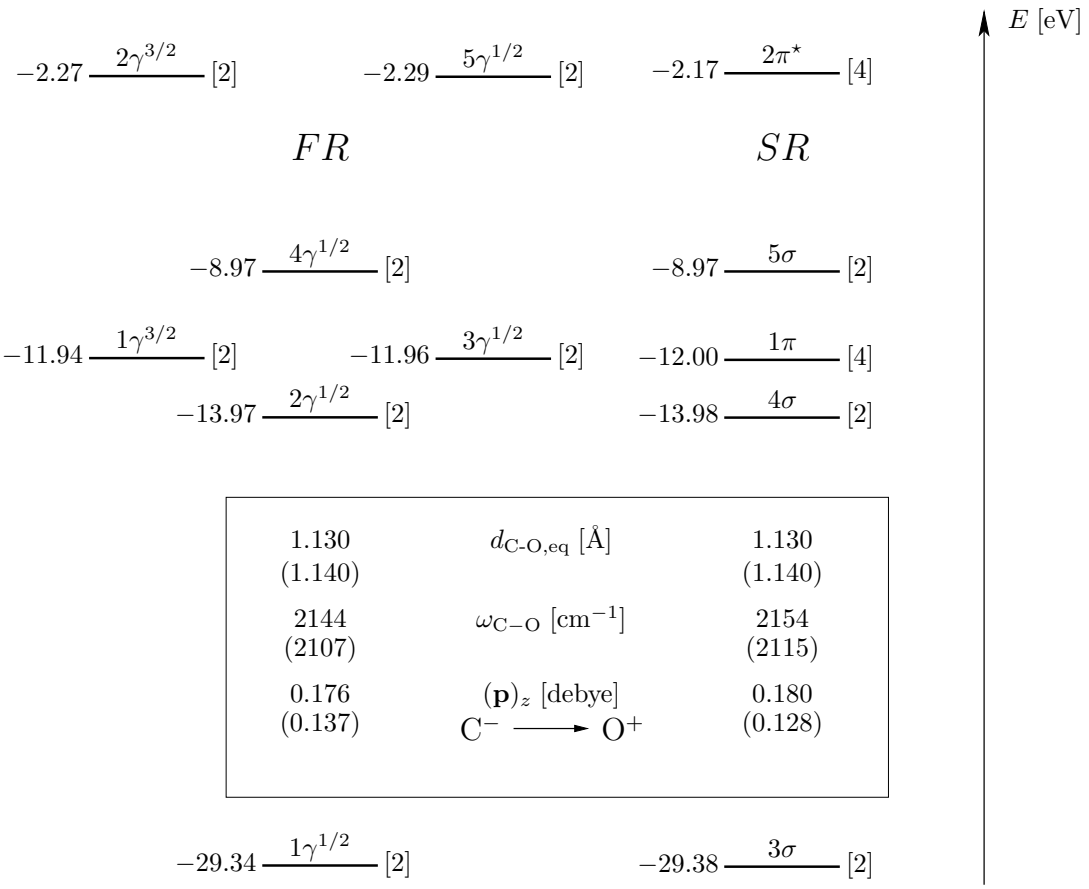

Figure B.1: *SR and FR molecular levels of carbon monoxide (right and left side, respectively). For each level the energy (in eV) and the degeneracy are indicated. LDA (GGA) values for the equilibrium distance, vibrational frequency and electric dipole moment along z are reported in the inset.*

O both have only s and p valence electrons. If the molecular axis is along z, then s and p_z atomic orbitals contribute to the σ levels, while p_x and p_y orbitals form two-fold degenerate π levels. In presence of SOC, SR states with $m = 0$ give rise to FR states with $|m_j| = 1/2$, while SR states with $|m| = 1$ separate into FR states with $|m_j| = 1/2$ or $|m_j| = 3/2$, the former being slightly shifted down in energy with respect to the latter. In Fig. B.1 we show the molecular levels of CO, in both the SR and FR cases (right and left column, respectively). Next to each level we report the corresponding energy eigenvalue and its total degeneracy, which includes (in addition to the geometrical degeneracy, already discussed) the spin degeneracy in the SR case and the degeneracy at $\pm|m_j|$ in the FR case.

In Fig. B.2 we show the SR pseudo wavefunctions calculated at the theoretical equilibrium distance and represented in a plane which contains the CO axis. The

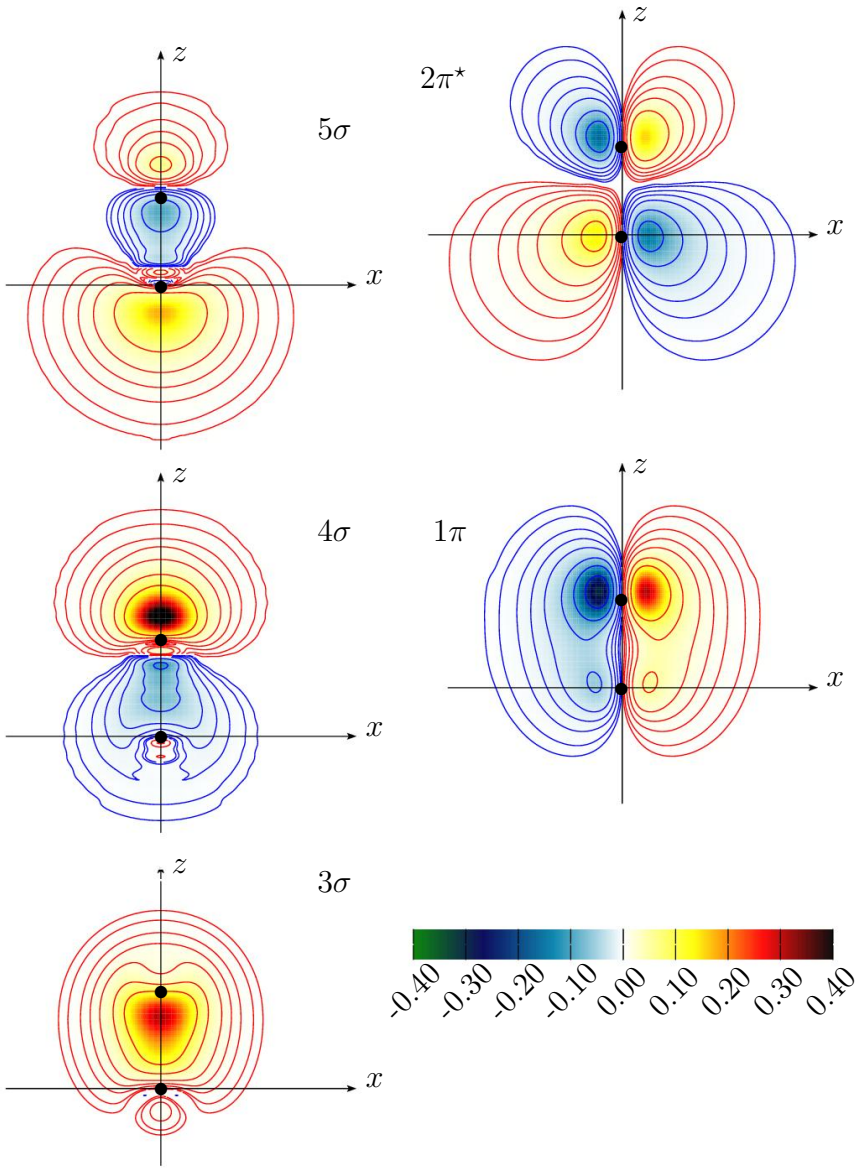

Figure B.2: *Pseudo-wavefunctions of the CO molecule calculated with SR LDA at the equilibrium distance. Dots indicate the atomic positions of C (in the origin) and O (along z), while solid lines are isolevels with the following values of density* ± 0.001, ± 0.002, ± 0.005, ± 0.01, ± 0.02, ± 0.05 *and* ± 0.1 *electrons/(a.u.)*^{3}.

valence orbitals of C and O form three occupied σ states, 3σ, 4σ and 5σ, the latter being the highest occupied molecular orbital (HOMO), and two pairs of two-fold degenerate π states, the occupied 1π and the empty $2\pi^\star$, the latter being the lowest unoccupied molecular orbital (LUMO). It is important here to notice that the HOMO of the molecule has σ-symmetry, while the LUMO has π-symmetry and that they are both characterized by a large charge spread on the C side (for which reason they are

called the "frontier orbitals" of the molecule). We compared the sum of the squared moduli of the FR spinor components (not shown here) with the SR wavefunctions and checked the inclusion of SOC does not modify substantially the electronic charge distribution on the molecule.

We also calculated the electric dipole moment of the molecule,

$$\mathbf{p} = \int \rho(\mathbf{r})\, \mathbf{r}\ \mathrm{d}^3 r\ , \tag{B.1}$$

where $\rho(\mathbf{r})$ is the sum of the ionic and the electronic charge densities. Our SR and FR results, calculated at the respective C-O equilibrium distance, are similar: indeed, the component of $\mathbf{p}$ along the CO axis[2] within LDA is 0.176 debye in the FR case and 0.180 debye in the SR case (0.137 debye and 0.128 debye, respectively, within GGA). Our LDA result agrees with previous DFT calculations within 10% (0.20 debye with USPP [115] and 0.189 debye AE [116]), but largely overestimates the experimental value[3] (0.122 debye in Ref. 118).

B.2 Isolated monatomic Pt and Au chains

Pt and Au monatomic chains have been calculated using a tetragonal cell with longitudinal size (i.e. along the z axis, the chain being aligned in that direction) equal to the interatomic spacing of the chain ($d_{\text{Pt-Pt}}$ or $d_{\text{Au-Au}}$, respectively), while its dimension in the perpendicular directions are fixed to $d_\perp = 18$ a.u. $\simeq 9.5$ Å (enough to ensure convergence of the total energy within 1 mRy). Along the wire direction, the BZ is sampled by a uniform mesh of $\mathbf{k}$-points, while in the perpendicular direction we use the Γ point. We calculate the isolated infinite chain with one metal atom per unit cell and 91 $\mathbf{k}$-points along z, while for supercell calculations (with or without CO) we reduce the number of $\mathbf{k}$-points according to the number of Pt or Au atoms in the cell. More details about the number of atoms per cell and the number of $\mathbf{k}$-points are given in the specific sections.

With these computational parameters we find that the equilibrium interatomic spacing in the isolated straight Pt chain is $d_{\text{chain}} = 2.34$ Å (2.35 Å) within LDA in the SR (FR) case, while a slightly larger value is found with GGA, $d_{\text{chain}} = 2.39$ Å (2.41 Å) in the SR (FR) case. These values are in good agreement with previous PP calculations (SR-GGA: 2.4 Å [119], 2.41 Å [10]) and also with non-magnetic AE

[2]It is the only non-vanishing component, given the rotational symmetry of the molecule. A positive value indicates that the dipole moment is directed from the carbon to the oxygen.

[3]The GGA value is closer to the experimental one mainly because of the larger theoretical equilibrium distance with respect to the LDA value.

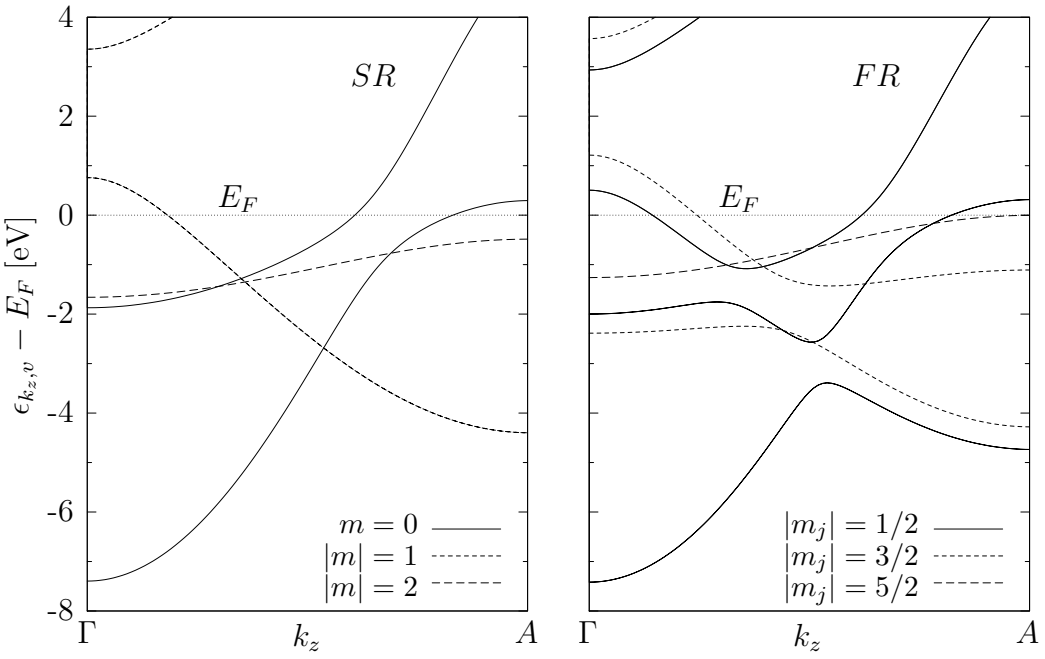

Figure B.3: *On the left (right): SR (FR) electronic band structure (within LDA) of a Pt chain at the equilibrium spacing. Bands are shown for* $0 \leqslant k_z \leqslant 1/2$, *(* k_z *in* $2\pi/a$ *units), and are labelled according to the eigenvalue* m *(*m_j*) of the operator* L_z *(*J_z*).*

calculations (SR-GGA: 2.42 Å [56]; they also consider FR-GGA magnetic configuration, which gives a larger spacing: 2.48 Å). Experimental estimates of bond lengths in tip suspended Pt nanowires have been reported by Smit et al. [6] in the range 2.3 ± 0.2 Å, compatible with the theoretical predictions. In Au chains, we find that the equilibrium interatomic distance is $d_{\text{chain}} = 2.51$ Å within SR-LDA, while a larger value is found with SR-GGA, $d_{\text{chain}} = 2.61$ Å. Previous calculations reported similar values (localized-basis PP-LDA: 2.57 Å [105]; PAW-LDA: $\simeq 2.52$ Å [106]; PAW-LDA: 2.48 Å, PAW-PBE: 2.61 Å [100]; all-electron, FR-GGA: 2.61 Å [56]). In STM and MCBJ experiments with gold nanocontacts, Untiedt et al. [7] have obtained values around 2.5 ± 0.2 Å for the interatomic distances in the atomic chains (in agreement with Smit et al. [6]), in contrast with the much longer distances formerly reported by Ohnishi et al. [4] (in the range $3.6 \div 4.0$ Å).

The isolated straight chain has full rotational symmetry along its axis plus the inversion, corresponding to $D_{\infty h}$ group symmetry.[4] In the SR case the symmetry group of a generic k_z is $C_{\infty v}$, thus we can label KS-eigenstates according to the irreducible

[4]Since we use a tetragonal cell the actual symmetry in the calculations is reduced to D_{4h}, which causes a small splitting between the two degenerate $|m| = 2$ bands. However this splitting can be made arbitrarily small by increasing the d_{cell} separation.

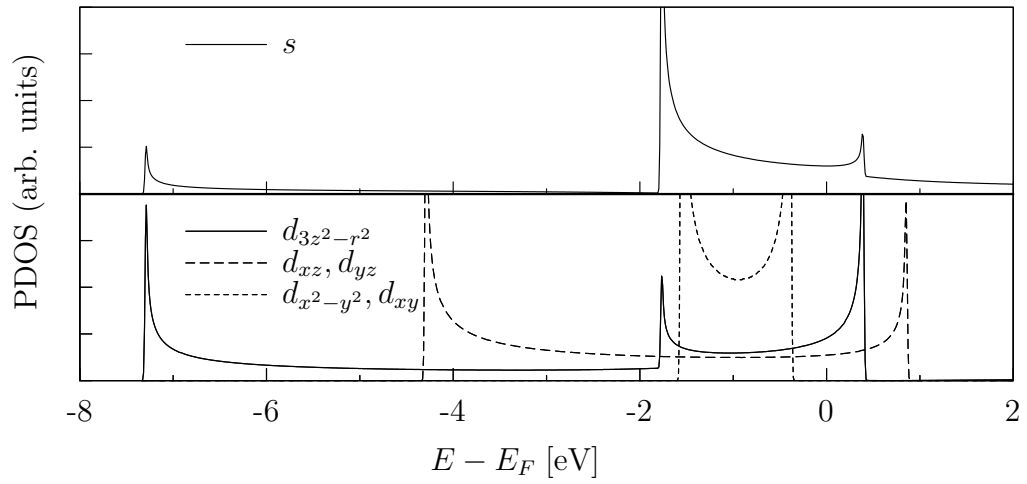

Figure B.4: *PDOS of the SR nanowire projected onto the Pt atomic orbitals. Solid lines in the upper panel (lower panel) indicate the PDOS projected on the s ($d_{3z^2-r^2}$) orbital; dashed (short-dashed) lines in the lower panel indicate the PDOS projected on d_{xz}, d_{yz} ($d_{x^2-y^2}$, d_{xy}) orbitals.*

representations of that group or, equivalently, with integer values m, eigenvalues of the orbital angular momentum projected along the wire axis, L_z. We report in Fig. B.3 (left panel) the SR-LDA band structure of a Pt chain at equilibrium distance; we find a good agreement with previous DFT calculations (see, for instance, Ref. 85). Valence bands are formed by $5d$ and $6s$ orbitals: there are two $m = 0$ bands, resulting from the hybridization of $6s$ and $5d_{3z^2-r^2}$ and characterized by a great bandwidth, a two-fold degenerate $m = 1$ band (derived from d_{xz} and d_{yz}) and a narrower two-fold degenerate[5] $m = 2$ band (derived from d_{xy} and $d_{x^2-y^2}$) entirely below the Fermi energy, $E_{\rm F}$. Since in the SR case each band has an additional degeneracy due to spin (our SR calculations are spin-unpolarized), in total there are 8 channel crossing $E_{\rm F}$, four having $m = 0$ and the other four $|m| = 1$.

We show in Fig. B.4 the electronic PDOS projected on the atomic orbitals of Pt (see Sec. 2.5 for the definition). Projecting onto an atomic orbital having angular momentum eigenvalue m gives a non-vanishing overlap only in those energy ranges spanned by bands which have been labeled with $|m|$ (for $m > 0$, the projections on the orbital with eigenvalue m are equal to those on the orbital with eigenvalue $-m$). The PDOSs have peaks at those energies which correspond to a vanishing value of the first derivative of electronic bands of the matching symmetry (this happens only at $k_z = 0$ and $k_z = 1/2$ in the SR case). Below 0.5 eV the s and $d_{3z^2-r^2}$ orbitals

[5]Because of the tetragonal cell the $|m| = 2$ bands are not exactly degenerate, but we verified that using a cell size $d_\perp \geqslant 18$ a.u. the eigenvalues differ by less than 5 meV.

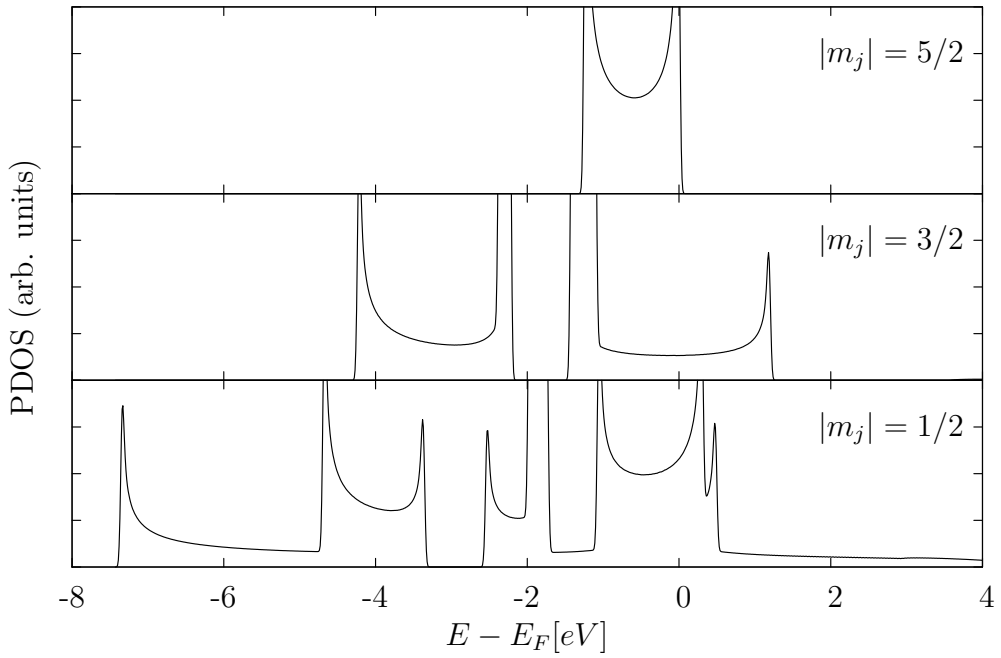

Figure B.5: *PDOS of the FR nanowire projected onto the Pt atomic orbitals. For each value of $|m_j|$, the projections with all possible values of l and j have been summed up.*

hybridize strongly and both give a contribution to the states belonging to the $m = 0$ bands, though the relative weights are different at each energy, while above 0.5 eV only s states are present.

When SOC is considered, the KS-eigenstates of the isolated chain transform according to the irreducible representations of the $C^D_{\infty v}$double group: $\Gamma^{1/2}$, $\Gamma^{3/2}$, $\Gamma^{5/2}$, and so on. Therefore we can label FR states with these representations[6] or, equivalently, with the value m_j of the projection of the total angular momentum along the wire axis, J_z (which, unlike L_z, is a conserved quantity in the FR case). The FR-LDA band structure of the Pt chain is reported in Fig. B.3 (right panel): SR states with $m = 0$ give rise to FR states with $|m_j| = 1/2$, SR states with $|m| = 1$ split into $|m_j| = 1/2$ and $|m_j| = 3/2$ FR states, while SR states with $|m| = 2$ split into $|m_j| = 3/2$ and $|m_j| = 5/2$ FR states [85]. Since in these calculations we did not include the effect of magnetism on the wire, states at $\pm|m_j|$ are degenerate, thus each FR band is two-fold degenerate; in presence of a net magnetization this degeneracy is removed [56].

The PDOS projected onto the FR atomic spinors of Pt are shown in Fig. B.5 (the

[6]In the tetragonal cell the small group of k_z is C^D_{4v} and thus both $\Gamma^{3/2}$ and $\Gamma^{5/2}$ states actually transform according to the same irreducible representation Γ_7.

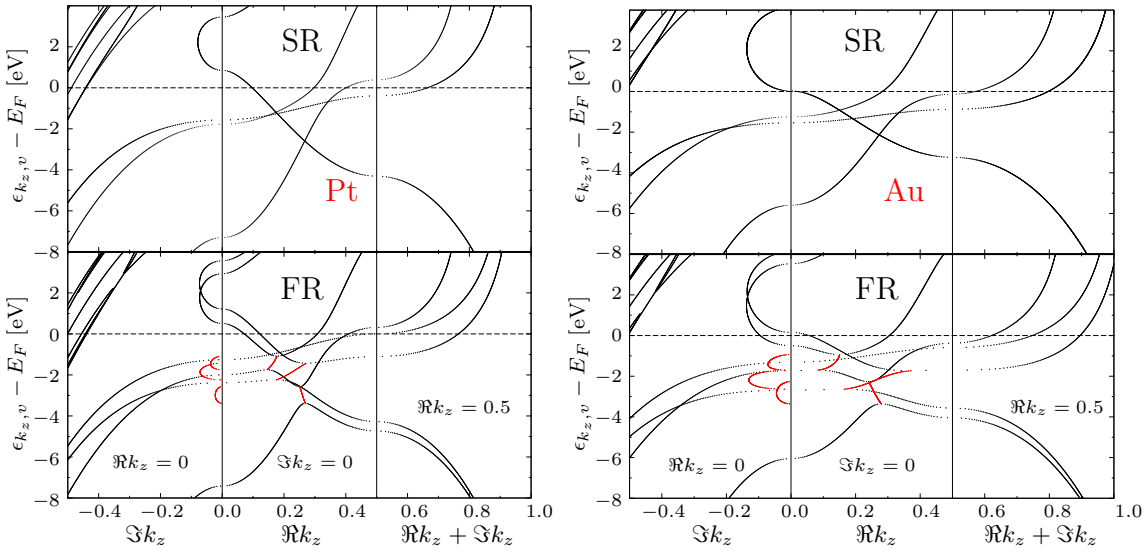

Figure B.6: *Complex band structure of a monatomic chain of Pt (left plot) or Au (right plot) from SR- and FR-LDA calculations (top and bottom panels, respectively). Each plot contains bands at real k_z (central panel), at imaginary k_z (right) and at $k_z = 1/2 + i\kappa$ (left). Bands at complex k_z (colored red) are projected on the left (central) panel for the imaginary (real) part of k_z (always in units of $2\pi/a$).*

projections have been summed up for all values of l and j compatible with a given $|m_j|$). The result is directly related to the SOC-induced splitting and hybridization of the SR bands. The PDOS projected on $|m_j| = 5/2$ orbitals has the shape of the SR $|m| = 2$ PDOS, since the FR $|m_j| = 5/2$ band derives from the SR $|m| = 2$ band. The PDOS projected on $|m_j| = 3/2$ orbitals can be understood as the sum of the SR $|m| = 1$ and $|m| = 2$ PDOSs, plus an hybridization gap because of an anticrossing of two $|m_j| = 3/2$ bands. The PDOS projected on $|m_j| = 1/2$ orbitals can also be explained in terms of sum of SR PDOSs and hybridization gaps, but there are three $|m_j| = 1/2$ bands that anticross so that a larger number of peaks and gaps arise in this case.

The CBS of a Pt chain, which is reported in Fig. B.6 (left side) for the SR case (panels at the top) and for the FR case (panels at the bottom), has been computed with the same unit cell used for the band structures and PDOSs shown previously in this section. The solutions of the scattering equation, Eq. (2.92), with a real k_z are shown in the central panels and coincide within the numerical accuracy to the band structures computed by solving the usual KS equation at different k_z points (compare Fig. B.6 with Fig. B.3). Solutions with imaginary k_z either belong to parabolic bands or form loops which connect bands with the same symmetry. In the FR case, solutions with a complex k_z are also possible: this kind of solutions connect a maximum and a

minimum of pairs of anticrossing real bands through small loops and can be projected on the real and imaginary planes as in Fig. B.6, where $\Re(k_z)$ and $\Im(k_z)$ indicate the real and imaginary part of k_z, respectively.

The symmetry considerations done for Pt chains apply to Au chains as well and the electronic structure of Au chains is similar to that just described of Pt chains, since also in Au there are $5d$ and $6s$ electrons in valence. The main differences between the band structures of the two metals can be understood by comparing the corresponding CBSs at real k_z, both reported in the central panels of Fig. B.6 (Pt on the left and Au on the right). Au chains have one more electron per atom and hence d bands are almost completely filled in this case. In the SR case at the equilibrium spacing only the upper edge of the $|m| = 1$ bands is touching E_{F}, while all the other d bands are completely occupied. Since the equilibrium distance in Au chains is larger than in Pt chains, the band dispersion is smaller in the former and, within LDA, the lowest valence band edge is at $-5.6\,\mathrm{eV}$ below E_{F} (instead in Pt it was at $-7.4\,\mathrm{eV}$).

The inclusion of SOC in the Hamiltonian has the same effect on the band structure of the Au chain as that seen for the Pt chain (Fig. B.3). The SOC-induced splitting of $|m| = 1$ bands brings the upper edge of the $|m_j| = 3/2$ band about 0.1 eV above E_{F}, thus enhancing the tendency for magnetism. This effect can be considered spurious since, as we elucidate in Sec. 4.5, the self-interaction error of d electronic states is responsible for the wrong position of those SR bands (which according to LDA+U calculations, which can partially remove the SIE, should be lower in energy).

List of Acronyms

STM	Scanning Tunneling Microscope
HRTEM	high-resolution transmission electron microscope
MCBJ	mechanically controllable break-junction
AFM	atomic force microscope
UHV	ultra-high vacuum
DFT	density-functional theory
KS	Kohn-Sham
LDA	local density approximation
LSDA	local spin density approximation
GGA	generalized gradient approximation
SOC	spin-orbit coupling
SIE	self-interaction error
SIC	self-interaction correction
EE	exact exchange
BZ	Brillouin zone
IBZ	irreducible Brillouin zone
PBC	periodic boundary condition
CBS	complex band structure
DOS	density of states
PDOS	projected-density of states

PW	plane wave
WF	Wannier function
PP	pseudopotential
USPP	ultrasoft pseudopotential
PAW	projector augmented-wave
AE	all-electron
PS	pseudo
SR	scalar-relativistic
FR	fully-relativistic

Bibliography

[1] S. Datta, *Electronic Transport in Mesoscopic Systems*, Cambridge Studies in Semiconductors Physics and Microelectronic Engineering (Cambridge University Press, Cambridge, 1995).

[2] Y. V. Sharvin, Sov. Phys.-JETP **21**, 655 (1965), [Zh. Eksp. Teor. Fiz. 48, 984-985 (1965)].

[3] N. Agraït, A. L. Yeyati, and J. M. van Ruitenbeek, Phys. Rep. **377**, 81 (2003).

[4] H. Ohnishi, Y. Kondo, and K. Takayanagi, Nature (London) **395**, 780 (1998).

[5] A. I. Yanson, G. R. Bollinger, H. E. van den Brom, N. Agraït, and J. M. van Ruitenbeek, Nature (London) **395**, 783 (1998).

[6] R. H. M. Smit, C. Untiedt, A. I. Yanson, and J. M. van Ruitenbeek, Phys. Rev. Lett. **87**, 266102 (2001).

[7] C. Untiedt, A. I. Yanson, R. Grande, G. Rubio-Bollinger, N. Agraït, S. Vieira, and J. van Ruitenbeek, Phys. Rev. B **66**, 085418 (2002).

[8] V. Rodrigues, J. Bettini, P. C. Silva, and D. Ugarte, Phys. Rev. Lett. **91**, 096801 (2003).

[9] H. Häkkinen, R. N. Barnett, A. G. Scherbakov, and U. Landman, J. Phys. Chem. B **104**, 9063 (2000).

[10] S. R. Bahn and K. W. Jacobsen, Phys. Rev. Lett. **87**, 266101 (2001).

[11] A. Grigoriev, N. V. Skorodumova, S. I. Simak, G. Wendin, B. Johansson, and R. Ahuja, Phys. Rev. Lett. **97**, 236807 (2006).

[12] A. Thiess, Y. Mokrousov, S. Heinze, and S. Blügel, Phys. Rev. Lett. **103**, 217201 (2009).

[13] S. R. Bahn, N. Lopez, J. K. Nørskov, and K. W. Jacobsen, Phys. Rev. B **66**, 081405(R) (2002).

[14] M. Valden, X. Lai, and D. W. Goodman, Science **281**, 1647 (1998).

[15] H. Häkkinen, R. N. Barnett, and U. Landman, J. Phys. Chem. B **103**, 8814 (1999).

[16] M. Mavrikakis, P. Stoltze, and J. K. Nørskov, Catal. Lett. **64**, 101 (2000).

[17] A. Kolmakov, Int. J. Nanotechnol. **5**, 450 (2008).

[18] R. N. Barnett, H. Hakkinen, A. G. Scherbakov, and U. Landman, Nano Letters **4**, 1845 (2004).

[19] R. H. M. Smit, Y. Noat, C. Untiedt, N. D. Lang, M. C. van Hemert, and J. M. van Ruitenbeek, Nature (London) **419**, 906 (2002).

[20] D. Djukic, K. S. Thygesen, C. Untiedt, R. H. M. Smit, K. W. Jacobsen, and J. M. van Ruitenbeek, Phys. Rev. B **71**, 161402(R) (2005).

[21] M. Kiguchi, R. Stadler, I. S. Kristensen, D. Djukic, and J. M. van Ruitenbeek, Phys. Rev. Lett. **98**, 146802 (2007).

[22] S. Csonka, A. Halbritter, G. Mihály, E. Jurdik, O. I. Shklyarevskii, S. Speller, and H. van Kempen, Phys. Rev. Lett. **90**, 116803 (2003).

[23] S. Csonka, A. Halbritter, and G. Mihály, Phys. Rev. B **73**, 075405 (2006).

[24] S. Csonka, A. Halbritter, G. Mihály, O. I. Shklyarevskii, S. Speller, and H. van Kempen, Phys. Rev. Lett. **93**, 016802 (2004).

[25] C. Untiedt, D. M. T. Dekker, D. Djukic, and J. M. van Ruitenbeek, Phys. Rev. B **69**, 081401(R) (2004).

[26] M. Kiguchi, D. Djukic, and J. M. van Ruitenbeek, Nanotechnology **18**, 035205 (2007).

[27] W. H. A. Thijssen, D. Marjenburgh, R. H. Bremmer, and J. M. van Ruitenbeek, Phys. Rev. Lett. **96**, 026806 (2006).

[28] F. D. Novaes, A. J. R. da Silva, E. Z. da Silva, and A. Fazzio, Phys. Rev. Lett. **96**, 016104 (2006).

[29] M. Strange, K. S. Thygesen, and K. W. Jacobsen, Phys. Rev. B **73**, 125424 (2006).

[30] Y. García, J. Chem. Phys. **131**, 014702 (2009).

[31] N. Nilius, T. M. Wallis, and W. Ho, Phys. Rev. Lett. **90**, 186102 (2003).

[32] N. Oncel, W. J. van Beek, J. Huijben, B. Poelsema, and H. J. Zandvliet, Surf. Sci. **600**, 4690 (2006).

[33] D. Kockmann, B. Poelsema, and H. J. W. Zandvliet, Phys. Rev. B **78**, 245421 (2008).

[34] D. E. P. Vanpoucke and G. Brocks, preprint **arXiv:0909.0729v1** (2009), URL `http://arxiv.org/abs/0909.0729`.

[35] O. Gurlu, O. A. O. Adam, H. J. W. Zandvliet, and B. Poelsema, Appl. Phys. Lett. **83**, 4610 (2003).

[36] D. E. P. Vanpoucke and G. Brocks, Phys. Rev. B **77**, 241308 (2008).

[37] F. D. Novaes, A. J. R. da Silva, E. Z. da Silva, and A. Fazzio, Phys. Rev. Lett. **90**, 036101 (2003).

[38] C. Zhang, R. N. Barnett, and U. Landman, Phys. Rev. Lett. **100**, 046801 (2008).

[39] N. V. Skorodumova and S. I. Simak, Phys. Rev. B **67**, 121404 (2003).

[40] N. V. Skorodumova, S. I. Simak, A. E. Kochetov, and B. Johansson, Phys. Rev. B **75**, 235440 (2007).

[41] S. B. Legoas, D. S. Galvão, V. Rodrigues, and D. Ugarte, Phys. Rev. Lett. **88**, 076105 (2002).

[42] M. Di Ventra, S. T. Pantelides, and N. D. Lang, Phys. Rev. Lett. **84**, 979 (2000).

[43] N. Sai, M. Zwolak, G. Vignale, and M. Di Ventra, Phys. Rev. Lett. **94**, 186810 (2005).

[44] C. Toher, A. Filippetti, S. Sanvito, and K. Burke, Phys. Rev. Lett. **95**, 146402 (2005).

[45] K. S. Thygesen and A. Rubio, in *The Oxford Handbook of Nanoscience and Technology*, edited by A. V. Narlikar and Y. Y. Fu (Oxford University Press, 2010), vol. 1, chap. 23.

[46] P. Lucignano, R. Mazzarello, A. Smogunov, M. Fabrizio, and E. Tosatti, Nat. Mater. **8**, 563 (2009).

[47] P. Giannozzi, S. Baroni, N. Bonini, M. Calandra, R. Car, C. Cavazzoni, D. Ceresoli, G. L. Chiarotti, M. Cococcioni, I. Dabo, et al., J. Phys.: Condens. Matter **21**, 395502 (2009), URL `http://www.quantum-espresso.org`.

[48] A. E. Kochetov and A. S. Mikhaylushkin, Eur. Phys. J. B **61**, 441 (2008).

[49] A. Calzolari, C. Cavazzoni, and M. Buongiorno Nardelli, Phys. Rev. Lett. **93**, 096404 (2004).

[50] M. Strange, I. S. Kristensen, K. S. Thygesen, and K. W. Jacobsen, J. Chem. Phys. **128**, 114714 (2008).

[51] F. Xu, R. Li, J. Zhang, Z. Qian, Z. Shen, X. Zhao, and S. Hou, Physica E **35**, 168 (2006).

[52] G. Blyholder, J. Phys. Chem. **68**, 2772 (1964).

[53] B. Hammer, Y. Morikawa, and J. K. Nørskov, Phys. Rev. Lett. **76**, 2141 (1996).

[54] A. Föhlisch, M. Nyberg, P. Bennich, L. Triguero, J. Hasselström, O. Karis, L. G. M. Pettersson, and A. Nilsson, J. Chem. Phys. **112**, 1946 (2000).

[55] J. P. Perdew and A. Zunger, Phys. Rev. B **23**, 5048 (1981).

[56] A. Delin and E. Tosatti, Phys. Rev. B **68**, 144434 (2003).

[57] M. Wierzbowska, A. Delin, and E. Tosatti, Phys. Rev. B **72**, 035439 (2005).

[58] M. Cococcioni and S. de Gironcoli, Phys. Rev. B **71**, 035105 (2005).

[59] S. L. Dudarev, G. A. Botton, S. Y. Savrasov, C. J. Humphreys, and A. P. Sutton, Phys. Rev. B **57**, 1505 (1998).

[60] O. Bengone, M. Alouani, P. Blöchl, and J. Hugel, Phys. Rev. B **62**, 16392 (2000).

[61] G. Sclauzero, A. Dal Corso, A. Smogunov, and E. Tosatti, in preparation.

[62] H. J. Choi and J. Ihm, Phys. Rev. B **59**, 2267 (1999).

[63] A. Dal Corso and A. Mosca Conte, Phys. Rev. B **71**, 115106 (2005).

[64] A. Dal Corso, Phys. Rev. B **76**, 054308 (2007).

[65] R. Wiesendanger, *Scanning Probe Microscopy and Spectroscopy* (Cambridge University Press, Cambridge, 1994).

[66] Y. Kondo and K. Takayanagi, Phys. Rev. Lett. **79**, 3455 (1997).

[67] M. Büttiker, IBM J. Res. Dev. **32**, 317 (1988).

[68] J. L. Costa-Krämer, N. García, and H. Olin, Phys. Rev. B **55**, 12910 (1997).

[69] N. W. Ashcroft and N. D. Mermin, *Solid State Physics*, The Science of the Solid State (Holt, Rinehart and Winston, New York, 1976).

[70] P. Hohenberg and W. Kohn, Phys. Rev. **136**, 864 (1964).

[71] W. Kohn and L. J. Sham, Phys. Rev. **140**, 1133 (1965).

[72] W. Kohn, Rev. Mod. Phys. **71**, 1253 (1999).

[73] D. M. Ceperley and B. J. Alder, Phys. Rev. Lett. **45**, 566 (1980).

[74] D. C. Langreth and J. P. Perdew, Phys. Rev. B **15**, 2884 (1977).

[75] J. P. Perdew, K. Burke, and M. Ernzerhof, Phys. Rev. Lett. **77**, 3865 (1996).

[76] J. Ihm, A. Zunger, and M. L. Cohen, J. Phys. C **12**, 4409 (1979).

[77] H. J. Monkhorst and J. D. Pack, Phys. Rev. B **13**, 5188 (1976).

[78] M. Methfessel and A. T. Paxton, Phys. Rev. B **40**, 3616 (1989).

[79] D. R. Hamann, M. Schlüter, and C. Chiang, Phys. Rev. Lett. **43**, 1494 (1979).

[80] L. Kleinman and D. M. Bylander, Phys. Rev. Lett. **48**, 1425 (1982).

[81] D. Vanderbilt, Phys. Rev. B **41**, 7892(R) (1990).

[82] A. Pasquarello, K. Laasonen, R. Car, C. Lee, and D. Vanderbilt, Phys. Rev. Lett. **69**, 1982 (1992).

[83] T. Oda, A. Pasquarello, and R. Car, Phys. Rev. Lett. **80**, 3622 (1998).

[84] R. Gebauer, S. Serra, G. L. Chiarotti, S. Scandolo, S. Baroni, and E. Tosatti, Phys. Rev. B **61**, 6145 (2000).

[85] A. Dal Corso, A. Smogunov, and E. Tosatti, Phys. Rev. B **74**, 045429 (2006).

[86] A. Smogunov, A. Dal Corso, and E. Tosatti, Phys. Rev. B **70**, 045417 (2004).

[87] K. S. Thygesen and K. W. Jacobsen, Phys. Rev. B **72**, 033401 (2005).

[88] P. A. Khomyakov and G. Brocks, Phys. Rev. B **74**, 165416 (2006).

[89] V. I. Anisimov and O. Gunnarsson, Phys. Rev. B **43**, 7570 (1991).

[90] V. I. Anisimov, J. Zaanen, and O. K. Andersen, Phys. Rev. B **44**, 943 (1991).

[91] A. I. Liechtenstein, V. I. Anisimov, and J. Zaanen, Phys. Rev. B **52**, 5467(R) (1995).

[92] P. E. Blöchl, Phys. Rev. B **50**, 17953 (1994).

[93] G. Sclauzero (2006), M.Sc. ("Laurea Magistrale") thesis, University of Udine.

[94] G. Sclauzero, A. Dal Corso, A. Smogunov, and E. Tosatti, in *Frontiers of Fundamental and Computational Physics: Ninth International Symposium* (AIP, Melville, NY, 2008), vol. 1018, pp. 201–204.

[95] G. Sclauzero, A. Dal Corso, A. Smogunov, and E. Tosatti, Phys. Rev. B **78**, 085421 (2008).

[96] P. Feibelman, B. Hammer, J. Norskov, F. Wagner, M. Scheffler, R. Stumpf, R. Watwe, and J. Dumesic, J. Phys. Chem. B **105**, 4018 (2001).

[97] H. Orita, N. Itoh, and Y. Inada, Chem. Phys. Lett. **384**, 271 (2004).

[98] A. Smogunov, A. Dal Corso, A. Delin, R. Weht, and E. Tosatti, Nat. Nanotechnol. **3**, 22 (2008).

[99] A. Smogunov, A. Dal Corso, and E. Tosatti, Phys. Rev. B **78**, 014423 (2008).

[100] E. Zarechnaya, N. Skorodumova, S. Simak, B. Johansson, and E. Isaev, Comp. Mat. Sci. **43**, 522 (2008).

[101] Y. Miura, R. Mazzarello, A. Dal Corso, A. Smogunov, and E. Tosatti, Phys. Rev. B **78**, 205412 (2008).

[102] X. Wu, L. Senapati, S. K. Nayak, A. Selloni, and M. Hajaligol, J. Chem. Phys. **117**, 4010 (2002).

[103] F. Mehmood, A. Kara, T. S. Rahman, and C. R. Henry, Phys. Rev. B **79**, 075422 (2009).

[104] N. E. Singh-Miller and N. Marzari, Phys. Rev. B **80**, 235407 (2009).

[105] D. Sánchez-Portal, E. Artacho, J. Junquera, P. Ordejón, A. García, and J. M. Soler, Phys. Rev. Lett. **83**, 3884 (1999).

[106] N. V. Skorodumova, S. I. Simak, A. E. Kochetov, and B. Johansson, Phys. Rev. B **72**, 193413 (2005).

[107] M. Okamoto and K. Takayanagi, Phys. Rev. B **60**, 7808 (1999).

[108] R. H. M. Smit, C. Untiedt, G. Rubio-Bollinger, R. C. Segers, and J. M. van Ruitenbeek, Phys. Rev. Lett. **91**, 076805 (2003).

[109] L. de la Vega, A. Martín-Rodero, A. L. Yeyati, and A. Saúl, Phys. Rev. B **70**, 113107 (2004).

[110] G. Rubio-Bollinger, P. Joyez, and N. Agraït, Phys. Rev. Lett. **93**, 116803 (2004).

[111] A. K. Rajagopal and J. Callaway, Phys. Rev. B **7**, 1912 (1973).

[112] A. H. MacDonald and S. H. Vosko, J. Phys. C **12**, 2977 (1979).

[113] F. Herman and S. Skillman, *Atomic Structure Calculations* (Prentice-Hall, Inc., Englewood Cliffs, New Jersey, 1963).

[114] G. Herzberg and J. W. T. Spinks, *Molecular Spectra and Molecular Structure*, vol. 1 (Prentice-Hall, New York, 1966).

[115] F. Favot, Ph.D. thesis, EPFL, Lausanne (2000).

[116] B. G. Johnson, P. M. W. Gill, and J. A. Pople, J. Chem. Phys. **98**, 5612 (1993).

[117] P. van Klooster, N. J. Trappeniers, and S. N. Biswas, Physica B & C **97**, 65 (1979).

[118] J. S. Muenter, J. Mol. Spectrosc. **55**, 490 (1975).

[119] J. Fernandez-Rossier, D. Jacob, C. Untiedt, and J. J. Palacios, Phys. Rev. B **72**, 224418 (2005).